Service and Limit State Performance of RC Beams with High-Strength Reinforcement

by

John Nicholas Hardisty

A dissertation submitted in partial satisfaction for the requirements of the degree of

Doctor of Philosophy

in

Engineering – Civil and Environmental Engineering

in the

Graduate Division

Of the

University of California, Berkeley

Committee in charge:

Professor Jack P. Moehle, Chair

Professor Matthew J. DeJong

Professor David R. Brillinger

Summer 2019

Service and Limit State Performance of RC Beams with High-Strength Reinforcement

by

John Nicholas Hardisty

Abstract

Service and Limit State Performance of RC Beams with High-Strength Reinforcement
by
John Nicholas Hardisty
Doctor of Philosophy in Engineering – Civil and Environmental Engineering
University of California, Berkeley
Professor Jack P. Moehle, Chair

An experimental and analytical research program was conducted to characterize performance of concrete beams longitudinally reinforced with high-strength steel subjected to monotonic loading. Performance was evaluated at both service and limit states.

Experimental tests were conducted in two series of four beams each. In each series, two beams were reinforced with Grade 60 steel and two with Grade 100 steel. All beams were designed to ultimately fail in flexure. In Series 1, failure of beams was expected at high longitudinal strains. For this series, the tensile-to-yield strength ratio of the longitudinal steel (T/Y) was varied to study its effects on beam performance. In Series 2, failure was expected at low longitudinal steel strains. The strain in the steel at the crushing strain of concrete was the variable under investigation for this test series. Load-deflection relations, strain distributions, and plastic deformations for beams in each series were compared with one another to evaluate relative performance. For the Series 1 tests with low reinforcement ratio and, hence, large reinforcement strain at failure, a reduction in T/Y caused a reduction in the spread of plasticity and, consequently, a reduction in displacement capacity. For the Series 2 tests with high reinforcement ratio, deformation capacity was reduced as net tensile strain was reduced. For a given value of net tensile strain, and for a given value of the difference between net tensile strain and yield strain, the beams with Grade 100 reinforcement had equal or greater deformation capacity than the beams with Grade 60 reinforcement. Considering service-level response, typical techniques for evaluating beam performance, such as crack widths and deflections in the elastic range, were adequate for assessing behavior of beams independent of steel grade.

Moment redistribution is a concept that allows designers to shift the static moment envelope by allowing for nonlinearity at certain sections. In the present study, an analytical program examined moment distribution capacity through finite-element models. Beams in the

analytical study had longitudinal reinforcement of Grade 60 and 100, with T/Y and aspect ratios spanning typical design values, which were variables identified as critical for determining moment-redistribution capability based on a theoretical derivation. The boundary condition for all beams was fixed-fixed and transverse reinforcement was provided to allow the formation of a mechanism starting with hinging at the fixed ends followed by hinging at the beam center. Input parameters for the models evaluated as part of this study were informed by the results of the experimental investigation. The theoretical moment-redistribution calculation was demonstrated to be conservative based on the output from these analyses. A relationship bounding percent allowable moment redistribution based on net tensile strain is proposed for grades of steel higher than Grade 60.

To Ana,
For patience and distractions.

ACKNOWLEDGEMENTS

I owe this to Ana, who provided the encouragement and time to finish this work.

I'd also like to acknowledge my adviser, Jack P. Moehle. Without his guidance, knowledge, and patience, I don't think I would be the engineer I am today. He made this endeavor an enjoyable experience, and ensured my enthusiasm persisted throughout.

I would like to thank Jonathan D. Bray, David R. Brillinger, Filip C. Filippou, Khalid M. Mosalam, and Deborah A. Nolan for serving as part of my qualifying examination and dissertation committees, with particular thanks to the latter for her last-minute efforts during my qualifying exam.

Laboratory tests were conducted in the Structural Research Laboratory of the Department of Civil and Environmental Engineering at University of California, Berkeley. I would like to give credit to the capable contributions of laboratory staff Matt Cataleta, Llŷr Griffith, Phillip Wong, and Cruz Carlos. Matt and his relative Shiloh Cataleta were especially helpful both inside and outside the lab, and for that I will be forever thankful.

Several graduate and undergraduate students contributed to the construction and testing program, including Duy To, Carlos Arteta, Isaac Williams, Edmond Yi, Pablo Azcona, Connie Chen, Judy Guo, Annie Zheng, Angela Tarng, and Sarah Stirniman. At Purdue University, Santiago Pujol, Lucas Laughery, Ash Puranam, Will Pollalis, Kinsey Skillen, and Lupe Molina helped test reinforcement.

The Charles Pankow Foundation and ACI Foundation provided financial support. Commercial Metals Company (CMC) and Nucor Corporation Seattle donated reinforcement used in the test specimens. Clark Construction Group and The Conco Companies constructed the test specimens as an in-kind contribution. The project benefitted greatly from discussion and advice from our Industry Advisory Committee comprising Dominic Kelly (Simpson Gumpertz & Heger), Andy Taylor (KPFF Consulting Engineers), Loring Wyllie (Degenkolb Engineers), and Ron Klemencic (Magnusson Klemencic Associates).

Last, I would like to thank my parents, John and Teresa. Your constant encouragement, love, and support have played just as much a part getting me to the start of this as they have getting me to the end of it. Thank you for all I have.

TABLE OF CONTENTS

LIST OF FIGURES

LIST OF TABLES

NOTATION

A_s : tension steel area

c : depth to neutral axis

d : effective depth

E_c : concrete elastic modulus

E_{shi} : steel initial elastic modulus at the onset of strain-hardening

f'_c : concrete compressive strength

f_s : steel stress

f_y : steel yield stress

f_{su} : ultimate steel stress

h : beam height

k_i : instantaneous ratio of neutral axis depth to effective depth

k_u : ultimate ratio of neutral axis depth to effective depth

k_y : ratio of neutral axis depth to effective depth at yield

ℓ : span from support to beam center (typ.)/beam span

ℓ_1 : shear span for Series 2 beams

ℓ_2 : constant-moment span for Series 2 beams

ℓ_p : plastic-hinge length

ℓ_{pi} : instantaneous plastic-hinge length

M_e : elastic moment

M_i : instantaneous moment

M_u : ultimate moment

M_o : static moment

M_{ou} : ultimate static moment

M_y : yield moment

ΔM_y : difference between yield moment and elastic moment

$P_{0.004}$: load corresponding to the maximum compressive fiber of concrete reaching a strain of 0.004 as calculated by moment-curvature analysis

$P_{first\ yield}$: load corresponding to first yielding of steel as calculated by moment-curvature analysis

P_y : applied load at midspan at yield

R : moment redistribution

w_e : elastic distributed load

w_o : distributed load

w_{ou} : ultimate distributed load

w_y : distributed load at yield

Δ_i : instantaneous midspan deflection

Δ_u : ultimate midspan deflection

Δ_y : midspan deflection at yield

ε_{cu} : concrete crushing strain

ε_s : steel strain

ε_{sf} : steel fracture strain

ε_{sh} : steel strain at the onset of strain hardening

ε_{si} : instantaneous steel strain

ε_{su} : steel uniform-elongation strain

ε_t : net tensile strain in steel

ε_y : steel strain at yield

ρ : tensile longitudinal reinforcement ratio

ρ' : compressive longitudinal reinforcement ratio

θ_p : plastic rotation

ϕ_i : instantaneous curvature

ϕ_u : ultimate curvature

ϕ_y : yield curvature

1. Introduction

1.1. Motivation

The use of higher-grade reinforcing steel has the potential benefit of reducing material quantities, thereby leading to reduced reinforcement congestion and reduced construction costs in reinforced concrete construction. Several steel mills in the United States can produce reinforcing steel of Grade 100 (nominal yield strength of 100 ksi) and higher. However, at the time of this writing, none of these higher grades can match the benchmark mechanical properties of Grade 60 A706 steel. A common characteristic is that the higher grades have reduced elongation capacity. Additionally, some higher grades have reduced ratio of tensile (T) to yield (Y) strengths. The reduced elongation and reduced T/Y raise questions about the performance characteristics of reinforced concrete construction that uses the higher-grade reinforcement.

1.2. Literature Review

1.1.1. High-Strength Reinforcement in Beams

The year 1911 saw the first development of provisions specific to reinforcing bars in the United States. This was the year that ASTM A15, which defined Grades 33 and 55, was first published (FEMA 273, 1997). Bars used as steel reinforcement were required to satisfy minimum mechanical properties as early as early as NACU4-1910, a predecessor to ACI 318 and ACI 318-41, the first version of ACI 318 that required reinforcement to follow the aforementioned standard. Grade limits set for longitudinal reinforcing steel in ACI 318-71 are essentially the same as those specified in ACI 31-14. The use of up to Grade 80 longitudinal reinforcement is permitted except in special seismic systems, where this limit is set at Grade 60. There has been hesitation to allow higher grades of steel for use as reinforcement due to insufficient test data and concerns related to decreases in strain-hardening and strain capacity as steel grade increases. Experimental programs considering tests of beams reinforced with high-strength steel are summarized in the following paragraph.

To gain information related to crack control across different reinforcement grades, Hognestad (1962) tested 36 concrete beams with reinforcement yield stresses between 45 and 110 ksi. Results showed that crack width was proportional to bar stress, regardless of reinforcement grade. Sugano et al. (1990) tested two beam-column subassemblies with the beams having both longitudinal and transverse reinforcement yield stresses of either 85 or 125 ksi. In both cases, reported beam drifts (measured as total displacement divided by the length from the point of maximum moment to the point of inflection) were over 5%. Kimura et al. (1993) tested seven cantilevers with longitudinal and transverse reinforcement yield stresses of 115 ksi. Again, beam drifts were reported to be greater than 5%. Aoyama (2001) tested a series of beams with high and normal-strength reinforcement. subject to reversed cycling loading. A beam with T/Y equal to 1.11 exhibited strength loss at a drift ratio of about 2.2%, while similar strength loss was displayed at a drift of 5.6% for a specimen with T/Y of 1.33. For a given reinforcement strain, a lower T/Y corresponded to lower drift, suggesting that inelastic strain, and plastic-hinge length, were more concentrated. Yotakhong (2003) tested four beams with yield stresses ranging from 62 to 124 ksi. Drift ratios at maximum load ranged from 2.5 to 4.3% and techniques for estimating the flexural response of beams with conventional-strength reinforcement were deemed adequate for beams with higher-strength longitudinal steel. Pfund (2012) reports tests of four specimens reinforced with longitudinal steel of Grade 60 through 120. Each specimen comprised two equal-length beams connected to a block. In these tests, all specimens proved capable of sustaining drift ratios of at least 5%. Seven beams subjected to displacement reversals were tested and analyzed by Tavallali (2011). Reinforcement yield stresses were 60 and 97 ksi. All specimens were designed to have the same flexural strength, so the quantity $A_s f_y$ was equal for all cases. All beams achieved a drift ratio of at least 5% and beams reinforced with high-strength steel showed approximately 25% more yield displacement than those with conventional reinforcement. Cheng and Giduquio (2014) performed cyclic tests of three cantilever beams with reinforcement of Grades 60 to 100. The specimen with Grade 60 reinforcement began to lose strength at a drift ratio around 4%, which was matched by both other beams with higher-strength reinforcement. To (2018) reports cyclic test of beams reinforced with normal and high-strength reinforcement. Specimens were designed such that the quantity $A_s f_y$ was constant between specimens. Actual yield stresses varied from 64.5 to 120 ksi with T/Y ranging from 1.17 to 1.48. All specimens achieved drift ratios between 4.5 and 6.5% with no clear connection between drift capacity and yield stress or T/Y, and calculated plastic-hinge lengths varied from 1.13 to 2 times the member depth.

1.1.2. Strain Limits

Values of net tensile strain (strain in extreme layer of longitudinal tension steel at nominal strength) defining the transition zone between compression and tension-controlled members for strength-reduction factors were proposed by Mast (1992), placed into an appendix in ACI 318-95, and finally adopted in ACI 318-02 with slight changes. Prior to this provision, strength-reduction factors were based on member type and had no dependence on net tensile strain, though net tensile strain limits were set indirectly through limits on reinforcement ratio. Net tensile strain values defining the transition zone were based on the yield strain at the lower end, and a conservative envelope of net tensile strain values calculated based on balanced failure for Grade 60 and 75 prestressed and plain concrete sections at the higher end. These limits are still present in ACI 318-14. Mast et al. (2008) proposed a relationship between the strength-reduction factor and net tensile strain defining the transition zone limits as 0.004 and 0.009 for Grade 100 reinforcement based on theoretical analyses of beams using MMFX steel reinforcing bars.

Most studies related to the use of high-strength reinforcement have investigated beams with traditional tensile reinforcement ratios around 1-1.5% for Grade 60 specimens, with reinforcement ratios for higher-strength companion tests scaled according to their ratio of yield strengths to keep ρf_y constant. The author knows of only one investigation of the performance of highly-reinforced members. Puranam (2018) conducted tests of continuous beams reinforced with steel of grades between 60 and 120 designed to reach net tensile strains of 0.005 to 0.006. Results demonstrated that even at low design net tensile strains (0.005-0.006), beams were capable of redistributing moments between 6 and 25%, and reached drift ratios from 2.5 to 4%. The need to consider the increased shear associated with the additional load as part of moment redistribution was also identified as part of these tests.

1.1.3. Moment Redistribution

ACI 318-63 was the first standard adopted in the United States to feature moment redistribution provisions. In this code, moment redistribution was limited to 10%, but only if certain criteria were met related to tensile, compressive, and balanced reinforcement ratios. Moment redistribution limits were mathematically derived by Cohn (1965) and related the percent change in moment to the tensile, compressive, and balanced reinforcement ratios. Mattock (1959) was among the first to observe that crack widths and deflections at service loads for beams that had been designed for high levels (up to 25%) of moment redistribution were no more severe than beams that had been designed for the elastic-theory distribution of moments. Taerwe and Espion (1989) later demonstrated this held true for beams under service loading for sustained periods. Based on the relationship from Cohn (1965) and the serviceability information from Mattock (1959), moment redistribution limits were defined for ACI 318-71 that allowed redistribution up to 20%, again provided certain criteria based on reinforcement ratios were met. With conservative assumptions, Mattock (1983) used this derivation to develop representative capacity curves for beams reinforced with different grades of steel. Mast (1992) later transformed the representative capacity curves to their current form and proposed new limits for moment redistribution based on sections reinforced with Grades 60 and 80 reinforcement, which were codified in ACI 318-02, and persist in ACI 318-14. The new provisions related available and limiting moment redistribution to net tensile strains rather than reinforcement ratios.

Cohn (1986) summarized the results of 159 prestressed and conventionally-reinforced concrete beams that demonstrated redistribution of moments ranging from 0 to 89%, recognizing the degree of plastic rotation required and shape of the moment diagram played a role in the degree of redistribution. Eligehausen and Langer (1987) consolidated data and conclusions drawn from 350 experiments of conventionally-reinforced beams, and described the effect that T/Y, uniform elongation strain, and shear cracking have on the spread of plasticity. Using portions of these data sets, efforts were made by these researchers and others to explain the test results using deformation compatibility at the ultimate load, but it was concluded that only a complete analysis based on moment-curvature response could predict behavior. Statistical analyses were also considered for setting lower-bounds for plastic rotations necessary for moment redistribution. Ultimately, using the plastic-hinge approach was determined to provide a simple and appealing solution for fixed-fixed end conditions as long as the method was limited to cases where excessive structural deformations were not expected, yielding did not occur in the span first, and sufficient ductility of the yielded section was provided by low to moderate amounts of reinforcement (away from the balanced point). The latter authors also suggested bounds for T/Y and net tensile strain required for certain levels of moment redistribution.

1.3. Objectives and Scope

In all cases except for Hognestad (1962), tests of beams with high-strength reinforcement reported here involved subjecting them to displacement reversals. In most cases, the subjects under investigation in the experiments reported above were strength and deformation capacity and did not focus on the spread of plasticity before failure. Of the studies cited, To (2018) was the only study to quantify the plastic-hinge length in a reinforced concrete beam using experimental results. Numerous studies exist to this end for members with Grade 60 reinforcement. The reason for this may be due to deformation limits imposed by structural standards, like the 2 to 2.5% story drift ratio bound ASCE 7-10 depending on the risk category of the structure, being given experimental focus. Thus, the goal of tests of beams with high-strength longitudinal steel, typically, has been to compare performance to similar specimens but reinforced with Grade 60 steel at high drift ratios, pushing the reinforcement towards its limiting strain. This has led to a paucity in comparative tests of beams with higher longitudinal reinforcement ratios, which fail due to concrete crushing at relatively lower steel strains. It has also led to limiting steel strain being a primary consideration rather than T/Y. Additionally, the topic of moment redistribution has remained largely quiet since being introduced in its current form. This study aims to provide insight in these areas where data are lacking. Namely, for beams with longitudinal steel of different yield stresses and T/Y, comparative evaluation of plastic spread and rotation capacity at high net tensile strains, rotation capacity at low net tensile strains, and revisiting and revising moment-redistribution provisions to allow for the use of steels of higher grade than 80.

This dissertation summarizes the tests of eight beams conducted at the University of California, Berkeley, in addition to the results of nonlinear finite-element models, to investigate the viability of using high-strength steel as the longitudinal reinforcement in reinforced concrete. As part of the experimental program, beams of both normal-strength and high-strength steel were tested monotonically in two series of four beams each. All beams were designed such that ultimate failure would be flexural in nature. In Series 1, failure of beams was expected at high longitudinal steel strains while in Series 2, failure was expected at low longitudinal steel strains. Informed by the experimental results, nonlinear finite-element models were used to conduct additional parametric studies examining the relative impact of different variables on moment-redistribution capacity.

1.4. Organization

Chapter 2 presents an overview of the experimental program, including both Series 1 and Series 2. Chapter 3 provides details and results for Series 1 beams while Chapter 4 provides details and results for the beams in Series 2. Chapter 5 discusses aspects of the tests related to serviceability. Chapter 6 discusses moment redistribution as it relates to the tests as well as the computer models. Chapter 7 summarizes the study and presents the main conclusions. Appendix A provides details of the test program including construction, test apparatus, materials, instrumentation, test procedure, and data reduction. Appendix B contains crack patterns and photos. Appendix C outlines information related to the nonlinear finite-element analyses.

2. Experimental Program Overview

2.1. Series 1

Series 1 consists of four beams tested in the idealized configuration shown in Figure 2.1. The intent of Series 1 was to investigate the effects of T/Y on the spread of plasticity in monotonically loaded reinforced-concrete beams. By so doing, the inelastic rotation capacity and moment redistribution capability could be indirectly assessed. The beams were selected to have relatively low longitudinal reinforcement ratios, such that failure would be dominated by large flexural tensile strains in the longitudinal reinforcement.

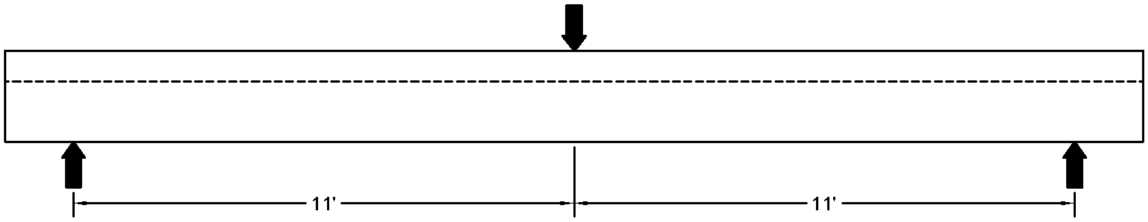

Figure 2.1: Idealized Series 1 loading elevation

The four beams in Series 1 consisted of two beams each of Grade 60 and Grade 100 longitudinal tension reinforcement, one having a relatively low T/Y and another having a relatively high T/Y. Figure 2.2 presents the tensile stress-strain relations based on monotonic tension tests of coupons for all steel types. The label on a particular curve corresponds to the beam with longitudinal tension steel having relation. Table 2.1 shows which T/Y corresponds to which beam and also lists their net tensile strains. The beam naming convention is as follows: “1” indicates the beam series, “GB” stands for gravity beam (to indicate that the beams were tested monotonically), “H” or “L” indicates whether the beam had the higher or lower T/Y ratio for that grade, and the last number indicates the steel grade.

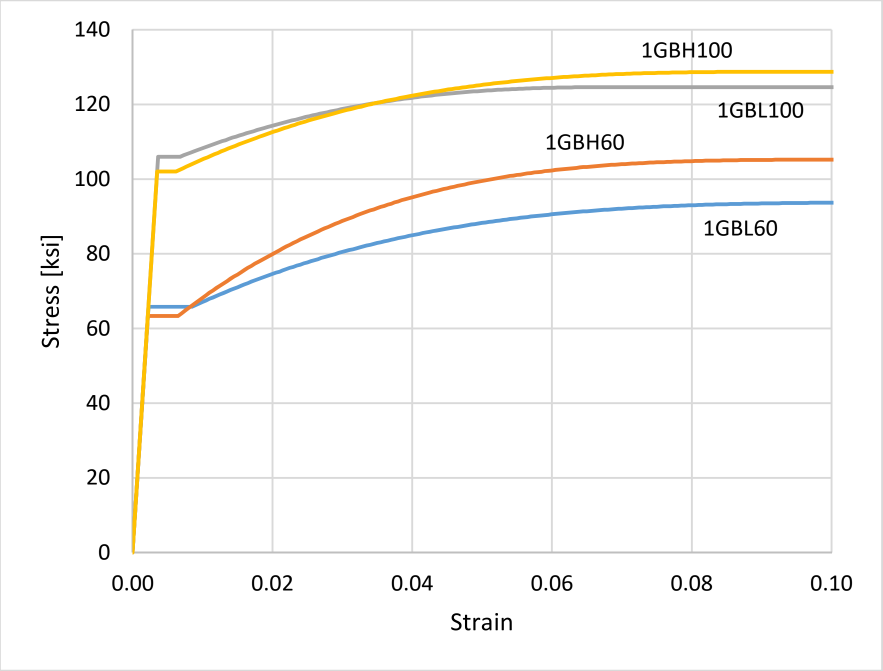

Figure 2.2: Series 1 tensile stress-strain relations for steel models based on coupon tests

Table 2.1: Series 1 T/Y ratios and net tensile strains

	T/Y	ε_t
1GBL60	**1.42**	0.025
1GBH60	**1.66**	0.024
1GBL100	**1.18**	0.024
1GBH100	**1.26**	0.026

2.2. Series 2

Series 2 consists of a total of four beams tested in the idealized configuration provided in Figure 2.3. The intent of Series 2 was to investigate the rotational capacity of beams having relatively large amounts of longitudinal reinforcement such that failure would be controlled by crushing of the flexural compression zone shortly after reinforcement yielding.

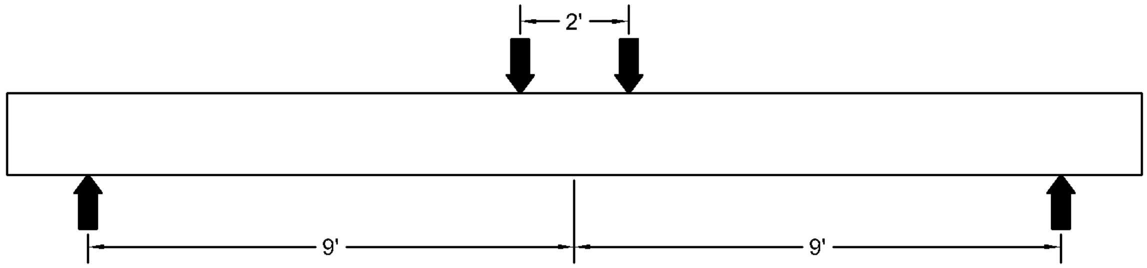

Figure 2.3: Idealized Series 2 loading elevation

ACI 318-14 limits the maximum reinforcement ratio indirectly through limits on the net tensile strain. Figure 2.4 shows the relationship between net tensile strain ε_t and strength reduction factor dictated by ACI 318-14 (solid black line) as well as the design net tensile strain for each beam in this series. These values were calculated using methods outlined in ACI 318-14, except using measured values of f'_c and f_y. The black dotted line is the lower limit for beams defined in ACI 318-14. In ACI 318-14, strains separating the compression-controlled, transition, and tension-controlled regions of the trilinear relationship are based on members reinforced with Grade 60 steel. The intent of Series 2 was to investigate where the net tensile strain limits for Grade 100 reinforcement should be set. Two beams used Grade 60 longitudinal reinforcement (actual yield stress of 66.7 ksi) and two beams used Grade 100 longitudinal reinforcement (actual yield stress 109 ksi). Figure 2.5 presents the tensile stress-strain relations based on monotonic tension tests of coupons for both steel types. The label on a particular curve corresponds to the beams with longitudinal tension steel having relation. For each grade, two different design values of ε_t were selected. The calculated values for the net tensile strains of each of the beams in Series 2 are in Table 2.2 beside the T/Y ratio of the bottom longitudinal steel. The beam naming convention is as follows: "2" indicates the beam series, "GB" indicates gravity beam (to show that the beams were tested monotonically), "H" or "L" indicates whether the beam had the higher or lower ε_t for that grade, and the last number indicates the steel grade.

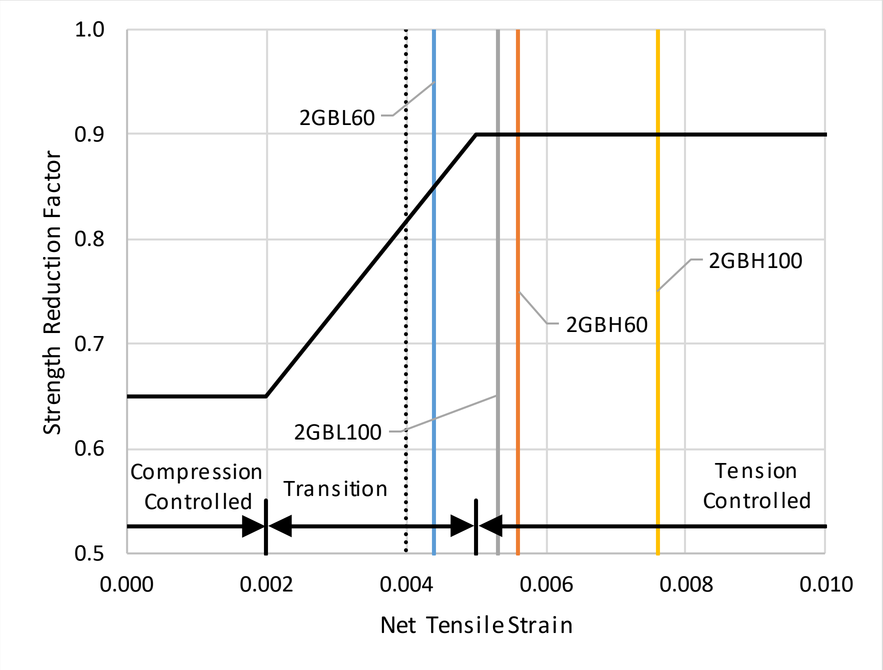

Figure 2.4: Series 2 net tensile strains for beam models

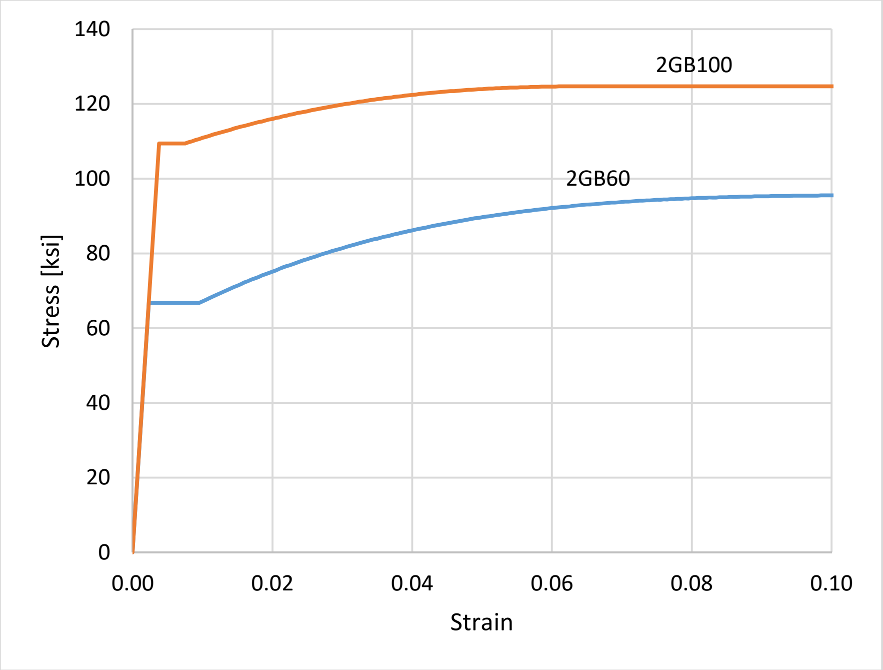

Figure 2.5: Series 2 tensile stress-strain relations for steel models based on coupon tests

Table 2.2: Series 2 T/Y ratios and net tensile strains

	T/Y	ε_t
2GBL60	1.43	**0.0044**
2GBH60	1.43	**0.0056**
2GBL100	1.14	**0.0053**
2GBH100	1.14	**0.0076**

3. Series 1 Tests

3.1. Cross Sections

The beams had the same cross section at all sections along the beam span without bar cutoffs or splices. Cross sections of the beams are provided in Figure 3.1. All beams had the same gross concrete cross-sectional dimensions. Flexural tension reinforcement was positioned at the bottom of the beams. Bar areas for the flexural tension reinforcement of the different beams were selected such that nominal product $A_s f_y$ was nearly the same for all beams. For the beams with Grade 60 reinforcement, longitudinal reinforcement comprised two No. 10 bars, such that $A_s f_y = 2 \times 1.27\text{ in.}^2 \times 60\text{ ksi} = 152\text{ k}$. For the beams with Grade 100 reinforcement, longitudinal reinforcement comprised two No. 8 bars, such that $A_s f_y = 2 \times 0.79\text{ in.}^2 \times 100\text{ ksi} = 158\text{ k}$.

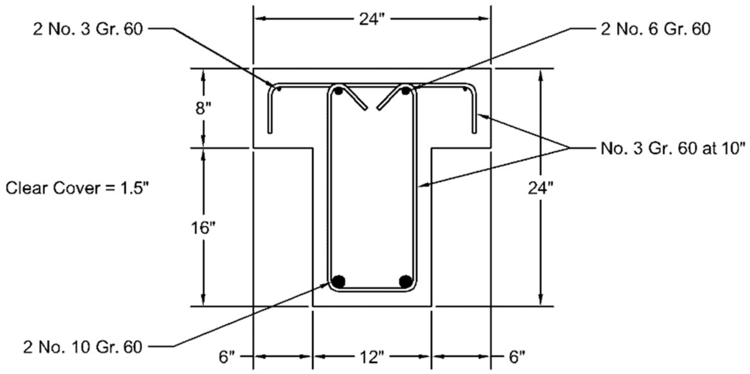

(a) 1GBL60 and 1GBH60

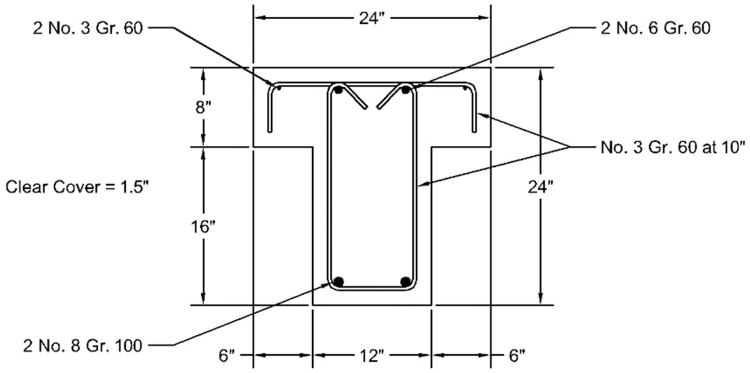

(b) 1GBL100 and 1GBH100

Figure 3.1: Series 1 cross sections

3.2. Loading

Each beam was simply supported near its ends. Loading comprised self-weight (test specimen plus loading apparatus) plus an applied concentrated force at midspan, as shown in Figure 3.2. Figure 3.3 shows a beam in the test apparatus. Information related to the load frame and support conditions is given in Appendix A.2.2. The loading protocol was to increase the concentrated load applied monotonically until failure of the beam was observed or the displacement limit of the test setup was reached, pausing at certain points to mark and measure cracks. Details of the loading are covered in Appendix A.5.

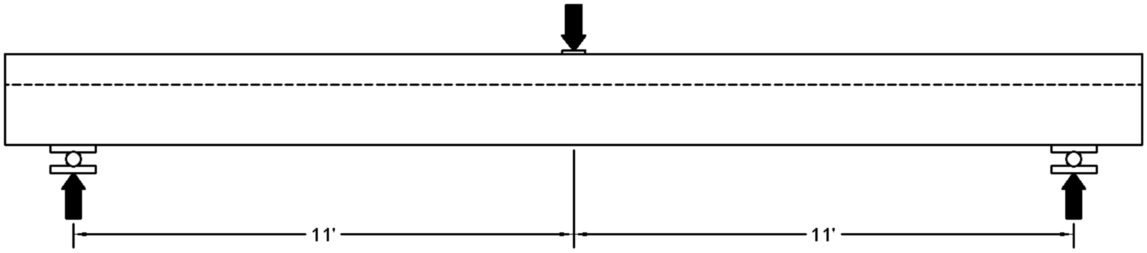

Figure 3.2: Series 1 loading elevation

Figure 3.3: Series 1 beam during testing

3.3. Test Results

3.3.1. Failure Mechanisms

Failure was defined as the occurrence of increasing deflection with decreasing load in addition to concrete spalling or reinforcement rupture. Tests of beams 1GBH60 and 1GBH100 were terminated before the beams could reach failure due to the limit of the test setup, beam 1GBL60 experienced concrete crushing followed by increasing deflection with decreasing load, and beam 1GBL100 failed by fracture of the longitudinal steel. Though some concrete in beam 1GBH60 was crushed, the load did not decrease with additional deflection. Photos and crack patterns for all beams are in Appendix B.1.3.

3.3.2. Load-Deflection Relations

Figure 3.4 provides measured relations between the applied midspan load and the resulting midspan deflection, where the applied load includes the jacking load and the weight of the loading apparatus. Figure 3.5 provides normalized load-deflection curves for all four beams in Series 1, where the load is normalized by the load corresponding to development of the beam nominal moment strength, calculated using the ACI 318-14 equivalent-stress-block method, except using measured values of f'_c and f_y. Moment due to self-weight was subtracted from the computed capacity, so normalization is relative to the remainder. Deflection is normalized by half the beam span. Drops in load indicating relaxation of the beam load resistance due to pause of loading for crack marking and measuring during the test have been removed for clarity. Non-normalized data for all beams without these portions removed are presented in Appendix B.1.1.

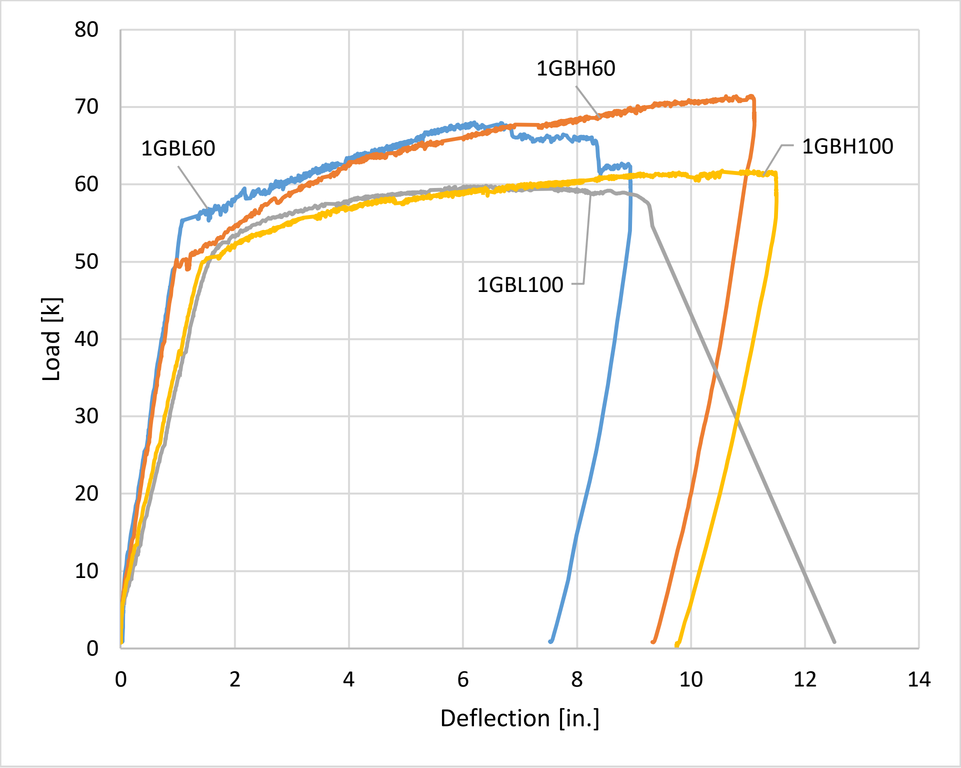

Figure 3.4: Series 1 load-deflection relations

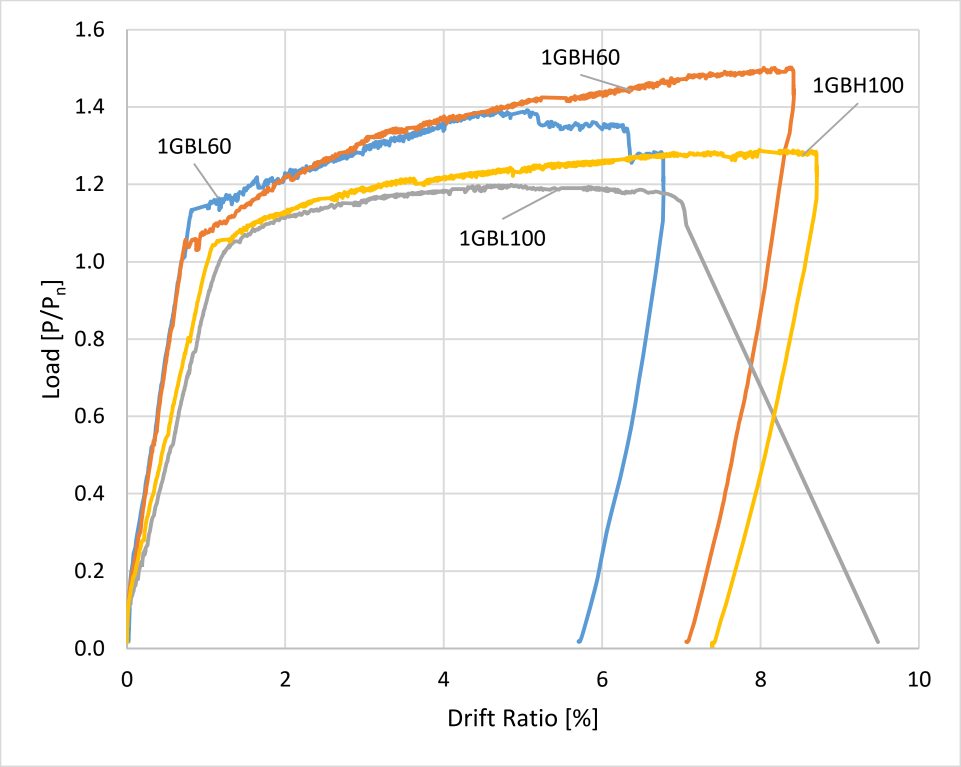

Figure 3.5: Series 1 normalized load-drift ratio relations

All beams sustained relatively large drifts and demonstrate high displacement ductility. The two beams with the lowest drift capacity, 1GBL60 and 1GBL100, resist their peak load at similar drifts (between about 4.5 and 5.0%), but beam 1GBL60 failed at a smaller drift ratio. Both beams reinforced with Grade 100 reinforcement had lower apparent stiffness compared to beams with Grade 60 reinforcement due to their lower reinforcement ratio.

The normalized load-deflection curves reflect the T/Y ratios of their tensile steel. As T/Y increases, so does each beam's capacity to sustain additional load beyond yield.

3.3.3. Strain Distributions

Average strain in the longitudinal reinforcement was taken equal to the elongation of LVDTs located just above the longitudinal reinforcement divided by their 10-in. gauge length. The layout of LVDTs is provided in Appendix A.4.1.3. The distribution of strain along each beam for different drift ratios is shown in Figure 3.6.

The values reported are the average strain over that gauge length, and are shown at the center of each spacing. The solid black line is the yield strain and the dotted black line is the strain at the onset of strain hardening, as determined from tension tests of reinforcement coupons.

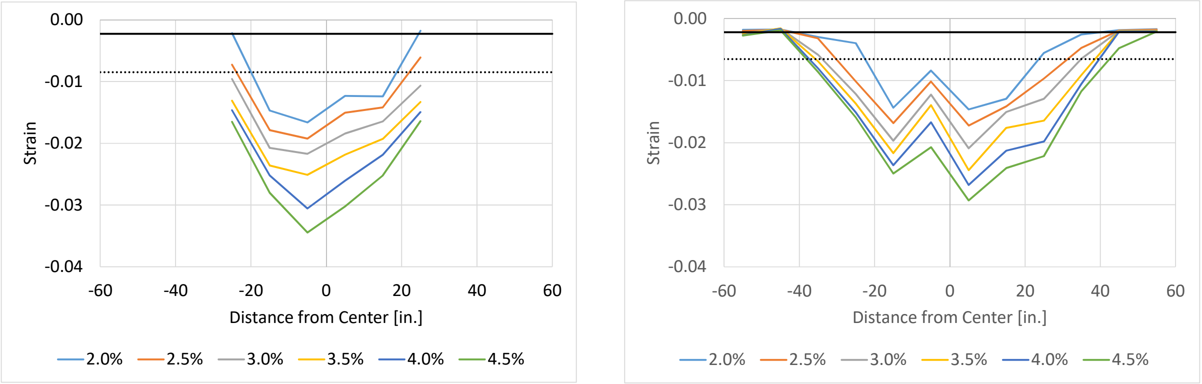

(a) 1GBL60* (b) 1GBH60

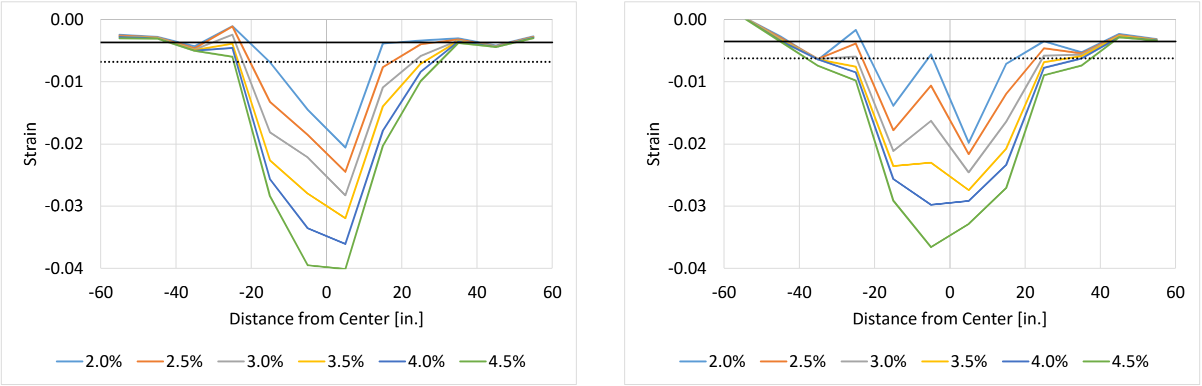

(c) 1GBL100 (d) 1GBH100

Figure 3.6: Series 1 strain distributions for different drift ratios

*Beam 1GBL60 did not have instrumentation beyond 30 in. from the centerline. This beam was tested first in Series 1, and the decision to add additional instrumentation to subsequent beams was based on observations from that test.

Based on their strain profiles, beam 1GBH60 demonstrates the largest apparent spread of plasticity, followed by beams 1GBL60 and 1GBH100, and finally beam 1GBL100. Due to lack of strain data farther from the center for beam 1GBL60, it is difficult to determine where beams 1GBL60 and 1GBH100 fall in relation to one another. Overall, for a given drift ratio, the strains tend to spread along a greater length and to be of a lesser magnitude for greater values of T/Y.

3.4. Analytical Models

3.4.1. Moment-Curvature Relations

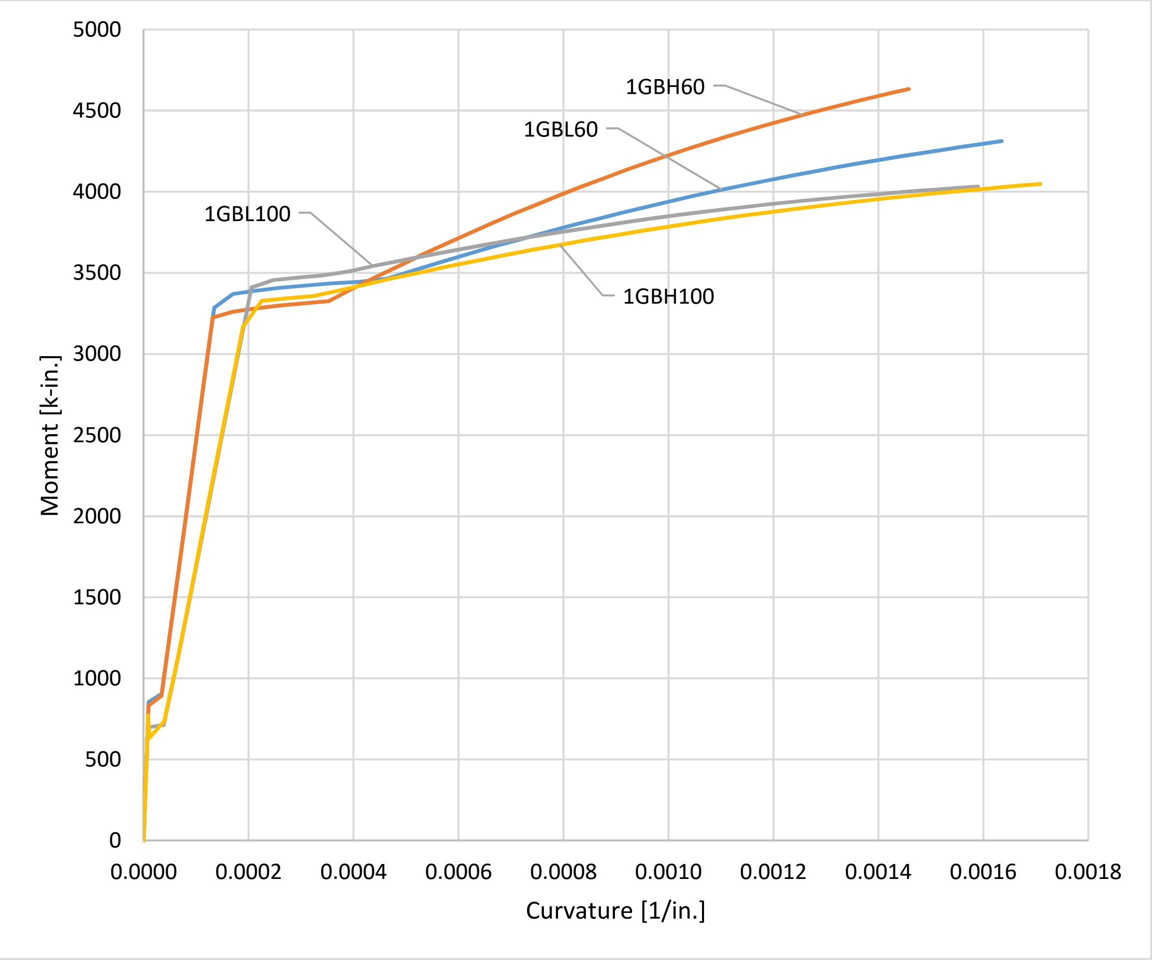

Figure 3.7: Series 1 moment-curvature relations

Figure 3.7 plots calculated theoretical relations between moment and curvature. Appendix A.6 provides the material relationships used to calculate them. The calculated moment-curvature relations show that all four beams of Series 1 are expected to yield at approximately the same bending moment (approximately 3400 k-in.), as intended. Initial stiffnesses are essentially equal before cracking. After onset of cracking (approximately 750 k-in.), the beams with Grade 60 reinforcement are noticeably stiffer than those with Grade 100 reinforcement. This difference in stiffness is because of the different steel ratios of the beams with different reinforcement grade.

After yielding, different degrees of strain-hardening are apparent in the moment-curvature relations, consistent with the different degrees of strain-hardening of the constituent longitudinal reinforcement.

Near ultimate load, the moment diagram for the test beams is approximately linear from point of support to point of concentrated midspan load. From theoretical considerations considering only flexure, as displacements progress from the yield displacement to a displacement infinitesimally above the yield displacement, the curvature at the midspan must jump from the yield curvature to the curvature at onset of strain-hardening, and this jump occurs along an infinitesimal length (ACI 352, 1976). As displacements increase further, strain-hardening occurs at the midspan, with inelastic curvature occurring along a short length. As such, calculated curvature did not vary linearly between adjacent instrumentation bays moving away from the beam center. In addition, the existence of discrete cracks, including inclined cracks associated with combined moment and shear as depicted in Figure 3.8, which act as sources of concentrated deformations, further complicated these calculations. Cracks often crossed between bays (10-in. horizontal, 11.75-in. vertical) of instruments and resulted in additional variations in curvature between adjacent bays. Efforts were made to extract moment-curvature relations from the recorded test data, but these efforts proved futile because of the issues described.

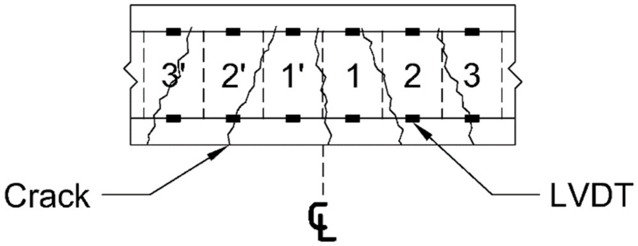

Figure 3.8: Elevation view of inclined cracking and instrumentation

3.4.2. Initial Stiffness

Theoretical values of the midspan load and displacement corresponding to cracking and yielding were determined according to the following procedures. First, the theoretical moment-curvature relation was simplified into a bilinear moment-curvature relation defined by lines from the origin to the cracking point and from the cracking point to the yielding point. Second, the applied midspan load required to reach either the cracking moment or yielding moment at midspan was calculated from equilibrium, including the moments due to self-weight and the load frame. Third, the entire moment diagram corresponding to either cracking or yielding was determined considering all applied loads. Fourth, the curvature distribution along the beam was determined from the moment distribution and the bilinear moment-curvature relation. This curvature distribution was then used to calculate the cracking deflection and yielding deflection considering curvature only. Finally, the moment due to self-weight and deflections due to self-weight and the load frame were subtracted, leaving the corresponding values associated with the applied concentrated load (which were the values measured). For this purpose, deflections due to self-weight and the load frame were calculated using the gross section properties and concrete elastic modulus determined from cylinder tests.

Calculated cracking and yielding points and measured yielding points are superimposed on measured load-deflection curves for each beam in Figure 3.9. In the legend, “C” denotes a calculated values while “M” denotes a measured value. The measured points are the load and deflection corresponding to when the average steel strain in the two instrument bays adjacent to the centerline, computed as described in Section 3.3.3, reached the yield strain. Calculated deflection and load at onset of yielding are close to their measured points. It is noted that the measured strains correspond to averages along lengths including cracked and uncracked sections. Consequently, the displacement at which “measured” strains would reach the yield value would tend to be greater than the displacement where yielding actually commenced at a cracked section.

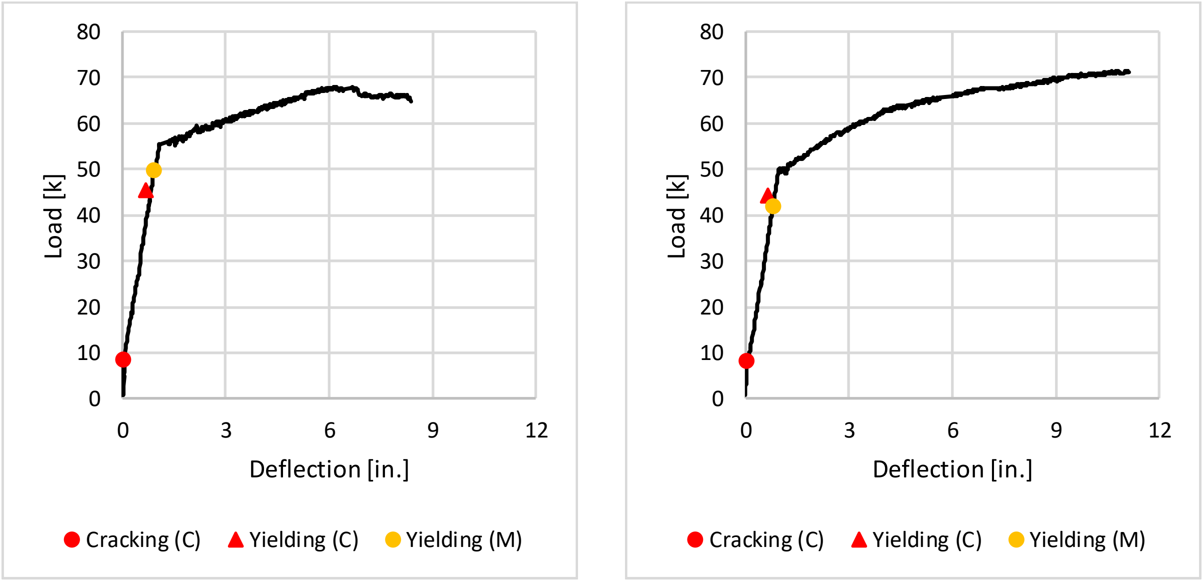

(a) 1GBL60 (b) 1GBH60

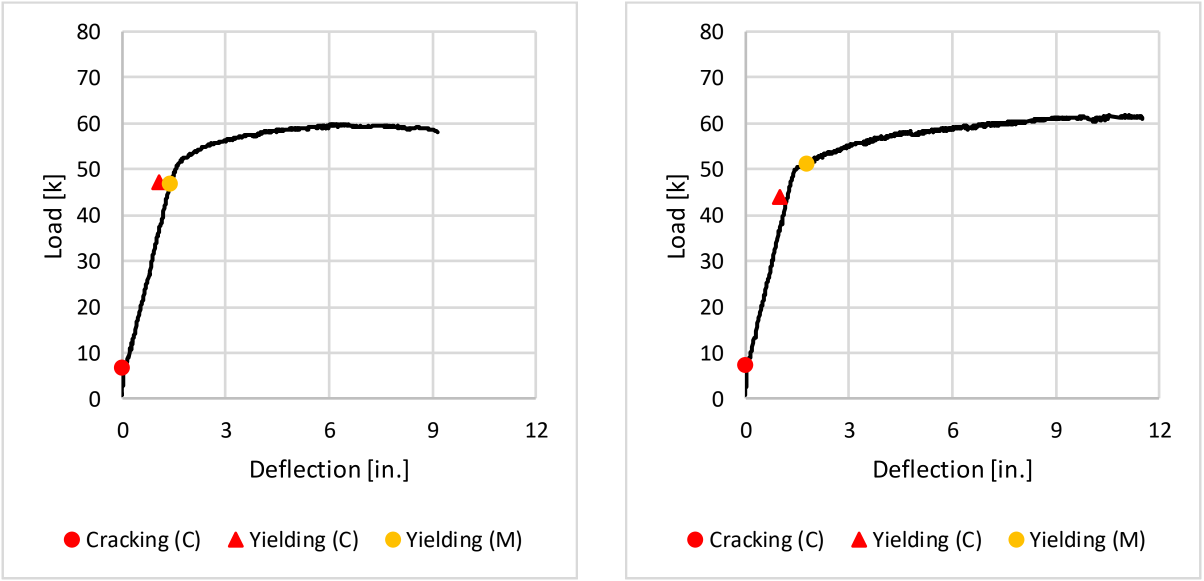

(c) 1GBL100 (d) 1GBH100

Figure 3.9: Series 1 calculated cracking and yielding points

Additional yield deflections were calculated using effective moments of inertia as defined by Branson (1965) and Bischoff (2005). In both cases, the effective moment of inertia at midspan was considered representative of the entire span. Concrete elastic moduli, and moduli of rupture were calculated using the methods outlined in ACI 318-14. For each beam, the cracking moment was determined based on the modulus of rupture while the yield moment was calculated using the ACI 318-14 equivalent-stress-block method. Except for the concrete elastic modulus, measured geometry and material properties were used in all cases. Using the moments of inertia, deflections due to self-weight, the load frame, and the concentrated load were calculated using elastic beam theory and superposition. The moment due to self-weight and deflections due to self-weight and the load frame were subtracted, leaving values corresponding to those measured. A comparison of these two additional methods and the one outlined above is provided in Figure 3.10.

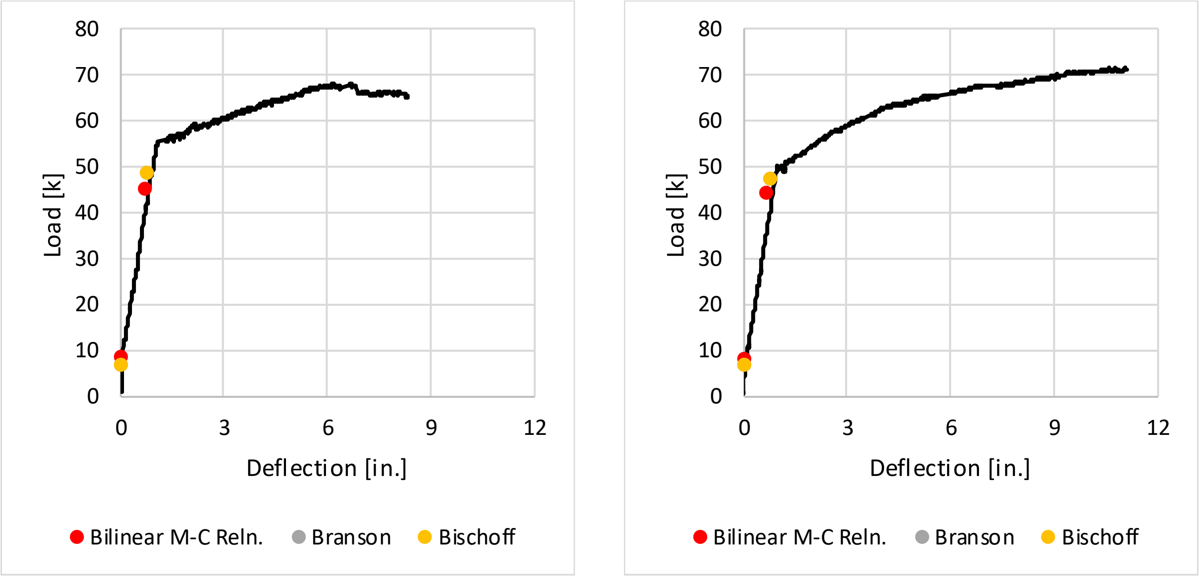

(a) 1GBL60 (b) 1GBH60

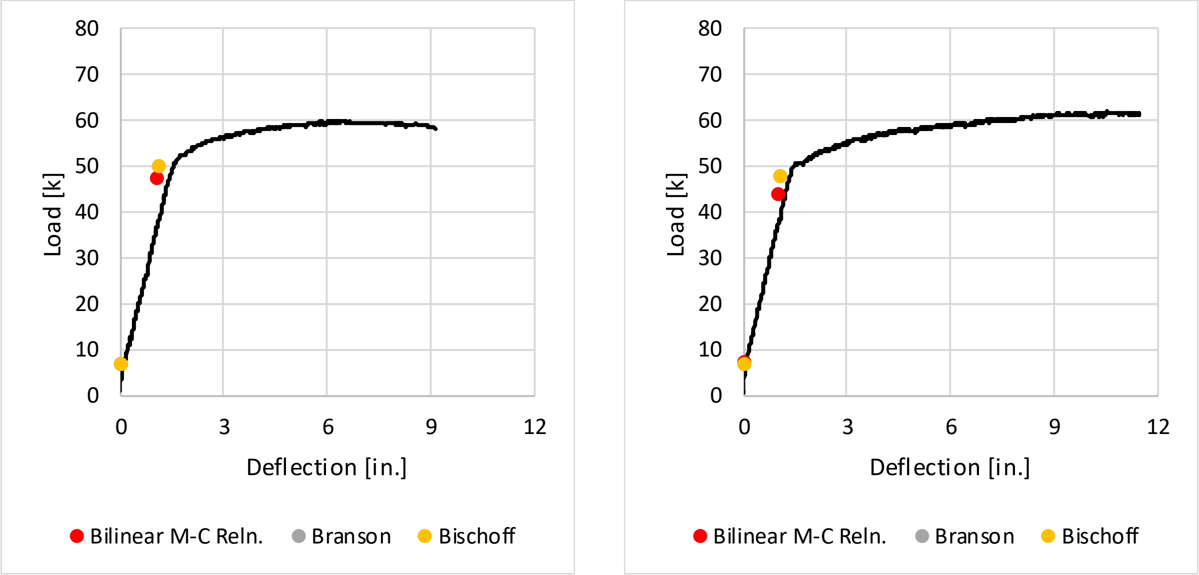

(c) 1GBL100 (d) 1GBH100

Figure 3.10: Series 1 calculated cracking and yielding point calculation comparison

At cracking, values given by the three calculations are close for all beams. At yielding, the effective moments of inertia given by the two different techniques were nearly identical and resulted in similar calculated deflections. However, both effective-moment-of-inertia-based techniques predict a higher yield load and displacement than the bilinear-moment-curvature-relationship calculation would suggest. Differences in calculated deflection and applied load at yield between the two calculation types can be explained by the different concrete elastic moduli used between the two (the first used the concrete elastic modulus measured from cylinder tests while the second calculated the it after ACI 318-14), and differences in the determination of the yield moment (using material relationships versus using the equivalent-stress-block method). Calculated values using all techniques are relatively similar and seem to do a reasonable job at predicting beam behavior up to the point of yielding.

3.4.3. Plastic Deformations

To compute plastic deformations, each beam was idealized as two cantilevers symmetric about the centerline. Plastic deformations were then computed using two different models: distributed and lumped plasticity.

The distributed-plasticity (plastic-hinge) model uses the idealized curvature distribution shown in Figure 3.11. Flexibility associated with shearing deformations is not explicitly considered. Furthermore, there is no anchorage zone and, consequently, no additional flexibility associated with reinforcement slip from an anchorage.

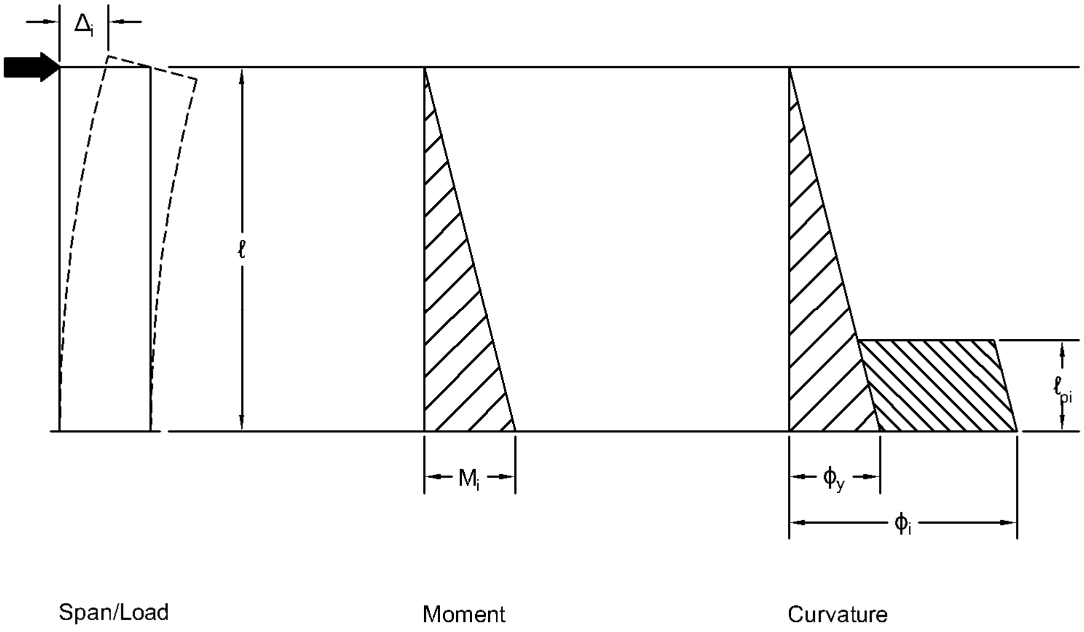

Figure 3.11: Series 1 plastic-hinge model

The member is assumed to develop linear-elastic curvature over its length, with additional inelastic curvature of magnitude $\phi_i - \phi_y$ developing over plastic-hinge length ℓ_{pi} beyond yield. According to the model, the displacement at the tip of the cantilever is

$$\Delta_i = \frac{\phi_y \ell^2}{3} + (\phi_i - \phi_y)\ell_{pi}\left(\ell - \frac{\ell_{pi}}{2}\right) \tag{3.1}$$

In the plastic-hinge model, the plastic-hinge length is determined empirically. The tip deflection Δ_i is recorded, ϕ_y is determined from moment-curvature analysis, ϕ_i is computed using test data, and the plastic-hinge length is then calculated so the calculated and recorded deflections match. As a result, deformation contributed from shear is accounted for implicitly in the plastic-hinge length.

Average curvatures at discrete points were determined to calculate plastic-hinge lengths for Series-1 beams. These curvatures were calculated using a combination of measured and calculated values and the assumed strain profile presented in Figure 3.12, which results in Eq. (3.2).

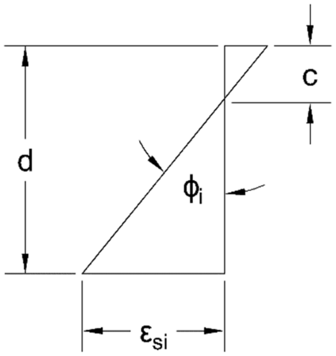

Figure 3.12: Assumed strain profile

$$\phi_i = \frac{\varepsilon_{si}}{d - c} \tag{3.2}$$

In Eq. (3.2), d was determined based on bar locations prior to casting coupled with as-built dimensions, c was determined from moment-curvature analysis for each beam, and ε_{si} was determined from test measurements.

At high curvatures the depth to the neutral axis becomes asymptotic, and for each beam this value was determined from moment-curvature analyses. For these analyses, it was assumed that sections that were plane before bending remained plane, such that axial strains vary linearly across the depth of the section, and that materials models were based on their cylinder and coupon tests. Additional information related to this calculation is in Appendix A.6.

The instantaneous steel strain ε_{si} was again taken equal to the strain measured by LVDTs mounted on rods inserted in the concrete just above the tensile reinforcement. This strain (calculated from the instantaneous change in length over original length) was averaged over two 10-in. gauge lengths, one on each side of the midspan, resulting in a total length of 20 in., which is approximately the depth of the section or half the member height on each side of the centerline. These measured strains and corresponding calculated curvatures were checked against the results from the moment-curvature analyses to ensure that steel strains and curvatures were sufficiently high to warrant the asymptotic assumption of c. Table 3.1 provides yield curvatures determined by moment-curvature analyses and instantaneous curvatures at different drift ratios. The drift ratio values are indicated by the subscript.

Table 3.1: Series 1 yield and instantaneous curvatures at different drift ratios

	ϕ_y [1/in.]	$\phi_{2.0\%}$ [1/in.]	$\phi_{2.5\%}$ [1/in.]	$\phi_{3.0\%}$ [1/in.]	$\phi_{3.5\%}$ [1/in.]	$\phi_{4.0\%}$ [1/in.]	$\phi_{4.5\%}$ [1/in.]
1GBL60	1.37E-04	7.50E-04	8.88E-04	1.04E-03	1.22E-03	1.47E-03	1.68E-03
1GBH60	1.32E-04	6.01E-04	7.14E-04	8.65E-04	1.00E-03	1.14E-03	1.31E-03
1GBL100	2.07E-04	8.97E-04	1.10E-03	1.29E-03	1.53E-03	1.78E-03	2.04E-03
1GBH100	1.96E-04	6.45E-04	8.19E-04	1.04E-03	1.28E-03	1.50E-03	1.76E-03

Figure 3.13 displays calculated plastic-hinge length normalized by the nominal beam height h as a function of drift ratio. Figure 3.14 shows normalized plastic-hinge length as a function of T/Y at five different drift ratios, and Figure 3.15 shows normalized plastic-hinge length averaged at those five different drift ratios as a function

of T/Y for all four beams tested. Drift ratios were selected to enable comparisons of plastic-hinge lengths at various drift levels that all beams attained before reaching their peak strengths.

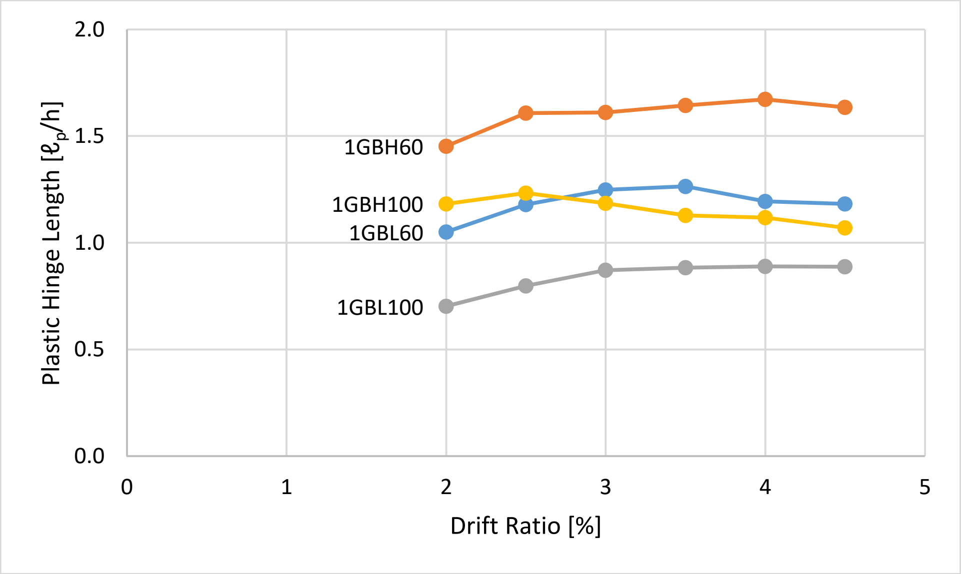

Figure 3.13: Series 1 normalized plastic-hinge length-drift ratio

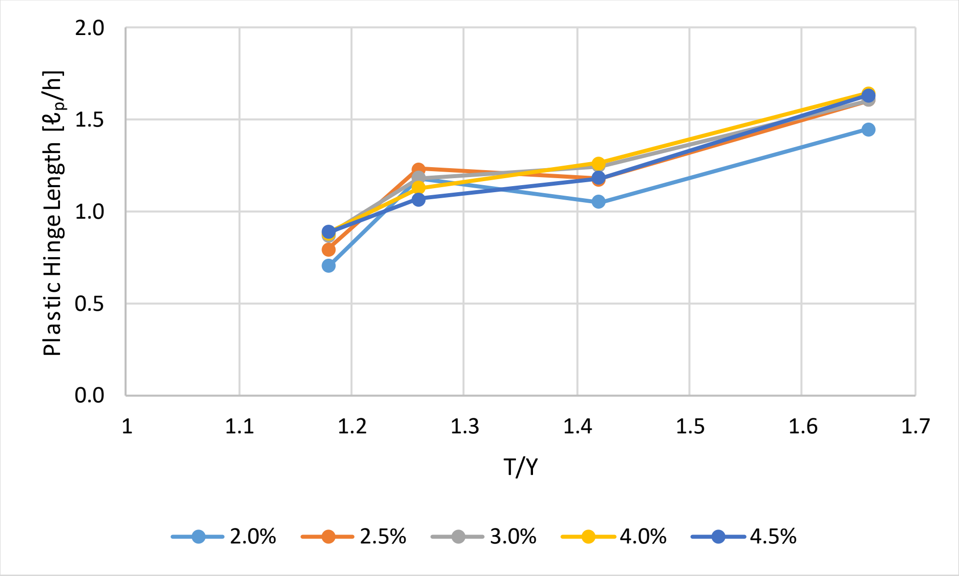

Figure 3.14: Series 1 normalized plastic-hinge length-T/Y

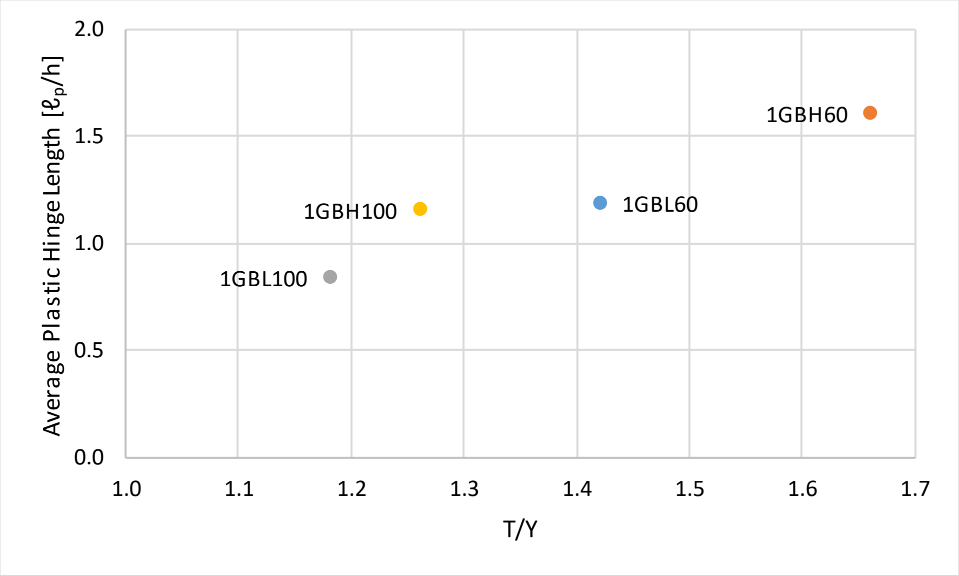

Figure 3.15: Series 1 average normalized plastic-hinge length-T/Y

As indicated in Figure 3.13, plastic-hinge length remains relatively constant with increasing drift ratio. Based on Figure 3.14 and Figure 3.15, the plastic-hinge length increases with increasing T/Y ratio. The rate of increase is not the same for Grade 60 and Grade 100.

The lumped plasticity (plastic-rotation) model uses the idealized moment-curvature relation shown in Figure 3.16.

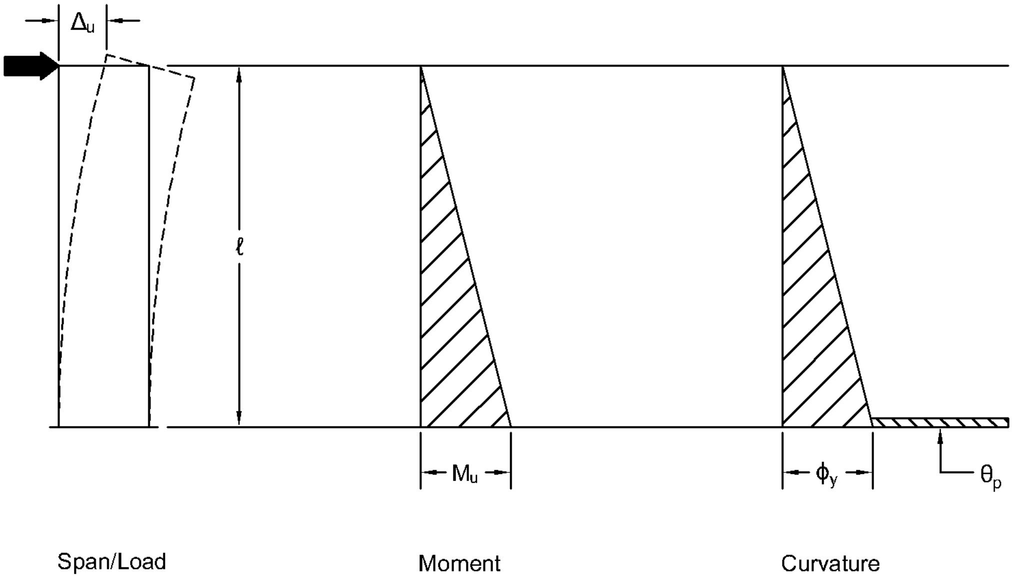

Figure 3.16: Series 1 conventional plastic-rotation model

The member is assumed to develop linear-elastic curvature over its height, with inelastic rotation of magnitude θ_p lumped at the point of maximum moment. The plastic rotation can be determined from

$$\Delta_u = \Delta_y + \theta_p\left(\ell - \frac{\ell_p}{2}\right) \tag{3.3}$$

considering an infinitesimally small ℓ_p at the point of maximum moment, then

$$\theta_p = \frac{\Delta_u - \Delta_y}{\ell} \tag{3.4}$$

Ultimate deflection Δ_u was defined as the displacement just before sudden drop in load capacity or as the maximum displacement during a test without apparent failure. Yield displacement was determined using a method outlined by Elwood and Eberhard (2009). For this purpose, the calculated moment-curvature relationship was used to determine the moment (and, hence, the load) at which (a) the strain in the tension reinforcement reaches the yield strain ($P_{first\ yield}$) and (b) the maximum concrete strain reaches 0.004 ($P_{0.004}$). A secant was drawn from the origin through the deflection data at $P_{first\ yield}$, and then the yield deflection was defined as displacement corresponding to the intersection between that secant and a horizontal line drawn at load equal to $P_{0.004}$. An example of this process is provided in Appendix A.6. Table 3.2 presents the yield and ultimate deflections for Series 1 beams found using the methods described above.

Table 3.2: Series 1 yield and ultimate deflections

	Δ_y [in.]	Δ_u [in.]
1GBL60	0.91	8.34
1GBH60	0.93	11.10
1GBL100	1.51	9.27
1GBH100	1.33	11.49

Figure 3.17 provides plastic rotation determined by Eq. (3.4) as a function of T/Y ratio for all beams in Series 1.

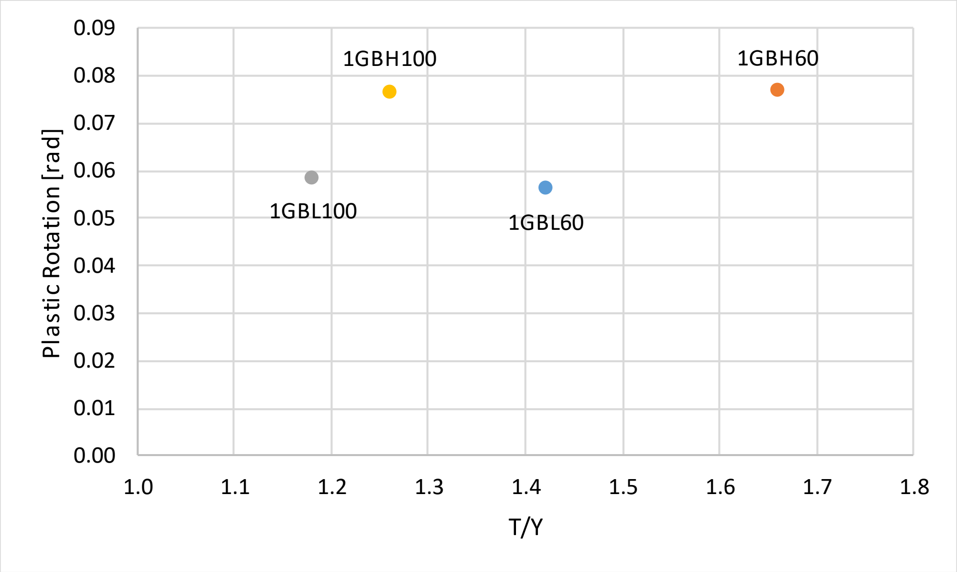

Figure 3.17: Series 1 plastic rotation-T/Y

Figure 3.17 demonstrates that beams with higher T/Y achieve greater plastic rotations. Quantitative comparisons, however, are complicated because the ultimate displacements of the different beams were controlled by various aspects (beam 1GBL60 experienced concrete crushing followed by increasing deflection with decreasing load, beam 1GBL100 failed by fracture of the longitudinal reinforcement, and tests of beams 1GBH60 and 1GBH100 were terminated due to the limit of the test setup before reaching a limit state of the beam cross section).

3.5. Numerical Models

Finite-element models were constructed and analyzed for all beams in Series 1. Dimensions and material properties were based on measured values. Details of the modeling process are provided in Appendix C.1. Finite-element models were built in GiD (2019) and analyzed using ATENA (2019).

3.5.1. Load-Deflection Relations

Comparisons between calculated and measured load-deflection relations for all beams in Series 1 are provided in Figure 3.18 through Figure 3.21. The length listed in the parentheses following “Calculated” denotes the approximate square-mesh size of the model. Similar output between models across mesh sizes suggests that behavior of the models is mesh-independent.

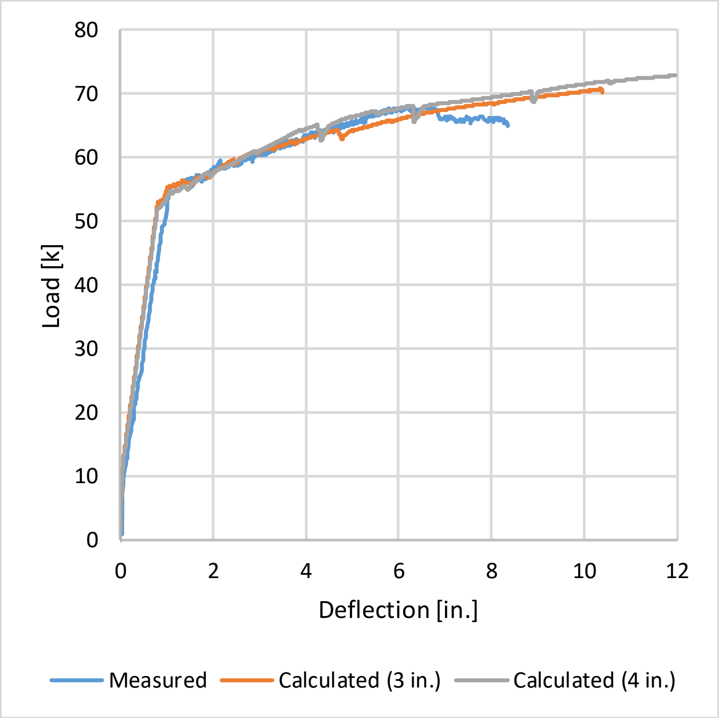

Figure 3.18: 1GBL60 load-deflection relation comparison

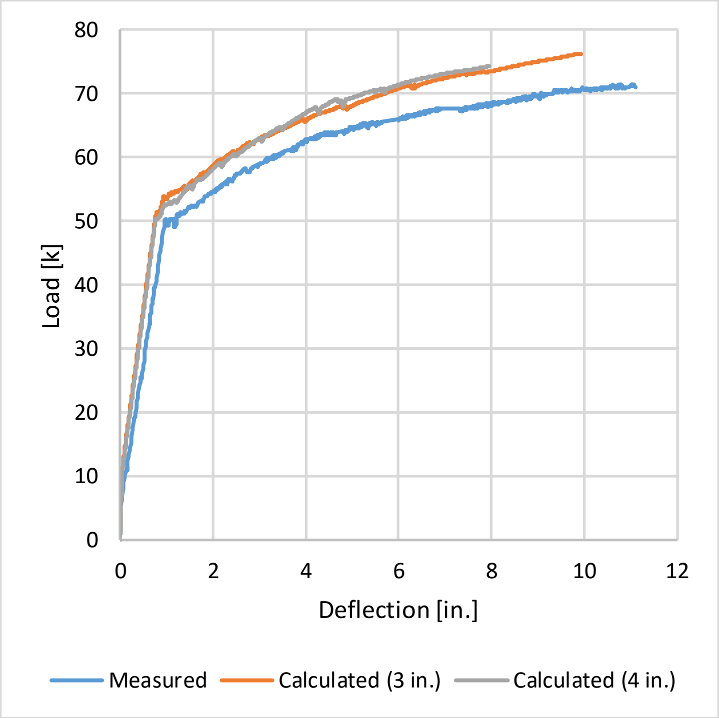

Figure 3.19: 1GBH60 load-deflection relation comparison

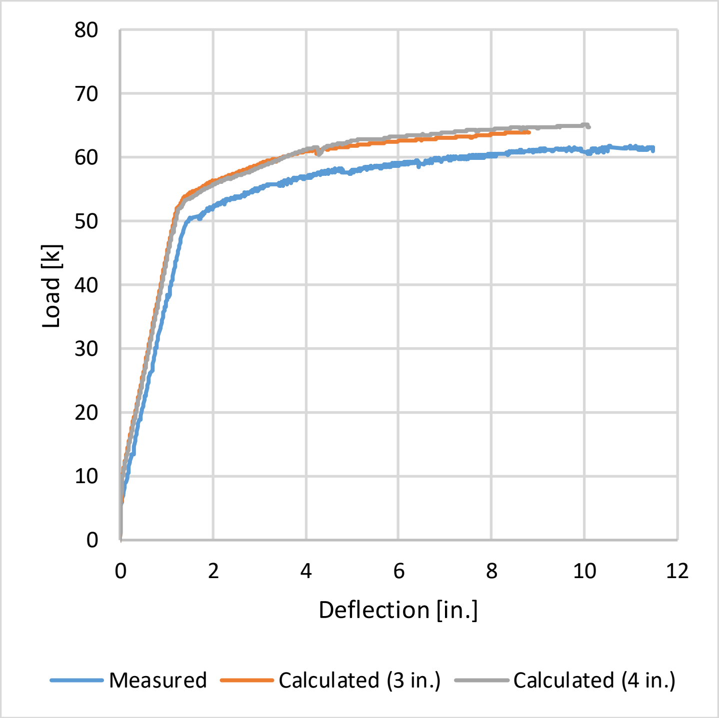

Figure 3.20: 1GBL100 load-deflection relation comparison

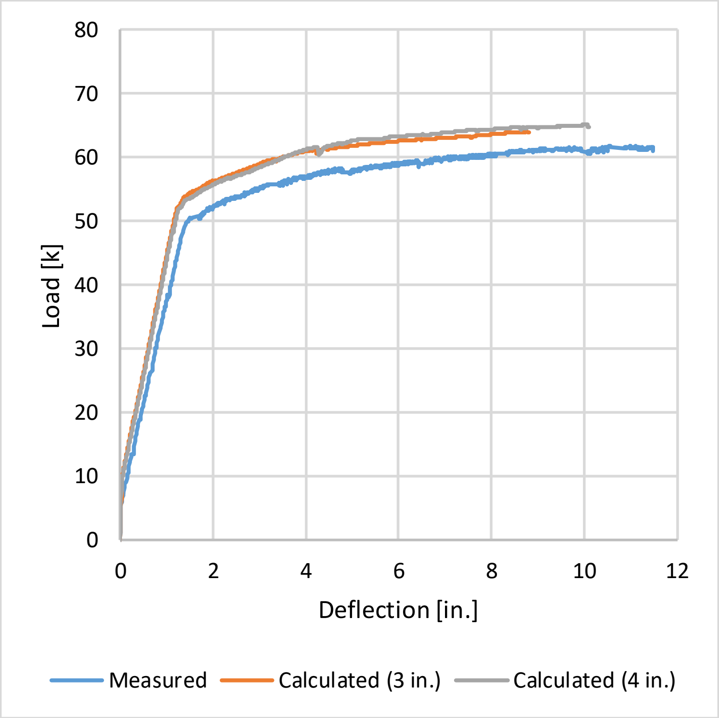

Figure 3.21: 1GBH100 load-deflection relation comparison

Initial model stiffnesses are slightly higher than the measured response for each beam. Calculated responses continue to mirror the tests data in the nonlinear range of response. Though most models indicate a larger yield load than what was measured, calculated values are within about 10% of the data. It is difficult to make comparisons between limiting test and model behavior. Maximum deflections for the tests were associated with limits in the test configuration in some cases and failure of materials in others. Maximum deflections in the analyses were limited by failures associated with strain softening of materials resulting in convergence issues. For these reasons, direct comparisons between measured and calculated end points should not be made.

Data are shown for all analysis steps for which the convergence error for any of the four monitored parameters were less than 1%. Element output indicated this threshold was exceeded when the longitudinal reinforcing was pushed far into its nonlinear range of response, where the slope of stress-strain relationship becomes quite shallow. This material behavior proved limiting to the analysis program, even with very small analysis steps or very large numbers of iterations. Thus, it is difficult to make comparisons between measured and calculated values at levels of high displacement ductility.

Comparing global behavior indicates the mathematical beam models are adequate for predicting physical beam behavior. Reasonable modeling assumptions and techniques are acceptable for modeling the response of beams with high-strength reinforcement, despite being calibrated to data taken from tests primarily examining members reinforced with normal-strength steel. The efficacy of modeling techniques seems consistent across all grades and T/Y ratios considered here.

3.5.2. Strain Distributions

Average strain in the longitudinal reinforcement was determined for each beam model, for both mesh sizes by placing maximum and minimum reinforcement-strain monitors on a 10-in. length of reinforcement, and averaging values obtained. The 10-in. gauge length mirrored the spacing of LVDTs in the tests, so that model results could be directly compared with those obtained experimentally, which were presented in Section 3.3.3. Comparisons of strain distributions along all beams for different drift ratios are provided in the following figures. The values reported are the average strain over that gauge length and are shown at the center of the measurement location. The solid black line is the yield strain and the dotted black line is the strain at the onset of strain hardening, as determined from tension tests of reinforcement coupons.

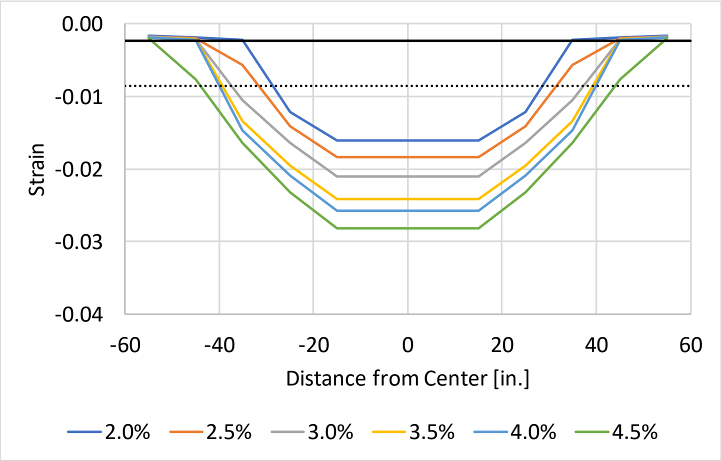

(a) 3-in. mesh

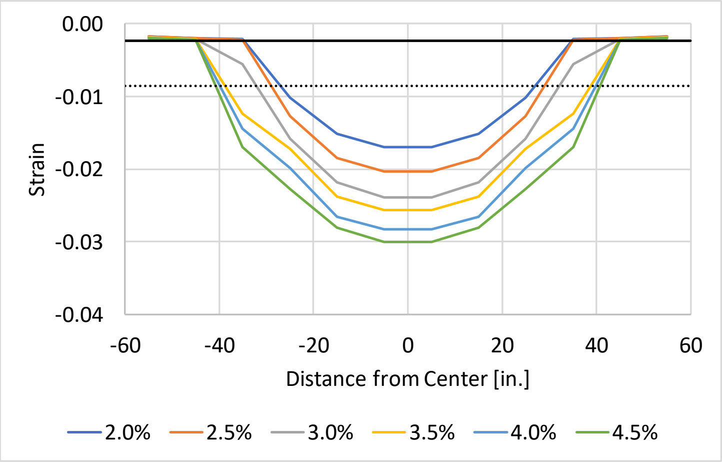

(b) 4-in. mesh

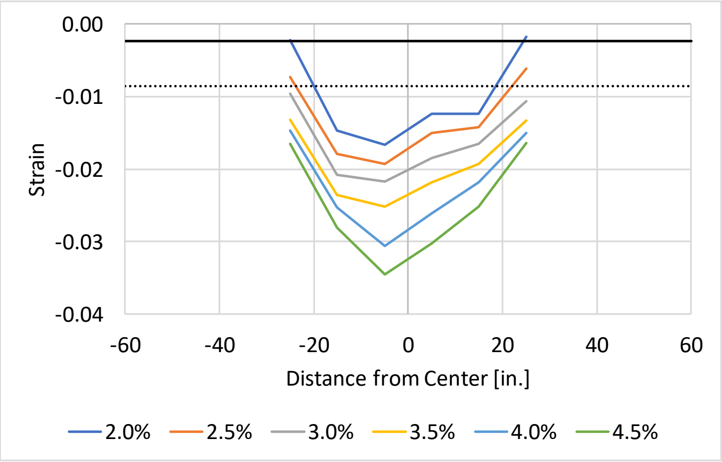

(c) Measured

Figure 3.22: 1GBL60 model and measured strain distributions for different drift ratios

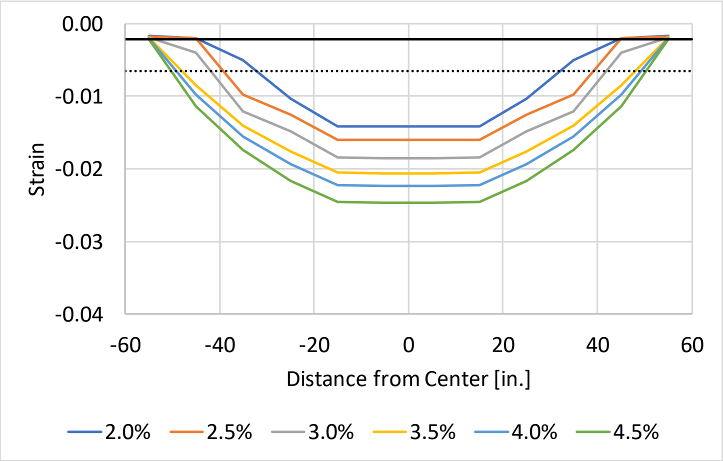

(a) 3-in. mesh

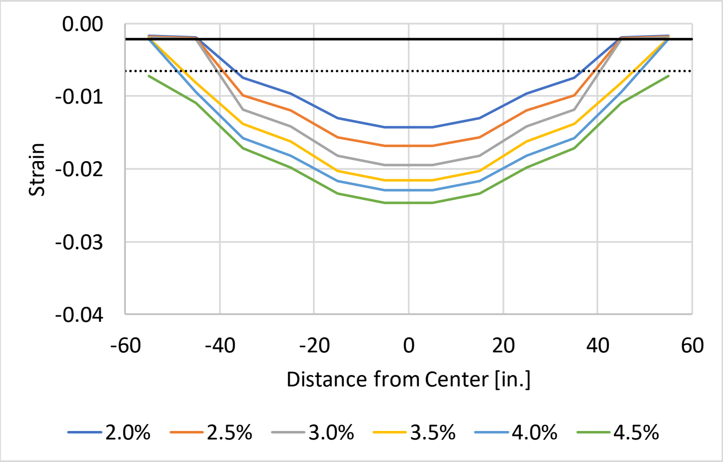

(b) 4-in. mesh

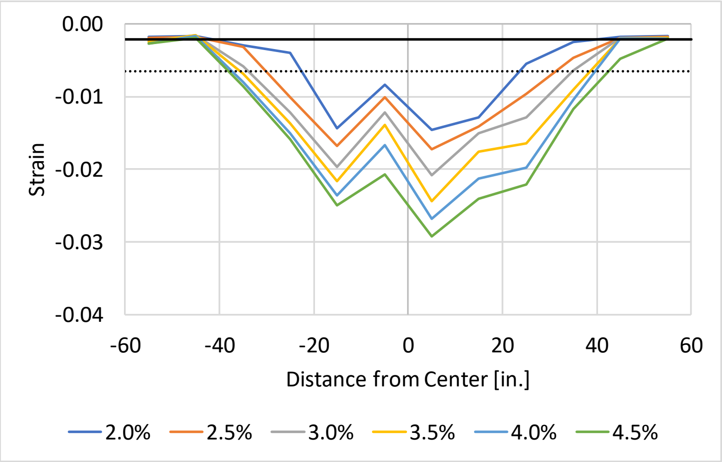

(c) Measured

Figure 3.23: 1GBH60 model and measured strain distributions for different drift ratios

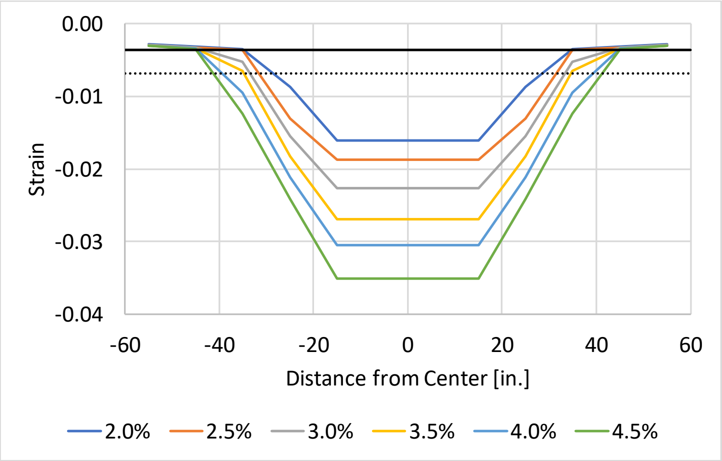

(a) 3-in. mesh

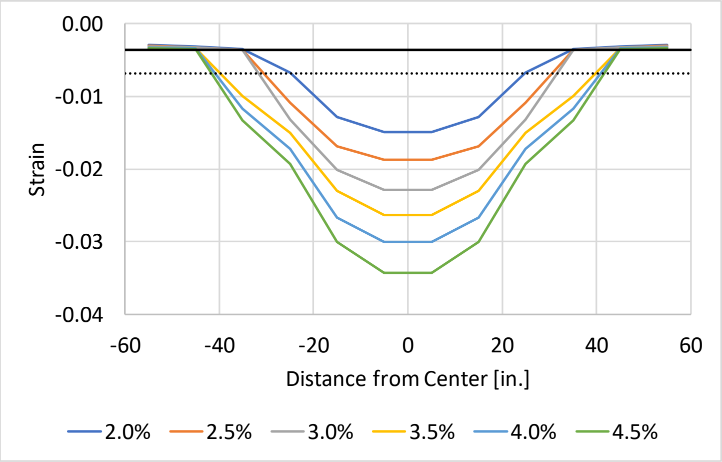

(b) 4-in. mesh

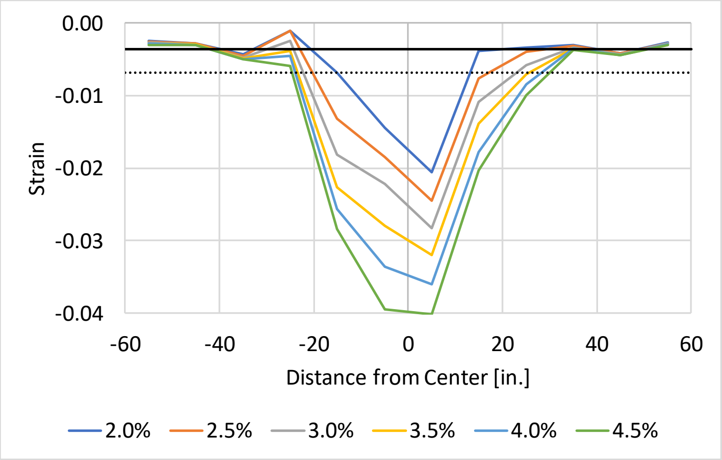

(c) Measured

Figure 3.24: 1GBL100 model and measured strain distributions for different drift ratios

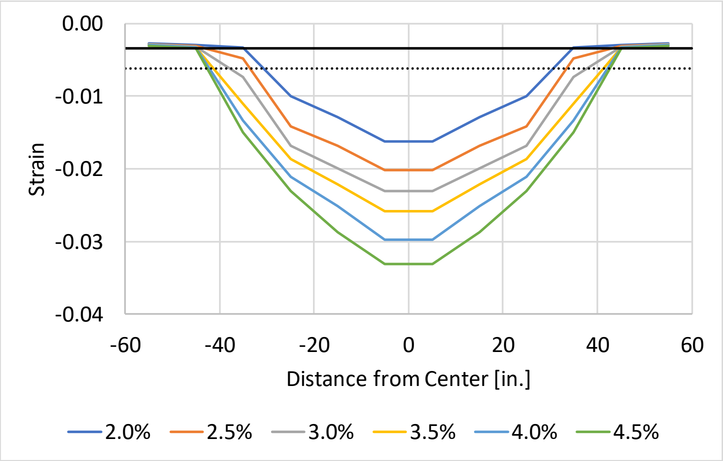

(a) 3-in. mesh

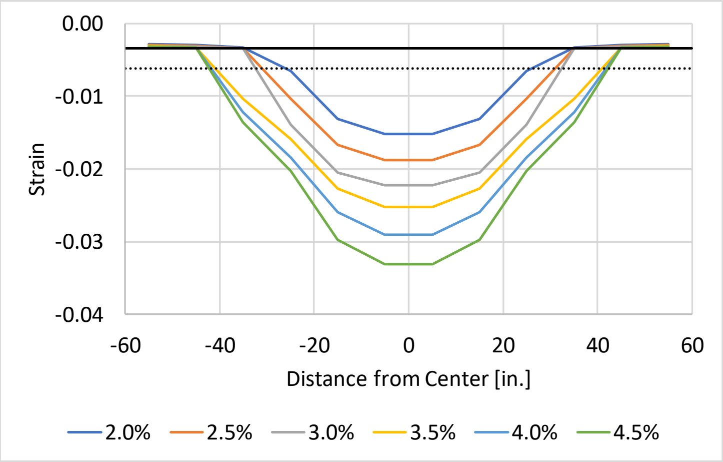

(b) 4-in. mesh

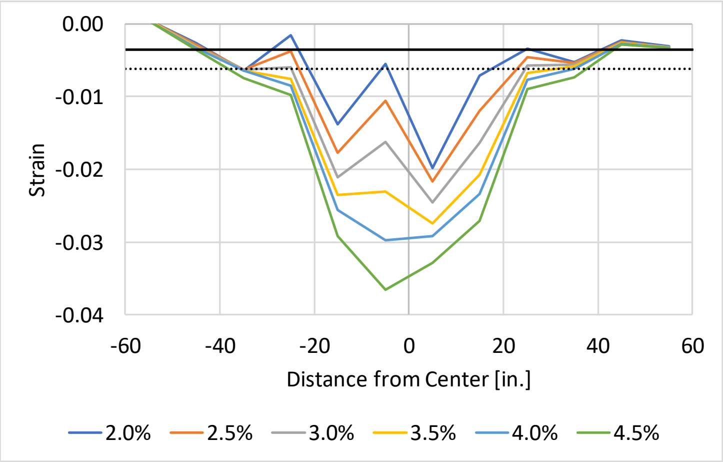

(c) Measured

Figure 3.25: 1GBH100 model and measured strain distributions for different drift ratios

Consistent with test observations, the calculated spread in plasticity in longitudinal reinforcement increased with increasing T/Y ratio. At a given drift ratio, strains decrease more rapidly away from the beam center and tend to have a higher maximum value as T/Y is decreased. Though the models indicate more apparent spread of strain than the experimental data, maximum measured strains are close to the model output. Due to the nature of the model "measurements" (inside the beam) and the experimental measurements (on the beam surface), some variability is to be expected. Differences in output between mesh sizes can be explained by the changing integration points caused by altering the mesh size, 10-in. gauge length over which reinforcement strain was determined was held constant.

3.5.3. Plastic Deformations

Plastic-hinge lengths were determined using the finite-element analysis output in the same way they were calculated for their experimental counterparts, as outlined in Section 3.4.3. In addition to modeling the four beams tested as a part of this series, an additional beam model was constructed with the same material properties and geometry as beam 1GBL100, but the tensile longitudinal steel was altered to have T/Y equal to 1.1. This additional beam is called "1.1" for simplicity. The results for all beams, including the additional one, are shown in the following figures. As plastic-hinge lengths calculated using the method here are based on peak strain rather than strain along the length of a beam, model results are only shown for the 3-in. mesh. These results are very similar to those using data from the 4-in. mesh models.

Figure 3.26 displays plastic-hinge length normalized by the nominal beam height *h* as a function of drift ratio. Figure 3.27 presents the same data but includes the experimental data for comparison. Those data are presented as dashed lines and open dots, with the same colors as the model results. Figure 3.28 shows normalized plastic-hinge length as a function of T/Y at five different drift ratios, and Figure 3.29 shows normalized plastic-hinge length averaged at those five different drift ratios as a function of T/Y for all four beams tested. Again, experimental data are included for comparison and are given by open dots of the same color as the analysis results for a given beam. Drift ratios were selected to enable comparisons of plastic-hinge lengths at drift levels that all experimental beams attained before reaching their peak strengths.

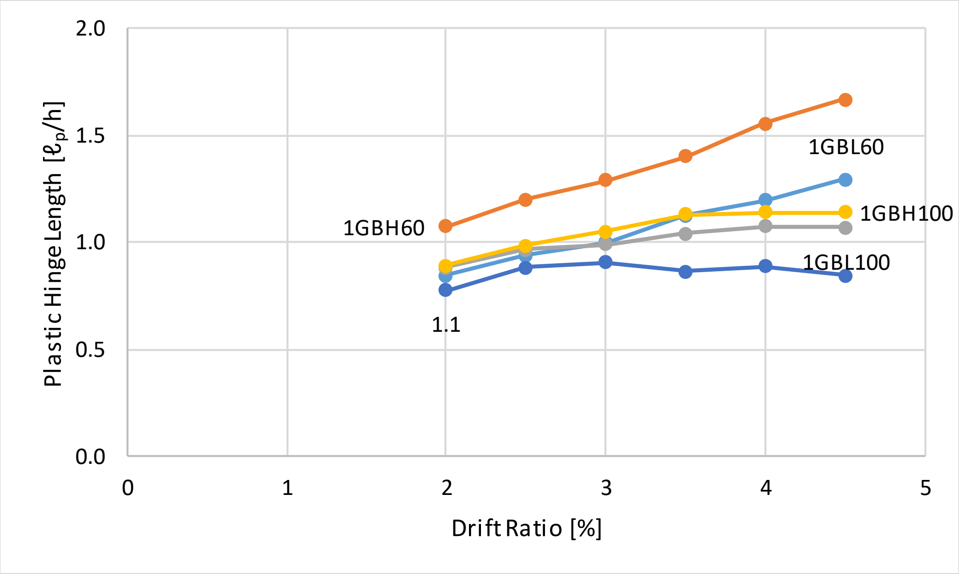

Figure 3.26: Series 1 model normalized plastic-hinge length-drift ratio

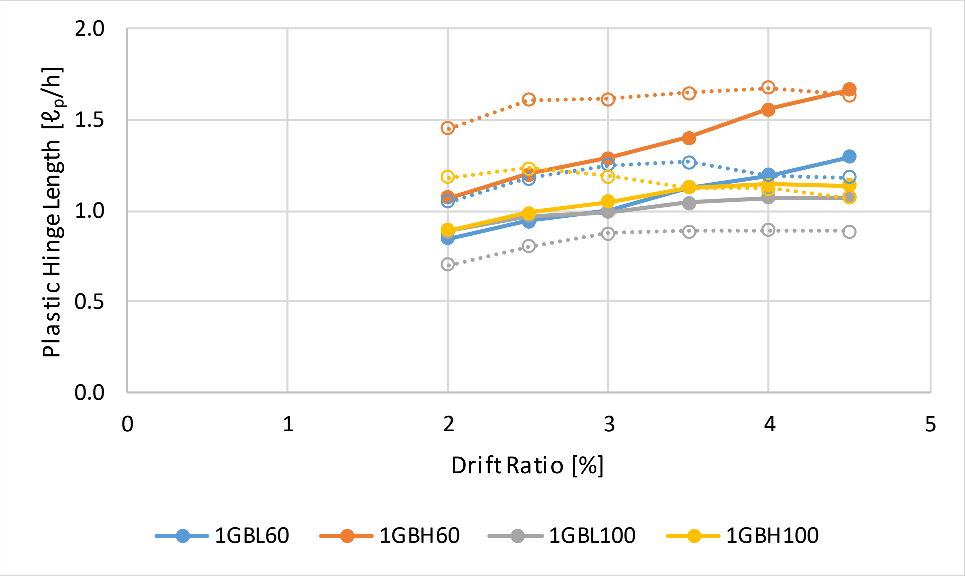

Figure 3.27: Series 1 normalized plastic-hinge length-drift ratio comparison

Figure 3.27 (or a comparison of Figure 3.13 and Figure 3.26) shows that the experimental and analysis calculations yield result in the same order of magnitude. Test results indicate a relatively-constant plastic-hinge length while model results indicate that plastic-hinge length increases with drift ratio, at a higher rate for higher T/Y. The greater strain hardening pushes the yielding farther along the beam length. At lower drift ratios, measured plastic-hinge lengths are greater than those calculated using model output for all beams except 1GBL100. At higher drift ratios, model output and test data are more consistent. In general, model results suggest larger plastic-hinge lengths than those computed using experimental results. At a given deflection, model results indicated higher load-carrying capacity than test measurements, which results in higher steel stresses and strains, and serves to increase the plastic-hinge length at each point. Results of beam 1.1 suggest a relatively-constant plastic-hinge length at all drift ratios considered. This is a result of the lower strain hardening, which leads to more concentrated plastic zone and shorter value for plastic-hinge length.

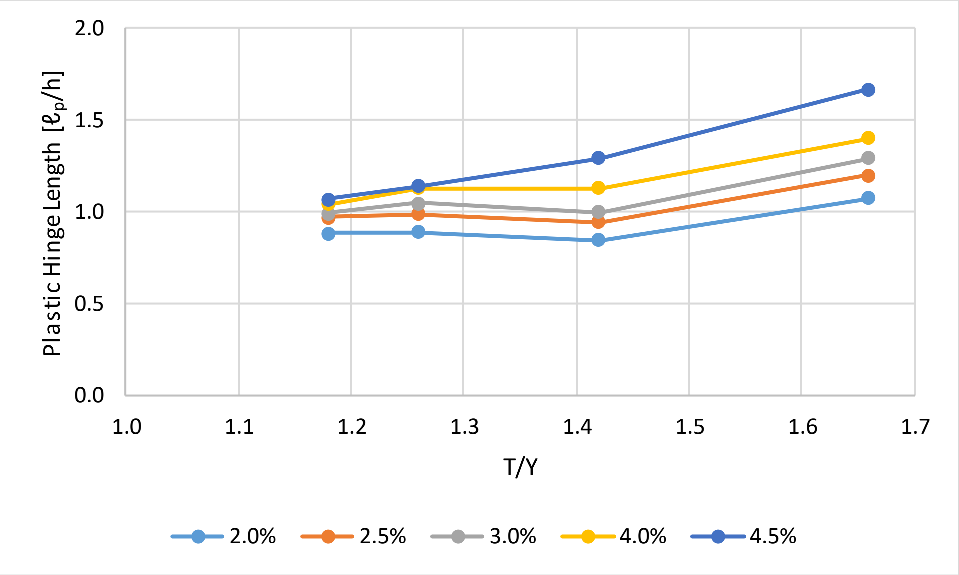

Figure 3.28: Series 1 model normalized plastic-hinge length-T/Y

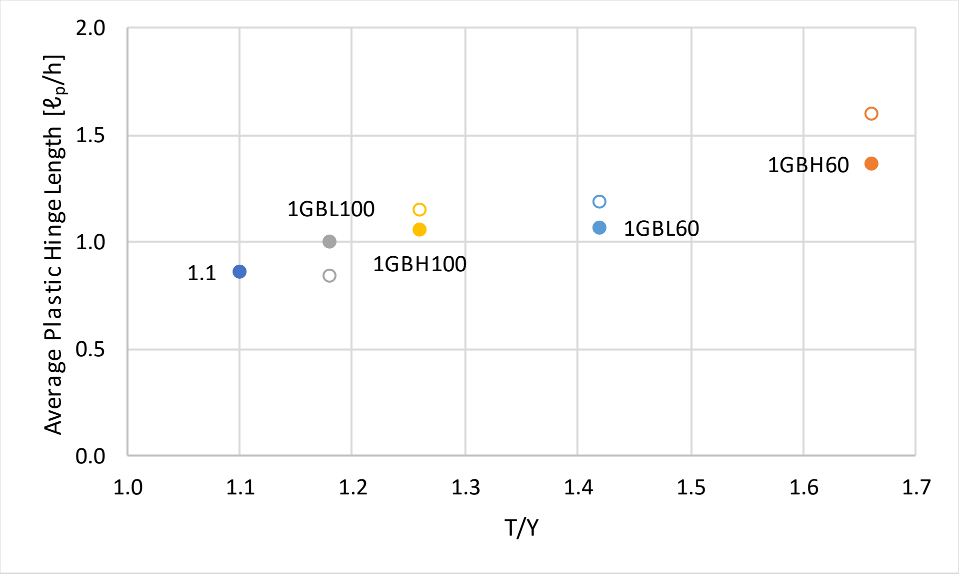

Figure 3.29: Series 1 average normalized plastic-hinge length-T/Y comparison

Considering both analytical and experimental results, Figure 3.28 and Figure 3.29 show that, despite variations in plastic-hinge length for a given T/Y as drift ratios increase, average plastic-hinge lengths over the drift ratios considered seem to increase linearly with increases in T/Y ratio, with an intercept around $0.7h$ for T/Y equal to 1.0. The existence of a finite plastic-hinge length for T/Y = 1.0 can be explained using concepts of the plastic truss model (Schlaich et al., 1987). In a disturbed (or D) region that occurs at a point of concentrated load application, applied load is distributed into the beam through a series of fan-shaped struts, leading to a length of nearly-constant stress in the tensile longitudinal reinforcement near the point load. This zone of nearly-constant stress leads to a finite plastic-hinge length for any reinforcement with strain hardening. Often in practice, a member's plastic-hinge length is considered half of its depth. Mattock (1965) was among the first to propose that a plastic-hinge length of half the effective depth of a member is conservative when compared with experimental results. The results of both the experimental and analytical studies considered here support this conclusion. Ultimately, half the member depth seems to provide a conservative lower-bound for plastic-hinge length.

4. Series 2 Tests

4.1. Cross Sections

Cross sections of all beams are shown in Figure 4.1.The four beams in Series 2 consisted of two beams with Grade 60 and two beams with Grade 100 longitudinal steel. All beams were the same height. For each grade, the longitudinal steel in both beams was identical and the width was varied to reach the desired net tensile strain. Bar areas of the different beams were selected such that nominal product $A_s f_y$ was nearly the same for all beams. For the beams with Grade 60 reinforcement, longitudinal reinforcement comprised three No. 10 bars, such that $A_s f_y = 3 \times 1.27$ in.$^2 \times 60$ ksi $= 229$ k. For the beams with Grade 100 reinforcement, longitudinal reinforcement comprised three No. 8 bars, such that $A_s f_y = 3 \times 0.79$ in.$^2 \times 100$ ksi $= 237$ k.

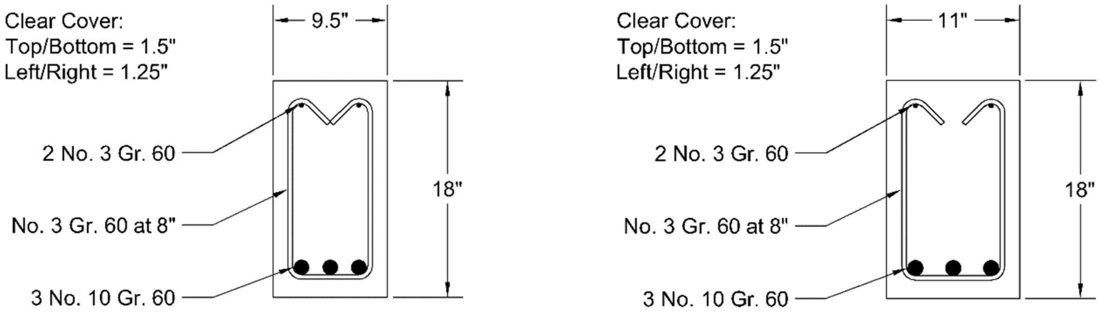

(a) 2GBL60 (b) 2GBH60

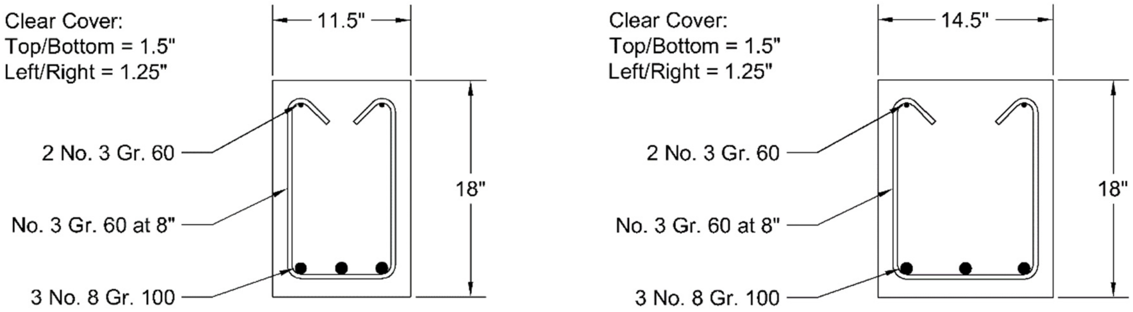

(c) 2GBL100 (d) 2GBH100

Figure 4.1: Series 2 cross sections

4.2. Loading

Each beam was simply supported near its ends. Loading comprised self-weight plus a pair of concentrated loads centered on the midspan as shown in Figure 4.2. Figure 4.3 shows a beam in the test apparatus. Details of the support conditions and loading apparatus are provided in Appendix A.2.3. The short separation between the pair of concentrated loads resulted in short beam length near midspan that was under nearly constant moment and in which the extreme fiber of concrete in the flexural compression zone was a free surface without confinement by steel bearing plates. This free surface was considered important because failure was expected to be due to spalling of the flexural compression zone. The loading protocol was to increase the concentrated loads monotonically until failure of the beam was observed, pausing at certain points to mark and measure cracks. Details of the loading are covered in Appendix A.5.

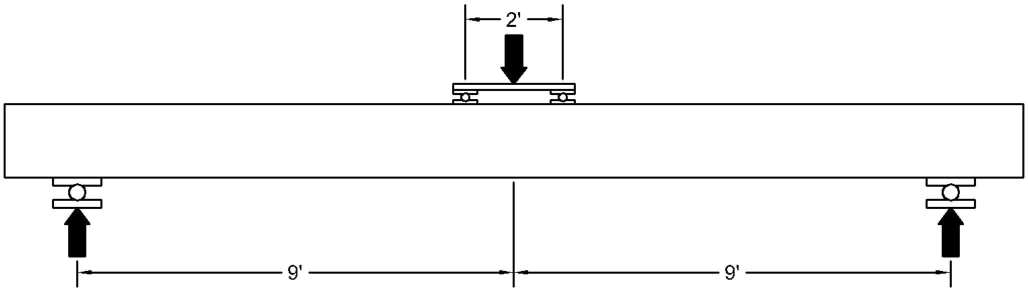

Figure 4.2: Series 2 loading elevation

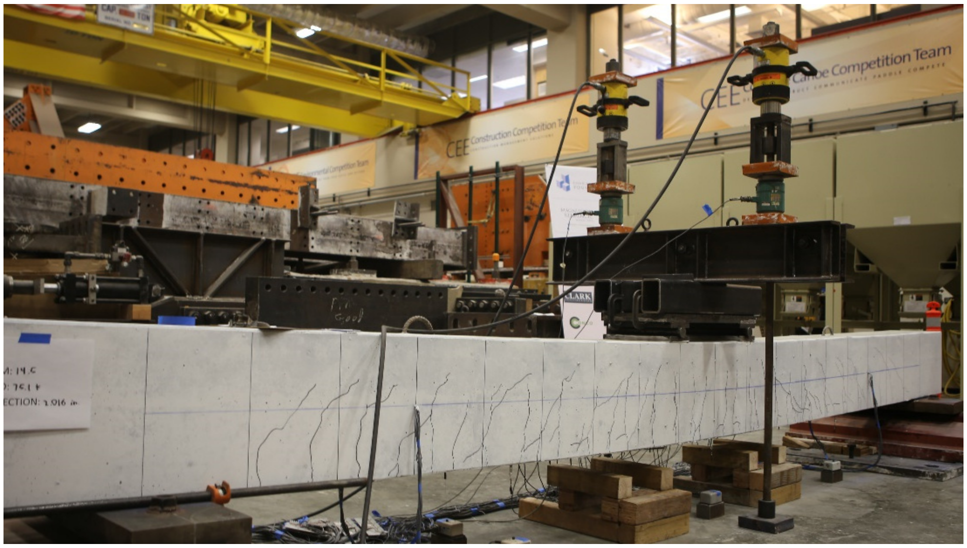

Figure 4.3: Series 2 beam during testing

4.3. Test Results

4.3.1. Failure Mechanisms

Failure was defined as the occurrence of increasing deflection with decreasing load in addition to concrete spalling or reinforcement rupture. The failure mechanism for all beams was the same, that is, failure of concrete in compression followed by decreasing load as deflection increased. Photos and crack patterns for all beams are in Appendix B.2.3.

4.3.2. Load-Deflection Relations

Figure 4.4 provides measured relations between the applied midspan load and the resulting midspan deflection, where load is the total value of the two concentrated forces applied near midspan and includes both the jacking load and the weight of the load apparatus. Figure 4.5 provides normalized load-deflection curves for all four beams in Series 2. Load is normalized by the load corresponding to development of the beam nominal moment strength, calculated using the ACI 318-14 equivalent-stress-block method, except using measured values of f'_c and f_y. This load was corrected to account for the weight of the beam and load apparatus. Deflection is normalized by half the beam span. Drops in load indicating relaxation of the beam load resistance due to pause of loading for crack marking and measuring during the test have been removed for clarity. Non-normalized data for all beams without these portions removed are presented in Appendix B.2.1.

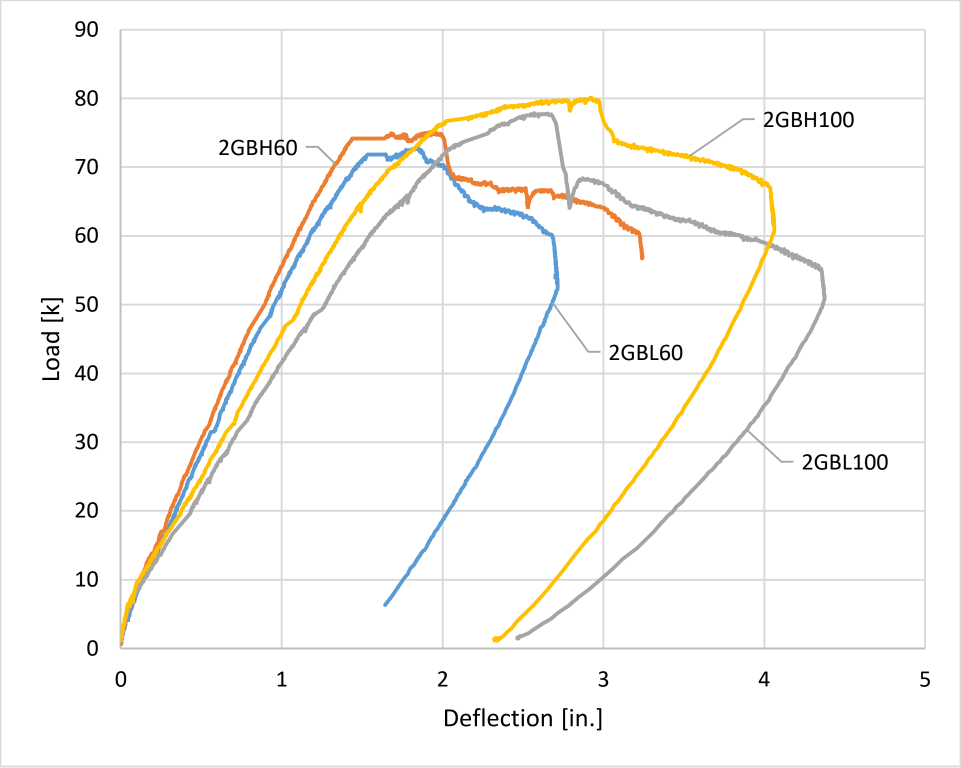

Figure 4.4: Series 2 load-deflection relations

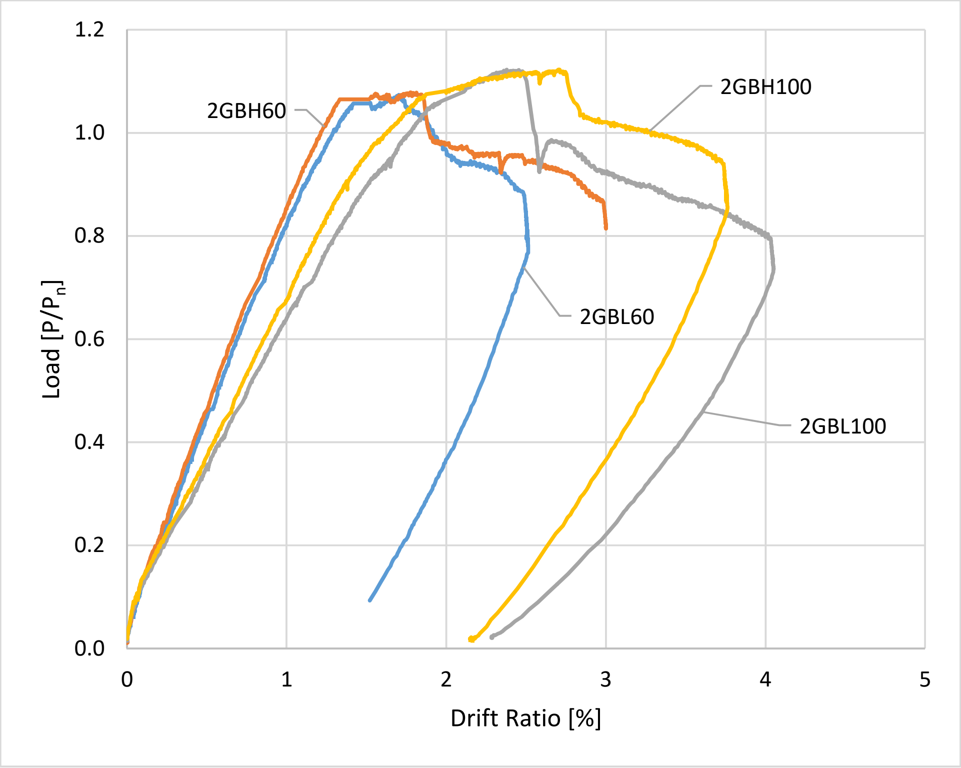

Figure 4.5: Series 2 normalized load-drift ratio relations

Beams of the same grade of steel had similar stiffness, with the Grade 100 beams exhibiting less stiffness than the Grade 60 beams. This was expected due to their lower reinforcement ratio. Measured force capacities were near the calculated capacities, with relatively little post-yield strength gain for all beams. Ultimate load-carrying capacity for all beams was nearly the same, as intended in their design.

Drift ratio at failure increased with increasing net tensile strain for each grade. Though they had similar net tensile strains, beam 2GBL100 achieved a higher drift ratio than 1GBH60, due in part to having both larger elastic drifts and larger inelastic drifts.

4.3.3. Strain Distributions

Average strain in the longitudinal reinforcement was calculated as described in Section 3.3.3, but instruments were spaced at 8 in. rather than 10 in. The layout of LVDTs is provided in Appendix A.4.1.3. The distribution of strain along each beam at the ultimate deflection is shown in Figure 4.6. Values are reported at the center of the instrument spacing. The solid black line is the yield strain and the dotted black line is the strain at the onset of strain hardening, as determined from tension tests of reinforcement coupons. Table 4.1 contains Series 2 strains at failure and compares them with calculated net tensile strains. The average strain in the two instrument bays on either side of center is designated ε_s, while the maximum strain over all bays of instruments is called ε_{smax}.

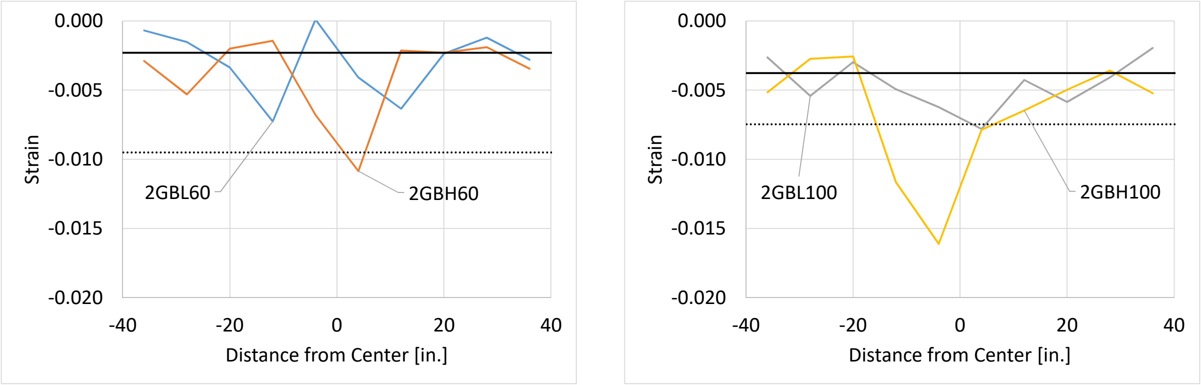

(a) 2GBL60 and 2GBH60

(b) 2GBL100 and 2GBH100

Figure 4.6: Series 2 strain distributions at failure

Table 4.1: Series 2 strains at failure

	ε_s	ε_{smax}	ε_t
2GBL60	0.0020	0.0073	0.0044
2GBH60	0.0088	0.0109	0.0056
2GBL100	0.0070	0.0078	0.0053
2GBH100	0.0120	0.0161	0.0076

In all cases, maximum tensile strains ε_{smax} exceeded the design net tensile strains ε_t. For a given grade of reinforcement, beams with higher net tensile strains achieved larger tensile strains than did beams with lower net tensile strains. The strain data did not show obvious trends in spread of plasticity.

4.4. Analytical Models

4.4.1. Moment-Curvature Relations

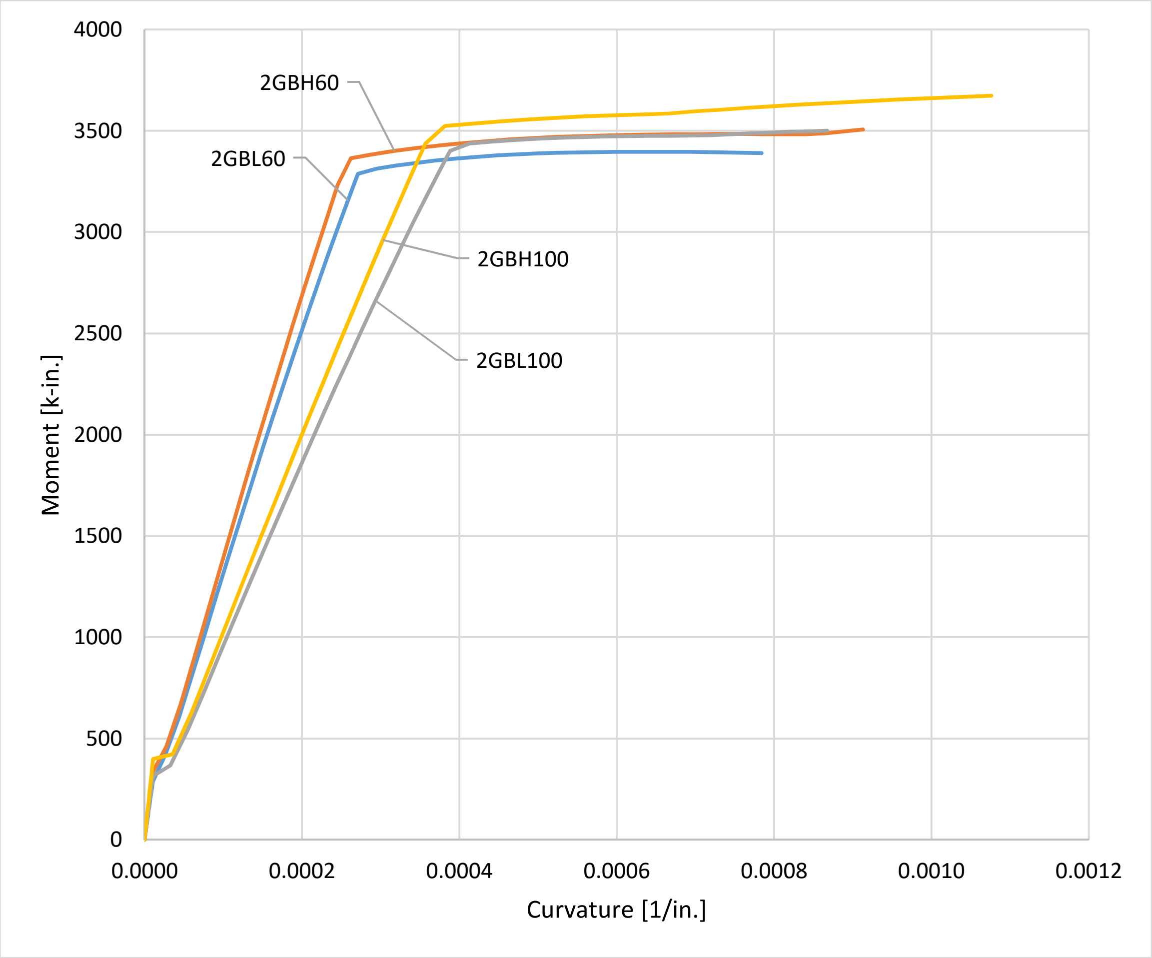

Figure 4.7: Series 2 moment-curvature relations

Figure 4.7 provides calculated theoretical moment-curvatures relations for Series 2 beams. Appendix A.6 outlines the method used to calculate them. The calculated moment-curvature relations show that all four beams of Series 2 are expected to yield at approximately the same bending moment (approximately 3400 k-in.), as intended. Initial stiffnesses are essentially equal before cracking. After onset of cracking (approximately 400 k-in.), the beams with Grade 60 reinforcement are noticeably stiffer than those with Grade 100 reinforcement. This difference in stiffness is because of the different steel ratios of the beams with different reinforcement grade.

After yielding, strain-hardening is relatively minor, primarily because failure is calculated to occur at relatively small longitudinal reinforcement tensile strains, before appreciable strain-hardening of the reinforcement. Failure is defined as the point at which the maximum strain in concrete reaches 0.004, which the end points correspond to.

Average curvatures during the tests were obtained by averaging measured curvatures over two 8-in. long bays of instruments on either side of the beam midspan, which is a nearly constant-moment region of the beam. These average curvatures were computed by taking strains measured by LVDTs below the top bars and above the bottom bars, finding their difference, and dividing by the distance between them. This process was not subject to the same issues described for Series 1 in Section 3.4.1 because of the lack of inclined cracks associated with the combined actions of shear and moment. Figure 4.8 compares the measured and theoretical moment-curvature relations. The theoretical moment-curvature relations of Figure 4.7 were adjusted to account for the initial moment due to self-weight and the load frame, and the curvature that results. This was accomplished by calculating the moment corresponding to the weight of the beam and the load frame, obtaining the curvature corresponding to that moment, and then subtracting that curvature and the moment due to self-weight of the beam. The measured and theoretical relations compare well up to the point of apparent yielding. The measured ultimate curvatures (points at which moment showed first appreciable drop) were generally less than the calculated ultimate curvatures. This may be associated with strain softening of the flexural compression zones, which would tend to result in localized maximum curvatures in the test beams. When averaged along the 16-in. gauge length, the average measured curvature would be less than the maximum curvature. The theoretical moment-curvature relations represent the maximum curvature location, rather than an average.

Crack patterns and measurements for all beams at different load steps are given in Appendix B.2.3 Further information related to beam instrumentation is in Appendix A.4.1.2.

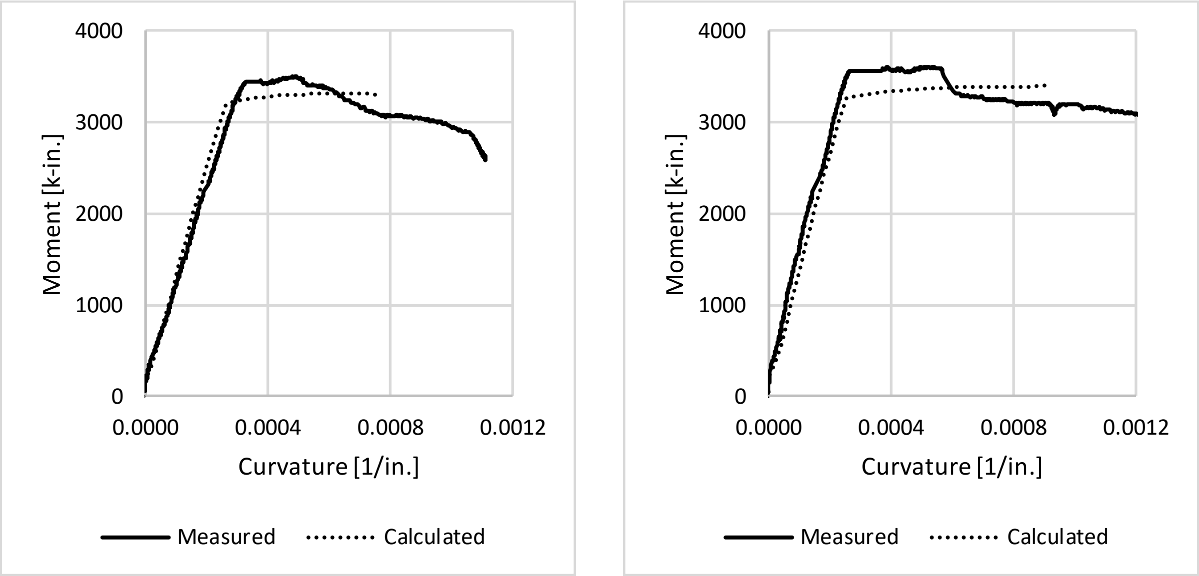

(a) 2GBL60 (b) 2GBH60

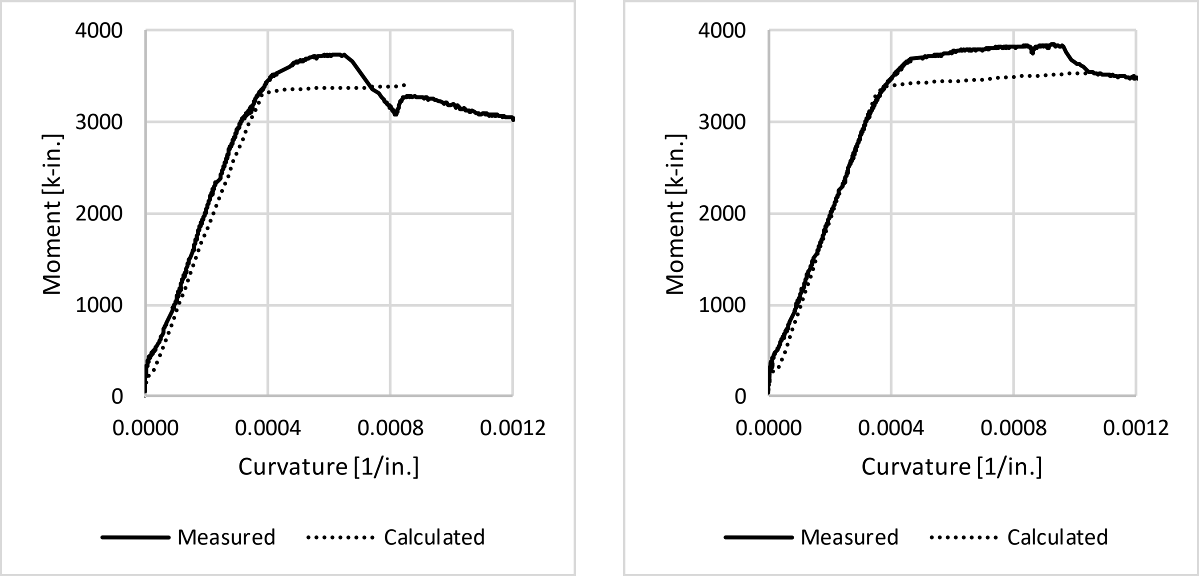

(c) 2GBL100 (d) 2GBH100

Figure 4.8: Series 2 measured and calculated moment-curvature relations

4.4.2. Initial Stiffness

Midspan load and displacement corresponding to cracking and yielding, both experimental and analytical, were determined using the procedures outlined in Section 3.4.2. Calculated cracking and yielding and measured yielding points are superimposed on measured load-deflection curves for each beam in Figure 4.9. In the legend, “C” denotes a calculated value while “M” denotes a measured value. The measured points are the load and deflection corresponding to when the average steel strain in the two instrument bays adjacent to the centerline, determined as described in Section 3.3.3, reached the yield value. Calculated yield points are close to their measured counterparts.

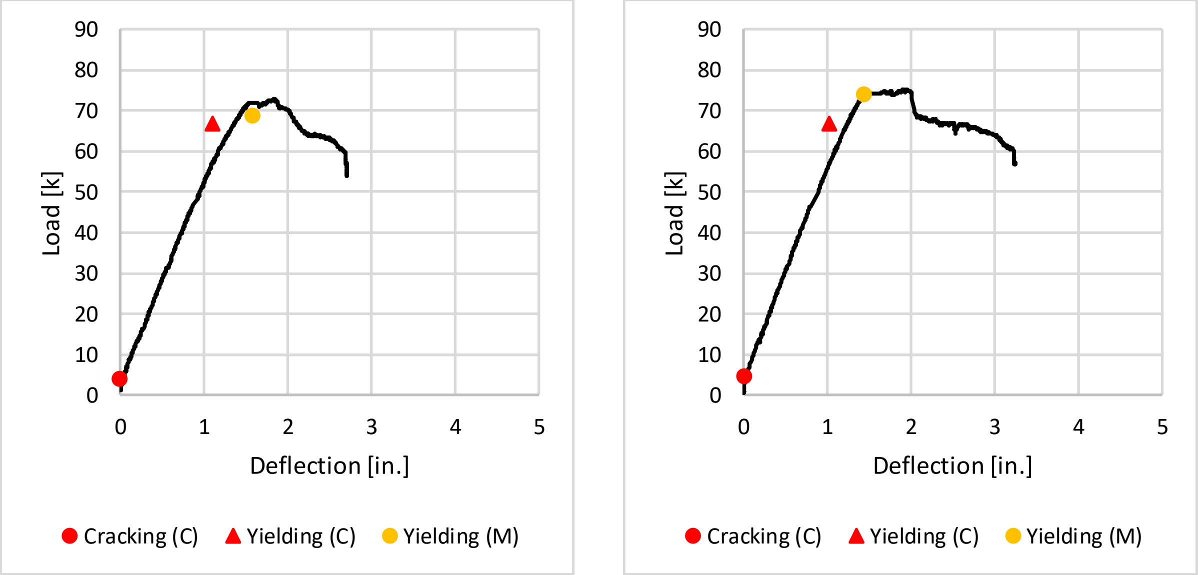

(a) 2GBL60

(b) 2GBH60

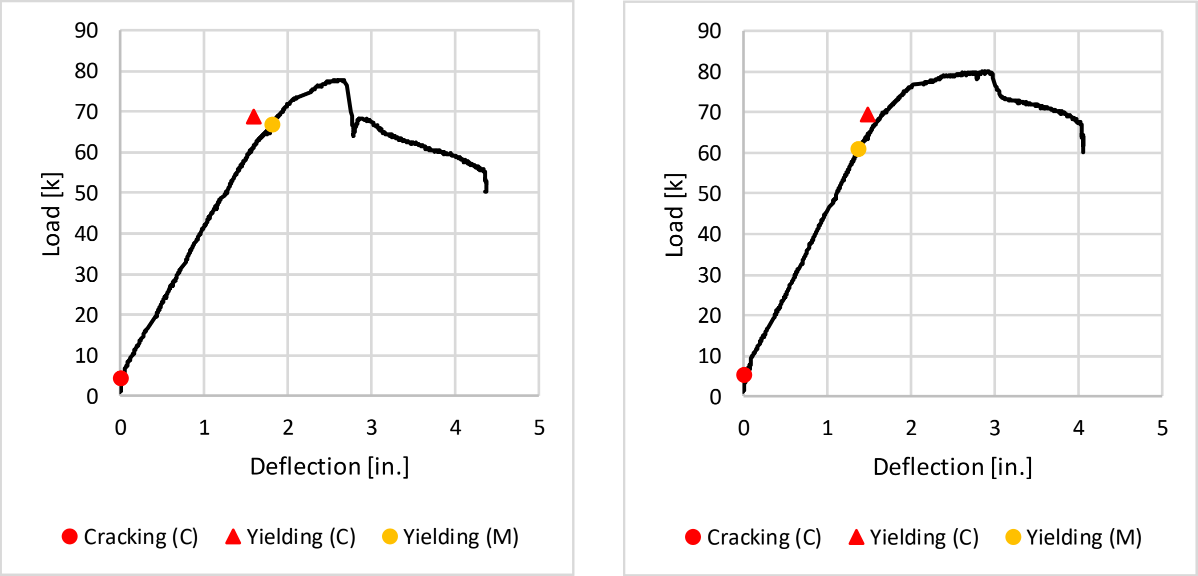

(c) 2GBL100

(d) 2GBH100

Figure 4.9: Series 2 calculated cracking and yielding points

As in Series 1, additional values of cracking and yielding load and displacement were calculated using the effective stiffness techniques described by Branson (1965) and Bischoff (2005), as described in Section 3.4.2. Comparisons of all techniques, as well as the measured response of each beam is provided in Figure 4.10.

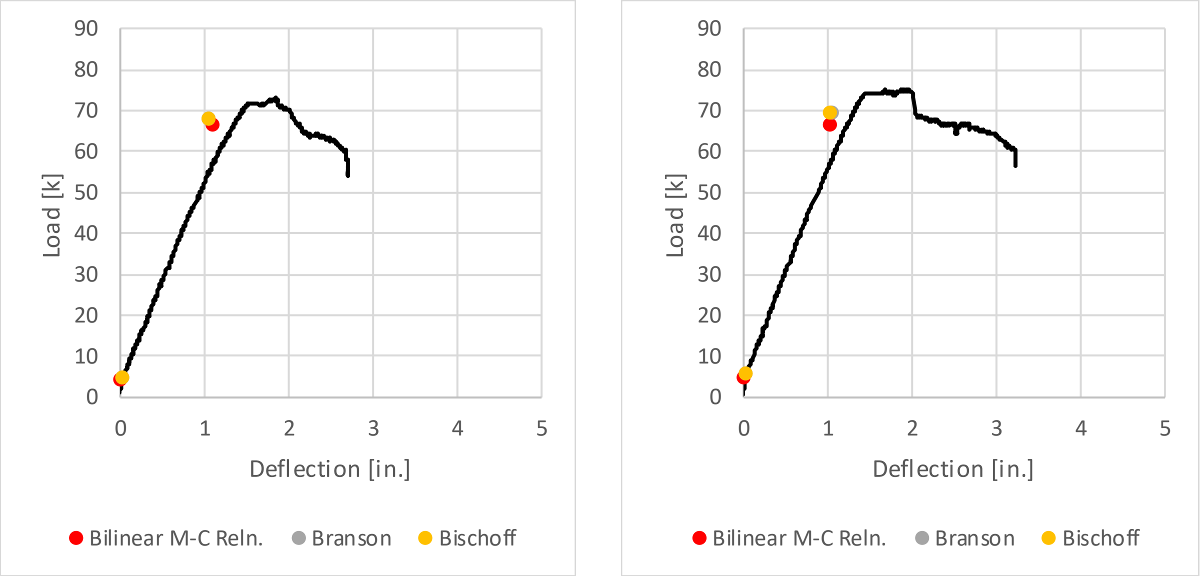

(a) 2GBL60 (b) 2GBH60

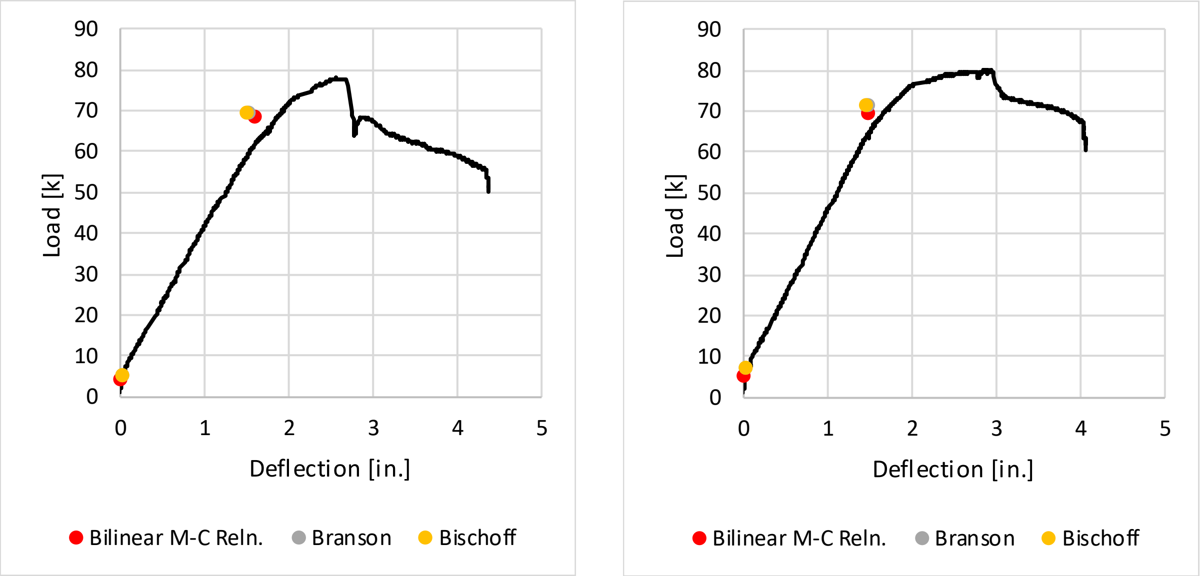

(c) 2GBL100 (d) 2GBH100

Figure 4.10: Series 2 calculated cracking and yielding point calculation comparison

The three methods produced similar cracking and yielding loads and displacements for all beams.

4.4.3. Plastic Deformations

As with Series 1, the Series 2 beams were idealized as two cantilevers symmetric about the centerline. Plastic deformations were calculated using the lumped-plasticity model, with all inelastic curvature assumed to be constrained to occur within the constant moment region. Yield and ultimate deflections were determined using the same methods outlined in Section 3.4.3 and shown in Appendix A.6. Table 3.2 presents the yield and ultimate deflections for Series 2 beams found using the methods described above.

Table 4.2: Series 2 yield and ultimate deflections

	Δ_y [in.]	Δ_u [in.]
2GBL60	1.40	1.84
2GBH60	1.31	1.99
2GBL100	1.85	2.68
2GBH100	1.72	2.97

The lumped plasticity (plastic-rotation) model uses the idealized moment-curvature relation shown in Figure 4.11. (Some plastic curvature is likely to have extended into the shear span, but no attempt is made here to model that effect.)

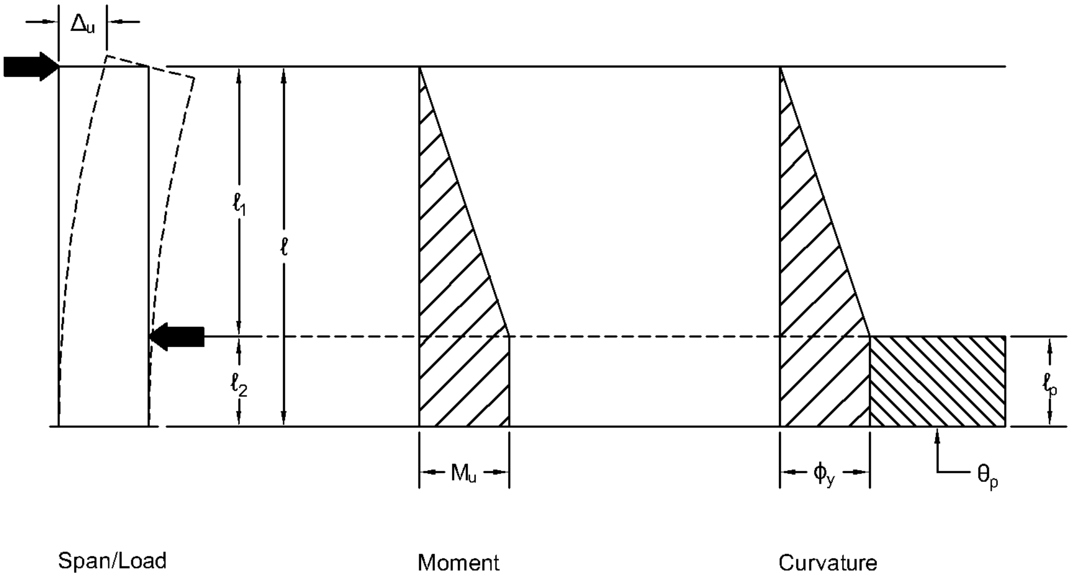

Figure 4.11: Series 2 plastic-rotation model

The member is assumed to develop linear-elastic curvature over its length, with inelastic rotation of magnitude θ_p lumped within the constant-moment region of the cantilever. Plastic rotation was calculated using the same method described in Section 3.4.3 using Eq. (3.3). However, the plastic-hinge length in this case is not infinitesimally small, so

$$\theta_p = \frac{\Delta_u - \Delta_y}{\ell - \ell_p/2} \tag{4.1}$$

where ℓ_p is one half of the constant-moment span.

Figure 4.12 shows plastic rotation as a function of net tensile strain for all beams in Series 2. Figure 4.13 shows plastic rotation as a function of the difference between net tensile strain and yield strain.

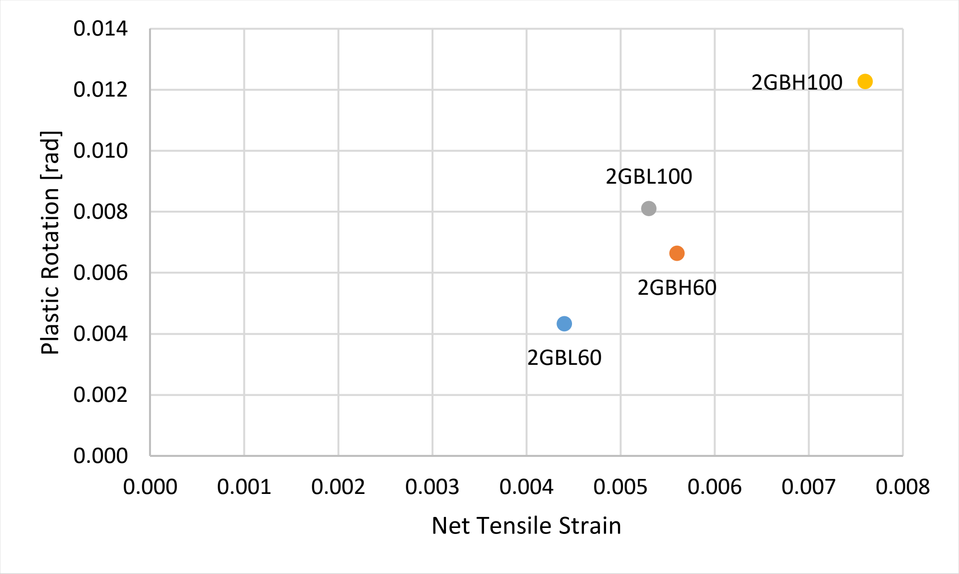

Figure 4.12: Series 2 plastic rotation-net tensile strain

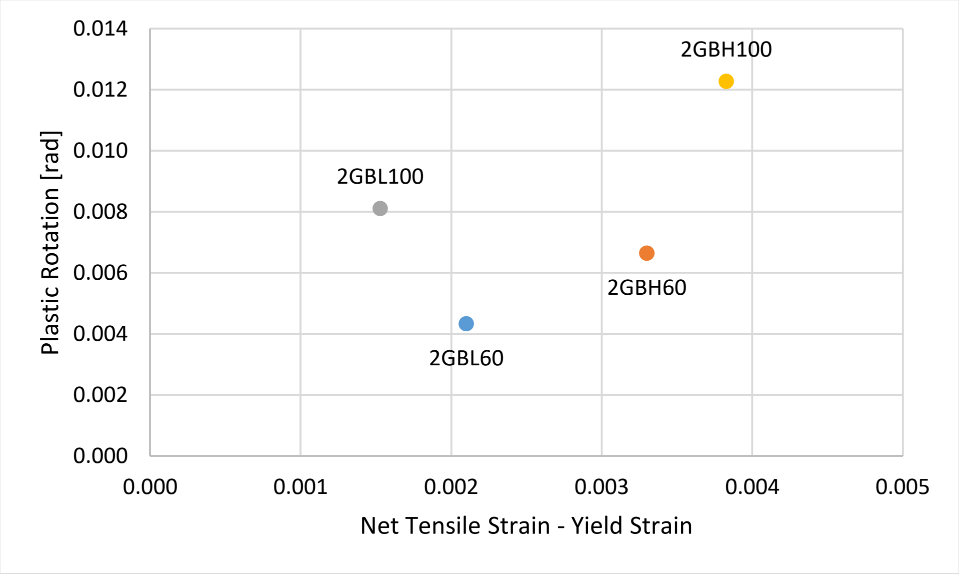

Figure 4.13: Series 2 plastic rotation-net tensile strain minus yield strain

For a given reinforcement grade, a beam with higher net tensile strain is expected to have higher inelastic deformation capacity. This behavior is apparent in both Figure 4.12 and Figure 4.13. For a fixed plastic-hinge length, theoretical considerations would suggest that the plastic rotation capacity should be proportional to the difference between net tensile strain and yield strain, as shown in Figure 4.13. However, for a given value of the difference between net tensile strain and yield strain, beams with Grade 100 reinforcement developed relatively higher plastic rotations than did beams with Grade 60 reinforcement. Figure 4.12 shows that plastic rotation capacity increased nearly linearly with net tensile strain, rather than with the difference between net tensile strain and yield strain. The reason for this behavior is discussed in more detail in Chapter 6.

4.5. Numerical Models

Finite-element models were constructed and analyzed for all beams in Series 2. Dimensions and material properties were based on measured values. Details related to the modeling process are outlined in Appendix C.1. Finite-element models were built in GiD (2019) and analyzed using ATENA (2019).

4.5.1. Load-Deflection Relations

Comparisons between calculated and measured load-deflection relations for all beams in Series 2 are provided in Figure 4.14 through Figure 4.17. The length in the parentheses following “Calculated” denotes the approximate size of the square mesh. Similarities in analysis output for different mesh dimensions suggests that model behavior is independent of mesh size.

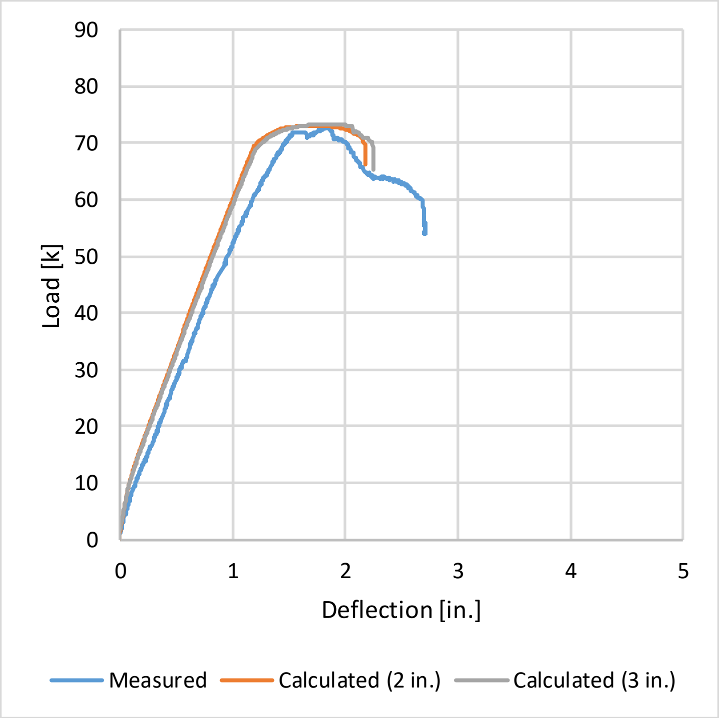

Figure 4.14: 2GBL60 load-deflection relation comparison

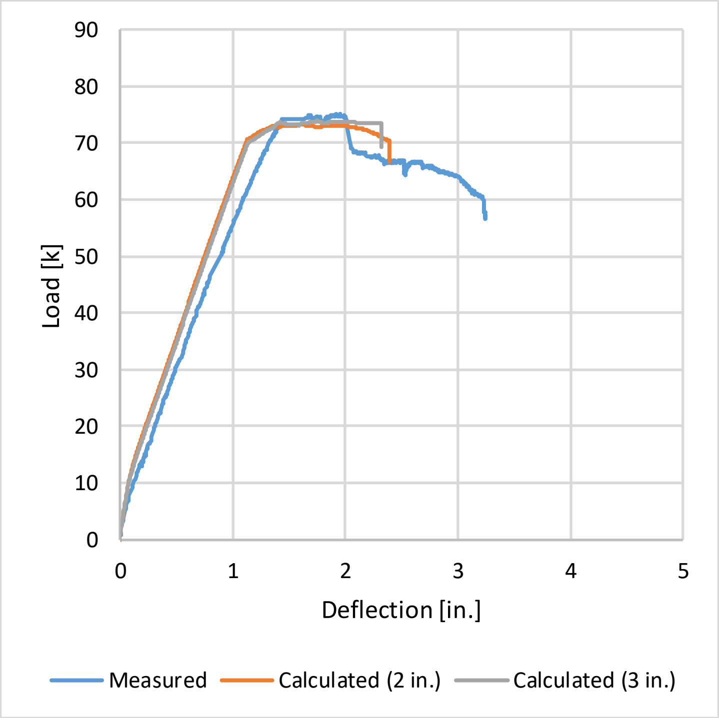

Figure 4.15: 2GBH60 load-deflection relation comparison

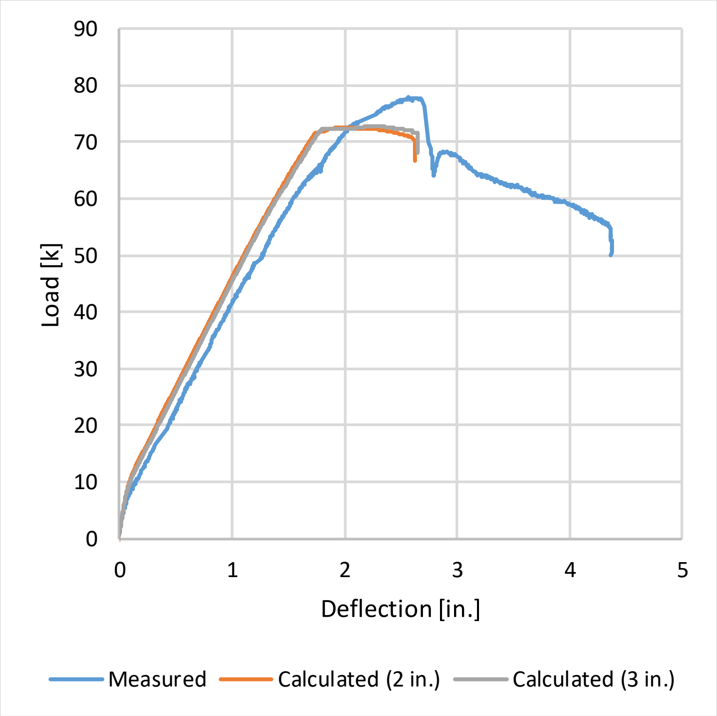

Figure 4.16: 2GBL100 load-deflection relation comparison

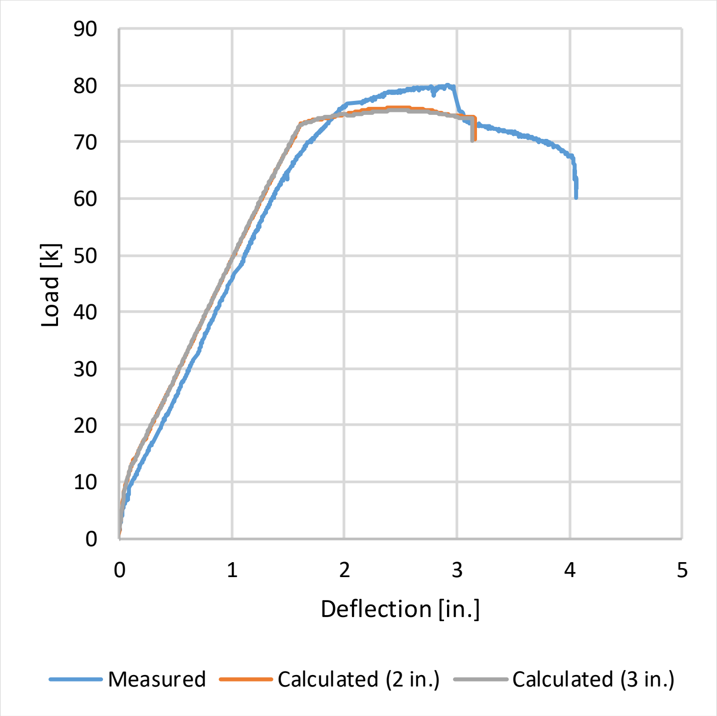

Figure 4.17: 2GBH100 load-deflection relation comparison

Initial stiffness of the finite-element models is higher than the measured stiffness. In the nonlinear range of response, agreement between measured and calculated values is not as close. Strengths compare well but deformation capacities are not as close, though they are the same order of magnitude. This latter shortcoming may be because failure is controlled by strain-softening behavior of unconfined concrete, making the model results sensitive to material properties and the modeling approach. Models show little strain-hardening behavior after yield, and plastic deflection increases with increasing net tensile strain.

Experimental results and analysis output seem reasonable based on comparisons of global behavior. The analysis output demonstrates that traditional modeling techniques and the assumptions that go into them (most of which have been calibrated against tests of members with normal-strength reinforcement) can be used be used to examine beams reinforced with normal-strength or high-strength steel reinforcement, with no obvious limitations as reinforcement grade is increased. This conclusion is consistent with the findings presented in Section 3.5.

5. Serviceability

5.1. Introduction

The service-level range of response comprises loads and deflections less than at yield. Serviceability requirements are those design criteria that relate to behavior other than strength and most often include limiting excessive deflections and crack widths. Serviceability is a greater concern for beams reinforced with high-strength reinforcement because, for the same design strength, those members will have proportionately less longitudinal reinforcement than beams reinforced with conventional-strength reinforcement. As a result, beams with higher-strength reinforcement will be less stiff which would result in larger deflections and crack widths for a given level of load.

5.2. Cracking

Often, cracking represents a limit state for design of reinforced concrete structures. Limiting crack widths is important for appearances and for protecting reinforcement from deterioration.

There are several well-known methods for estimating the maximum crack widths in a reinforced concrete member in the linear range of response. Among these, two methods (Gergely and Lutz, 1968; Frosch, 1999) are considered here. The former is known as the Gergely-Lutz Equation, and the latter is known as the Cracking Model. According to these methods, crack width depends on member geometry, material properties, and the stress in the longitudinal reinforcing steel.

In past editions of the ACI Building Code (e.g. ACI 318-95), empirical equations were calibrated to limit crack widths to 0.016 in. for interior exposure and 0.013 in. for exterior exposure. When phasing out these provisions, committee members recognized that crack width and reinforcement deterioration were not explicitly linked, so requirements for interior and exterior conditions were combined. Current code provisions (ACI 318-14) for crack control are based on the premise that limiting the spacing of flexural reinforcement will provide sufficient resistance against crack-width development, though no maximum acceptable crack width is specified.

For beams designed for the same ultimate strength, those with higher-strength reinforcement will have higher working stresses in the tension steel than those with lower-strength reinforcement. The equations and provisions above were developed primarily using tests of specimens with Grade 60 reinforcement where working stresses were limited to 50 ksi. As such, their applicability to higher grades of reinforcement may be limited. Comparisons of crack widths measured during testing and crack widths calculated using the two methods mentioned above are provided in Figure 5.1 and Figure 5.2. The steel stresses used to calculate crack widths in both equations were determined from moment-steel stress relationships and corresponded to points during each test where loading was paused to mark and measure cracks. Measured and calculated crack widths are reported at the tension face of the member.

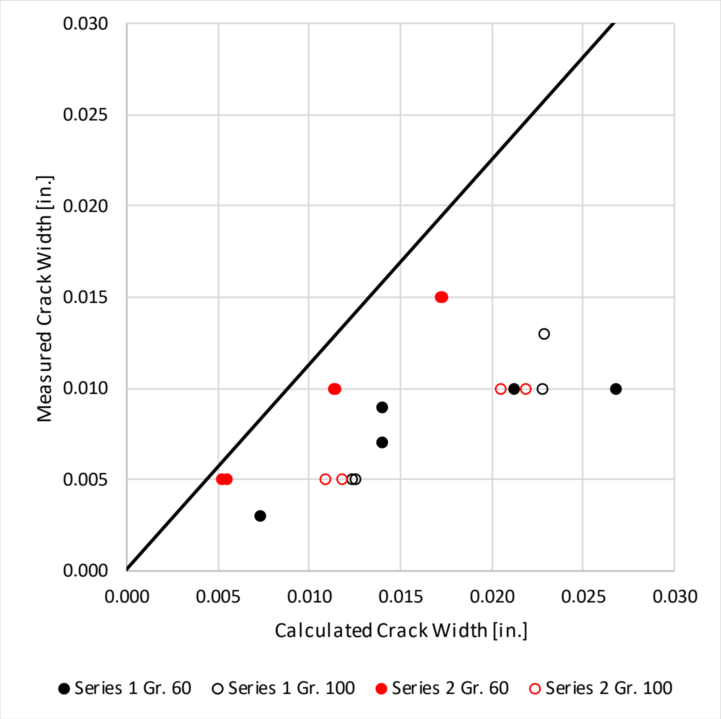

Figure 5.1: Comparison of measured and calculated (Gergely-Lutz Equation) crack widths

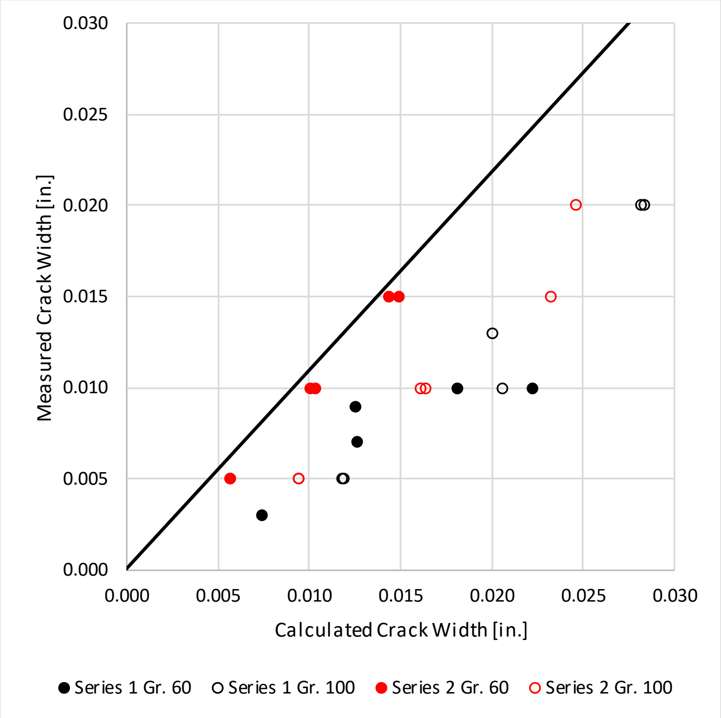

Figure 5.2: Comparison of measured and calculated (Cracking Model) crack widths

The Cracking Model provides slightly more accurate estimations of crack width than the Gergely-Lutz Equation (the residual sum of squares from the 1:1 line of the former is approximately half that of the latter).

Figure 5.3 and Figure 5.4 show the relationship between maximum measured crack width and reinforcement stress for each beam in Series 1 and Series 2, respectively. Steel stress was calculated as the applied load divided by the yield load, as determined using the method outlined in Appendix A.6, multiplied by the yield stress. These figures suggest, for a given beam, that steel stress is linearly proportional to maximum crack width. Beam 1GBH60 is the only specimen that seems to contradict this assertion. Beam 1GBL60 only has two data points, so does not provide useful information in this case. In all instances, the slopes of these relationships are similar. In Series 2, beams with higher-strength reinforcement exhibited smaller maximum crack widths for a given steel stress. Figure 5.5 shows the variation of maximum measured crack width with corresponding reinforcement steel stress for all beams together.

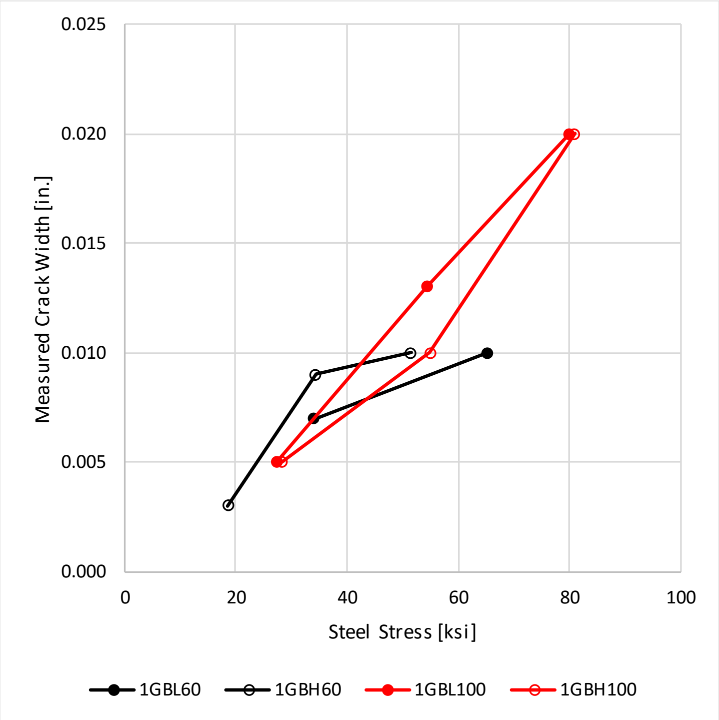

Figure 5.3: Series 1 measured crack width-steel stress

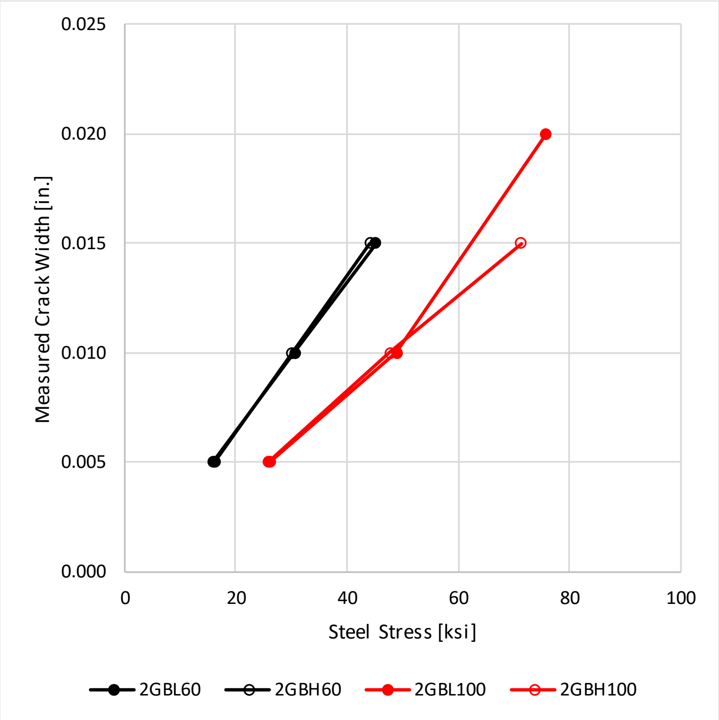

Figure 5.4: Series 2 measured crack width-steel stress

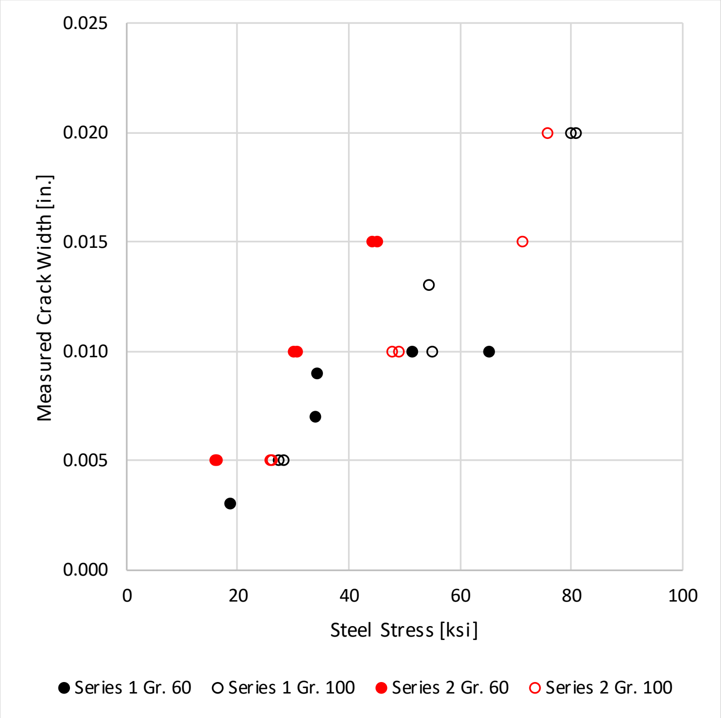

Figure 5.5: Measured crack width-steel stress

Figure 5.5 suggests that the overall relationship between measured crack width and steel stress is linear and has no dependence on the grade of steel or reinforcement ratio of the member. Using that result, working stresses in the steel should be limited to approximately 65 ksi to conform with the now-defunct provisions of ACI 318-95. This follows the conclusions of Soltani et al. (2013) that for reinforcing bar stresses lower than approximately 70 ksi, crack widths in beams were limited to an acceptable level (less than 0.017 in.) regardless of reinforcement grade and relatively independent of reinforcement ratio. Puranam (2018) confirmed these results for beams but suggested that ACI 318-14 provisions relating bar spacing to control cracking may need to be adjusted to account for higher grades of reinforcement in slabs, where bar spacing is generally larger than in beams.

5.3. Deflections

Figure 5.6 and Figure 5.7 provide comparisons of measured and calculated response for all beams from cracking through yielding using the effective stiffness techniques described by Branson (1965) and Bischoff (2005), as outlined in Section 3.4.2. The lowest point gives the predicted response at cracking and the highest predicts the behavior at yielding. The points in between are at 30 and 60% of the nominal yield capacity.

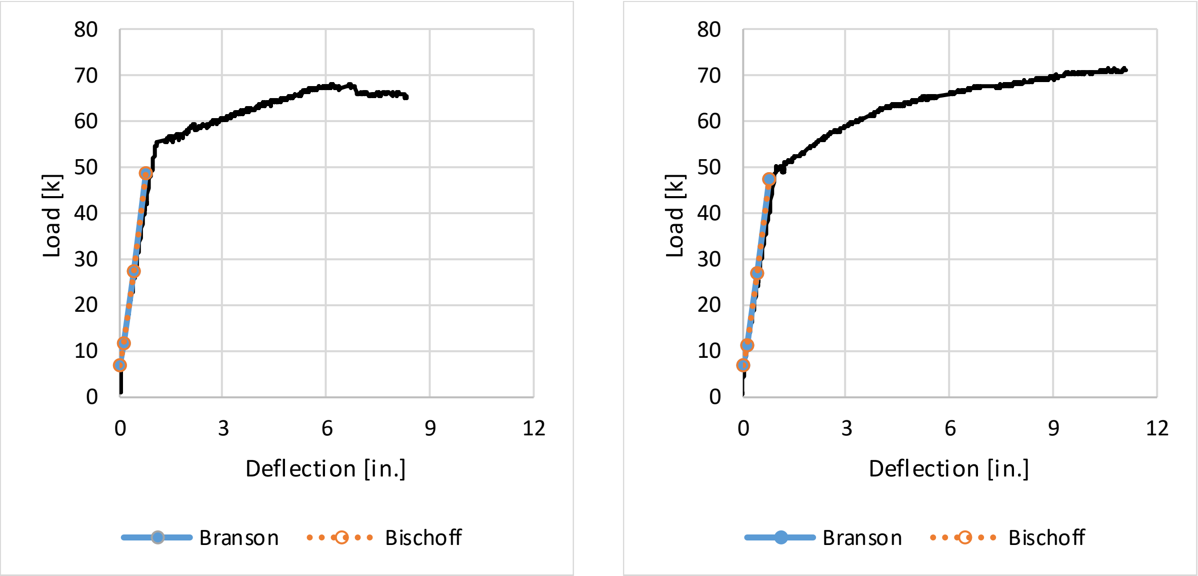

(a) 1GBL60

(b) 1GBH60

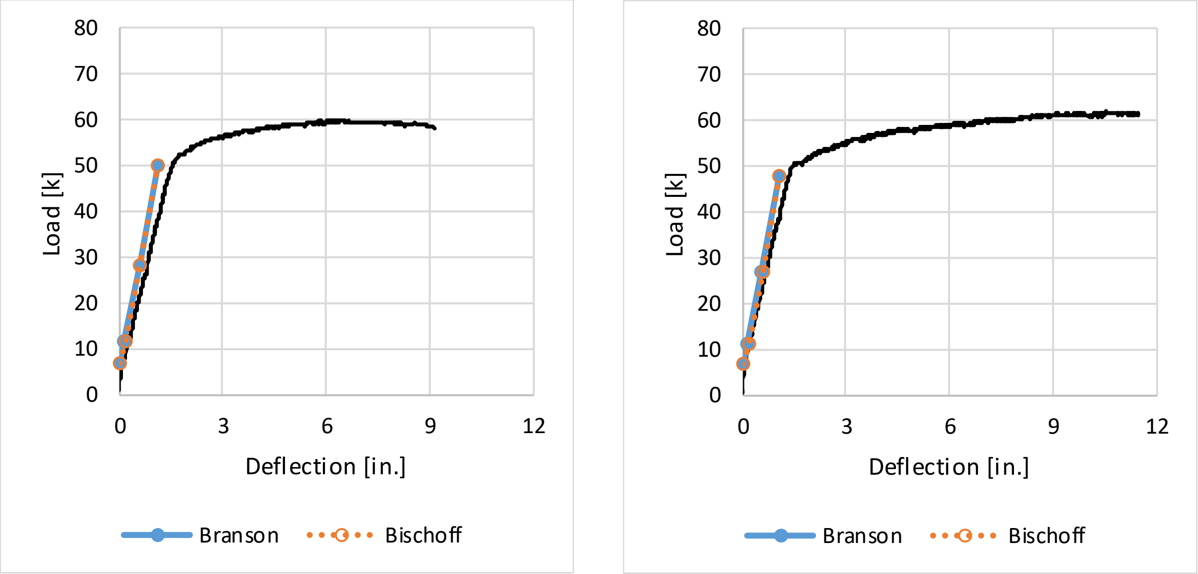

(c) 1GBL100

(d) 1GBH100

Figure 5.6: Series 1 calculated service-level response

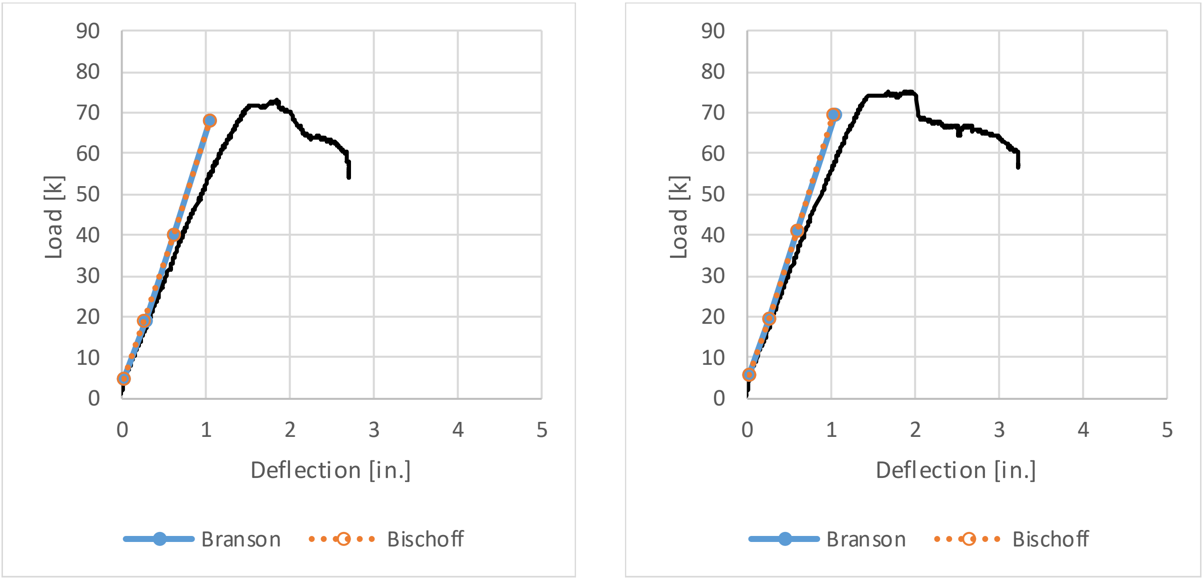

(a) 2GBL60

(b) 2GBH60

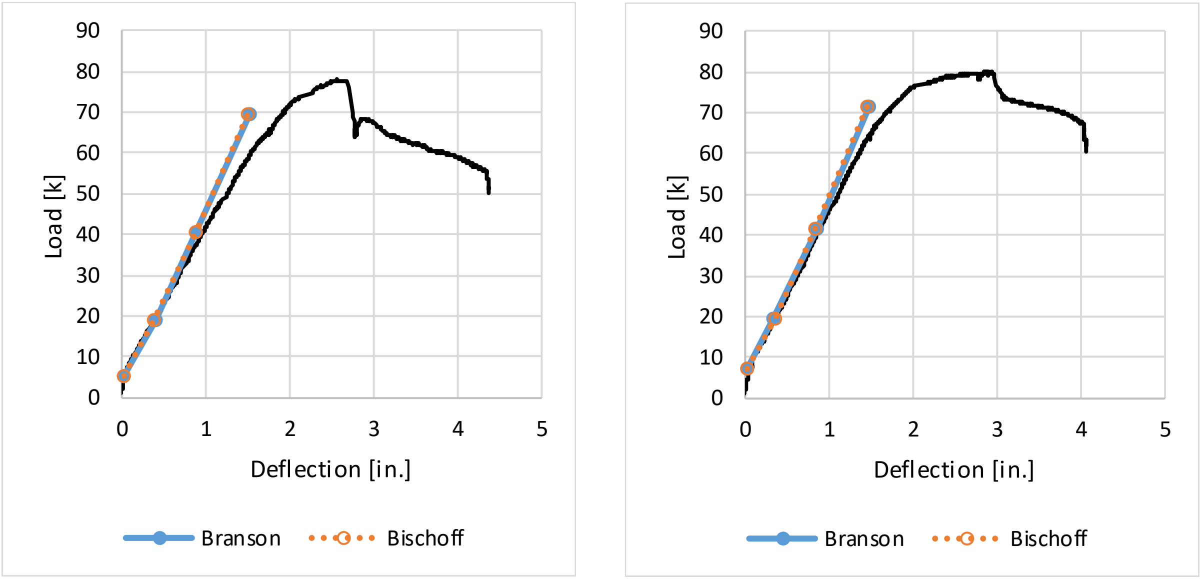

(c) 2GBL100

(d) 2GBH100

Figure 5.7: Series 2 calculated service-level response

In all cases, both calculation techniques predict similar behavior at all computed points. In the service-level range of response, computed loads and deflections are closer to the measured response than at yield.

For the same strength, beams with higher-grade steel have less reinforcement. For reinforcement with the same elastic modulus across strengths, this will result in lower beam stiffnesses. It is important then, for designers to be cognizant of the increased displacement demands associated with the use of higher-grade reinforcing steel. Section 3.4.2 and 4.4.2 demonstrated that elastic beam theory coupled with ACI 318-14 techniques for calculating effective cross-sectional stiffnesses, as well as methods employing mechanics and beam geometry, provide a reasonable estimate for beam deflections, even as the steel grade is increased. This is consistent with the assertions of Puranam (2018), who examined the efficacy of these techniques over a variety of support conditions, spans, and yield stresses of steel reinforcement.

6. Moment Redistribution

6.1. Introduction

Moment redistribution describes the shifting of the moment diagram from the diagram for linear-elastic response to a different diagram as a result of nonlinear-flexural response at one or more cross sections. Moment redistribution is commonly used in design as a means of reducing maximum design moments by shifting moment to other cross sections. It is permitted for gravity-load design by many building codes, including ACI 318-14.

As an example, consider the beam in Figure 6.1. The beam is weightless, both ends are fixed, and a uniformly distributed load is applied across its span. The negative-moment strengths at each of the beam ends are equal and less than twice the positive-moment strength of the beam at its center. Flexural strengths in both bending directions are assumed constant across the length of the beam. Often, inelastic behavior in indeterminate concrete members is idealized by an elastic-perfectly plastic moment-curvature relationship. Under this assumption, the sections that reach their capacities develop a plastic hinge and incremental curvature or rotation occurs at these sections with no change in moment.

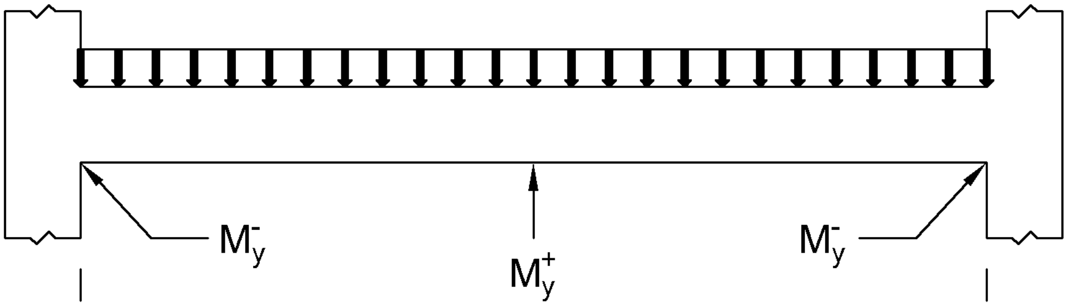

Figure 6.1: Example beam

The resulting moment diagram for the loading and boundary conditions shown is parabolic, with maximum moment demand at supports double that in the span. As load is increased, this demand eventually reaches the moment strength of one or more sections. Figure 6.2 shows the beam load and moment demands when demand first reaches strength, which in this idealized case is simultaneously at the supports.

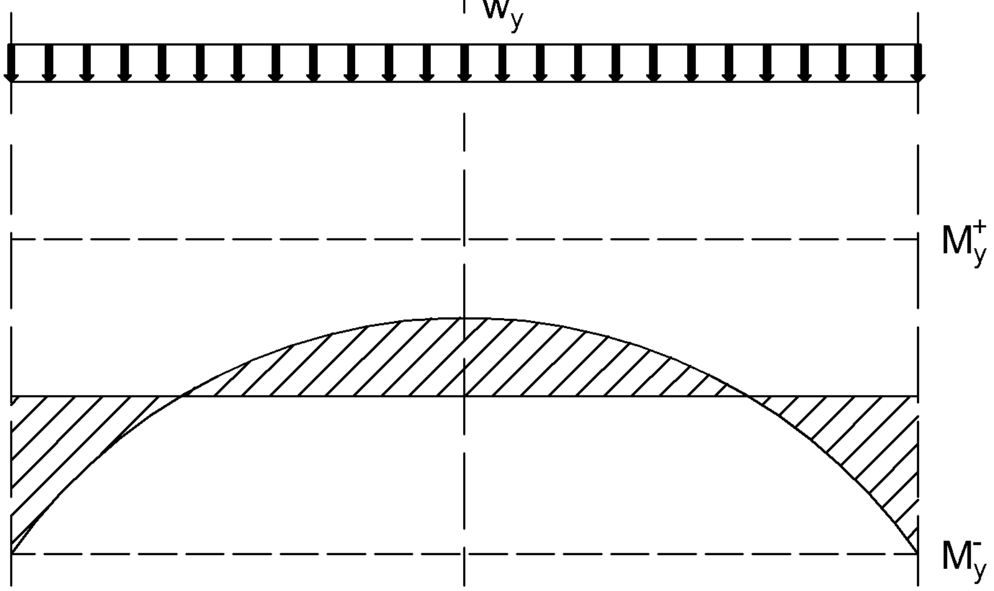

Figure 6.2: Example beam load and moment diagram at first hinge formation

Because demand on the beam in Figure 6.2 has reached strength at the ends, any additional deformation of the ends will occur without increase in moment, hence, they act like hinges. At this point, the assembly is still stable and can continue to carry additional load as a simple-span determinate beam with pinned ends and a constant end moment. Considering only the load increment, the resulting system is provided in Figure 6.3, which illustrates an idealization of how the beam will behave under additional loading.

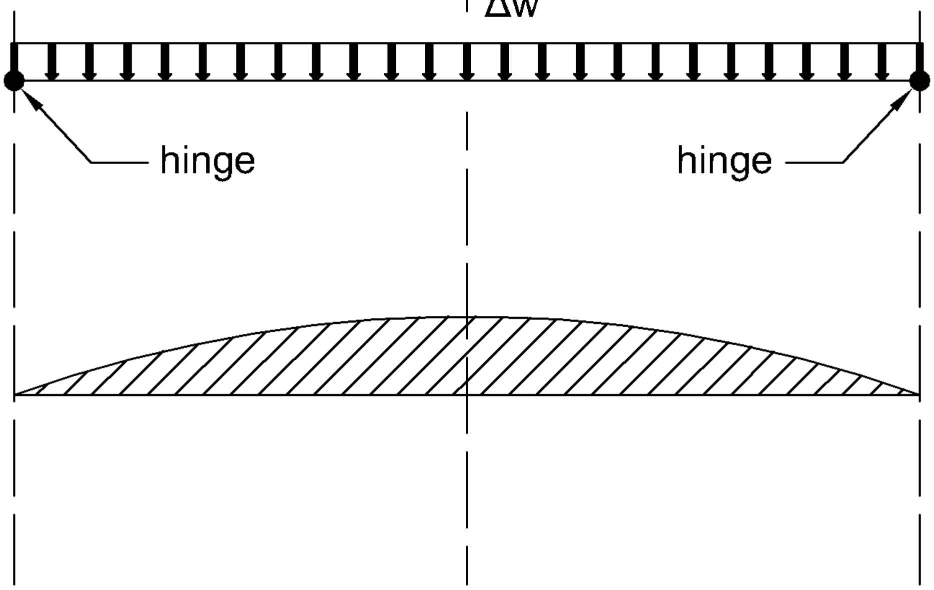

Figure 6.3: Example beam load and moment diagram for increment beyond hinge formation

This incremental loading can continue until a mechanism is formed that renders the system unstable. Figure 6.4 shows such a result for the example beam. At this point, the resulting hinges mean the beam can carry no additional load and the system is at incipient collapse.

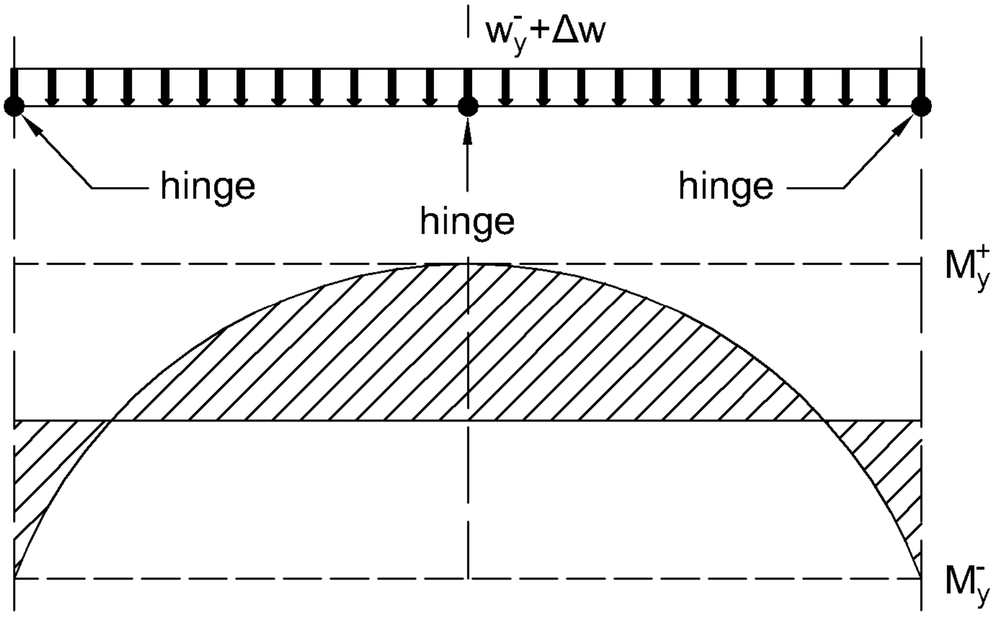

Figure 6.4: Example beam load and moment diagram at mechanism formation

In engineering practice, this extra load-carrying capacity allows designers to shift design demands. In a sense, the beam is stronger than its weakest cross section would suggest, provided a mechanism isn't formed when that section yields, so designers are permitted to redistribute design moments by allowing for nonlinear behavior at certain sections. Detailed applications of this process are provided in Bondy (2003).

Developing this additional load-carrying capacity, or redistribution of moments, is predicated on the ability of the hinges to undergo plastic rotation. The plastic rotation capacity of a section is limited and depends on many factors, such as material strengths, member geometries, plastic-hinge lengths, and limiting strains. Thus, it is important to establish relationships relating parameters for designers to use. Traditionally, designers have determined permissible moment redistribution from the net tensile strain. Relationships were demonstrated by Mast (1992) to be different depending on the grade of steel selected. Thus, the relationship was an analog for plastic steel strain.

In Section 6.2, moment redistribution is examined with code-based assumptions, such as a fixed plastic-hinge length, elastic-perfectly plastic steel behavior, consistent stiffness along the length of the beam, and an equivalent-stress-block for limiting concrete behavior. In reality, such an idealized system could never exist, so it is important to consider moment redistribution with nonlinear behavior such as strain-hardening behavior in the reinforcement, spread of plasticity, and variable stiffness along the length of the beam. Section 6.3 contains such an analysis.

6.2. Limits for Idealized Beams

6.2.1. Formulation

Consider the case of a beam with both ends fixed against rotation, with cross sections having elastic-perfectly plastic moment-rotation behavior, with yield strengths at the center and ends equal to M_y^+ and M_y^-, and subjected to uniformly distributed load. The static moment for the beam under these conditions is

$$M_o = \frac{w_o \ell^2}{8} \tag{6.1}$$

The static moment at the ultimate load can be related to the moment strengths as

$$M_{ou} = \frac{w_{ou}\ell^2}{8} = M_y^+ + M_y^- \tag{6.2}$$

The ultimate load determined from Eq. (6.2) can be used to determine the moment at a yielded section if that section had remained elastic under the same load. If $M_y$is the yield moment at the section that yields first and M_e is the moment at that section if it had remained elastic, then

$$R = \frac{M_e - M_y}{M_e} = 1 - \frac{M_y}{M_e} \tag{6.3}$$

where R is the required moment redistribution at the critical section. Calling the ultimate load the elastic load ($w_{ou} = w_e$), the resulting elastic moment would be given by Eq. (6.4) or (6.5) for the negative-moment or positive-moment section, respectively.

$$M_e^- = \frac{w_e\ell^2}{12} \tag{6.4}$$

$$M_e^+ = \frac{w_e\ell^2}{24} \tag{6.5}$$

Assuming the fixed ends of the beam have equal strengths and yield first, the moment increase at the center of the beam due to additional superimposed load required to form a mechanism after yielding at the supports is given by

$$\Delta M^+ = \frac{\Delta w\ell^2}{8} \tag{6.6}$$

and the plastic rotation at the supports corresponding to that moment increase is

$$\theta_p^- = \frac{\ell}{3EI}\Delta M^+ \tag{6.7}$$

The elastic load is the sum of the load that causes yielding at the supports (w_y^-) and the additional superimposed load that is required to form a mechanism (Δw), or

$$w_e = w_y^- + \Delta w \tag{6.8}$$

which, in turn, can be related to the elastic and yield support moments by

$$M_e^- = \frac{w_e \ell^2}{12} = M_y^- + \Delta M_y^- = \frac{w_y^- \ell^2}{12} + \frac{\Delta w \ell^2}{12} \tag{6.9}$$

Rearranging Eq. (6.6) results in

$$\Delta w = \frac{8\Delta M^+}{\ell^2} \tag{6.10}$$

which can be combined with Eq. (6.9) to show that

$$\Delta M^+ = \frac{3}{2}\left(M_e^- - M_y^-\right) = \frac{3}{2}M_y^-\left(\frac{M_e^-}{M_y^-} - 1\right) \tag{6.11}$$

because

$$\Delta M_y^- = \frac{\Delta w \ell^2}{12} = \frac{8}{12}\Delta M^+ = \frac{2}{3}\Delta M^+ \tag{6.12}$$

Since it was assumed that yielding at the fixed supports takes place first, then Eq. (6.3) becomes

$$R = 1 - \frac{M_y^-}{M_e^-} \tag{6.13}$$

which can be arranged to show

$$\frac{M_e^-}{M_y^-} = \frac{1}{1 - R} \tag{6.14}$$

Combining Eq. (6.11) and (6.14) gives

$$\Delta M^+ = \frac{3}{2} M_y^- \left(\frac{1}{1 - R} - 1 \right) = \frac{3}{2} M_y^- \frac{R}{1 - R} \tag{6.15}$$

which can be substituted into Eq. (6.7) to show that

$$\theta_p^- = \frac{\ell}{3EI} \frac{3}{2} M_y^- \frac{R}{1 - R} = \frac{1}{2} \ell \frac{M_y^-}{EI} \frac{R}{1 - R} = \frac{1}{2} \ell \phi_y^- \frac{R}{1 - R} \tag{6.16}$$

in which

$$\phi_y^- = \frac{M_y^-}{EI} = \frac{\varepsilon_y}{d(1 - k_y)} \tag{6.17}$$

for which k_y is the ratio of the neutral axis depth to the effective depth at yielding. Similarly, the ultimate curvature can be calculated as

$$\phi_u^- = \frac{\varepsilon_t}{d(1 - k_u)} \tag{6.18}$$

for which k_u is the ratio of the neutral axis depth to the effective depth at the limiting curvature. The plastic rotation at a section is limited to the maximum possible plastic rotation, or mathematically

$$\theta_p \leq \theta_{p,max} \tag{6.19}$$

where that maximum plastic rotation for the negative-moment section can be calculated from

$$\theta_{p,max}^{-} = \ell_p\left(\phi_u^{-} - \phi_y^{-}\right) \tag{6.20}$$

Substituting Eq. (6.16) and (6.20) into Eq. (6.19) gives

$$\frac{1}{2}\ell\phi_y^{-}\frac{R}{1-R} \leq \ell_p\left(\phi_u^{-} - \phi_y^{-}\right) \tag{6.21}$$

which can be rearranged and combined with Eq. (6.17) and Eq. (6.18) to show that

$$\frac{R}{1-R} \leq 2\frac{\ell_p}{\ell}\left(\frac{\phi_u^{-}}{\phi_y^{-}} - 1\right) = 2\frac{\ell_p}{\ell}\left(\frac{\varepsilon_t}{\varepsilon_y}\frac{1-k_y}{1-k_u} - 1\right) \tag{6.22}$$

Moment redistribution at the critical (negative-moment) section is then given by

$$R \leq \frac{C}{1+C} \tag{6.23}$$

where the constant, C, is

$$C = 2\frac{\ell_p}{\ell}\left(\frac{\varepsilon_t}{\varepsilon_y}\frac{1-k_y}{1-k_u} - 1\right) \tag{6.24}$$

Cohn (1965) demonstrated the formulation above is conservative given that (1) the assumption of elastic-perfectly plastic steel behavior provides the largest plastic rotation at the critical section, (2) the study of a single-span beam free to rotate at both ends provides larger hinge rotations than when multiple spans are considered, (3) the inelastic rotation at the critical section is independent of the loading scheme, and (4) consideration of constant rigidity along the length of the beam yields larger inelastic support rotations than if variable rigidity was considered instead.

Others have proposed similar equations for moment redistribution. Rearranged as to match the format of Eq. (6.24), Cohn (1965) proposed that moment redistribution for a propped-cantilever beam could be calculated from

$$C = 3\frac{\ell_p}{\ell}\left(\frac{\varepsilon_t}{\varepsilon_y}\frac{1-k_y}{1-k_u} - 1\right) \tag{6.25}$$

where $\ell_p/\ell = 1/30$, k_y was determined without considering the effect of the compression reinforcement when calculating the neutral-axis depth at yield, and k_u was calculated from a closed-form equation.

Mast (1992) proposed that moment redistribution could be determined by

$$C = \frac{3}{2}\left(\frac{\varepsilon_t}{\varepsilon_y} - 1\right)\left(\frac{d}{\ell} + 0.01\right) \tag{6.26}$$

which itself is a rearrangement of Mattock (1983), who derived it using Eq. (6.25), assuming $k_u = k_y$ and $\ell_p = d/2 + \ell/100$.

To minimize R it is necessary to minimize C. Thus, Eq. (6.24), calculated considering the beam to be fixed-fixed produces a lower limit to permissible redistribution than Eq. (6.25) or (6.26), which were derived considering the beam end conditions fixed-free. As a result, Eq. (6.24) gives the more conservative solution.

ACI 318-14 imposes limits on moment redistribution based on net tensile strain, which were determined based on redistribution capacities calculated using Eq. (6.26). These capacities were calculated considering $\ell/d = 23$ and $b/d = 1/5$. Selecting f'_c = 5 ksi, $\rho' = \rho/2$, and $d = 24$ in., comparisons of all methods above are provided in Figure 6.5 for Grade 60 steel and Figure 6.6 for Grade 80 steel. For Eq. (6.24), $\ell_p/\ell = 1/30$ to provide a comparison with Eq. (6.25). It may be useful to note that the equivalent ℓ_p/ℓ in Eq. (6.26) is approximately $1/37$. Unless otherwise stated, all other values used in each calculation were determined following ACI 318-14. In the following figures, the black line is the moment redistribution limit defined by ACI 318-14, and the dashed line is the “calculated available” capacity listed in commentary of the same document.

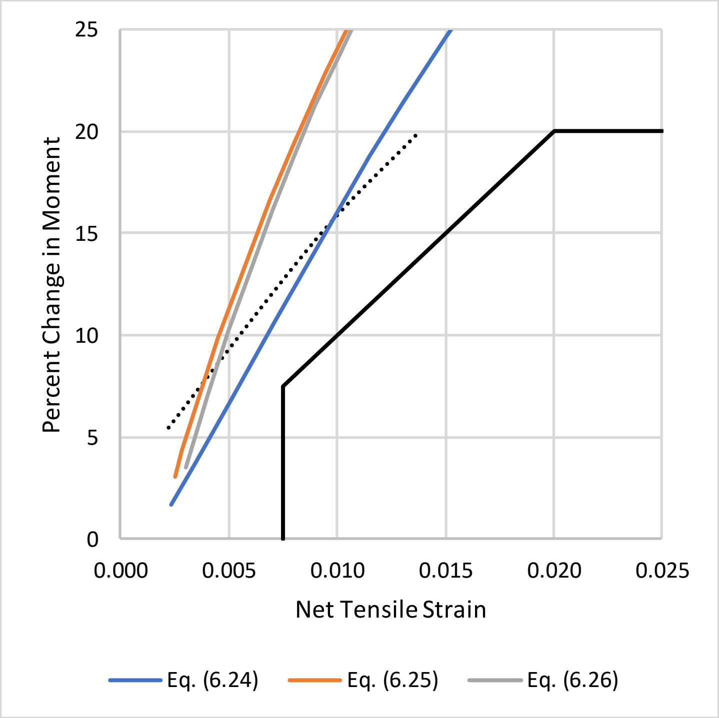

Figure 6.5: Moment redistribution limits for Grade 60 steel

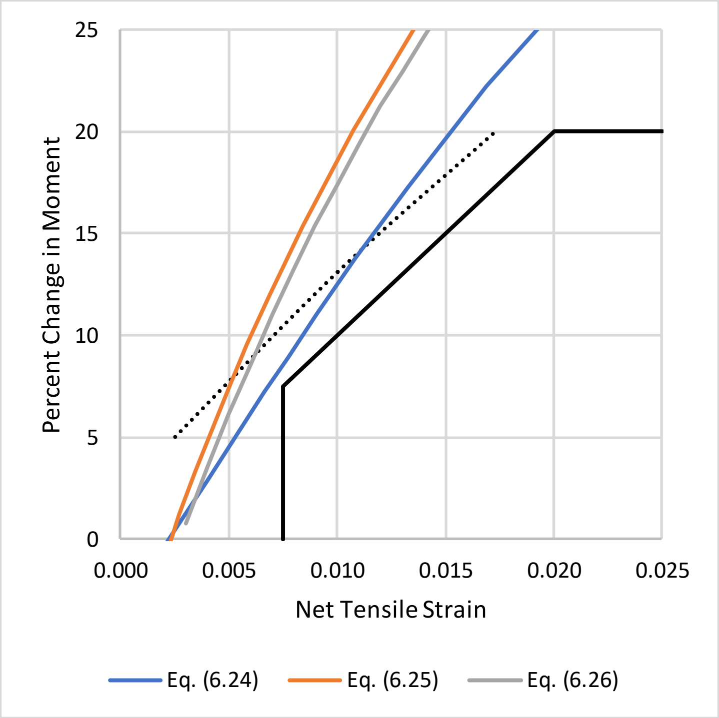

Figure 6.6: Moment redistribution limits for Grade 80 steel

From these figures, considering the equations discussed, it is clear that Eq. (6.24) provides the most conservative limit to moment redistribution and the percent change in moment for a given net tensile strain decreases as the grade of steel increases. The curves for Eq. (6.25) and (6.26) are close to each other. As expected considering their equations, available moment redistribution increases with an increase in net tensile strain and zero moment redistribution is available for a beam for which the yield and net tensile strains are equal. It is interesting to note that the lack of moment redistribution for a beam at balanced failure does not seem to be consistent with the "calculated available" curves featured in ACI 318-14 (the dotted black curves).

To better compare the equations, they were rederived for the more-conservative, fixed-fixed condition. This transformed Eq. (6.25) into (6.24) and Eq. (6.26) into (6.27). Results are provided in Figure 6.7 and Figure 6.8. In all cases $\ell_p/\ell = 1/30$ and other values left the same. In these figures, the Eq. (6.24) suffix "A" or "E" denotes whether k_y and k_u were "approximate" or "exact" values. The former does not consider the effect of the compression steel on k_y and uses the closed-form solution for

k_u given by Cohn (1965), while the latter does consider compression steel in the k_y calculation and determines k_u using principles outlined in ACI 318-14.

$$C = 2\frac{\ell_p}{\ell}\left(\frac{\varepsilon_t}{\varepsilon_y} - 1\right) \tag{6.27}$$

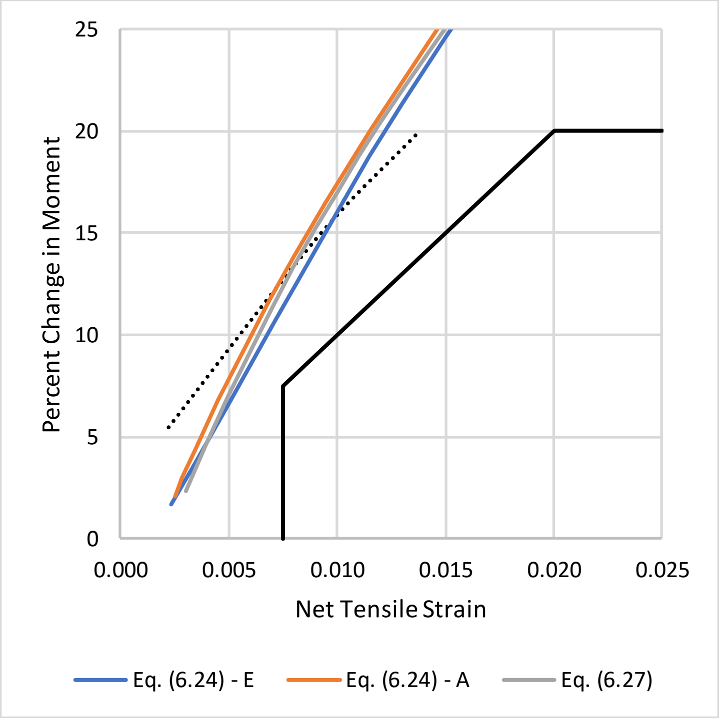

Figure 6.7: Moment redistribution limits for Grade 60 steel

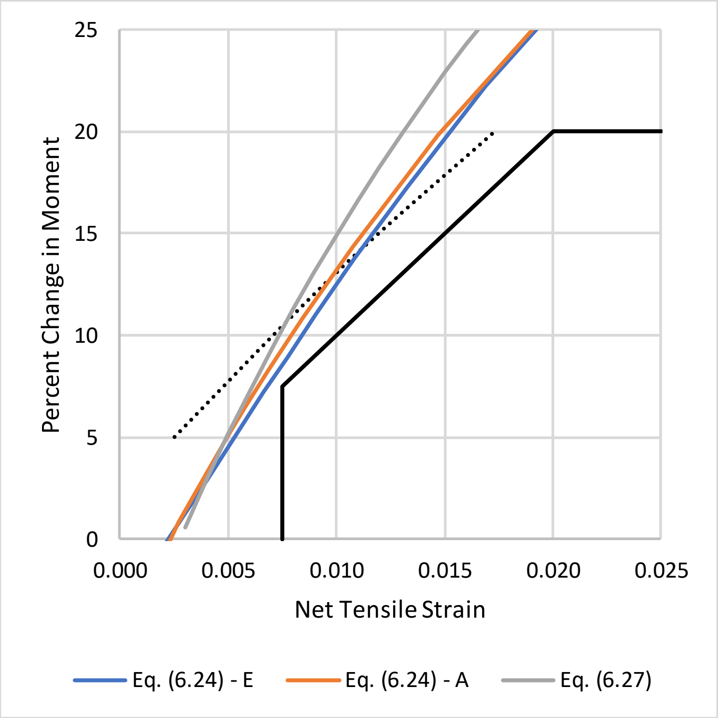

Figure 6.8: Moment redistribution limits for Grade 80 steel

Using this formulation, the results of all equations become relatively consistent. Eq. (6.24) - A and in nearly all cases, Eq. (6.24) – E gives the most conservative limits to moment redistribution. As a result, the use of Eq. (6.24) with the more rigorous "exact" formulation for the calculation of k_u and k_y is adopted in the following parametric studies.

6.2.2. Parametric Studies

The variables that impact the result of Equation (6.24) are h, f'_c, ε_{cu}, ρ'/ρ, ℓ_p/h, and h/ℓ. A parametric study was conducted to asses the relative impact these variables have on the result. In order to do this, first a standard beam was defined. Values defining the standard beam can be found in Table 6.1.

Table 6.1: Standard beam values

Variable	Standard Value	Unit
h	24	in.
f'_c	5000	psi
ε_{cu}	0.003	-
ρ'/ρ	1/2	-
ℓ_p/h	1/2	-
h/ℓ	1/12	-

Having defined a standard beam, variables were systematically altered over a range of typical design values to assess their individual impact on the relationship. The results are provided in the following figures. The number in the legend of each figure indicates the value of the variable under investigation. All results correspond to Grade 60 reinforcement.

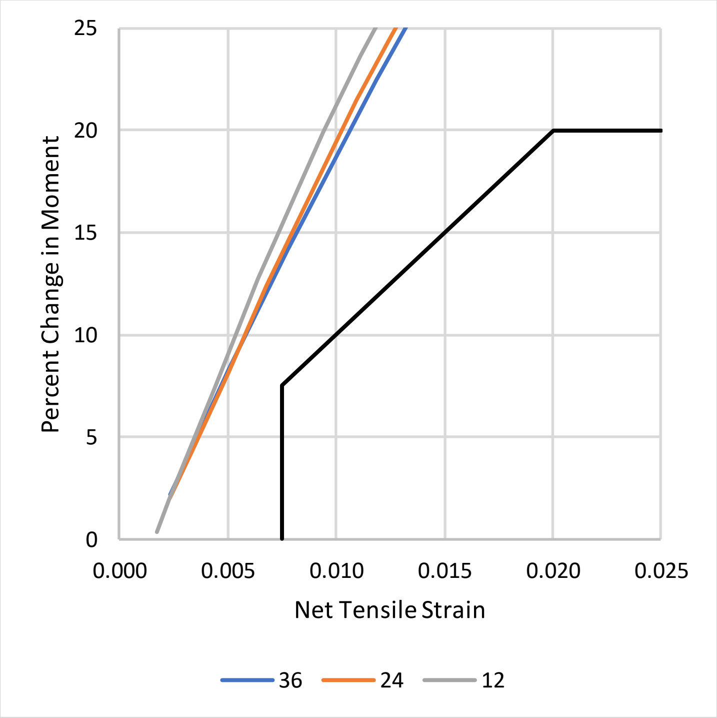

Figure 6.9: Effect of varying beam height

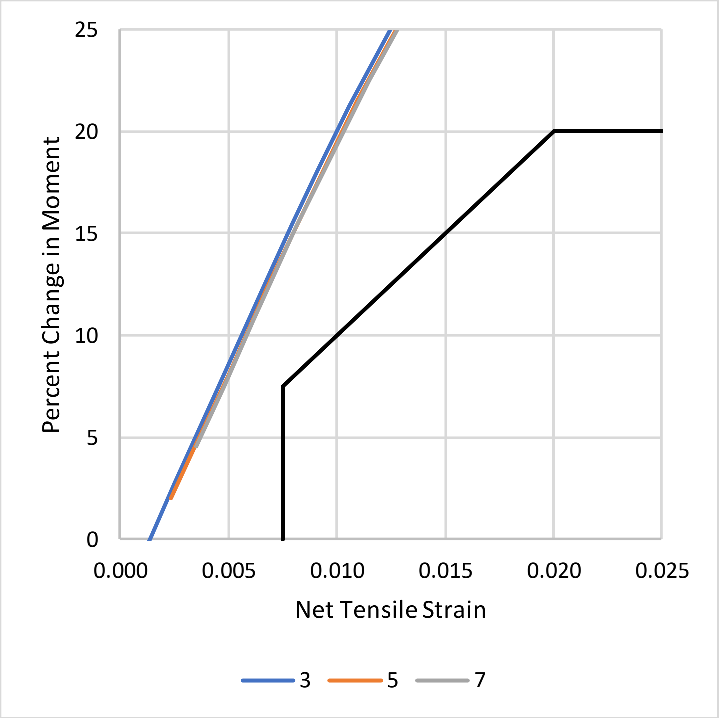

Figure 6.10: Effect of varying concrete compressive strength

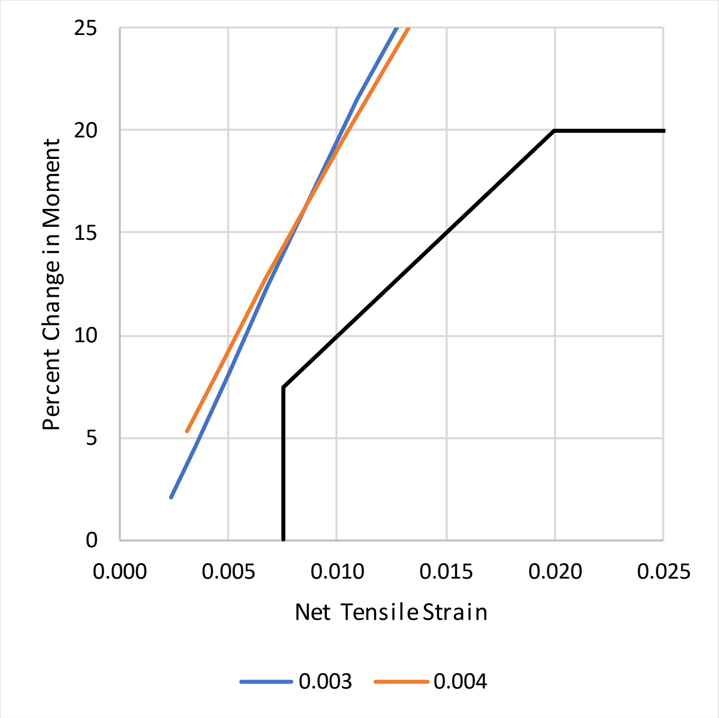

Figure 6.11: Effect of varying concrete crushing strain

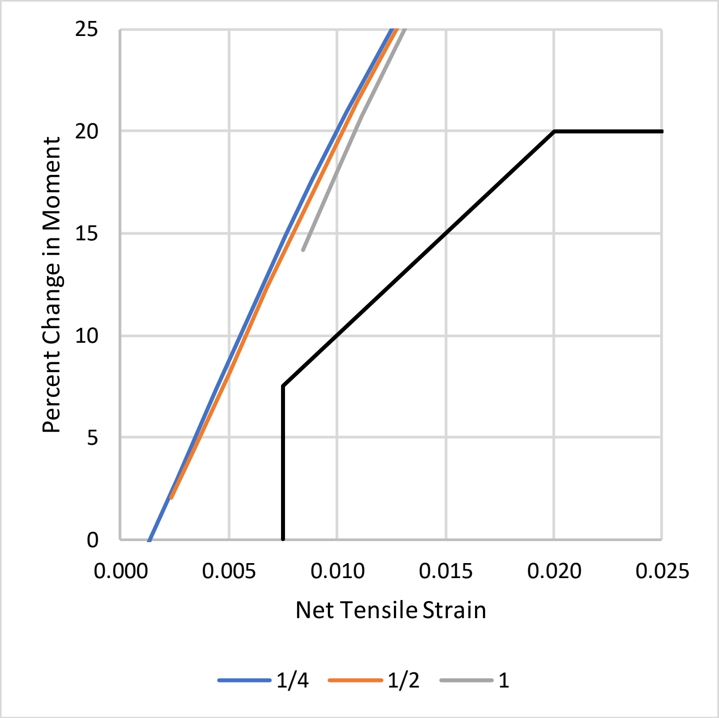

Figure 6.12: Effect of varying compressive to tensile longitudinal reinforcement ratios

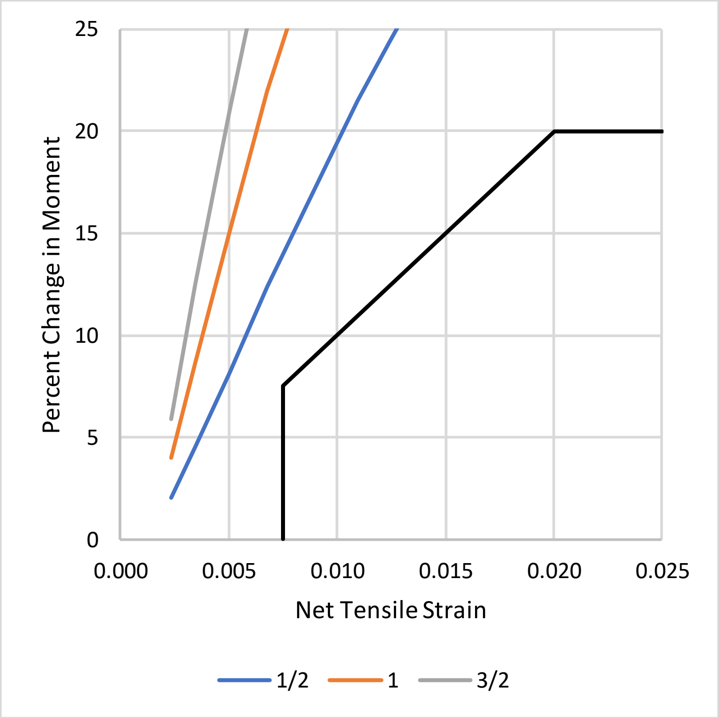

Figure 6.13: Effect of varying plastic-hinge length to beam height

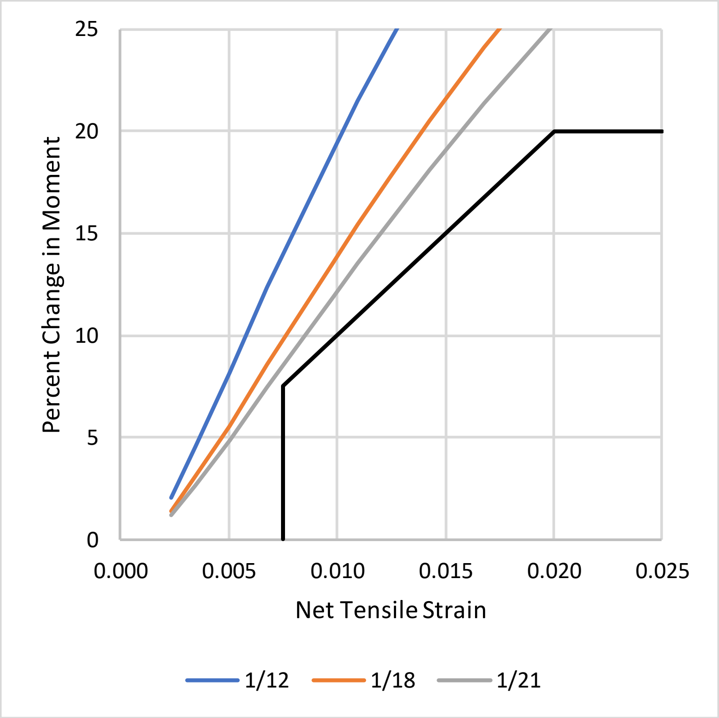

Figure 6.14: Effect of varying beam height to span ratio

It is clear from this investigation that the two variables with the largest impact on the relationship between percent change in moment and net tensile strain are the ratios of plastic-hinge length to beam height, and beam height to span. Since the plastic-hinge length is a fixed fraction of the beam height in the latter case, ultimately, both are related to the plastic-hinge length. The slope of the relationship decreases as the aspect ratio of the beam increases, and as the length of the plastic hinge decreases relative to the height of the beam. It is important then, to consider lower bounds for both ℓ_p/h, and h/ℓ.

The value $1/2$ for ℓ_p/h is common in engineering practice and seems to be a reasonable lower bound based on the results of Section 3.4.3. Adopting this as a standard value, h/ℓ was varied over steels of Grade 60, 80, and 100. The results are presented in Figure 6.15 through Figure 6.17. The values $1/12$ and $1/18$ were selected for ℓ_p/h because these values are common in current structural design. The value $1/21$ was selected because it is the minimum allowed by ACI 318-14.

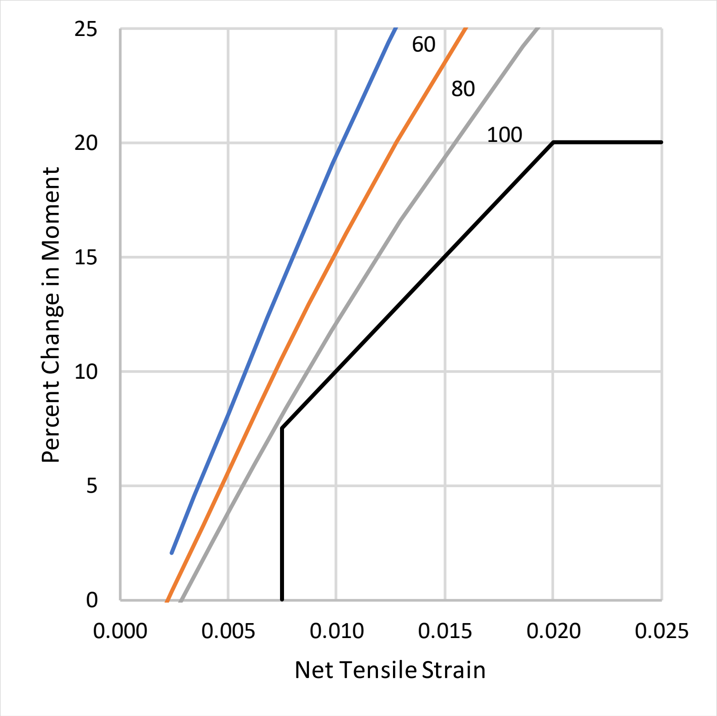

Figure 6.15: Moment redistribution with beam height to span = 1/12

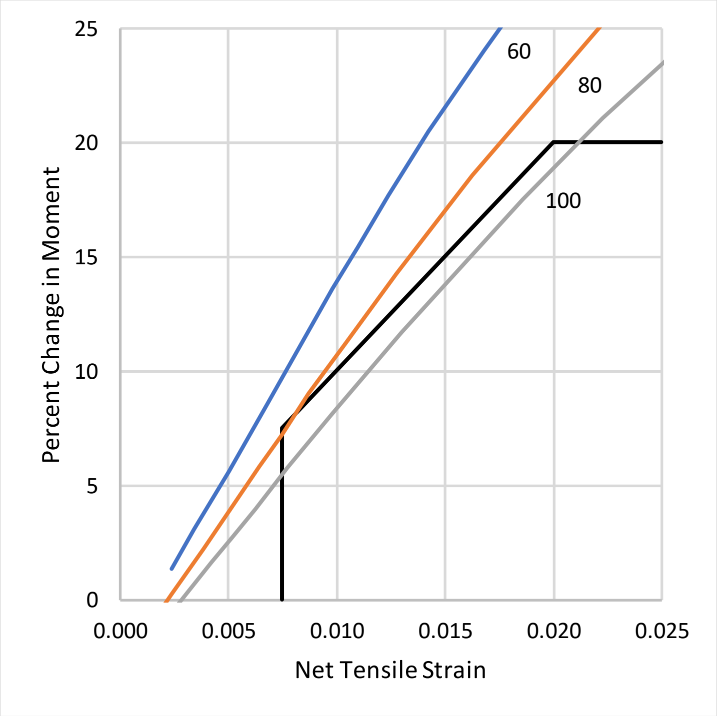

Figure 6.16: Moment redistribution with beam height to span = 1/18

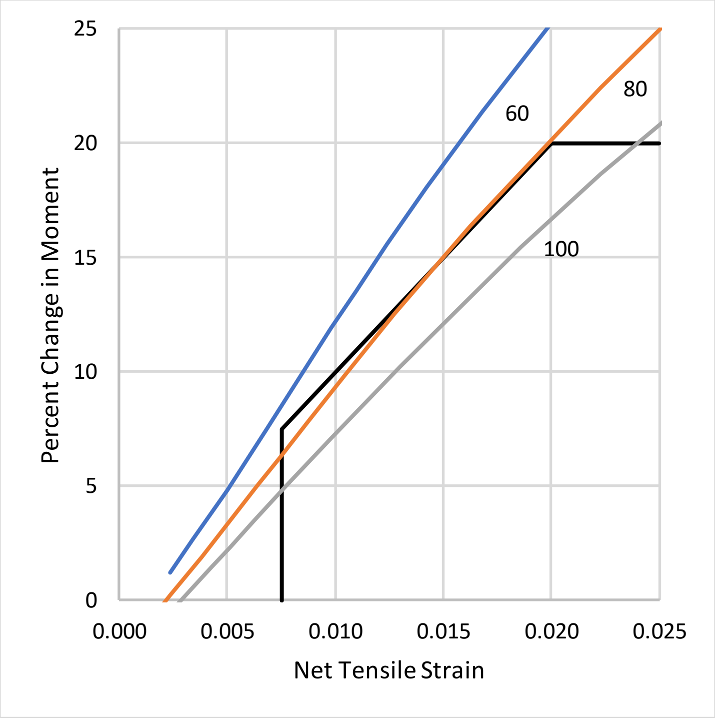

Figure 6.17: Moment redistribution with beam height to span = 1/21

Based on these results, it seems apparent that the moment redistribution limits should be based on the yield stress of the longitudinal reinforcement rather than defining a single set of limits to apply for all grades of reinforcement. The most-conservative allowable moment redistribution relationships for all grades of longitudinal reinforcement are provided by Figure 6.17. However, it is important to consider the assumptions inherent in the calculation. These are the elastic-perfectly plastic steel relationship and a lower-bound plastic-hinge length. Additionally, though permitted by ACI 318-14, an aspect ratio of $1/21$ is uncommon in design. Recognizing these limitations, a new set of equations to govern the redistribution of moments is suggested below.

$$R = [1600 - 300(f_y - 60)](\varepsilon_t - 2\varepsilon_y) \leq 20 \tag{6.28}$$

for which

$$\varepsilon_t \geq 4\varepsilon_y \tag{6.29}$$

which when compared to the theoretical moment redistribution limits for different grades considering an aspect ratio of 1/18, results in the following figures. It is worth noting that the redistribution limits for an aspect ratio of 1/21 fall outside the proposed envelopes, but 1/18 here is shown to illustrate the envelopes' comparison to more-common dimensions.

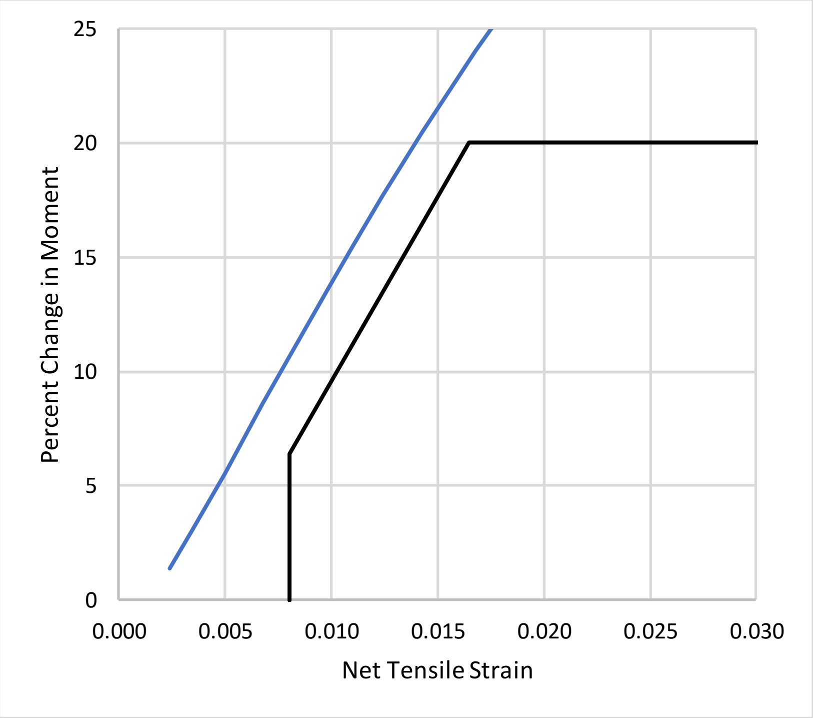

Figure 6.18: Proposed moment redistribution for Grade 60

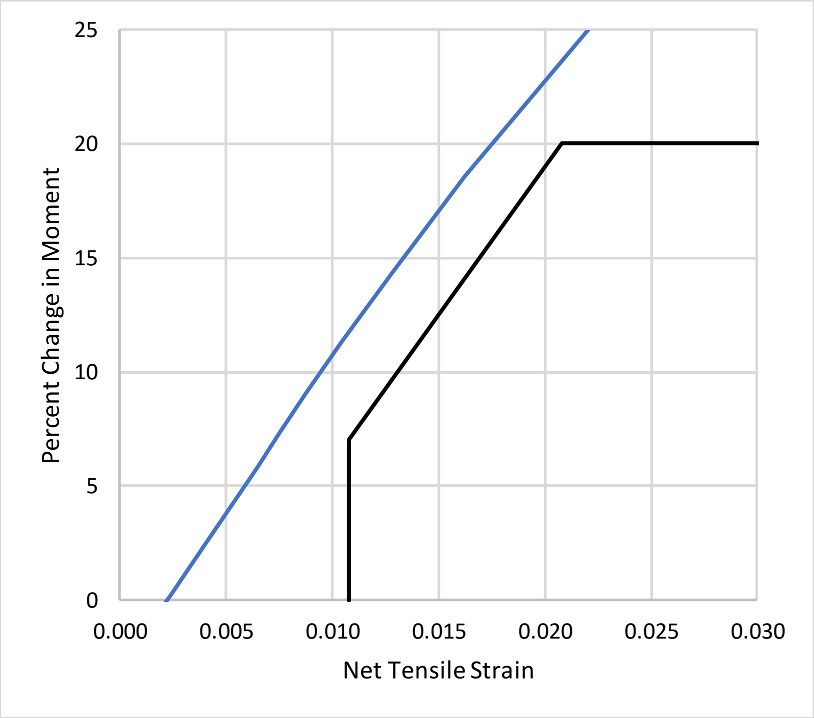

Figure 6.19: Proposed moment redistribution for Grade 80

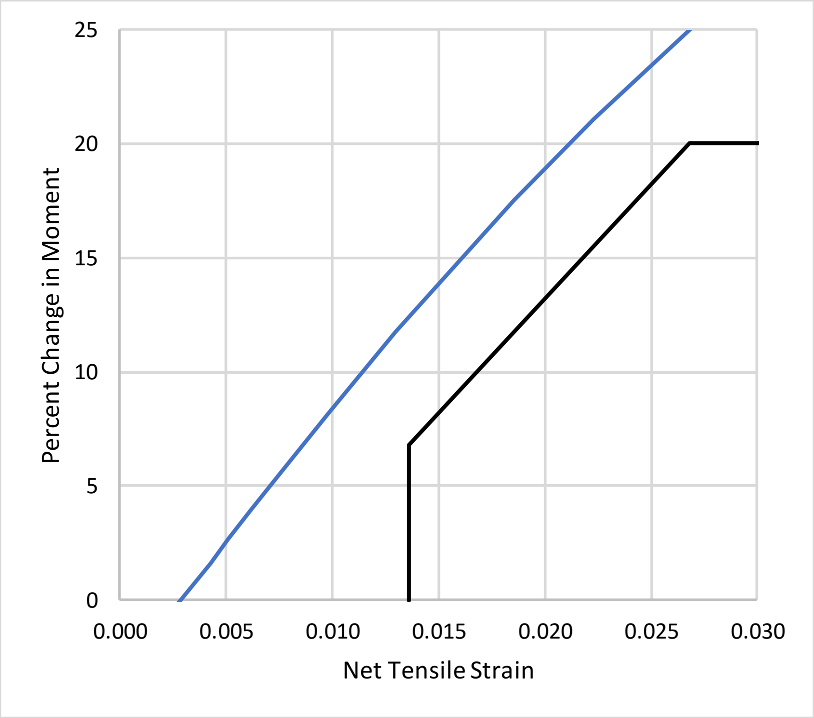

Figure 6.20: Proposed moment redistribution for Grade 100

As strain hardening serves to increase plastic-hinge length and therefore maximum-theoretical redistribution, these envelopes are conservative. Across different grades, the limits proposed here are positioned intentionally farther from the theoretical curves to reflect the likely reduction in plastic-hinge length for higher-strength steels with lower T/Y.

6.3. Numerical Models

To contextualize the results of the previous section, finite-element models considering behaviors more realistic than elastic-perfectly plastic behavior were constructed and analyzed to evaluate moment redistribution. Their cross sections are provided in Figure 6.21 and Figure 6.22. The naming convention is as follows: the first number provides the height of the beam, "FB" describes the end conditions of the model (fixed beam), and the last number gives the longitudinal steel grade. Both sets of beams were identical across grades, except for height, which was varied to produce aspect ratios of $1/18$ and $1/12$ for a fixed span distance. Longitudinal reinforcement was selected so that bending strengths for different grades were approximately equal. Stirrup spacing was selected such that the strength in shear could accommodate load corresponding to hinging at all cross sections of peak moment based on calculated probable moment strengths. Stirrup hoops were modeled as U-shaped with a cap tie, with all bends at 90 degrees, so that concrete would behave relatively unconfined. Two additional modes, 24FB60V and 24FB100V, which do not have their cross sections depicted, had stirrups spaced at 10 in. This spacing corresponded to shear resistance adequate only for formation of a single hinge. For these design calculations, nominal, rather than probable strengths, were used.

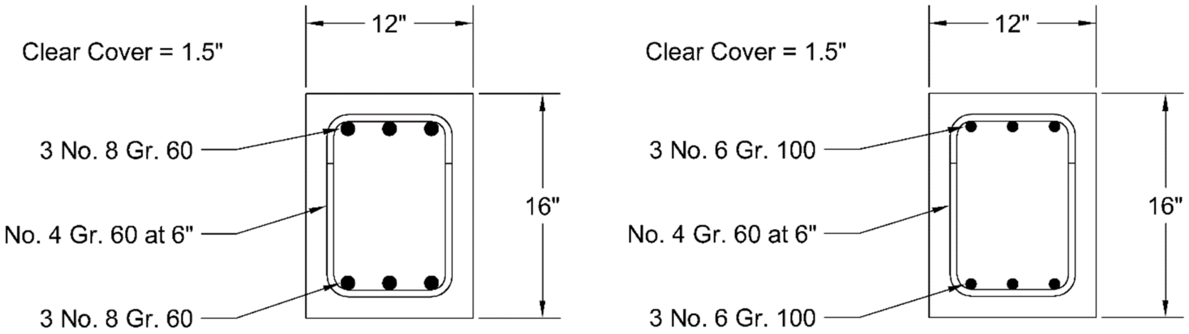

(a) 16FB60 (b) 16FB100

Figure 6.21: Height to span ratio = 1/18 beam cross sections

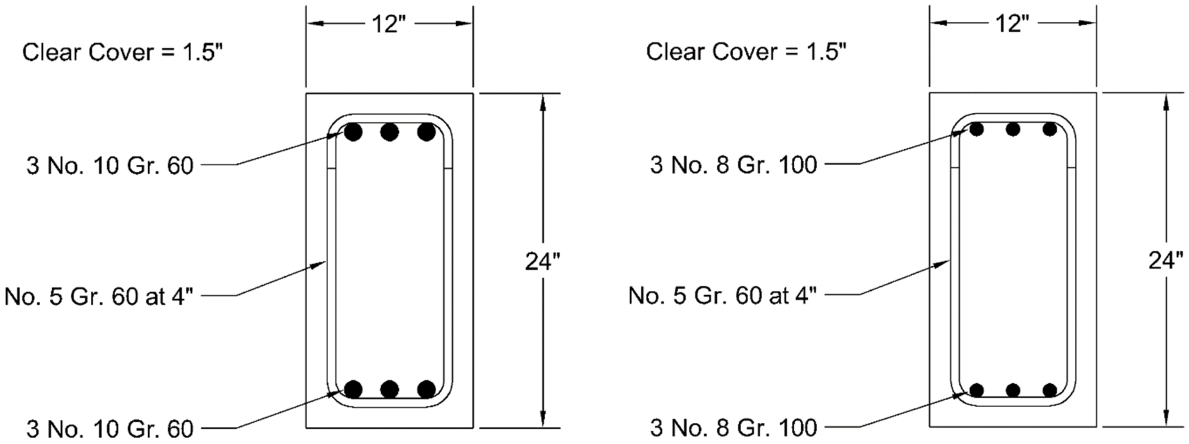

(a) 24FB60 (b) 24FB100

Figure 6.22: Height to span ratio = 1/12 beam cross sections

Support and loading conditions are provided in Figure 6.23. Details of how these conditions were enforced in the model are provided in Appendix C.1.4. Based on this configuration, yielding occurred at the points of highest negative moment (the supports) first.

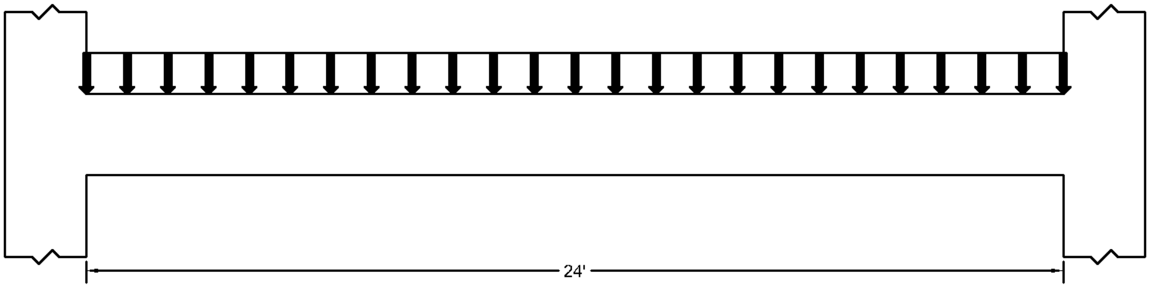

Figure 6.23: Parametric study loading elevation

Stress-strain relationships for the longitudinal reinforcing steel used in the models are shown in Figure 6.24. The letters "PS" designate the steel model that was used in these parametric studies, "H" or "L" denotes whether T/Y was higher or lower for the given grade, which is stated in the last number. A summary of reinforcing steel properties is provided by Table 6.2. Properties were determined using a combination of Bournonville et al. (2004), and stress-strain data recorded during tests of steel coupons as part of the present research. Properties of PS-60 are based on average data, while PS-100 uses lower-bound properties for Grade 100 reinforcement set in ACI 318-19 (unreleased at the time of this writing). These relationships were varied to provide a representative "sample" of possible relationships that steel manufacturers can produce. Higher and lower T/Y for each grade was calculated by multiplying or dividing T/Y for the representative relationship for each grade by 1.1. Uniform elongation strains were determined from test data using judgment. In all finite-element models, the stress-strain relationship for the transverse reinforcing steel was PS-60.

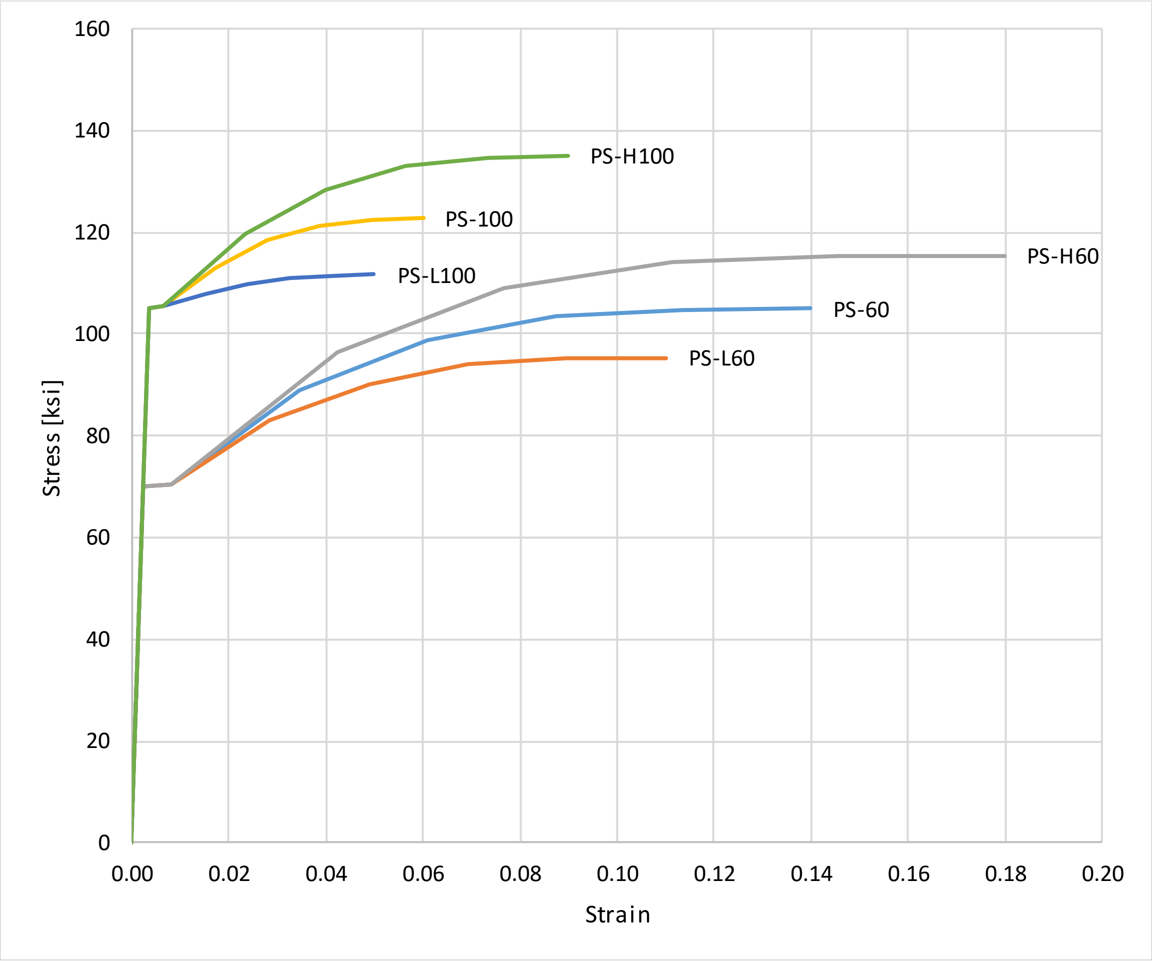

Figure 6.24: Parametric study stress-strain relations for steel

Table 6.2: Parametric study reinforcing steel summary

Reinforcement	f_y [ksi]	f_{su} [ksi]	T/Y	ε_{sh}	ε_{su}
PS-H60	70.0	115.5	1.65	0.0080	0.18
PS-60	70.0	105.0	1.50	0.0080	0.14
PS-L60	70.0	95.5	1.36	0.0080	0.11
PS-H100	105.0	135.1	1.29	0.0065	0.09
PS-100	105.0	122.9	1.17	0.0065	0.06
PS-L100	105.0	111.7	1.06	0.0065	0.05

Details related to the modeling process are outlined in Appendix C.1. Finite-element models were built in GiD (2019) and analyzed using ATENA (2019).

Normalized load-drift ratio relationships obtained from analyses of the models described are provided in the following figures. Load has been normalized by the load corresponding to the development of the beam's nominal moment strength at a section, where nominal moment strength was computed using the ACI 318-14 equivalent-stress-block method. Drift ratio is the deflection at the beam centerline divided by half of the beam span. The normalized load described can be used to provide a direct measure of redistribution at a given drift ratio through $w/w_n - 1$ expressed as a percentage. For a symmetrically-reinforced beam considering the assumptions made here, calculated redistribution is approximately 33%. So, the third hinge is "expected" to occur at a normalized-load value near 1.33. Points where the strain in the longitudinal tension reinforcement at the support reached a multiple of 10% of the uniform elongation strain of the steel used in the model are highlighted with markers.

Consider beam 16FBL60 in Figure 6.25(a). The response of the beam is roughly multilinear, with four distinct segments and three transition zones between them. The first linear segment of the response is before cracking at any section. This occurs prior to a normalized load of about 0.15. The sections of highest moment demand, the supports, crack first, followed by the section of next-highest moment demand, the midspan. As load is increased, cracks form along the beam's length away from the points of maximum moment demand until a distributed system of cracks is present. This progressive cracking is the transition zone between the first two linear segments and lasts until a normalized load of approximately 0.3. The next linear segment of response spans between normalized loads of 0.3 and 1.25. During this period, all longitudinal reinforcement is within the linear range of response, and concrete behavior is in compression is approximately linear, with tensile behavior dominated by crack propagation rather than crack formation. The transition zone that follows marks the onset of yielding in the top longitudinal steel at the supports and the formation of the first two hinges at those locations. This transition in stiffness is much sharper than the gradual change between the first two linear segments due to the sharp change in steel behavior. Response is nearly linear between normalized loads of about 1.25 to 1.35 and during this segment the strain in the top longitudinal reinforcement reaches 10% of the uniform elongation strain, as highlighted with a marker. The next transition zone, at a normalized load of about 1.35, indicates the onset of yielding in the bottom longitudinal reinforcement at midspan and the formation of the final hinge. This transition is also sudden and reflects the behavioral change of the steel in tension here. As load is increased beyond this point, beam behavior follows the fourth approximately-linear segment and strain in the longitudinal tension steel at the supports reaches 20% of the uniform elongation strain. During this segment of response, longitudinal steel behavior at all critical sections shows decreasing stiffness with increasing load and deflection. Also, at these sections, concrete behavior in compression is nonlinear and begins to approach a strain-softening point. Eventually, the model had convergence issues related to this material behavior causing numerical instabilities in the iteration process, and the run was terminated.

The location of the point of model instability and termination varied across beams. To compare beam results, data for different models were cut off at standardized points. Since moment redistribution capacity limits are dependent on the net tensile strain, which is related to plastic rotation and deformation capacity, the decision was made to truncate model output using deformation-based criteria. The results for beam models with a height of 16 in. are truncated at a drift ratio of 2.5% in the case of the beams with Grade 60 reinforcement, and 2.0% in the case of the beams with Grade 100 reinforcement. This represents the maximum drift ratio all models of that type reached. The results of the 24-in. deep beams are truncated at a drift ratio of 3%, or the maximum multiple of 10% of the uniform elongation strain that the tensile longitudinal reinforcement at the support reached. The full numerical response is shown for the beams with inadequate shear reinforcement, as output from the model indicated concrete shear failure, rather than a numerical instability related to strain softening of the materials, was the reason for terminating the model run. Models with different mesh sizes were examined to gauge mesh sensitivity.

In Figure 6.25 through Figure 6.28, labeled curves or dots of a certain color indicate the response of that particular beam. Markers spaced more closely as drift ratio is increased indicate a higher rate of relative strain increase. Markers are closer for steel with lower T/Y. As a function of drift ratio, strain as a fraction of the uniform elongation strain in the tensile steel at the support is provided after these displays of global response.

All models demonstrated moment redistribution capacities in excess of the limit of 20%, including beams that had not been designed to carry the additional shear associated with the increased load. Neglecting the results of the beams that had not been designed for the additional shear, moment redistribution capacities ranged from approximately 40-60%.

As anticipated, beams reinforced with Grade 100 reinforcement were less stiff than those with Grade 60 reinforcement because they had lower reinforcement ratios for the same strength. For a given aspect ratio, ultimate and yield strengths were similar but corresponded to different displacements for different grades. Response after hinge formation showed no strong dependence on T/Y in the case of beams reinforced with Grade 60 steel, a result that was not reflected in the results of the beams with Grade 100 reinforcement, where lower T/Y corresponded to larger drift ratio for a given load. For a given beam, response seemed relatively independent of mesh size.

Beams with reinforcement having higher T/Y showed a lower rate of strain increase (as a percentage of the uniform elongation strain) in the tensile steel at the support. At a load, the tension force provided by the reinforcement is approximately the same for each beam regardless of T/Y. Since Grade 100 steel stress-strain relationships tend to have a smaller strain hardening slopes than those for Grade 60 steel, an increase in load is accompanied by a larger increase in strain. This difference in rate of change is also due to the relationship between yield or ultimate stress and uniform elongation strain. As these stresses are increased, uniform elongation strain tends to decrease, so the same strain increment in steel of two different grades represents a different relative increased towards the uniform elongation strain. Not only is the strain increment larger for steel with a lower T/Y ratio, but for higher steel grades the increment represents a greater percentage of the uniform elongation strain.

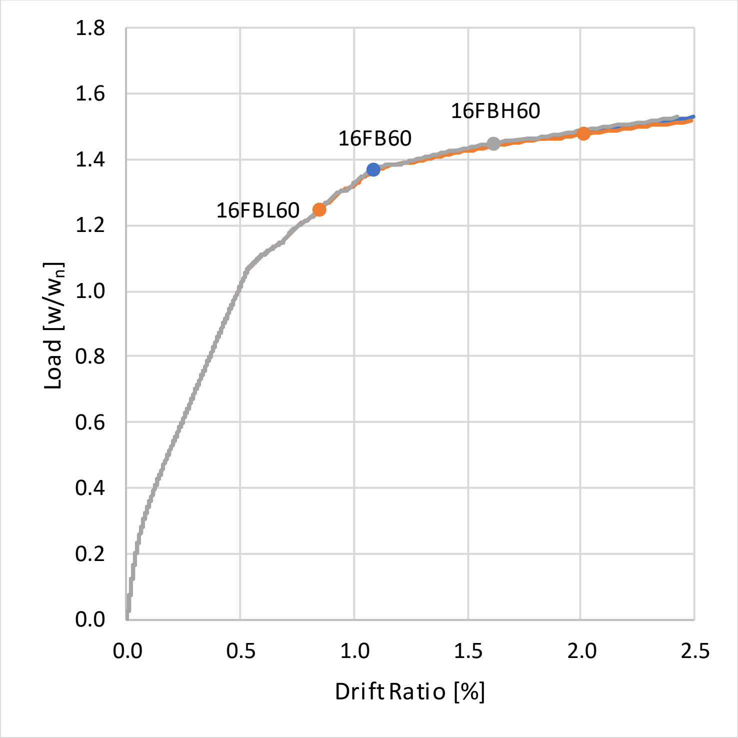

(a) 2-in. mesh

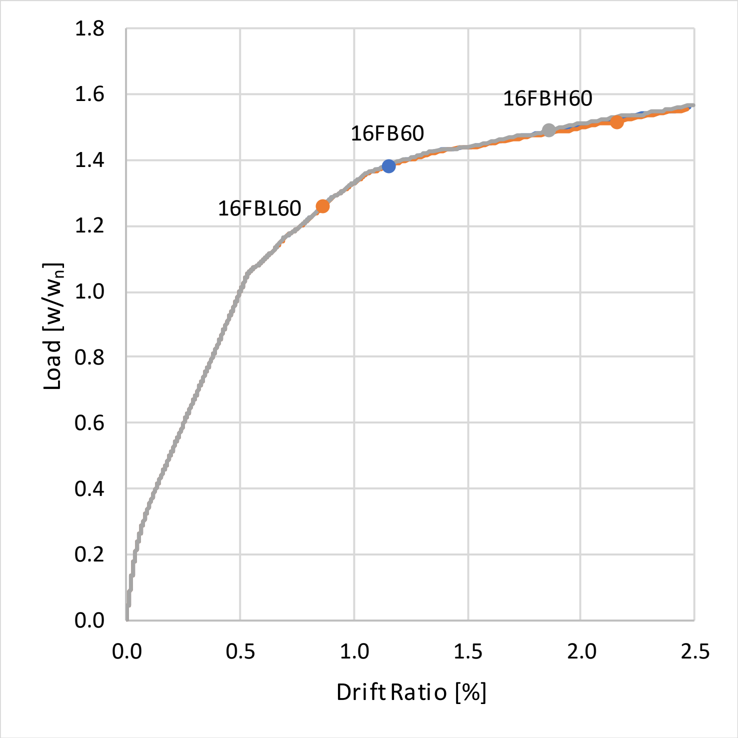

(b) 3-in. mesh

Figure 6.25: 16FB60 normalized load-drift ratio relations

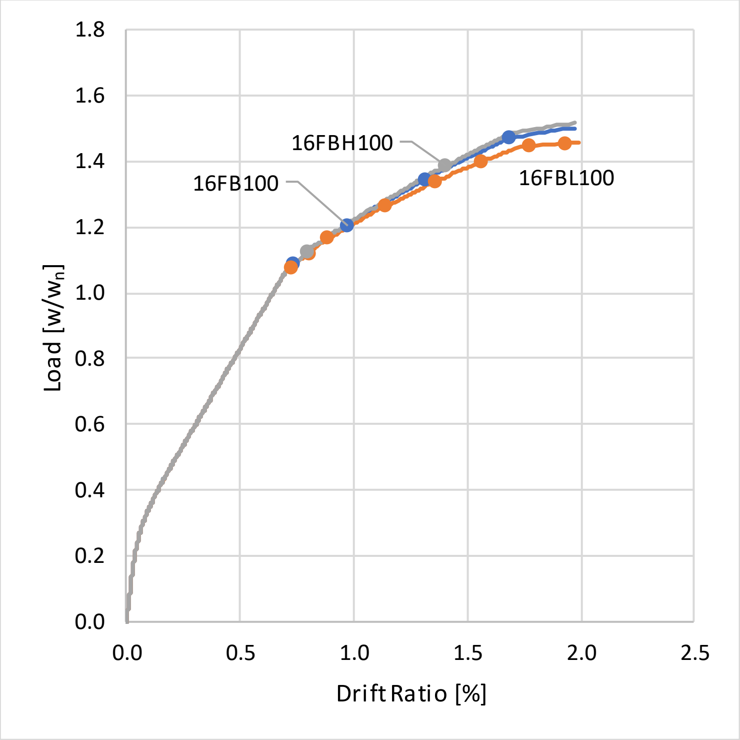

(a) 2-in. mesh

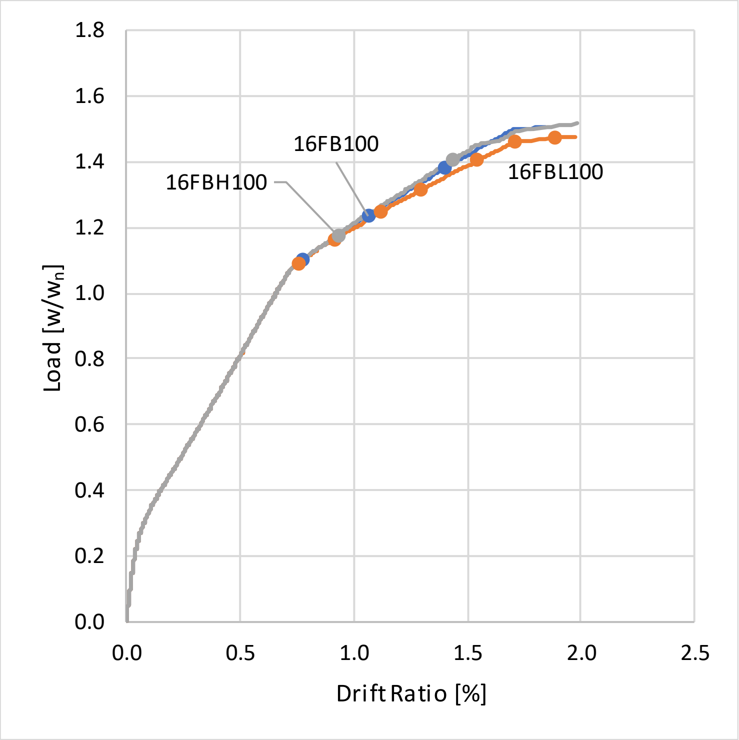

(b) 3-in. mesh

Figure 6.26: 16FB100 normalized load-drift ratio relations

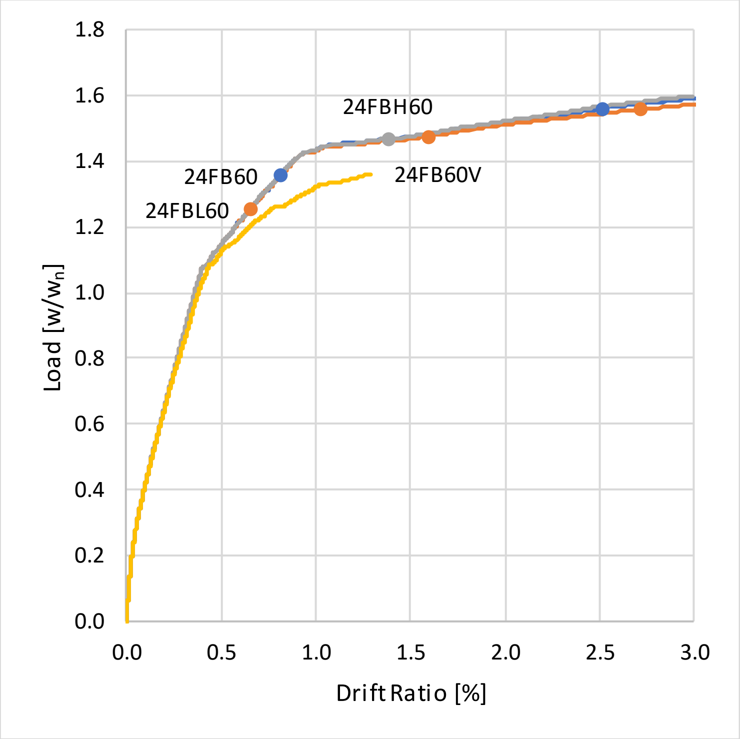

(a) 2-in. mesh

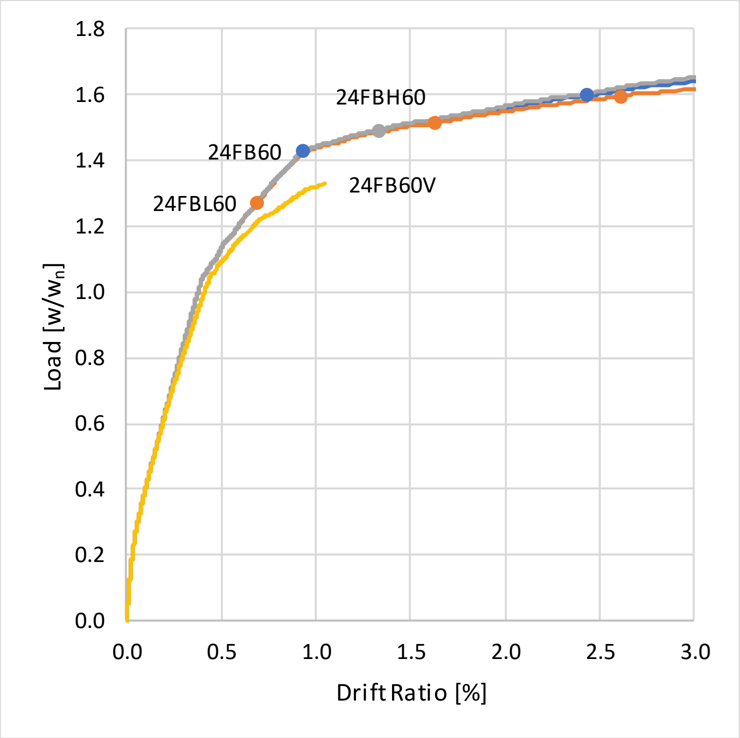

(b) 3-in. mesh

Figure 6.27: 24FB60 normalized load-drift ratio relations

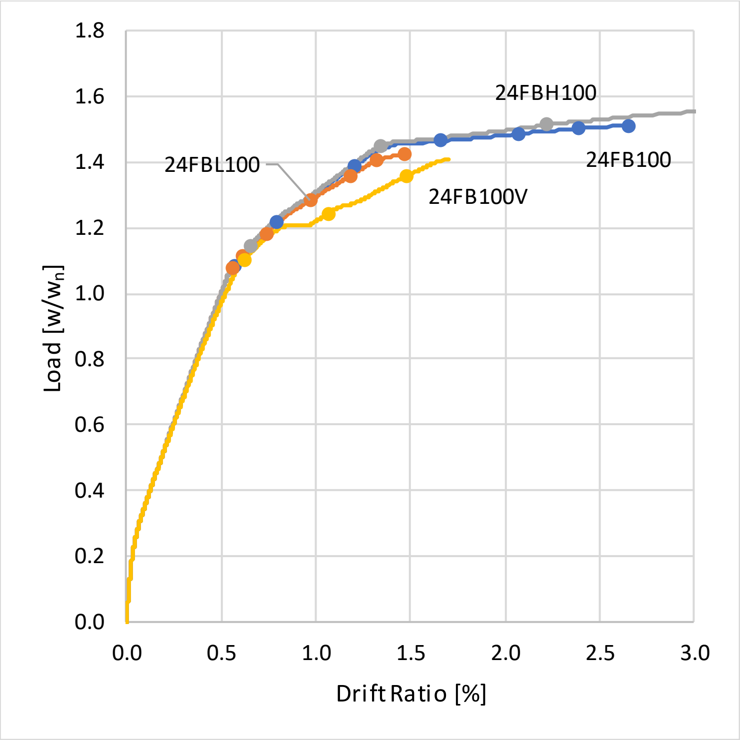

(a) 2-in. mesh

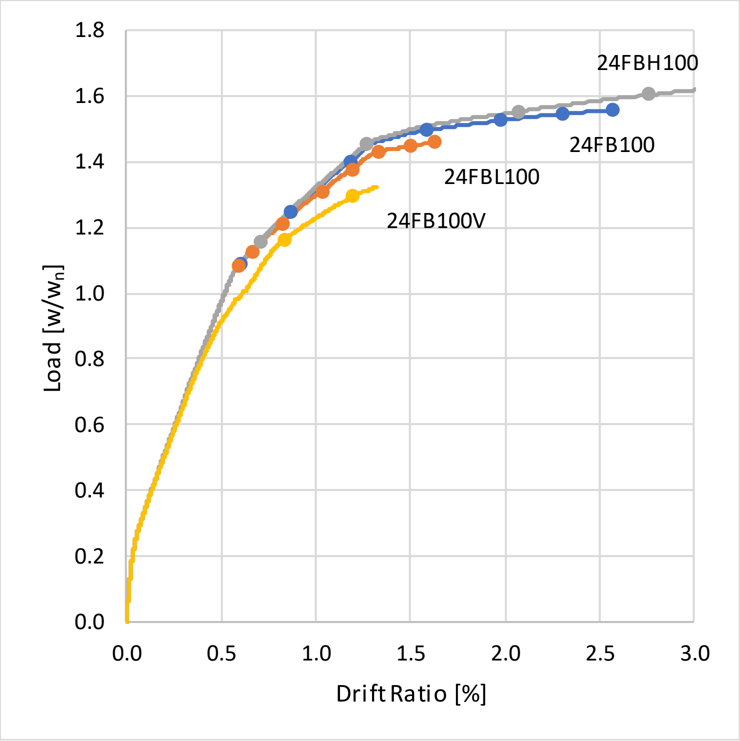

(b) 3-in. mesh

Figure 6.28: 24FB100 normalized load-drift ratio relations

Figure 6.29 through Figure 6.32 show normalized strain-drift ratio relationships for the beams considered. Strains reported are the maximum longitudinal strains in the tensile reinforcement at the supports. They are normalized by uniform elongation strain. As was the case before, drift ratio is the deflection at the beam centerline divided by half of the beam span. Three mostly-linear segments are apparent for each beam in each figure. The two divisions separating these segments mark the formation of hinges in the member, first at the supports and then at the beam centerline. Models of different mesh sizes produced similar results.

For a given deflection, reinforcement with lower T/Y demonstrated relatively larger strain demand as a percentage of the uniform elongation strain. This is due, in part, to the spread of plasticity along the beam's length. Reinforcement with higher T/Y tends to spread plasticity along a greater length, resulting in smaller maximum strains in the longitudinal reinforcement. Additionally, an increase in steel grade is generally accompanied by a decrease in ultimate strain capacity. As a result, for lower T/Y maximum strains tend to be larger, and for higher grades, these maximum strains can represent a larger percentage of the uniform elongation capacity.

Comparing the response of beams 16/24FBL60 and 16/24FBH100, which have the most similar T/Y and uniform elongation strain between the two grades, rates of strain increase were dissimilar due to the compounding effects of the actions listed above.

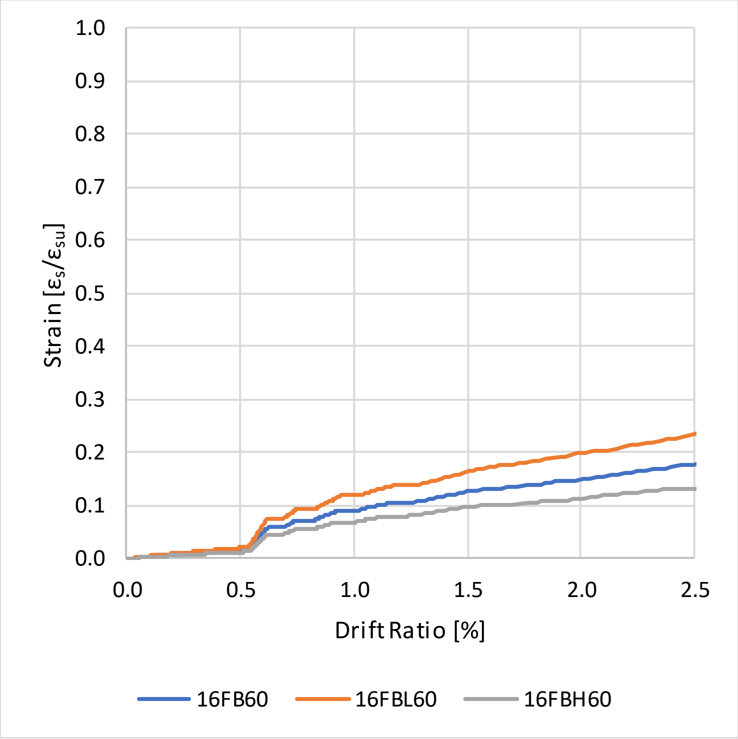

(a) 2-in. mesh

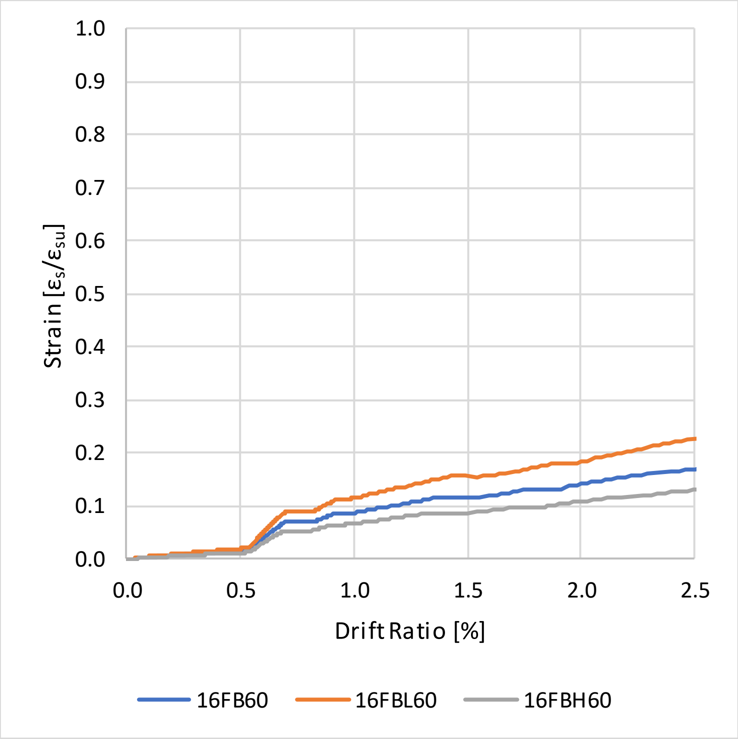

(b) 3-in. mesh

Figure 6.29: 16FB60 normalized strain-drift ratio relations

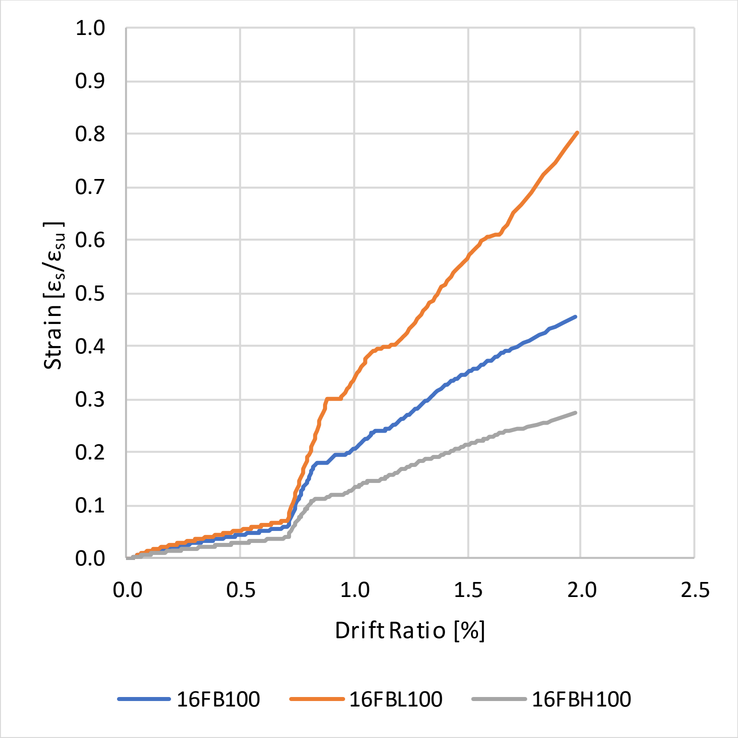

(a) 2-in. mesh

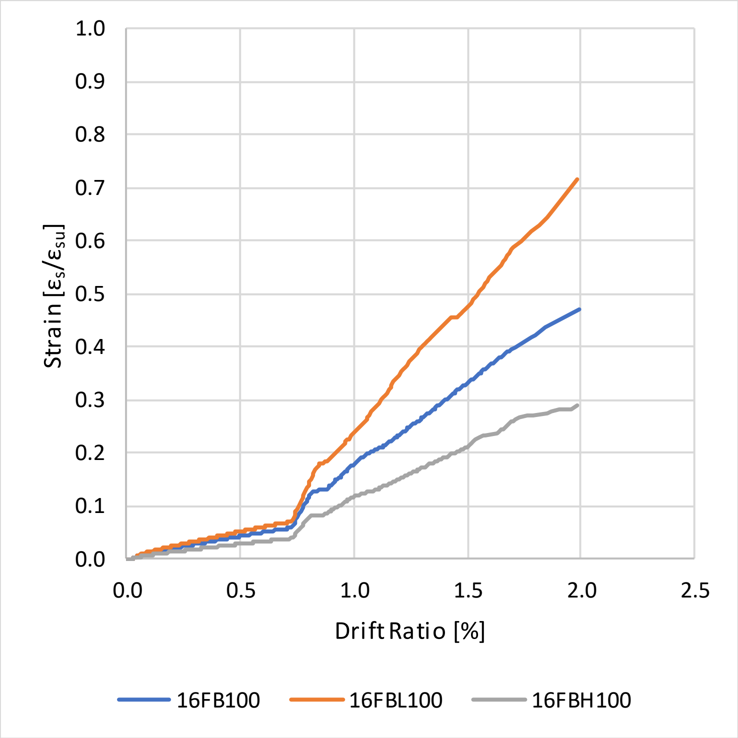

(b) 3-in. mesh

Figure 6.30: 16FB100 normalized strain-drift ratio relations

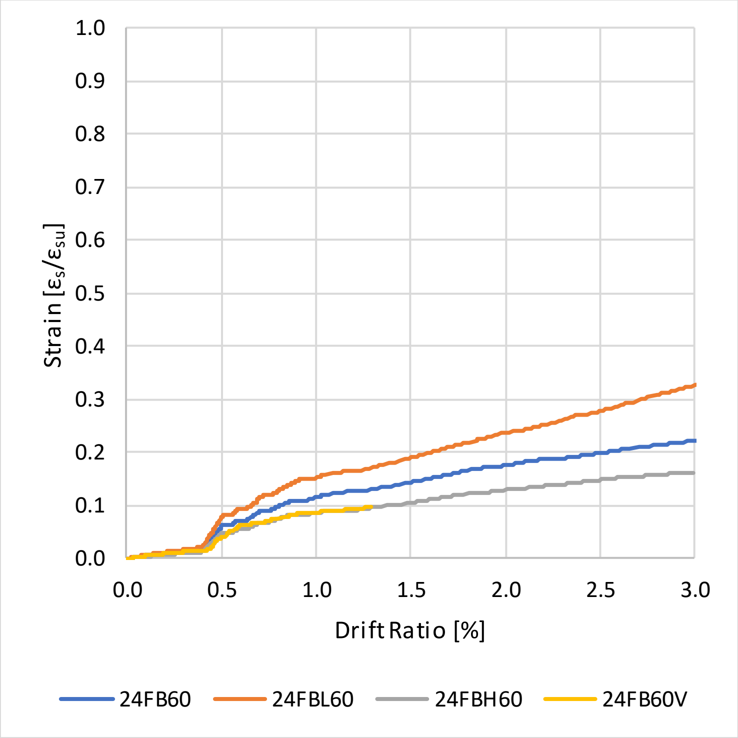

(a) 2-in. mesh

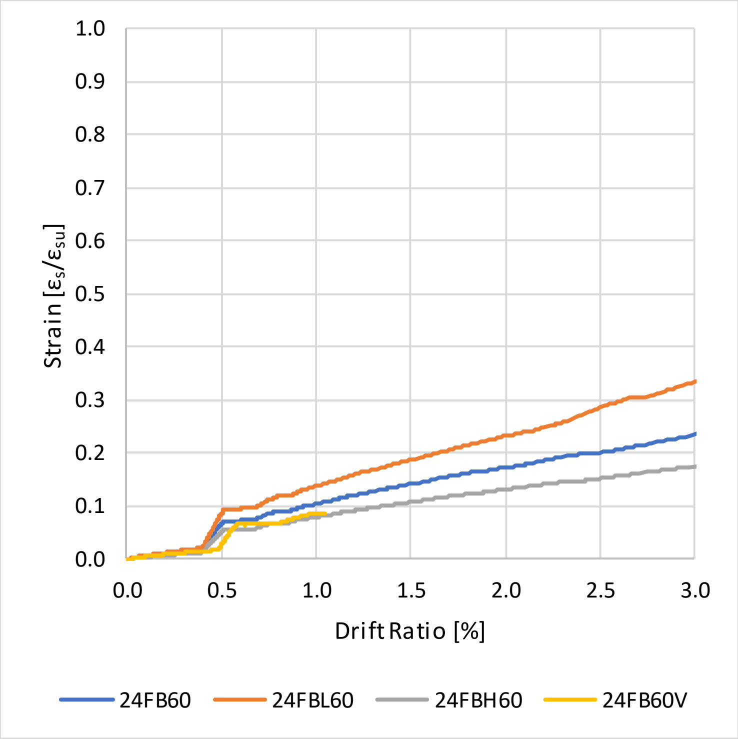

(b) 3-in. mesh

Figure 6.31: 24FB60 normalized strain-drift ratio relations

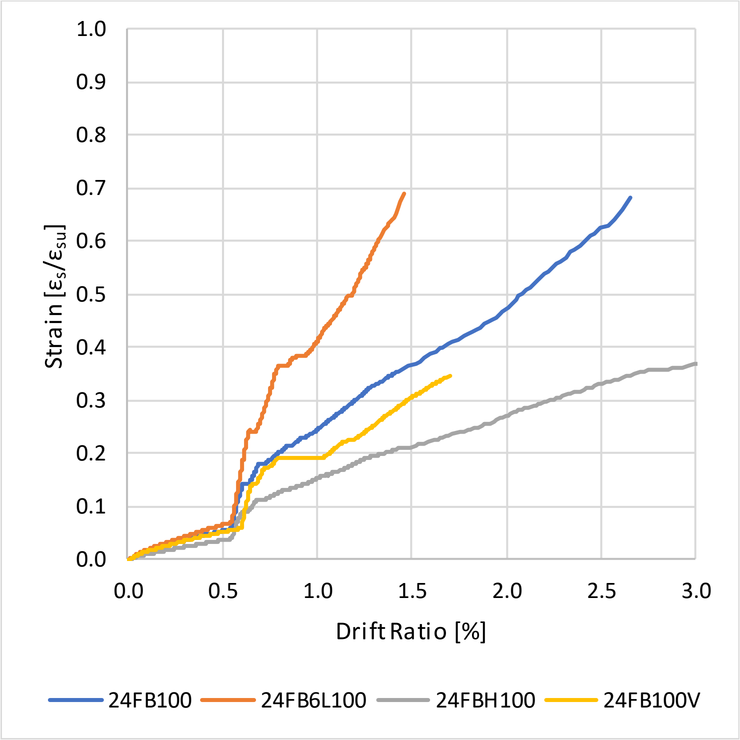

(a) 2-in. mesh

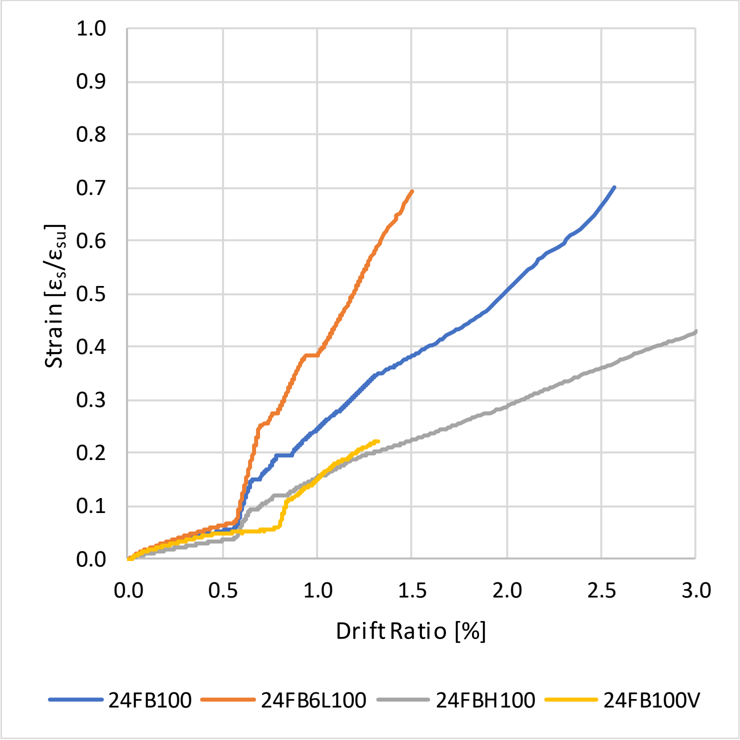

(b) 3-in. mesh

Figure 6.32: 24FB100 normalized strain-drift ratio relations

Table 6.3 through Table 6.10 provide the strains in the longitudinal steel at the points of maximum negative and maximum positive moment for different drift ratios. For the beams with inadequate shear reinforcement for full moment redistribution, the red values indicate the strain ratios at the point of failure and do not correspond to the drift ratio for the row they are in.

Table 6.3: Strain ratios for 16FB60, 2-in. mesh

Drift Ratio	16FBL60		16FB60		16FBH60	
	$(\varepsilon_s/\varepsilon_{su})^-$	$(\varepsilon_s/\varepsilon_{su})^+$	$(\varepsilon_s/\varepsilon_{su})^-$	$(\varepsilon_s/\varepsilon_{su})^+$	$(\varepsilon_s/\varepsilon_{su})^-$	$(\varepsilon_s/\varepsilon_{su})^+$
1.0%	12%	2%	9%	1%	7%	1%
1.5%	16%	4%	12%	3%	9%	2%
2.0%	19%	6%	15%	4%	11%	3%
2.5%	23%	7%	17%	5%	13%	4%

Table 6.4: Strain ratios for 16FB60, 3-in. mesh

Drift Ratio	16FBL60		16FB60		16FBH60	
	$(\varepsilon_s/\varepsilon_{su})^-$	$(\varepsilon_s/\varepsilon_{su})^+$	$(\varepsilon_s/\varepsilon_{su})^-$	$(\varepsilon_s/\varepsilon_{su})^+$	$(\varepsilon_s/\varepsilon_{su})^-$	$(\varepsilon_s/\varepsilon_{su})^+$
1.0%	11%	2%	9%	1%	7%	1%
1.5%	16%	4%	12%	3%	9%	2%
2.0%	18%	5%	14%	4%	11%	3%
2.5%	22%	7%	16%	5%	13%	4%

Table 6.5: Strain ratios for 16FB100, 2-in. mesh

Drift Ratio	16FBL100		16FB100		16FBH100	
	$(\varepsilon_s/\varepsilon_{su})^-$	$(\varepsilon_s/\varepsilon_{su})^+$	$(\varepsilon_s/\varepsilon_{su})^-$	$(\varepsilon_s/\varepsilon_{su})^+$	$(\varepsilon_s/\varepsilon_{su})^-$	$(\varepsilon_s/\varepsilon_{su})^+$
1.0%	31%	5%	20%	4%	13%	3%
1.5%	54%	6%	34%	5%	21%	4%
2.0%	77%	13%	44%	10%	27%	7%

Table 6.6: Strain ratios for 16FB100, 3-in. mesh

Drift Ratio	16FBL100		16FB100		16FBH100	
	$(\varepsilon_s/\varepsilon_{su})^-$	$(\varepsilon_s/\varepsilon_{su})^+$	$(\varepsilon_s/\varepsilon_{su})^-$	$(\varepsilon_s/\varepsilon_{su})^+$	$(\varepsilon_s/\varepsilon_{su})^-$	$(\varepsilon_s/\varepsilon_{su})^+$
1.0%	22%	5%	17%	4%	11%	3%
1.5%	46%	6%	32%	5%	20%	4%
2.0%	66%	13%	47%	10%	29%	6%

Table 6.7: Strain ratios for 24FB60, 2-in. mesh

Drift Ratio	24FBL60		24FB60		24FBH60		24FB60V	
	$(\varepsilon_s/\varepsilon_{su})^-$	$(\varepsilon_s/\varepsilon_{su})^+$	$(\varepsilon_s/\varepsilon_{su})^-$	$(\varepsilon_s/\varepsilon_{su})^+$	$(\varepsilon_s/\varepsilon_{su})^-$	$(\varepsilon_s/\varepsilon_{su})^+$	$(\varepsilon_s/\varepsilon_{su})^-$	$(\varepsilon_s/\varepsilon_{su})^+$
1.0%	15%	3%	11%	3%	9%	2%	8%	1%
1.5%	18%	8%	14%	6%	10%	5%	-	-
2.0%	23%	11%	17%	8%	13%	6%	-	-
2.5%	27%	13%	20%	10%	15%	8%	-	-
3.0%	32%	16%	22%	12%	16%	9%	-	-

Table 6.8: Strain ratios for 24FB60, 3-in. mesh

Drift Ratio	24FBL60		24FB60		24FBH60		24FB60V	
	$(\varepsilon_s/\varepsilon_{su})^-$	$(\varepsilon_s/\varepsilon_{su})^+$	$(\varepsilon_s/\varepsilon_{su})^-$	$(\varepsilon_s/\varepsilon_{su})^+$	$(\varepsilon_s/\varepsilon_{su})^-$	$(\varepsilon_s/\varepsilon_{su})^+$	$(\varepsilon_s/\varepsilon_{su})^-$	$(\varepsilon_s/\varepsilon_{su})^+$
1.0%	14%	3%	10%	2%	8%	2%	9%	1%
1.5%	18%	9%	14%	7%	11%	5%	-	-
2.0%	23%	10%	17%	8%	13%	6%	-	-
2.5%	28%	13%	20%	10%	15%	7%	-	-
3.0%	32%	15%	23%	11%	17%	9%	-	-

Table 6.9: Strain ratios for 24FB100, 2-in. mesh

Drift Ratio	24FBL100		24FB100		24FBH100		24FB100V	
	$(\varepsilon_s/\varepsilon_{su})^-$	$(\varepsilon_s/\varepsilon_{su})^+$	$(\varepsilon_s/\varepsilon_{su})^-$	$(\varepsilon_s/\varepsilon_{su})^+$	$(\varepsilon_s/\varepsilon_{su})^-$	$(\varepsilon_s/\varepsilon_{su})^+$	$(\varepsilon_s/\varepsilon_{su})^-$	$(\varepsilon_s/\varepsilon_{su})^+$
1.0%	40%	6%	24%	5%	15%	3%	19%	4%
1.5%	67%	15%	35%	10%	21%	7%	29%	6%
2.0%	-	-	46%	16%	26%	11%	35%	8%
2.5%	-	-	60%	22%	32%	14%	-	-
3.0%	-	-	-	-	36%	17%	-	-

Table 6.10: Strain ratios for 24FB100, 3-in. mesh

Drift Ratio	24FBL100		24FB100		24FBH100		24FB100V	
	$(\varepsilon_s/\varepsilon_{su})^-$	$(\varepsilon_s/\varepsilon_{su})^+$	$(\varepsilon_s/\varepsilon_{su})^-$	$(\varepsilon_s/\varepsilon_{su})^+$	$(\varepsilon_s/\varepsilon_{su})^-$	$(\varepsilon_s/\varepsilon_{su})^+$	$(\varepsilon_s/\varepsilon_{su})^-$	$(\varepsilon_s/\varepsilon_{su})^+$
1.0%	38%	6%	24%	5%	15%	3%	14%	4%
1.5%	66%	15%	38%	12%	22%	8%	22%	5%
2.0%	-	-	48%	18%	28%	11%	-	-
2.5%	-	-	63%	22%	35%	14%	-	-
3.0%	-	-	-	-	42%	17%	-	-

For a given cross section, beams of different steel grades with most-similar mechanical properties, 16/24FBL60 and 16/24FBH100, showed different strain ratios at a given drift. This is due to the compounding effects differences of spread of plasticity and strain capacity when steels of different grades and T/Y ratios are considered. Comparisons of beams considering "lower-bound" properties of Grade 60 reinforcement with "upper-bound" properties of Grade 100 reinforcement indicate large differences in performance. When "average" properties are considered, this performance disparity is even greater.

With steels having smaller T/Y and uniform elongation strain, the ratio of strain to uniform elongation strain increases at a faster rate as displacement is increased, meaning beams with these materials would have lower redistribution capacity. As such, it is important to place lower bounds on these values to limit the reinforcement strain to an acceptable percentage of the failure strain. Based on the results here, the decision to limit T/Y to 1.17 and ε_{su} to 0.06 for Grade 100 reinforcement in ACI 318-19 (unreleased at the time of this writing) seems conservative given that it limits the steel strain to 40-50% of the maximum at a drift ratio of 2.0% across a range of typical geometries and reinforcement ratios. Extending limits on mechanical properties lower than these limits seems unadvisable given the performance of beams 16GBL100 and 24GBL100. At a drift ratio of 2.0%, these beams indicated steel strains could be nearly 65% of the strain capacity, with some models reaching that percentage at drift ratios as low as 1.5%.

7. Summary and Conclusions

7.1. Summary

A research program was devised to explore the monotonic load-deformation behavior of flexurally dominated beams reinforced with Grade 60 and Grade 100 reinforcement. The research included both laboratory tests and analytical studies. The experimental program was organized in two series of four beams each. The analytical study consisted of investigating the behavior of those beams tested, as well as several archetype beams.

Series 1 beams were lightly reinforced such that failure occurred at relatively large displacement ductility and longitudinal tensile reinforcement strains, thereby exposing the effects of different reinforcement grades and different strain-hardening properties on inelastic flexural deformation capacity. Two beams used Grade 60 reinforcement and two beams used Grade 100 reinforcement. For each grade, the reinforcement had either a relatively high T/Y or relatively low T/Y (where T is the reinforcement ultimate stress capacity and Y is the reinforcement yield stress capacity, both in tension). The beams were tested as simply supported beams with a monotonically increasing load at midspan. Measurements included applied load and resulting global and local displacements, reinforcement strains, crack patterns and widths, and failure modes.

Series 2 beams were heavily reinforced, near the limits set by ACI 318-14. Beams were designed to fail at relatively small displacement ductility and longitudinal reinforcement steel strains to investigate the effect of different reinforcement ratios on inelastic flexural deformation capacity. Two beams used Grade 60 reinforcement and two beams used Grade 100 reinforcement. For each grade, beams were designed to fail at either a relatively high or relatively low net tensile strain. The beams were tested in four-point bending with a monotonically increasing load centered at midspan. This was done to create a span of constant moment over which the concrete on the compression face of the beam would be free, as concrete failure in compression was the expected to limit beam behavior. Measurements included applied loads and resulting global and local displacements, reinforcement strains, crack patters and widths, and failure modes.

The parametric analytical study explored the behavior of archetype beams to identify those variables with the largest impact on moment redistribution. Beam cross sections, aspect ratios, and material properties were selected to provide a representative span of those commonly found in design. With the variables with the largest effect on moment redistribution identified, nonlinear finite-element models were constructed and analyzed to determine the relative impact of those variables. Beams had both ends fixed with a monotonically increasing distributed load over the beam span. Monitored behavior included applied load and resulting global displacements and reinforcement strains.

7.2. Conclusions

7.2.1. Experimental Investigation

- Behavior of beams was dominated by flexural action, although inclined cracks were observed in shear spans. These behaviors are consistent with expectations given the relatively slender beam aspect ratios and proportions selected for moment and shear strength.
- Beam moment strengths were close to strengths calculated using conventional moment-strength calculations. For a given series, ultimate load-carrying capacity for beams was nearly the same, as was intended in design.
- Beams reinforced with Grade 100 reinforcement had lower apparent stiffness compared with beams with Grade 60 reinforcement due to their lower reinforcement ratio. When designed for the same nominal strength, beams with higher-strength reinforcing steel will exhibit larger deflections under the same loading.
- Methods outlined in ACI 318-14 for calculating effective cross-sectional stiffnesses used in conjunction with elastic beam theory, as well as approaches employing mechanics and beam geometry, provide a reasonable estimate for beam deflections, even as the steel grade is increased.
- Maximum measured crack widths varied approximately linearly with longitudinal reinforcing stress. In most cases, calculated maximum crack widths exceeded those measured during testing but values were the same order of magnitude.

Series 1

- All beams had relatively large displacement ductility capacity.

- As T/Y was increased, so did the capacity to sustain additional load beyond yield.
- For a given drift ratio, inelastic strains tended to spread along a greater length and to be of a lesser amplitude for greater values of T/Y, regardless of steel grade.
- Plastic-hinge length for each beam remained relatively constant with increasing drift ratio. Plastic-hinge length increased with increasing T/Y ratio, although the rate of increase was not the same for Grade 60 and Grade 100.
- Beams with higher T/Y achieved greater plastic rotations. A reduction in T/Y caused a reduction in the spread of plasticity and, consequently, a reduction in displacement capacity.

Series 2

- All beams failed at displacements less than twice the measured yield displacement.
- In all cases, maximum tensile strains achieved during the tests exceeded the design net tensile strains. The strain data did not show obvious trends in spread of plasticity.
- Drift ratio at failure increased with increasing design net tensile strain for each grade.
- Though they had similar net tensile strains, beam 2GBL100 achieved a higher drift ratio than 1GBH60. Both Grade 60 beams failed at similar drift ratios despite having different net tensile strains.
- For a given value of net tensile strain, and for a given value of the difference between net tensile strain and yield strain, the beams with Grade 100 reinforcement had equal or greater deformation capacity than the beams with Grade 60 reinforcement.
- Plastic rotation capacity increased nearly linearly with net tensile strain, rather than with the difference between net tensile strain and yield strain. This is due to the complex interaction between T/Y, plastic strain, and plastic-hinge length which prevents plastic rotation from being related to a single variable.

7.2.2. Analytical Investigation

- All beam models demonstrated moment redistribution capacities greater than the limit of 20%, even for beams not detailed for full moment redistribution, though these beams did exhibit undesirable shear-failure mechanisms and should be avoided in practice.

When adequate detailing was provided, redistribution capacities ranged from approximately 40 to 60%.

- Beams with reinforcement having higher T/Y showed a lower rate of strain increase (as a percentage of the uniform elongation strain) in the tensile steel at the support for increases in either load or deflection. This is due to a combination of the slope of the strain-hardening portion of the stress-strain response of steel, spread of plasticity, and the uniform elongation strain.
- Performance comparisons of beams with reinforcement having "lower-bound" Grade 60 properties against beams with "upper-bound" Grade 100 properties illustrated large performance differences, which only stand to grow when considering "average" properties.
- ACI 318-14 moment redistribution limits are less conservative for Grade 100 reinforcement than for Grade 60 reinforcement, suggesting that revisions be made to design provisions to result in more uniform reliability. Based on results presented here, a new equation defining percent change in moment as a function of net tensile strain is given as

$$R = \left[1600 - 300\left(f_y - 60\right)\right]\left(\varepsilon_t - 2\varepsilon_y\right) \leq 20 \tag{6.28}$$

for which

$$\varepsilon_t \geq 4\varepsilon_y \tag{6.29}$$

References

ACI 318 (1941). “Building Regulations for Reinforced Concrete,” *American Concrete Institute*, 66 pp.

ACI 318 (1963). “Building Code Requirements for Reinforced Concrete,” *American Concrete Institute*, 148 pp.

ACI 318 (1971). “Building Code Requirements for Reinforced Concrete,” *American Concrete Institute*, 78 pp.

ACI 318 (1995). “Building Code Requirements for Structural Concrete and Commentary,” *American Concrete Institute*, 370 pp.

ACI 318 (2002). “Building Code Requirements for Structural Concrete and Commentary,” *American Concrete Institute*, 443 pp.

ACI 318 (2008). “Building Code Requirements for Structural Concrete and Commentary,” *American Concrete Institute* 471 pp.

ACI 318 (2014). “Building Code Requirements for Structural Concrete and Commentary,” *American Concrete Institute*, 524 pp.

ACI 352 (1976), “Recommendations for Design of Beam-Column Joints in Monolithic Reinforced Concrete Structures,” *Journal of the American Concrete Institute*, Vol. 73, No. 7, pp. 375-393.

Aoyama, H. (2001), “Design of Modern Highrise Reinforced Concrete Structures,” *Imperial College Press*, 460 pp.

ASCE/SEI 7 (2010), “Minimum Design Loads for Buildings and Other Structures,” *American Society of Civil Engineers/Structural Engineering Institute*, 650 pp.

ASTM A370 (2014), “Standard Test Methods and Definitions for Mechanical Testing of Steel Products,” *ASTM International*, 50 pp.

ASTM C39 (2012), “Standard Test Method for Compressive Strength of Cylindrical Concrete Specimens,” *ASTM International*, 8 pp.

ASTM C469 (2010), “Standard Test Method for Static Modulus of Elasticity and Poisson’s Ratio of Concrete in Compression,” *ASTM International*, 5 pp.

ASTM E8 (2016), “Standard Test Methods for Tension Testing of Metallic Materials,” *ASTM International*, 30 pp.

ATC 115 (2014), “Roadmap for the Use of High-Strength Reinforcement in Reinforced Concrete Design,” *Applied Technology Council*, 197 pp.

ATENA: Advanced Tool for Engineering Nonlinear Analysis (2019), “ATENA 5.6.1,” *Červenka Consulting*, www.cervenka.cz.

Baker, A.L.L. (1963), “Ultimate Load Design of Reinforced Concrete Frames: A Recapitulation and Appraisal,” *IABSE Publications*, Vol. 23, pp. 33-51.

Baker, A.L.L. and A.M.N, Amarkone (1965), “Inelastic Hyperstatic Frames Analysis,” *ACI Special Publication*, Vol. 12, pp. 85-142.

Bondy, K.B. (2003), “Moment Redistribution: Principles and Practice Using ACI 318-02,” *PTI Journal*, Vol.18, No. 16, pp. 3-21.

Bischoff, P.H. (2005), “Reevaluation of Deflection Prediction for Concrete Beams reinforced with Steel and Fiber Reinforced Polymer Bars,” *Journal of Structural Engineering*, Vol 131, No. 5, pp. 752-762.

Bournonville, M., J. Dahnke, and D. Darwin. (2004), “Statistical Analysis of the Mechanical Properties and Weights of Reinforcing Bars,” *The University of Kansas Structural Engineering and Materials Laboratory*, No. 1, 198 pp.

Branson, D.E. (1965), “Instantaneous and Time-Dependent Deflections of Simple and Continuous Reinforced Concrete Beams,” *HPR Report*, No. 7, pp 1-78.

CEB-FIP Model Code (1990), “Design Code,” *Comité Euro-International du Béton-Fédération Internationale de la Précontrainte (Euro-International Committee for Concrete-International Federation for Prestressing)*, 460 pp.

Červenka, V. (1985), “Constitutive Model for Cracked Reinforced Concrete,” *ACI Journal Proceedings*, Vol. 82, No. 6, pp 877-882.

Červenka, J., S.C. Keating, and C.A. Felippa (1993), “Comparison of Strain Recovery Techniques for the Mixed Iterative Method,” *Communications in Numerical Methods in Engineering*, Vol. 9, pp. 925-932.

Červenka, V., L. Jendale, and J. Červenka (2018), “ATENA Program Documentation, Part 1: Theory,” *Červenka Consulting*, 334 pp.

Chen, W.F. and A.F. Saleeb (1994), “Constitutive Equations for Engineering Materials,” *Elsevier Science Limited*, 594 pp.

Cheng, M.Y. and M.B. Giduquio (2014), “Cyclic Behavior of Reinforced Concrete Flexural Members Using High-Strength Flexural Reinforcement,” *ACI Structural Journal, Vol.* 111, No. 4, pp. 893-902.

Cohn, M.Z. (1965), "Rotation Compatibility in the Limit Design of Reinforced Concrete Continuous Beams," *ACI Special Publication*, Vol. 12, pp. 359-382.

Cohn, M.Z. (1986), "Partial Prestressing, From Theory to Practice, Part 1: Survey Reports," *Springer Science and Business Media*, 863 pp.

Darwin, D. and D.A.W. Pecknold (1974), "Inelastic Model for Cyclic Biaxial Loading of Reinforced Concrete," *University of Illinois at Urbana-Champaign*, 176 pp.

Eligehausen, R. and P. Langer (1987), "Rotation Capacity of Plastic Hinges and Allowable Degree of Moment Redistribution," *University of Stuttgart*, 35 pp.

Elwood, K.J. and M.O. Eberhard (2009), "Effective Stiffness of Reinforced Concrete Columns," *ACI Structural Journal*, Vol. 106, No. 4, pp. 476-484.

FEMA 273 (1997), "NEHRP Guidelines for the Seismic Rehabilitation of Buildings," *Federal Emergency Management Agency*, 444 pp.

Frosch, R.J. (1999), "Another Look at Cracking and Crack Control in Reinforced Concrete," *ACI Structural Journal*, Vol. 96, No. 3, pp. 437-442.

Gergely, P. and L.A. Lutz (1968), "Maximum Crack Width in Reinforced Concrete Flexural Members," *ACI Special Publication*, Vol. 10, No. 12, pp. 87-117.

GiD (2019), "GiD 14.0.2," *International Center for Numerical Methods in Engineering*, www.gidhome.com.

Hognestad, E. (1951), "A Study of Combined Bending and Axial Load in Reinforced Concrete Members," *University of Illinois Engineering Experiment Station*, No. 399, 128 pp.

Hognestad, E. (1962), "High Strength Bars as Concrete Reinforcement, Part 2: Control of Flexural Cracking," *University of Illinois Engineering Experiment Station*, Vol. 4, No. 1, pp. 45-63.

Hordijk, D.A. (1991), "Local Approach to Fatigue of Concrete," *Ph.D. Dissertation, Delft University of Technology*, 216 pp.

Kent, D.C. and R. Park (1971), "Flexural Members with Combined Concrete," *Journal of the Structural Division,* Vol. 97, No. 7, pp. 1969-1990.

Kimura, H., S. Sugano, T. Nagashima, and A. Ichikawa (1993), "Seismic Loading Tests of Reinforced Concrete Beams using High Strength Concrete and High Strength Steel Bars," *Proceedings of the 3rd International Symposium on Utilization of High Strength Concrete*, pp. 377-384.

Kollegger, J. and G. Melhorn (1988), "Experimentelle und Analytische Untersuchungen zur Aufstellung eines Materialmodells für Gerissene Stahbetonscheiben (Experimental and

Analytical Investigations to Establish a Material Model for Cracked Concrete Slabs)," *Gesamthochschule Kassel (Comprehensive University Kassel)*, No. 6.

Kupfer, H., H.K. Hilsdorf, and H Rusch (1969), "Behavior of Concrete under Biaxial Stress," *ACI Journal Proceedings*, Vol. 66, No. 8, pp. 656-666.

Mast, R.F. (1992) "Unified Design Provisions for Reinforced and Prestressed Concrete Flexural and Compression Members," *ACI Structural Journal*, Vol. 89, No. 2, pp. 185-199.

Mast, R.F., M. Dawood, S.H. Rizkalla, and P. Zia. (2008), "Flexural Strength Design of Concrete Beams Reinforced with High-Strength Steel Bars," *ACI Structural Journal*, Vol. 105, No. 4, pp. 570-577.

Mattock, A.H. (1959), "Redistribution of Design Bending Moments in Reinforced Concrete Continuous Beams," *Proceedings of the Institution of Civil Engineers*, Vol. 12, No. 1, pp. 35-46.

Mattock, A.H. (1965), "Rotational Capacity of Hinging Regions in Reinforced Concrete Beams," *ACI Special Publication*, Vol. 12, pp.143-181.

Mattock, A.H. (1983), "Secondary Moments and Moment Redistribution in ACI 318-77 Code," *International Symposium on Nonlinearity and Continuity in Prestressed Concrete*, Vol. 3, pp. 27-48.

NACU4 (1910), "Standard Building Regulations for the Use of Reinforced Concrete," *National Association of Cement Users*, 13 pp.

Pfund, S.J. (2012), "Cyclic Response of Concrete Beams Reinforced with ASTM A1035 Grade 120 Steel Bars," *M.S. Thesis, The Pennsylvania State University*, 217 pp.

Pugh, J.S., L.N. Lowes, and D.E. Lehman (2017), "Accurate Methods for Elastic Seismic Demand Analysis of Reinforced Concrete Walled Buildings," *Journal of Structural Engineering*, Vol. 143, No. 8, 13 pp.

Pujol, S., J.A. Ramirez, and M.A. Sozen (1999), "Drift Capacity of Reinforced Concrete Columns Subjected to Cyclic Shear Reversals," *ACI Special Publication*, Vol. 187, pp. 255-274.

Puranam, A.Y. (2018), "Strength and Serviceability of Concrete Elements Reinforced with High-Strength Steel," *Ph.D Dissertation, Purdue University*, 402 pp.

Roy, H.E.H. and M.A. Sozen (1964), "Ductility of Concrete," *Proceedings of the International Symposium on Flexural Mechanics of Reinforced Concrete*, pp. 213-224.

Sawyer, H.A. (1965), "Design of Concrete Frames for Two Failure Stages," *ACI Special Publication*, Vol. 12, pp. 405-431.

Schlaich, J., K. Schäfer, and M. Jennewein (1987), "Toward a Consistent Design of Structural Concrete," PCI Journal, Vol. 32, No. 3, pp. 74-150.

Soltani, A., K.A. Harries, and B.M. Shahrooz (2013), "Crack Opening Behavior of Concrete Reinforced with High Strength Reinforcing Steel," *International Journal of Concrete Structures and Materials*, Vol. 7, No. 4, pp. 253-264.

Sugano, S., T. Nagashima, H. Kimura, and A. Ichikawa (1990), "Experimental Study on High-Strength Concrete Beams Using High-Strength Main Bars," *Proceedings of the Japan Concrete Institute*, Vol. 12, No. 2, pp. 215-220.

Taerwe, L. and B. Espion (1989), "Serviceability and the Nonlinear Design of Concrete Structures," *IABSE Proceedings*, pp. 61-76.

Tavallali, H. (2011), "Cyclic Repsonse of Concrete Beams Reinforced with Ultrahigh Strength Steel," *Ph.D. Dissertation, The Pennsylvania State University*, 329 pp.

Thomas, K. and M.A. Sozen (1965), "A Study of the Inelastic Rotation Mechanism of Reinforced Concrete Connections," *University of Illinois Engineering Experiment Station*, No. 301, 129 pp.

To, D.V. (2018), "Performance Characterization of Beams with High-Strength Reinforcement," *Ph.D. Dissertation, University of California, Berkeley*, 264 pp.

van Mier, J.G.M. (1986), "Multi-Axial Strain-Softening of Concrete, Part 1: Fracture," *Materials and Structures*, Vol. 19, No. 3, pp. 179-190.

Vecchio, F.J. and M.P. Collins (1986), "Modified Compression-Field Theory for Reinforced Concrete Beams Subjected to Shear," *ACI Journal Proceedings*, Vol. 83, No. 2, pp. 219-231.

Yotakhong, P. (2003), "Flexural Performance of MMFX Reinforcing Rebars in Concrete Structures," *M.S. Thesis, North Carolina State University*, 162 pp.

Zienkiewicz, O.C. and R.L. Taylor (1989), "The Finite Element Method, Volume 1: The Basis," *McGraw-Hill Book Company*, 689 pp.

Appendix A

A.1. Test Specimens

A.1.1. Construction

Figure A.1.1 provides representative photos of the beam construction process. Specimen formwork was designed and delivered by the Conco Companies based on provided dimensions. Reinforcement cages were fabricated outside of the forms by Conco and were placed in by crane. Beams were cast in two lifts in the orientation they were tested. Concrete was vibrated between lifts. Series 1 specimens were cast using a crane and hopper. Specimens in Series 2 were cast using a pump truck. Concrete cylinders in both series were cast concurrently. After casting, the concrete was allowed to set for approximately three hours and was then covered with burlap and plastic. Starting the day of casting, the burlap was watered every weekday until form removal. Series-1 specimens were removed from their forms at 34 days while Series-2 specimens were removed from their forms at 11 days.

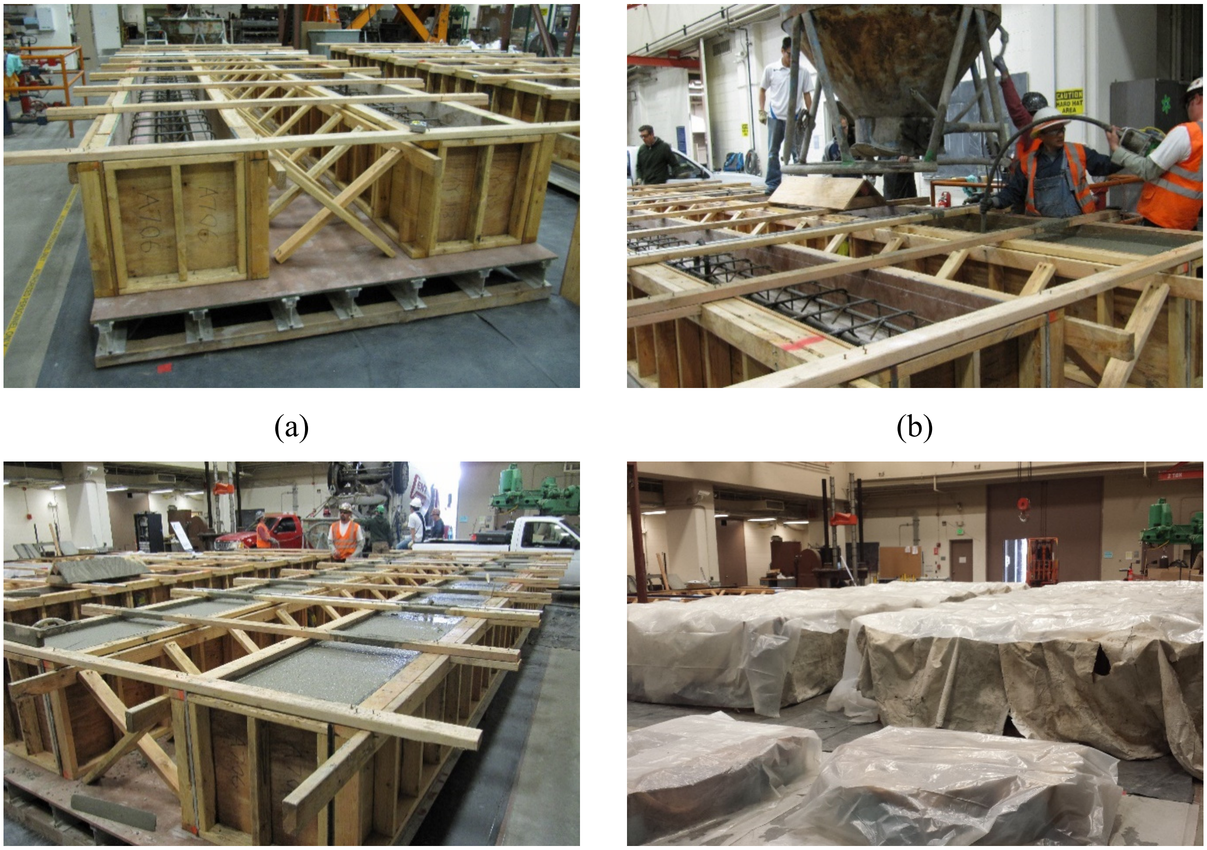

(a) (b)

(c) (d)

Figure A.1.1: Phases of specimen construction

A.1.2. Measured Dimensions

A.1.2.1. Series 1

Bar locations measured before casting are summarized in Figure A.1.2 and Table A.1.1. Exterior dimensions measured after casting are summarized in Figure A.1.3 and Table A.1.2. Both sets of reported values are the average of dimensions at seven locations along the length of each beam.

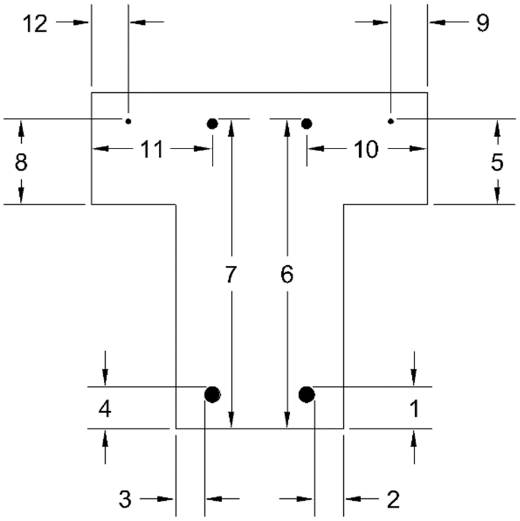

Figure A.1.2: Series 1 bar locations

Table A.1.1: Series 1 bar locations

	1GBL60	1GBH60	1GBL100	1GBH100
1 [in.]	3.20	3.21	3.04	3.00
2 [in.]	2.05	1.82	2.05	1.96
3 [in.]	2.14	1.95	2.05	1.89
4 [in.]	3.13	3.14	2.98	2.96
5 [in.]	5.46	5.45	5.36	5.39
6 [in.]	21.82	21.46	21.48	21.79
7 [in.]	21.83	21.43	21.52	21.80
8 [in.]	5.27	5.07	5.34	5.50
9 [in.]	2.59	2.46	2.63	2.57
10 [in.]	8.71	8.84	8.68	8.80
11 [in.]	8.77	8.52	8.68	8.82
12 [in.]	2.43	2.66	2.46	2.55

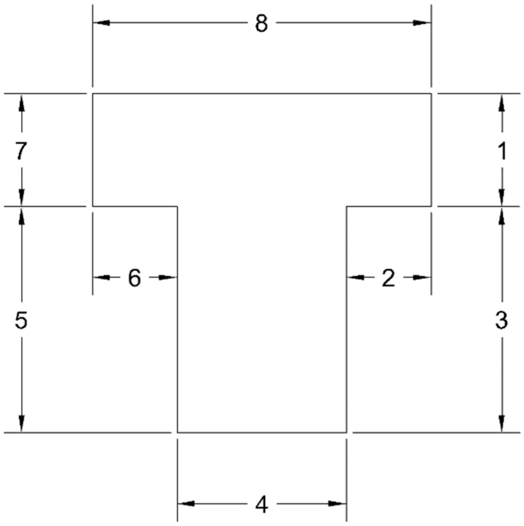

Figure A.1.3: Series 1 gross dimensions

Table A.1.2: Series 1 dimensions

	1GBL60	1GBH60	1GBL100	1GBH100
1 [in.]	8.25	8.29	8.21	8.29
2 [in.]	6.01	6.04	6.04	6.02
3 [in.]	16.03	16.14	16.11	16.09
4 [in.]	12.29	12.05	12.20	12.18
5 [in.]	16.04	16.17	16.14	16.07
6 [in.]	6.00	6.03	6.04	6.05
7 [in.]	8.21	8.19	8.35	8.27
8 [in.]	24.08	24.09	24.09	24.05

A.1.2.2. Series 2

Bar locations measured before casting are summarized in Figure A.1.4 and Table A.1.3. Exterior dimensions measured after casting are summarized in Figure A.1.5 and Table A.1.4. Both sets of reported values are the average of dimensions at five locations along each beam's length.

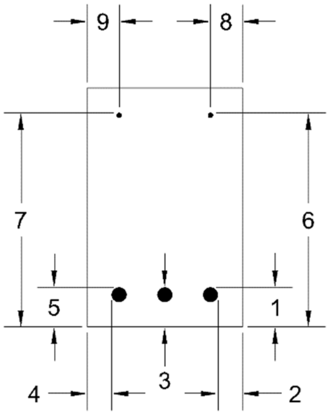

Figure A.1.4: Series 2 bar locations

Table A.1.3: Series 2 bar locations

	2GBL60	2GBH60	2GBL100	2GBH100
1 [in.]	3.30	3.30	3.25	3.25
2 [in.]	1.85	1.85	1.75	1.95
3 [in.]	3.30	3.30	3.25	3.25
4 [in.]	1.85	1.85	1.95	1.95
5 [in.]	3.30	3.30	3.25	3.25
6 [in.]	16.25	16.25	16.25	16.45
7 [in.]	16.30	16.35	16.25	16.35
8 [in.]	2.35	2.15	2.20	2.20
9 [in.]	2.40	2.45	2.35	2.33

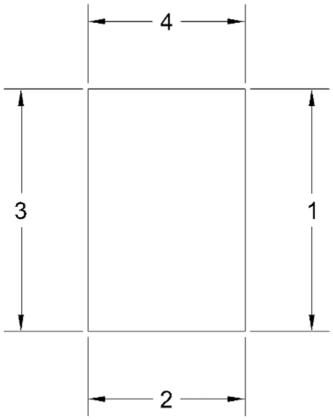

Figure A.1.5: Series 2 gross dimensions

Table A.1.4: Series 2 dimensions

	2GBL60	2GBH60	2GBL100	2GBH100
1 [in.]	18.13	18.08	18.03	18.13
2 [in.]	9.68	11.35	11.65	14.75
3 [in.]	18.15	18.30	18.08	18.11
4 [in.]	9.73	11.08	11.73	14.88

A.2. Test Apparatus

A.2.1. General

A.2.1.1. Pedestals

To support the beams, steel blocks with welded, 4-in. diameter cylinders were post tensioned to the laboratory strong floor. On top of the cylinders, 4-in. thick and 1-ft wide plates rotated about channels that were cut for the cylinders. Beams were placed on the rotating plates. To allow for beams to elongate during testing, the distance between supports was allowed to vary during the tests. The methods used to accomplish this are outlined in Section A.2.2.1 for Series 1 and A.2.3.1 for Series 2.

A.2.1.2. Hydraulic Jacks

Hydraulic jacks used to load both series of beams were Enerpac Model RCH-603. Detailed information can be found at http://www.enerpac.com/sites/default/files/products/downloads/rch_e327_us.pdf. The stroke capacity of the jacks was 3 in., but deflections greater than 3 in. were expected for both series of tests. Thus, the test setup was designed to allow the jacks to be reset without unloading the beam.

A.2.2. Series 1

A.2.2.1. Support Conditions

Beams 1GBL60 and 1GBH100 were placed directly on the rotating plates and the north pedestal was allowed to slide in a track. In addition to having a sliding north pedestal, beams 1GBH60 and 1GBL100 sat on thin, greased plates which slid in tracks on the rotating plates. These two conditions for the north support are shown in Figure A.2.1(a) and (b).

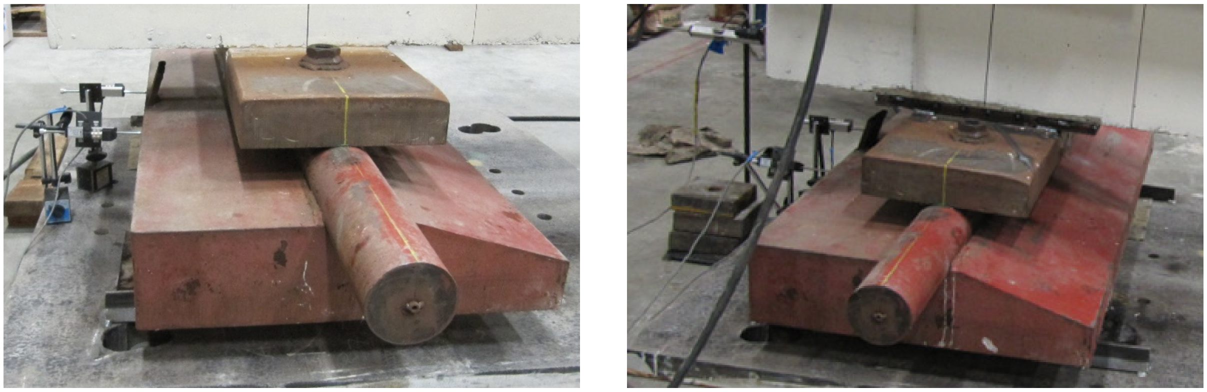

(a) (b)

Figure A.2.1: Series 1 support conditions

A.2.2.2. Load Frame

A frame was pulled towards the strong floor to load specimens. Figure A.2.2(a) shows individual components of the load frame, while Figure A.2.2(b) shows the load frame on a beam.

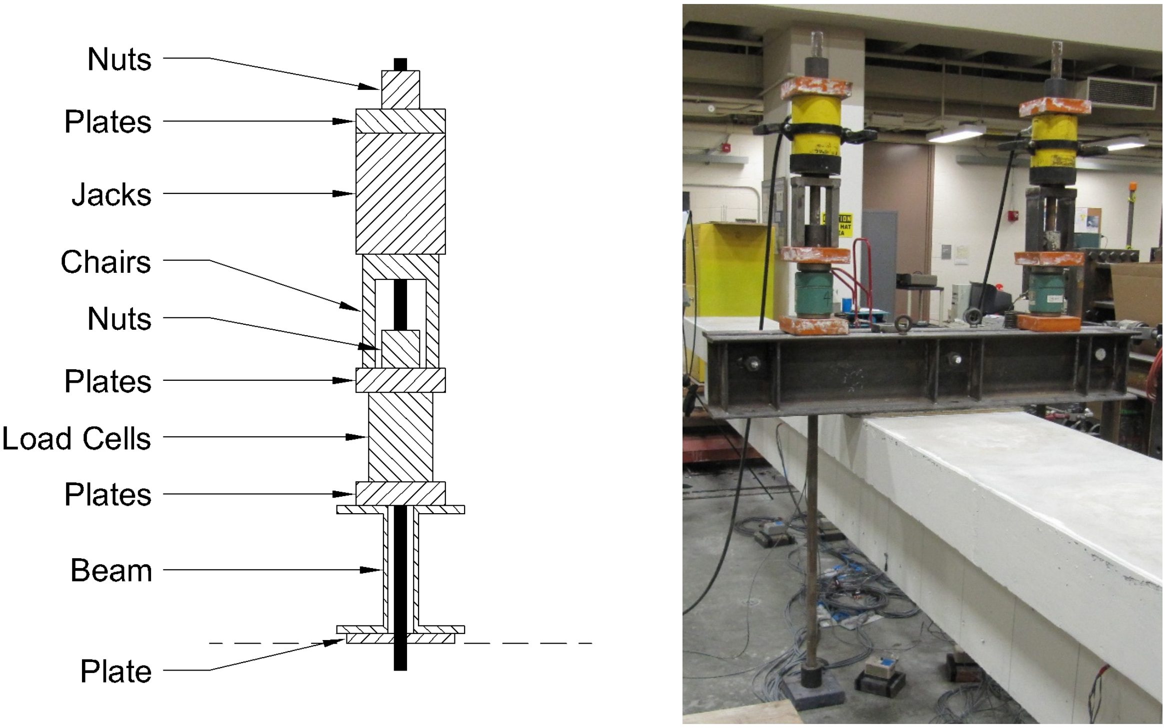

(a) (b)

Figure A.2.2: Series 1 load frame

A.2.3. Series 2

A.2.3.1. Support Conditions

For this test series, the steel blocks with the cylindrical steel bearing were fixed to the strong floor. The rotating plates identified in Section A.2.1.1 were then placed atop the cylindrical steel bearing, and a thin, greased sliding plate was placed atop the rotating plate. The beams were then set atop the sliding plate. This setup enabled the beams to slide horizontally relative to the rotating plates, approximating a roller support. When sliding on one side of a beam was much greater than the other, the disparity was corrected by arresting the movement of the side that had translated more by placing a C-clamp between the end of the beam and the rotating plate, as shown in Figure A.2.3.

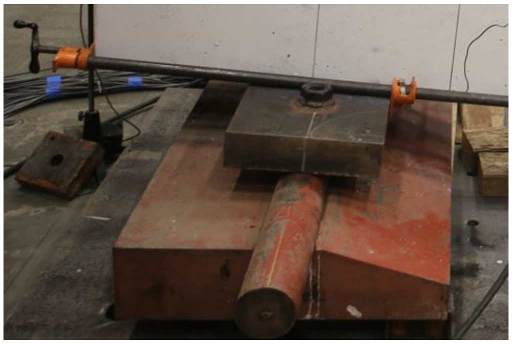

Figure A.2.3: Series 2 support with movement arrested

A.2.3.2. Load Frame

A frame was pulled towards the strong floor to load specimens. Figure A.2.4(a) shows individual components of the load frame, while Figure A.2.4(b) shows the load frame on a beam. The interface between the plate and tubes was polished and greased to allow differential movement. Sliding of the tubes with respect to the plate was monitored, but not measured.

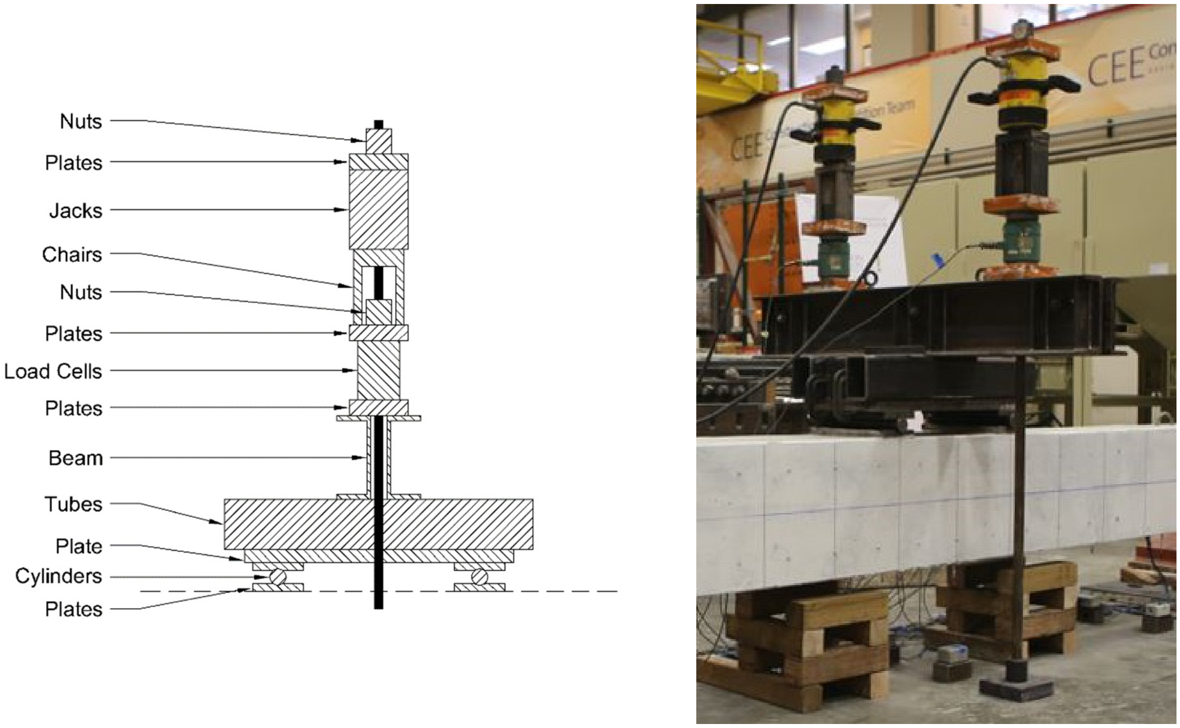

(a) (b)

Figure A.2.4: Series 2 load frame

A.3. Materials

A.3.1. Concrete

A.3.1.1. Specified and Delivered Mixes

Normal-weight concrete with a compressive strength of 5 ksi and slump of 6 in. was specified for all mixes. For Series 1, the water-to-cement ratio was specified to be 0.49, while for Series 2 it was specified to be 0.44. Table A.3.1 and Table A.3.2 list specified and delivered quantities of materials for Series 1 and 2, respectively. Series-1 beams required two trucks to cast while a single truck was sufficient for all beams in Series 2. In Series 1, Truck 1 had 21 gallons added upon arrival to increase the slump from 2.5 to 5.5 in. and Truck 2 had 9 gallons added to increase the slump from 4.5 to 6.25 in. In Series 2, no additional water was necessary to meet slump requirements.

Table A.3.1: Series 1 design and actual material quantities

Material Code	Specification	Design Quantity	Truck 1	Truck 2
			Actual Quantity	Actual Quantity
Sand	ASTM C33	709 lb/yd^3	737 lb/yd^3	740 lb/yd^3
Fine Aggregate	ASTM C33	709 lb/yd^3	740 lb/yd^3	737 lb/yd^3
Coarse Aggregate	ASTM C33	1675 lb/yd^3	1683 lb/yd^3	1687 lb/yd^3
Cement	ASTM C150	420 lb/yd^3	420 lb/yd^3	421 lb/yd^3
Fly Ash	ASTM C618	140 lb/yd^3	143 lb/yd^3	142 lb/yd^3
Water	ASTM C1602	33 gal/yd^3	33 gal/yd^3	33 gal/yd^3

Table A.3.2: Series 2 design and actual material quantities

Material Code	Specification	Design Quantity	Actual Quantity
Sand	ASTM C33	371 lb/yd^3	380 lb/yd^3
Fine Aggregate	ASTM C33	1053 lb/yd^3	1049 lb/yd^3
Coarse Aggregate	ASTM C33	1675 lb/yd^3	1663 lb/yd^3
Cement	ASTM C150	547 lb/yd^3	550 lb/yd^3
Fly Ash	ASTM C618	97 lb/yd^3	97 lb/yd^3
Water	ASTM C1602	34 gal/yd^3	26 gal/yd^3

A.3.1.2. Cylinder Tests

For all trucks, concrete was cast into plastic cylinders of 6-in. diameter and 12-in. height. These were cured alongside the beams in the same fashion as the beams. These cylinders were tested periodically, as well as on test days. To test them, the cylinders were first removed from their plastic molds, weighed, and then sulfur-capped. The intent of the sulfur caps was to minimize stress concentrations by ensuring a uniform loading surface. Then, the cylinders were tested to determine either their compressive strength, or their elastic modulus. Compressive-strength tests were performed according to ASTM C39. Results of these tests are summarized graphically in Figure A.3.1 and Figure A.3.2. A summary of test-day values is given in Table A.1.1. Reported results are the averages of three cylinders tested.

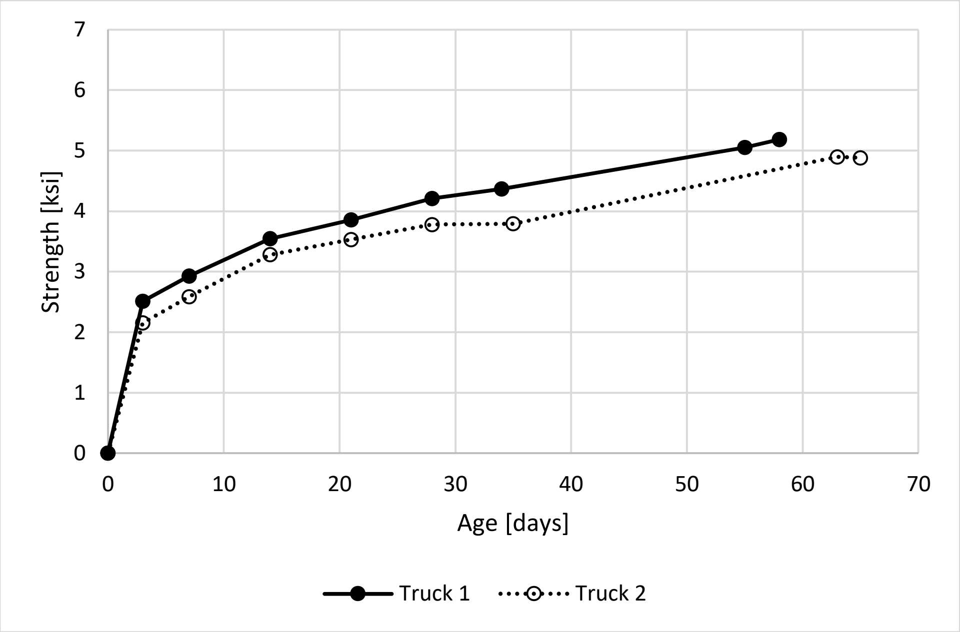

Figure A.3.1: Series 1 compressive strength-age relationships for concrete cylinders

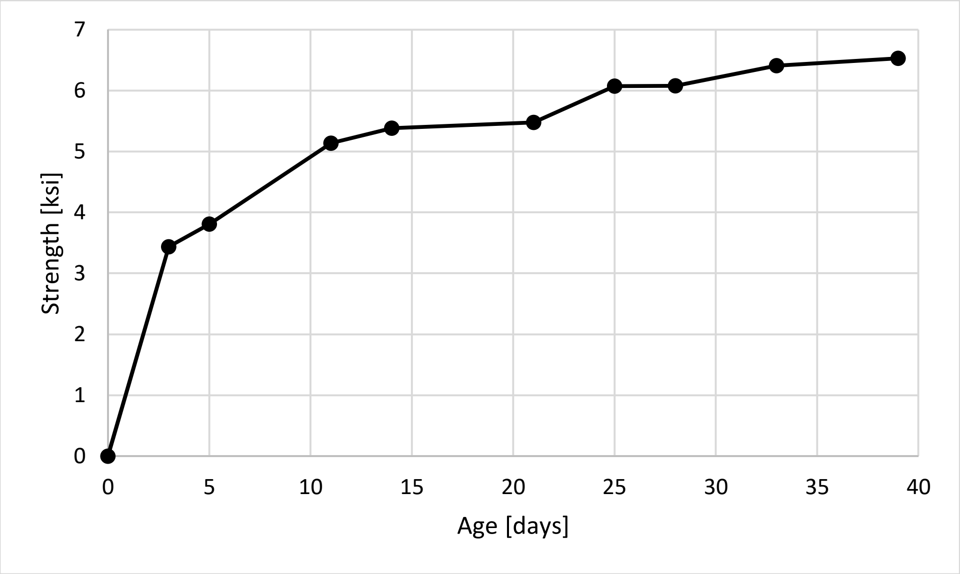

Figure A.3.2: Series 2 compressive strength-age relationship for concrete cylinders

Table A.3.3: Test-day concrete-strength summary

	Truck	f'_c	Age
		[ksi]	[days]
1GBL60	1	5.05	55
1GBH60	2	4.89	63
1GBL100	2	4.88	65
1GBH100	1	5.18	58
2GBL60	-	6.41	33
2GBH60	-	6.53	39
2GBL100	-	6.07	25
2GBH100	-	6.08	28

Modulus of elasticity tests were performed in accordance with ASTM C469. Tests were performed after the completion of testing of Series 2. The results of these tests are shown in Figure A.3.3. Based on these two samples, the modulus of elasticity for the concrete in Series 2 is 3840 ksi. Modulus of elasticity tests were not conducted for Series 1.

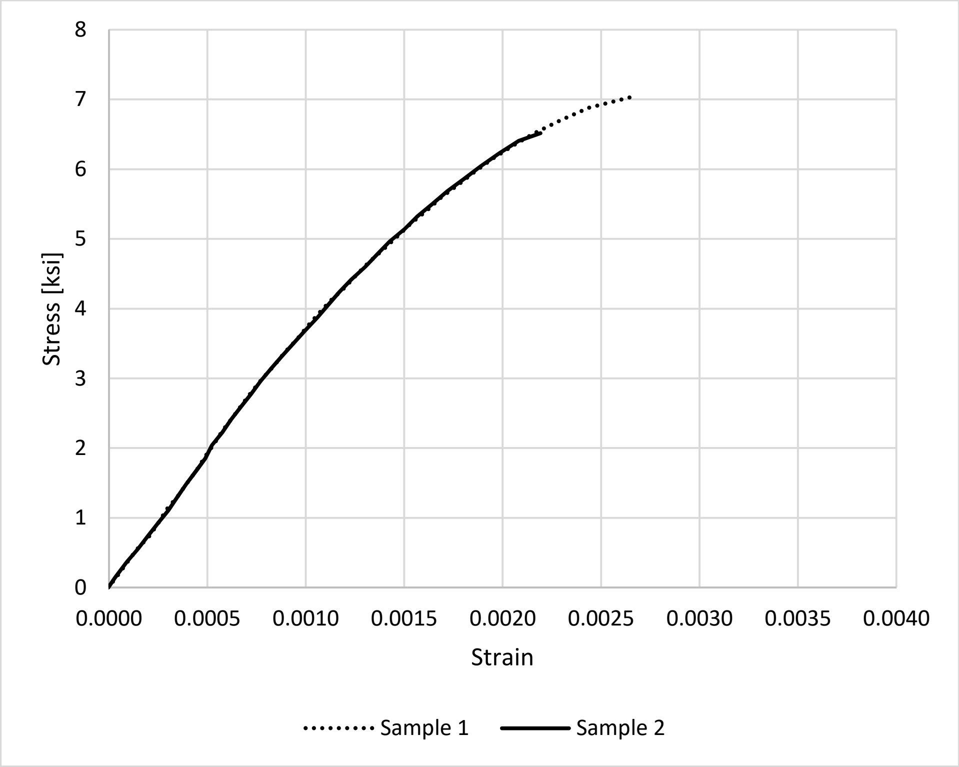

Figure A.3.3: Series 2 compressive stress-strain relationships for concrete cylinders

A.3.2. Reinforcement

A.3.2.1. Coupon Tests

Coupons were cut from longitudinal reinforcement of each beam and tested in monotonic tension in accordance with ASTM A370. Strain was measured over an 8-in. gauge length. Based on these tests, mechanical properties were determined following ASTM E8 with yield stress determined by the 0.2% offset method. Uniform-elongation strain was determined by finding the center of two vertical lines intersecting the data at 99.5% of the ultimate steel stress. For highly non-parabolic data, this percentage was adjusted to 99.75%. Figure A.3.4 shows this graphically. A summary of these mechanical properties is presented in Table A.3.4. Reinforcement designations are as follows: S1 and S2 indicate Series 1 and Series 2, respectively; the number given after "N" represents the bar nominal size; the letter "T" denotes a top bar; the letters "H" and "L" indicate whether the bar had relatively high or low T/Y; and the number 60 and 100 indicate the nominal yield stress. Because coupons of full cross-sectional area were tested, stress here is the force measured by the testing equipment divided by the nominal cross-sectional area of the bar. Values presented are the average of three coupons tested. The results of the coupon tests for Series 1 are given in Figure A.3.5 and the results from Series 2 are given in Figure A.3.6.

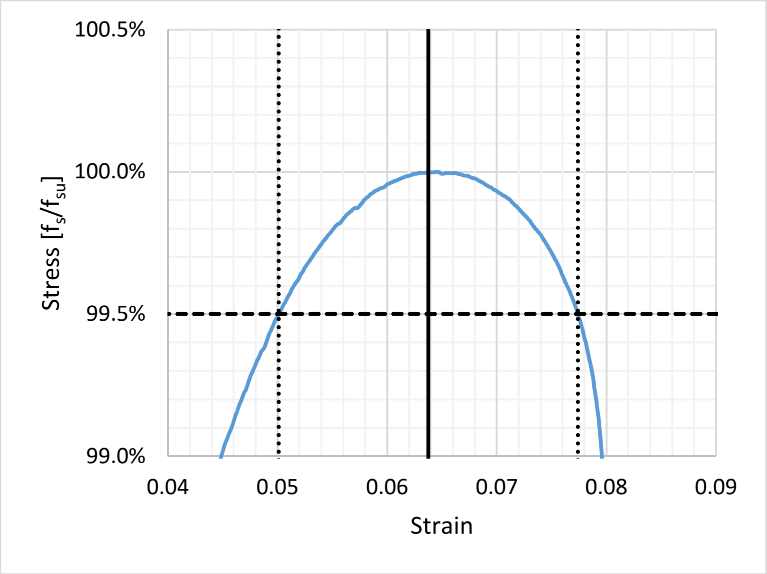

Figure A.3.4: Uniform-elongation strain determination example

Table A.3.4: Reinforcing steel summary

Reinforcement	f_y [ksi]	f_{su} [ksi]	T/Y	ε_{sh}	E_{shi} [ksi]	ε_{su}	ε_{sf}
S1-N3-T	67.5	104.1	1.54	0.0084	1150	0.103	0.37
S1-N6-T	63.2	102.5	1.62	0.0080	1250	0.113	0.33
S1-N10-L60	65.8	93.7	1.42	0.0085	800	0.116	0.30
S1-N10-H60	63.3	105.2	1.66	0.0065	1300	0.106	0.26
S1-N8-L100	106.0	124.6	1.18	0.0068	600	0.069	0.19
S1-N8-H100	102.0	128.7	1.26	0.0062	850	0.094	0.26
S2-N3-T	62.8	93.4	1.49	0.0064	900	0.120	0.48
S2-N10-60	66.7	95.6	1.43	0.0095	850	0.120	0.32
S2-N8-100	109.4	124.7	1.14	0.0075	500	0.067	0.20

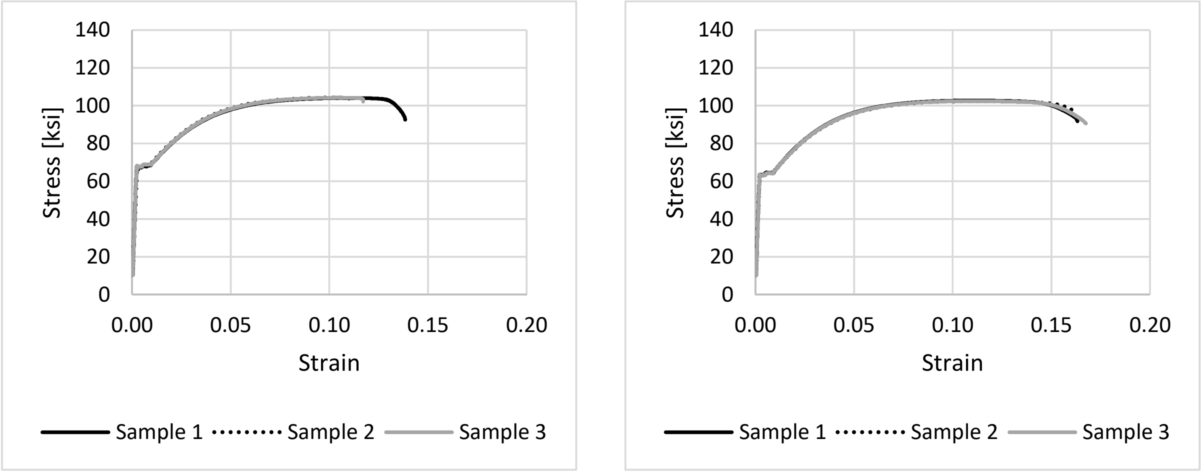

(a) S1-N3-T

(b) S1-N6-T

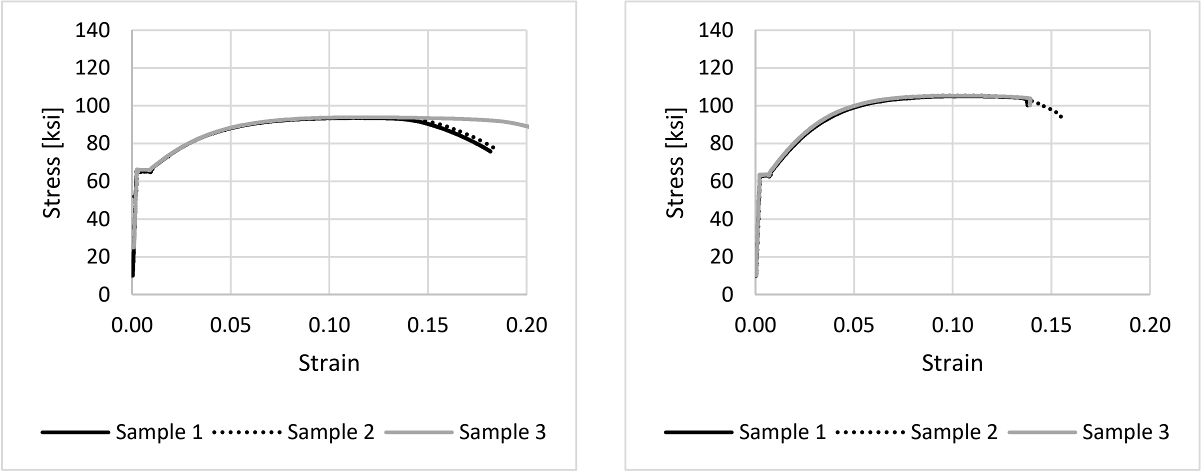

(c) S1-N10-L60

(d) S1-N10-H60

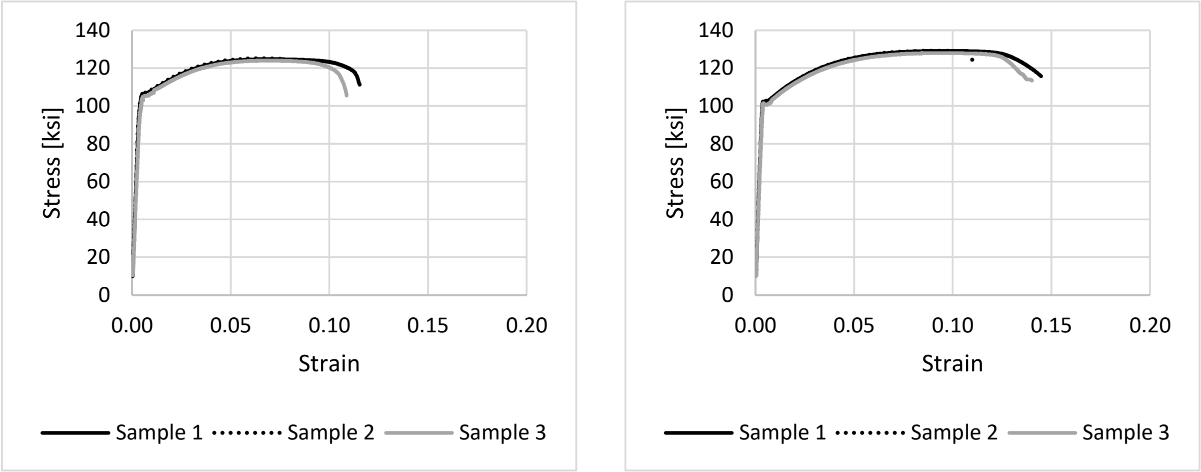

(e) S1-N8-L100

(f) S1-N8-H100

Figure A.3.5: Series 1 tensile stress-strain relationships for steel coupons

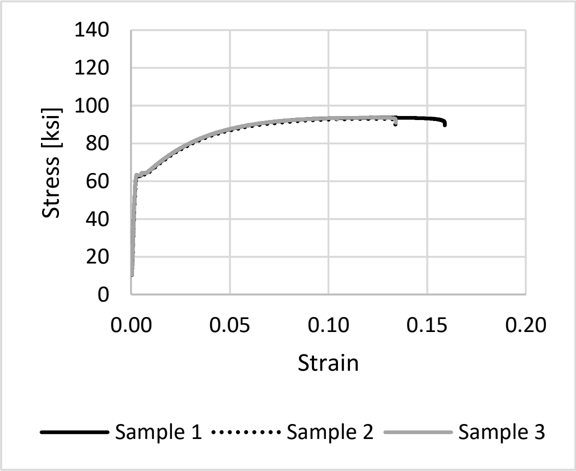

(a) S2-N3-T

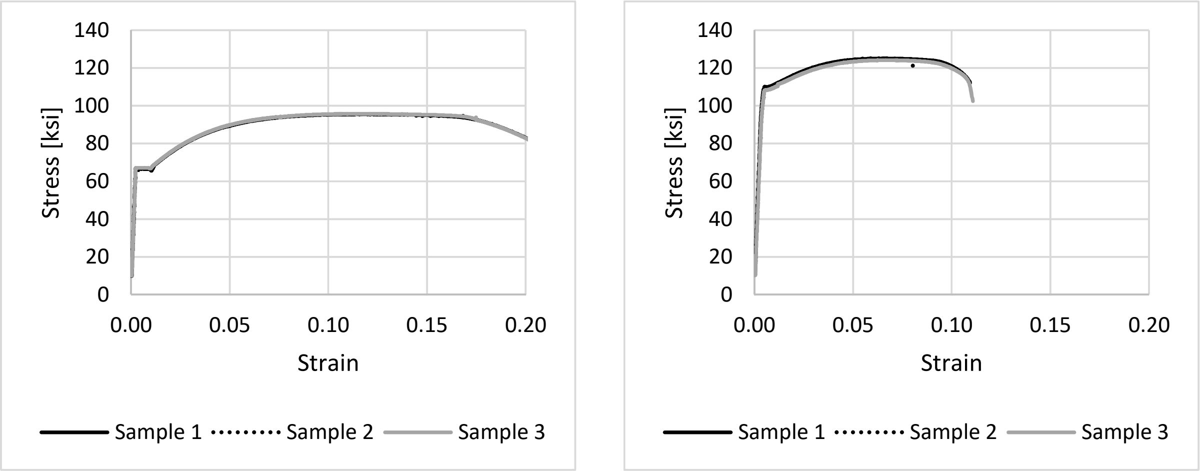

(b) S2-N10-60

(c) S2-N8-100

Figure A.3.6: Series 2 tensile stress-strain relationships for steel coupons

A.4. Test Instrumentation and Data Acquisition System

A.4.1. Test Instrumentation

A.4.1.1. Series 1

In the interior of each beam, strain gauges installed on the bottom longitudinal bars measured strain. Typical locations of these gauges are shown in Figure A.4.1. Strain gauges were placed on the bar tops.

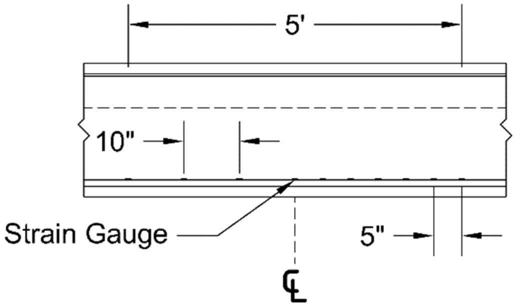

Figure A.4.1: Series 1 interior instrumentation

On the exterior of each beam, an array of LVDTs attached to threaded rods anchored into the beam monitored local deformations. Such an array was selected to provide both flexural and shear deformations. The arrangement and typical locations of the LVDTs are provided in Figure A.4.2. Beam 1GBL60 lacked the three outside bottom LVDTs on each side present in all other beams. Beam 1GBL60 was tested first in this series, and the decision to add additional instrumentation to subsequent beams was based on observations from this test.

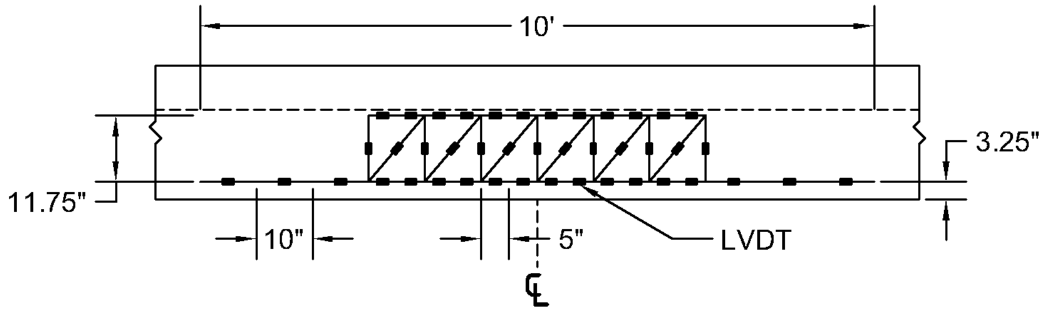

Figure A.4.2: Series 1 exterior instrumentation

Global deflections were monitored with string potentiometers anchored to the strong floor on both sides of each beam at half and quarter points. In the case of beams 1GBH100 and 1GBL60, sliding of the north pedestal was monitored by two horizontal LVDTs positioned on either side of it. In addition to monitoring the movement of the north pedestal, beams 1GBH60 and 1GBL100 added a horizontal LVDT at both ends to monitor sliding with respect to the supports.

A.4.1.2. Series 2

In the interior of each beam, strain gauges installed on the top and bottom corner longitudinal bars measured strain. Typical locations of these gauges are shown in Figure A.4.3. The strain gauges were placed on the top of the bottom bars and on the bottom of the top bars.

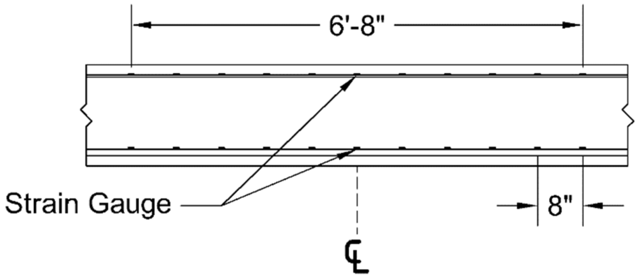

Figure A.4.3: Series 2 interior instrumentation

On the exterior of each beam, an array of LVDTs attached to threaded rods anchored into the beam monitored local deformations. Such an array was selected to provide both flexural and shear deformations. The arrangement and typical locations of the LVDTs are provided in Figure A.4.4.

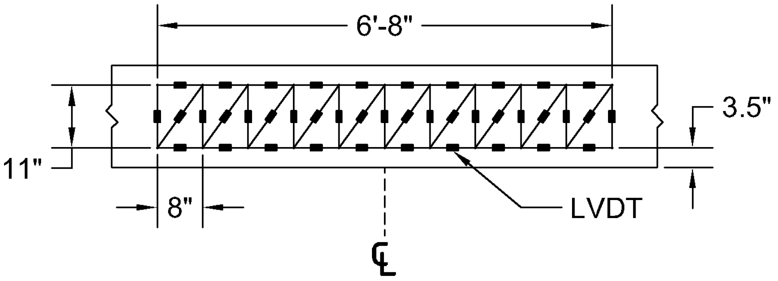

Figure A.4.4: Series 2 exterior instrumentation

Global deflections were monitored with string potentiometers anchored to the strong floor on both sides of each beam at half and quarter points. A horizontal LVDT at both ends monitored sliding with respect to the supports.

A.4.1.3. LVDTs

LVDTs used to measure both local deformations and global deflections were Novotechnik models TRS-0025, TRS-0050, and TRS-0100. Detailed information can be found at http://www.novotechnik.com/pdfs/TRTRS.pdf. In the case of local deformations, instruments were affixed near the surface of each beam using eyelets on threaded rods that allowed them to rotate without distorting their line of measurement. For global deflections, instruments were attached to weighted stands placed near their surface of measurement. Where the instrument bore on a concrete surface, a thin sheet of galvanized steel was epoxied to the concrete to prevent distortion due to the uneven surface.

A.4.1.4. Load Cells

Load cells used were Transducers Inc. Model WCL-PP78-NS-200K. They were calibrated on May 1, 2012. Correlation coefficients from the calibration exceeded 0.99998.

A.4.1.5. Strain Gauges

Strain gauges used were Tokyo Measuring Instruments Laboratory Co., Ltd. Model YLFA-5-5LT. Detailed information can be found at https://www.tml.jp/e/product/strain_gauge/catalog_pdf/YEF_YF_YHFseries.pdf. These gauges are designed for measurements of strains up to 15-20%. All gauges were 0.2-in. long and 0.08-in. wide. To attach the strain gauges to a reinforcing bar, the bar was smoothed using a grinder and sandpaper, prepped with an acid, base, and alcohol, and then the gauges were glued to the bar with CN-Y adhesive. After the glue had cured, gauges were coated with wax, SB tape, and epoxy to protect them during casting. Care was taken to ensure these layered materials took up as little area as possible at each location on the surface of the bar. SB tape and CN-Y adhesive are manufactured by Tokyo Measuring Instruments Laboratory Co., Ltd. and detailed information about them can be found at http://www.tml.jp/e/product/strain_gauge/coat_list/#c5 and http://www.tml.jp/e/product/strain_gauge/adhesives_list/#a4.

A.4.1.6. String Potentiometers

String potentiometers used to measure global deflections were Celesco Model PT 101-0015-111-110. Detailed information is located at http://www.te.com/commerce/DocumentDelivery/DDEController?Action=showdoc&DocId=Data+Sheet%7FPT101%7FA%7Fpdf%7FEnglish%7FENG_DS_PT101_A.pdf%7FCAT-CAPS0014. In all cases, sensors with a 15-in. stroke length were used. In cases where sensors had to be placed more than 15 in. from the point on the specimen they measured, thin braided-steel wires were used to extend from the point of placement to the point of measurement. This was done because accuracy is related to stroke length, so it was undesirable to use instruments with greater extension capacity.

A.4.2. Data Acquisition System

The data acquisition control system enclosure was Pacific Instruments Model 6000. Detailed information can be found here http://catalog.pacificinstruments.com/item/conditioning-acquisition-control-system-enclosures/16-slot-usb-data-control-interface-enclosures/6000u-1?&bc=100|1016|1014. The data acquisition system control system input/output modules were Pacific Instruments Model 6035. Further material about them is located at http://catalog.pacificinstruments.com/item/6000-series-analog-i-o-modules/model-6035-8-channel-strain-bridge-transducer-ampl/6035-6. These modules are suited to strain gauges in particular.

A.5. Test Procedure

During testing, loading was paused during two stages of loading stages for marking cracks, recording crack widths, and checking the test setup. Crack widths were recorded at elevations corresponding approximately the longitudinal reinforcement and beam mid-heights; these pauses took approximately 30 minutes. The test procedure was the same for both series of beams. Figure A.5.1 displays the loading protocol graphically. Tests in Series 1 lasted approximately four hours while tests in Series 2 lasted approximately two hours.

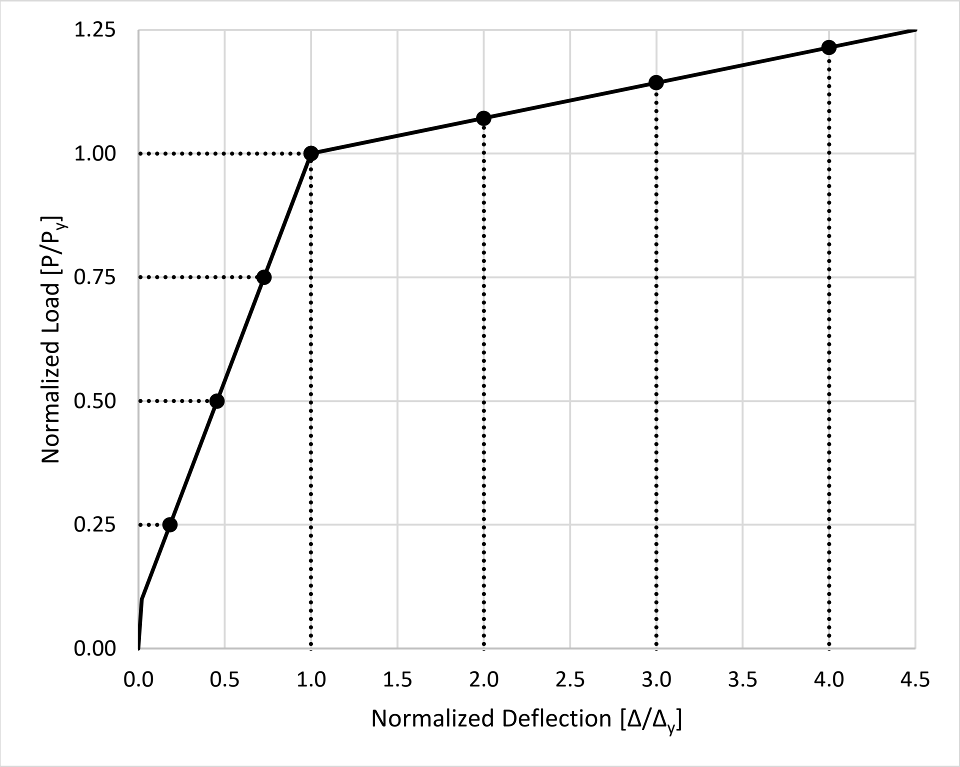

Figure A.5.1: Loading protocol for all beams

A.5.1. Stage 1 – Force Controlled

Load was stopped at 0.25, 0.50, and 0.75 times the calculated yield load. These load stops were to allow for a comparison of the cracking characteristics in the beams within the serviceability range of response.

A.5.2. Between Stages

Load was stopped when yield was perceived based on measurements of load-deflection.

A.5.3. Stage 2 – Deflection Controlled

Load was stopped at 1, 2, 3… times the measured yield deflection until failure or the deflections reached the limit of the test setup.

A.6. Data Reduction

A.6.1. Material Models

Figure A.6.1 shows the normalized stress-strain curve for concrete and is based on Hognestad (1951). Compression is shown as positive and tension is negative. The model assumes the concrete behaves parabolically in compression until reaching a strain of 0.0025 (based on cylinder tests and typical strain-at-peak-stress values for concrete produced locally) at its peak stress (compressive strength measured on companion cylinders on the day of the test), and then linearly from the peak to $0.85f'_c$ at a strain of 0.004. In tension, the concrete reaches a peak stress of $7.5\sqrt{f'_c}$ at a strain of $7.5\sqrt{f'_c}/E_c$, where is E_c is computed using the ACI 318-14 method. Steel stress-strain models were based on their tensile coupon tests. Table A.3.4 provides the variables used in the steel models. Models assumed equal behavior in tension and compression.

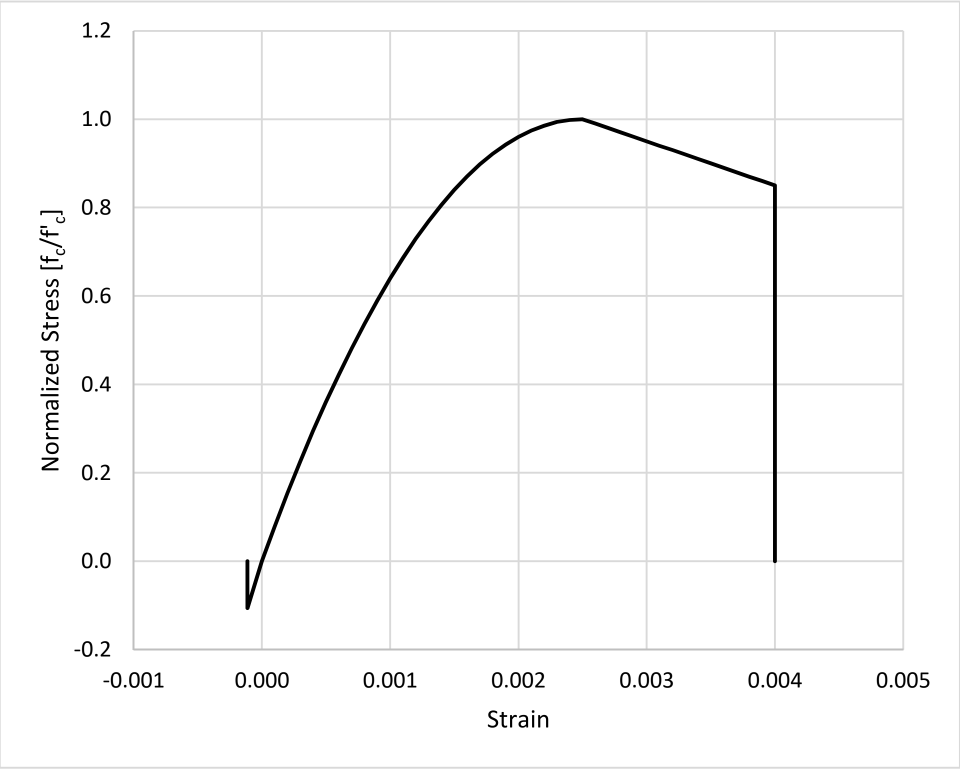

Figure A.6.1: Concrete normalized stress-strain relationship

A.6.2. Initial Stiffness

Initial stiffnesses were determined for each beam by finding loads and deflections that correspond to cracking and yielding. To do this, a bilinear moment-curvature relation was defined by a line from the origin to the cracking point and second line form the cracking point to the yielding point. Figure A.6.2 shows an example of this. The calculated moment-curvature relation is shown in black while the bilinear relation is gray.

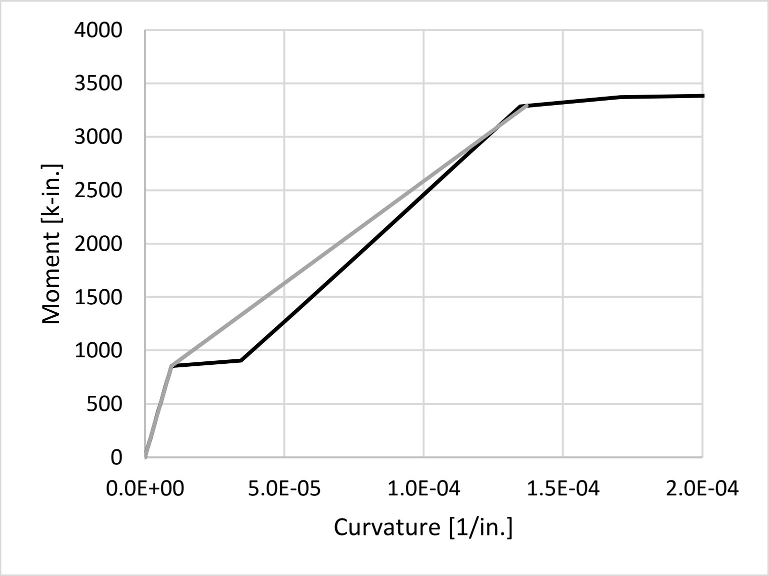

Figure A.6.2: 1GBL60 calculated and bilinear moment-curvature relations

Next, the applied midspan load required to reach either the cracking moment or yielding moment at midspan was determined, including the moments due to self-weight and the load frame. Then, the entire moment diagram corresponding to either cracking or yielding was determined considering all applied loads. A representative moment profile showing all associated moments at yielding are shown in Figure A.6.3.

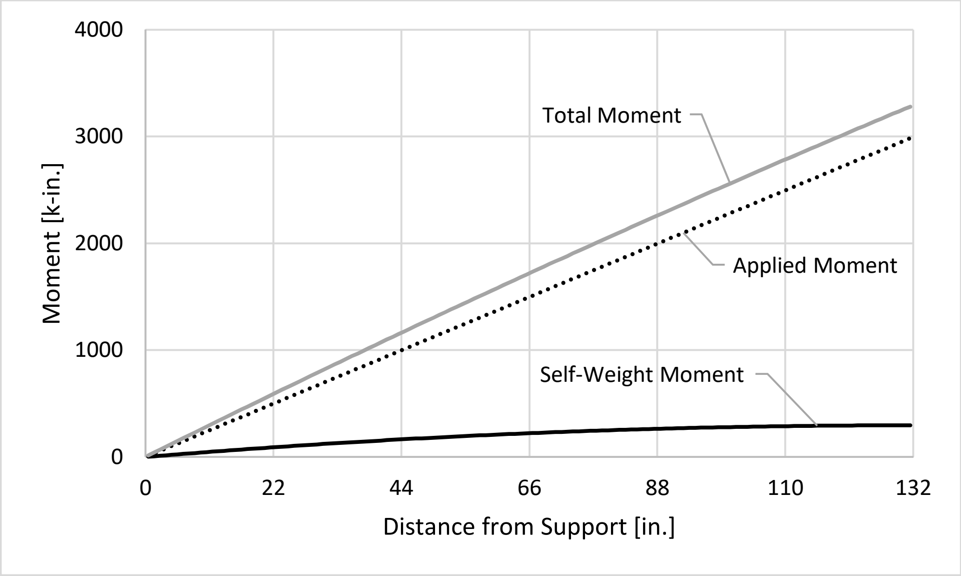

Figure A.6.3: 1GBL60 moment distribution

Using the moment distribution along the beam and the bilinear moment-curvature relation, the curvature distribution along the beam was determined. Figure A.6.4 provides an example of this step. Next, either the cracking deflection or yielding deflection was determined from the curvature diagram. Finally, the moment due to self-weight and deflections due to self-weight and the load frame were subtracted, leaving the corresponding values associated the applied concentrated load (which were the values measured). Deflections due to self-weight and the load frame were calculated using the gross section properties and concrete elastic modulus determined from cylinder tests. These deflections could not be measured since the beam could not be instrumented before being placed, so they were subtracted from the total calculated deflection to represent the measured values.

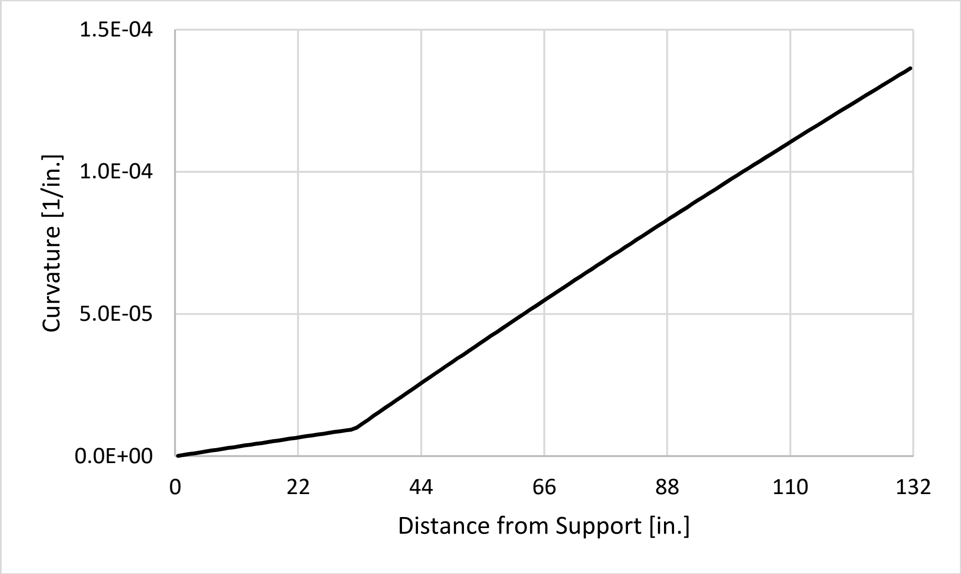

Figure A.6.4: 1GBL60 curvature distribution

A.6.3. Plastic Deformations

For both series of beams, yield and ultimate deflections were determined and used to calculate plastic rotations. The method outlined by Elwood and Eberhard (2009) was used to define yield deflections. This method involves using moment-curvature relationships to determine the moments (and, hence, the loads) corresponding to when the strain in the tension steel first reaches the yield strain ($P_{first\,yield}$) and the maximum concrete strain reaches 0.004 ($P_{0.004}$), running a secant from the origin through the deflection data at $P_{first\,yield}$, and taking the yield deflection as the intersection of that secant and a horizontal line drawn at load equal to $P_{0.004}$. Figure A.6.5 shows relevant values in this process for a beam in each series. In the figure, the lower dashed line is $P_{first\,yield}$ and the higher dashed line is $P_{0.004}$. Ultimate deflections were determined by inspection.

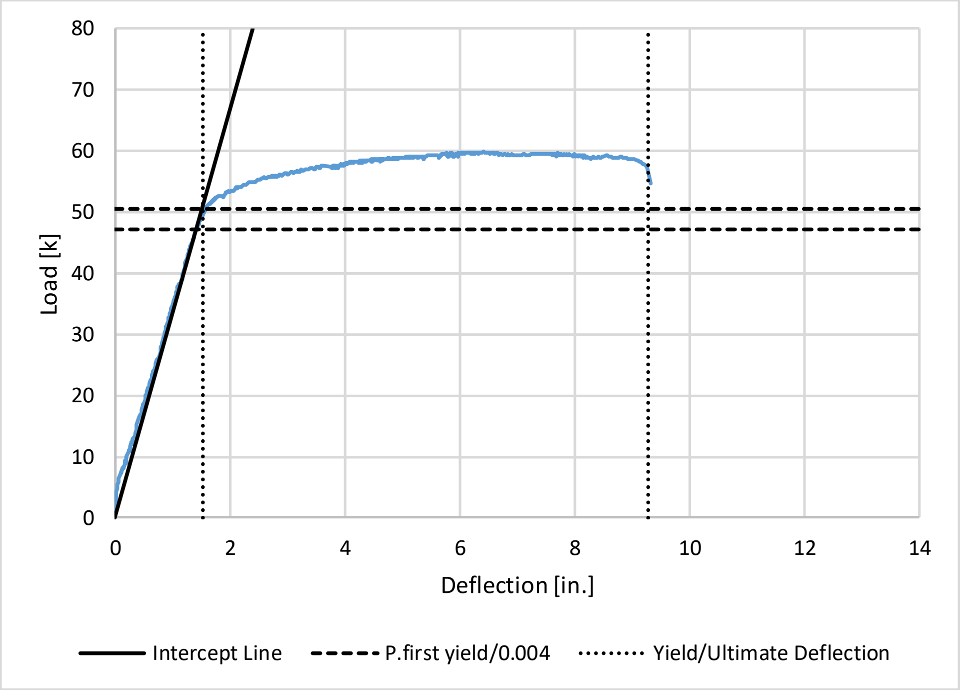

(a) 1GBL100

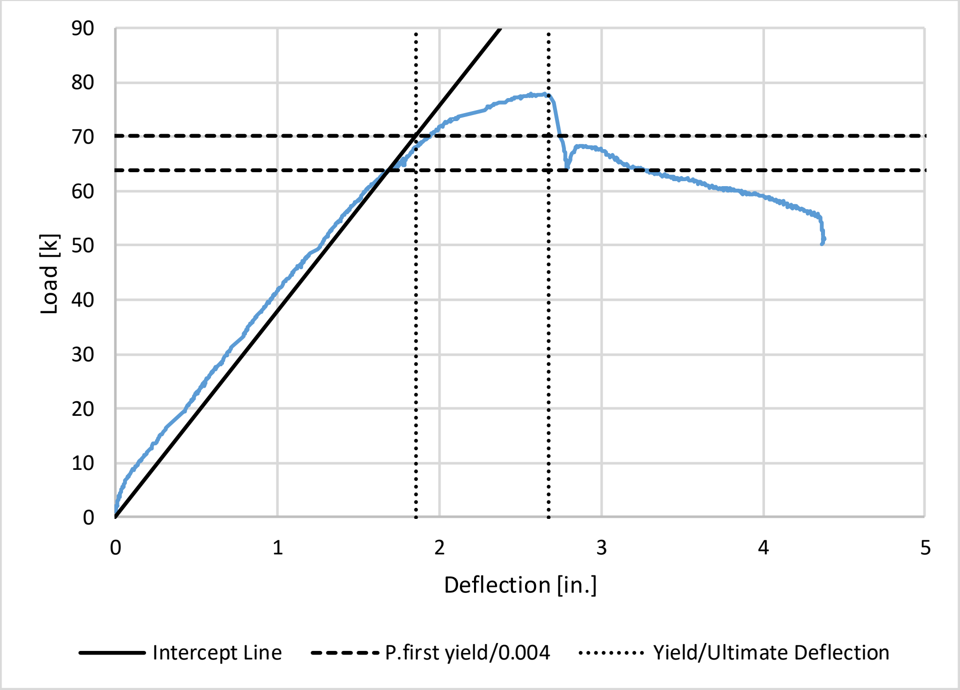

(b) 2GBL100

Figure A.6.5: Determination of yield and ultimate deflections

Appendix B

B.1. Series 1

B.1.1. Load-Deflection

Figure B.1.1 presents the measured relations between concentrated load applied at midspan and measured vertical displacement at midspan.

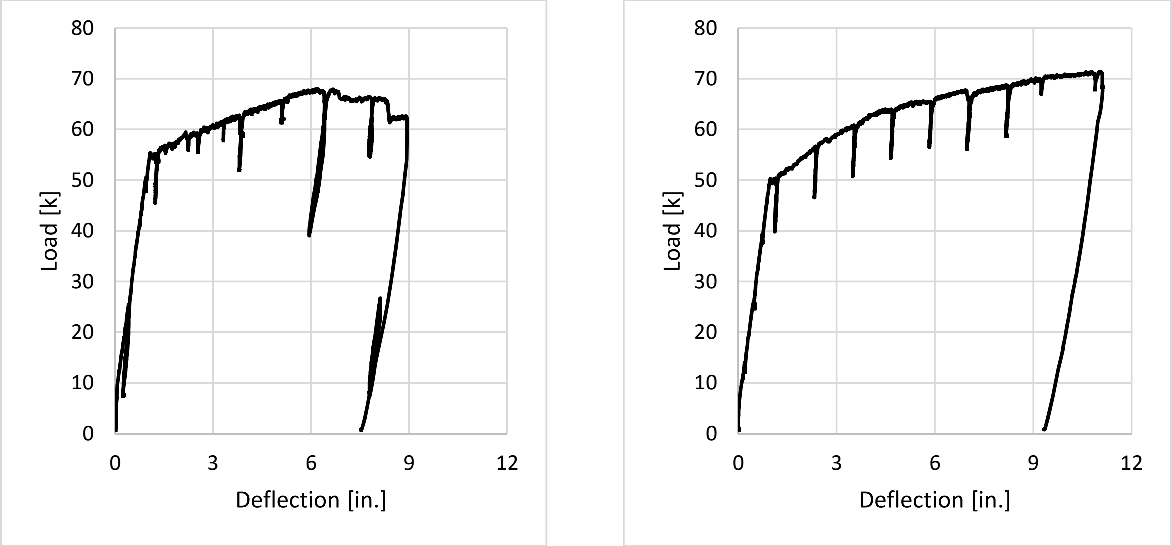

(a) 1GBL60 (b) 1GBH60

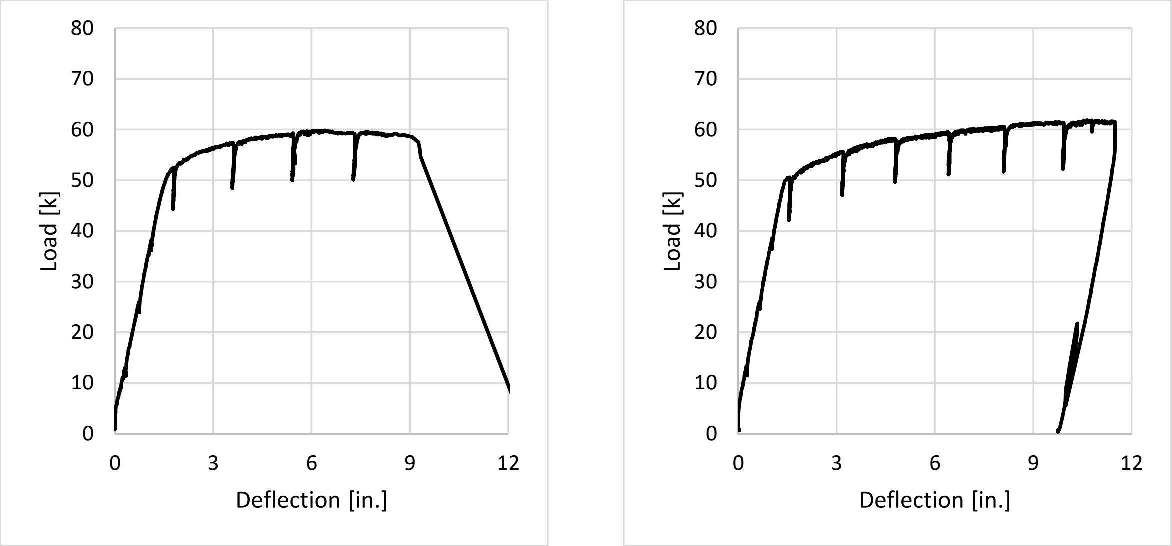

(c) 1GBL100 (d) 1GBH100

Figure B.1.1: Series 1 load-deflection relations

B.1.2. Crack Patterns

Crack patterns were recorded at various points during each test. The drawings below show the recorded crack patterns. The figure sub-caption indicates the midspan applied load and/or midspan measured deflection. Reported top values are crack widths at the intersection of the flange and web. Bottom values are crack widths at the beam bottom. If only one value is shown, it is the width at the bottom. The "<" symbol denotes a crack that was visible, but less than 0.002-in. wide (the smallest width that could be measured). All measurements are reported in inches.

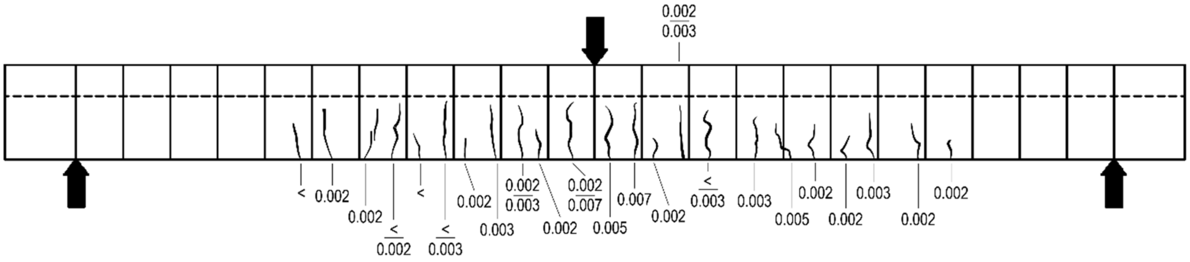

(a) $0.50P_y$

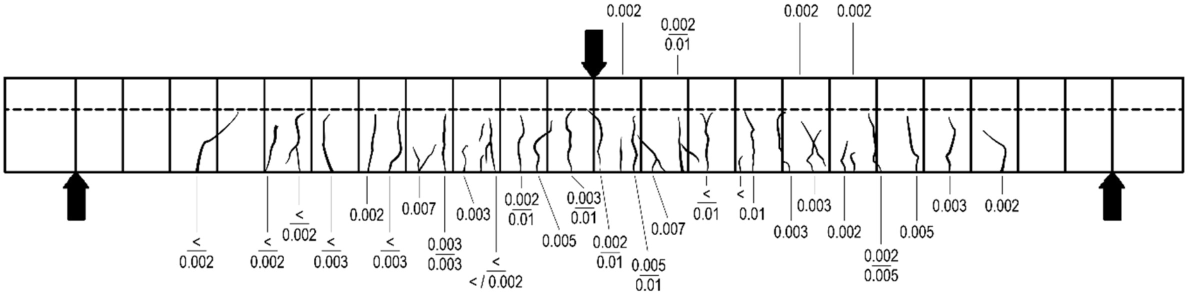

(b) $0.75P_y$

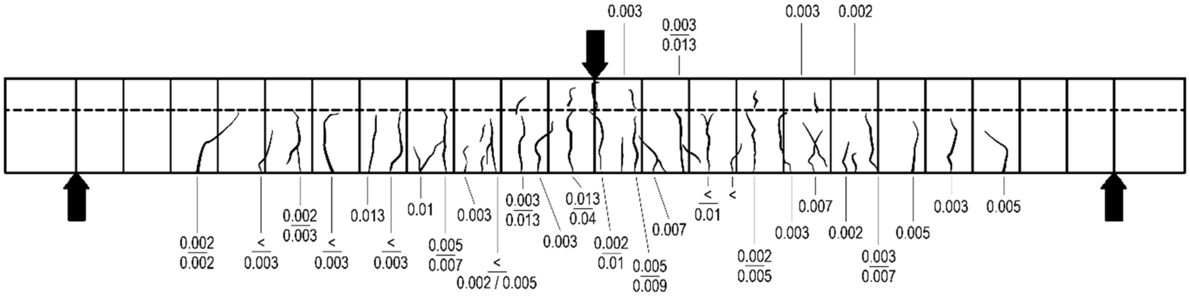

(c) Δ_y, P_y

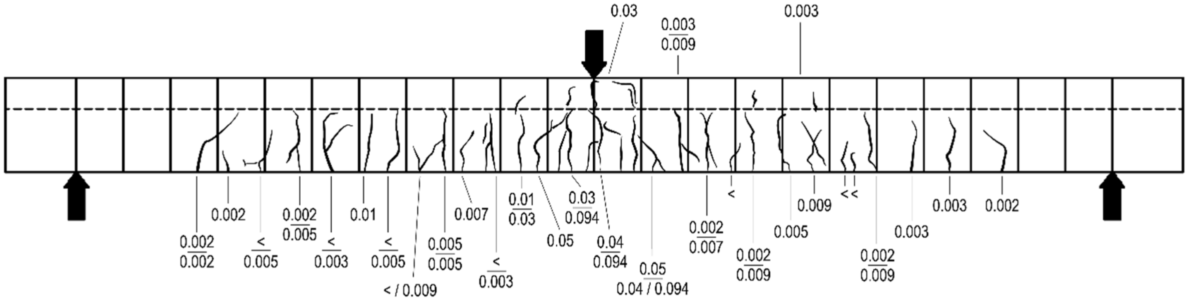

(d) $2\Delta_y$

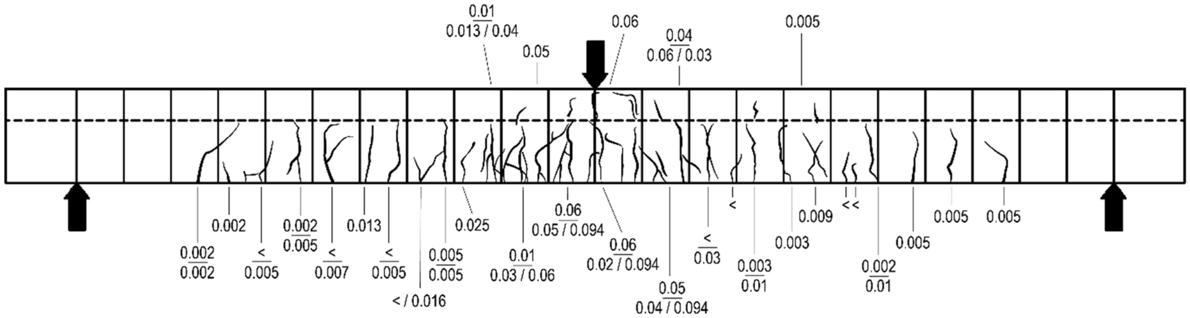

(e) $3\Delta_y$

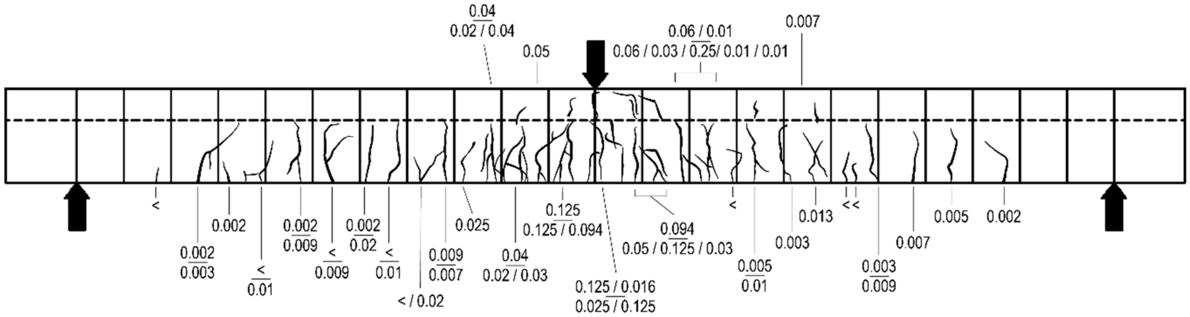

(f) $4\Delta_y$

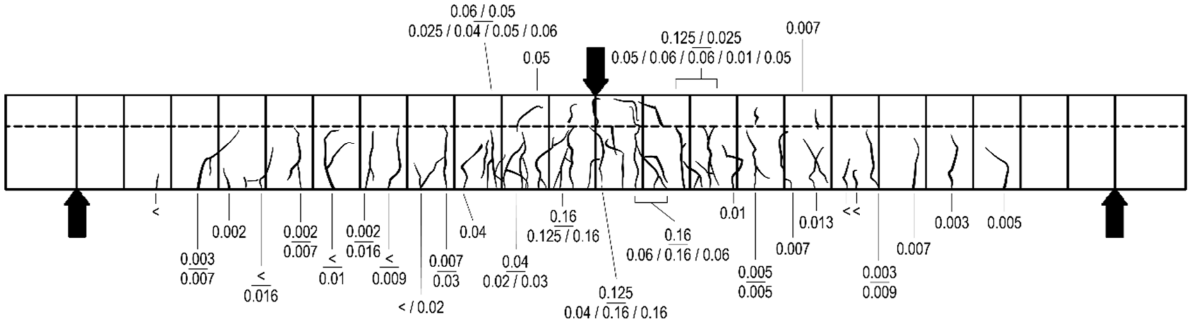

(g) $5\Delta_y$

Figure B.1.2: 1GBL60 crack patterns

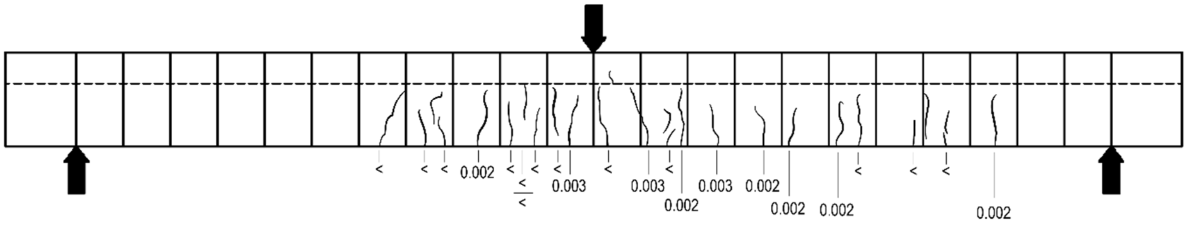

(a) 0.25P_y

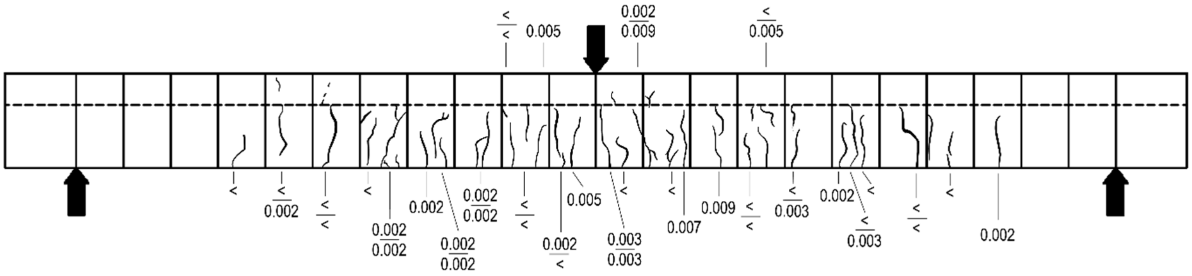

(b) 0.50P_y

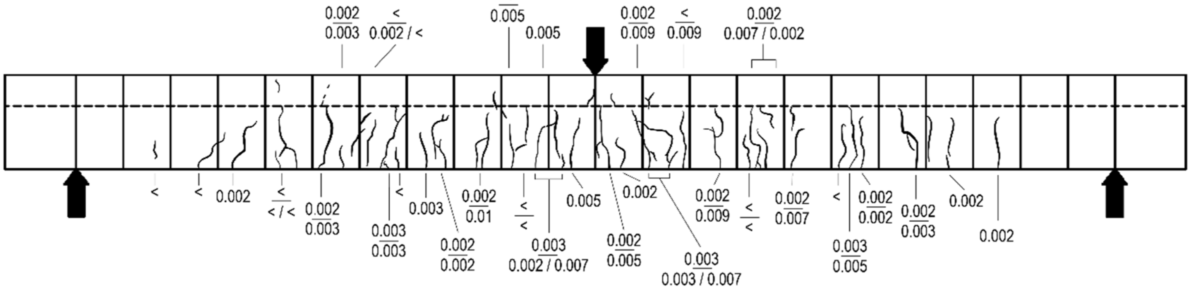

(c) 0.75P_y

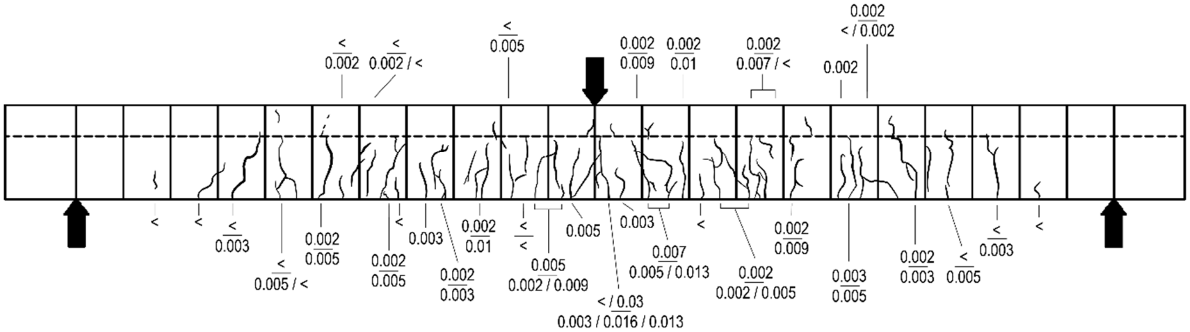

(d) Δ_y, P_y

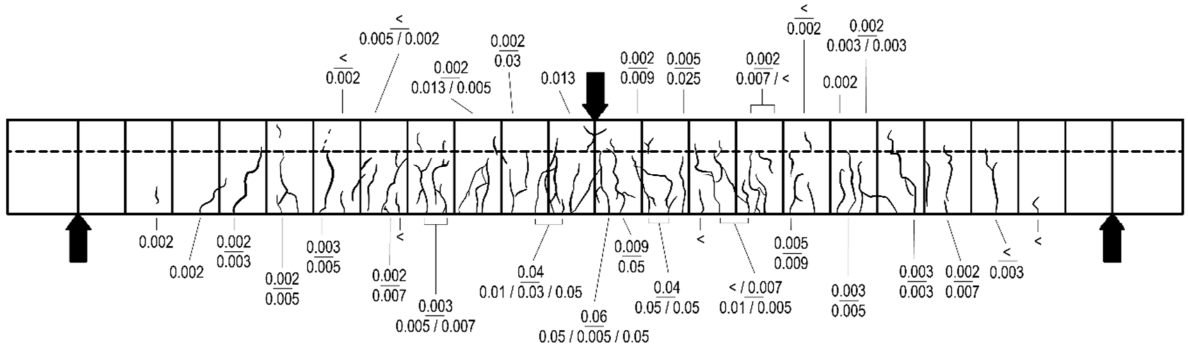

(e) $2\Delta_y$

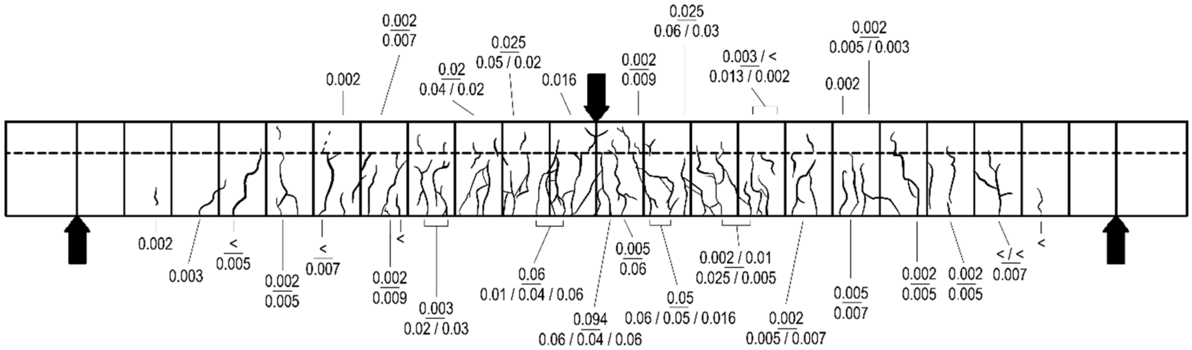

(f) $3\Delta_y$

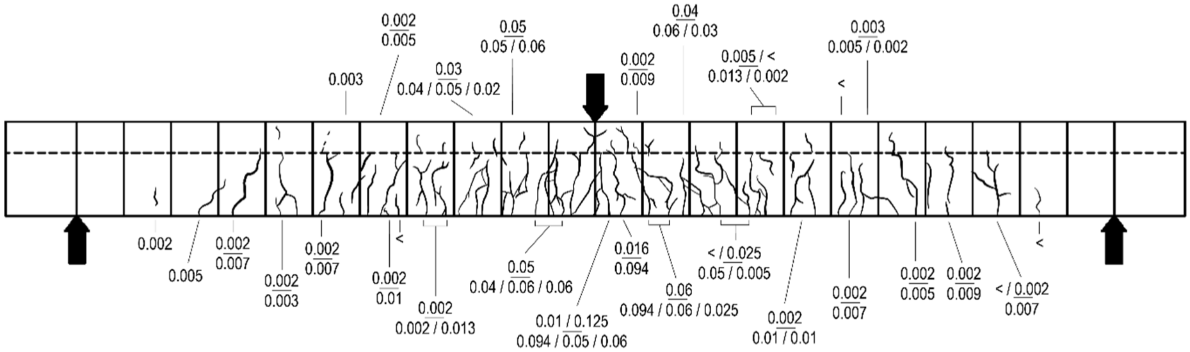

(g) $4\Delta_y$

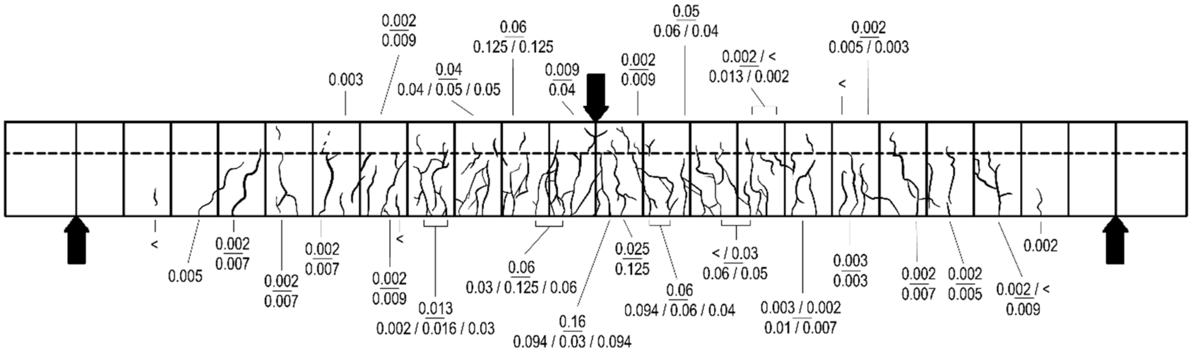

(h) $5\Delta_y$

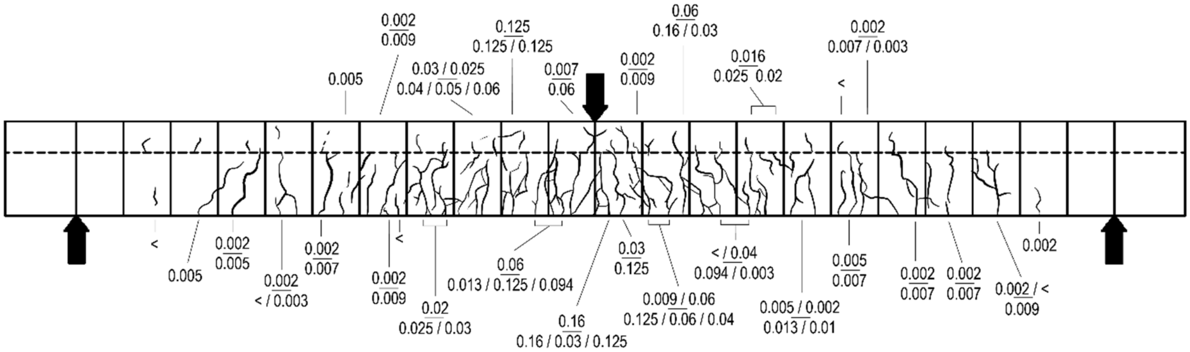

(i) $6\Delta_y$

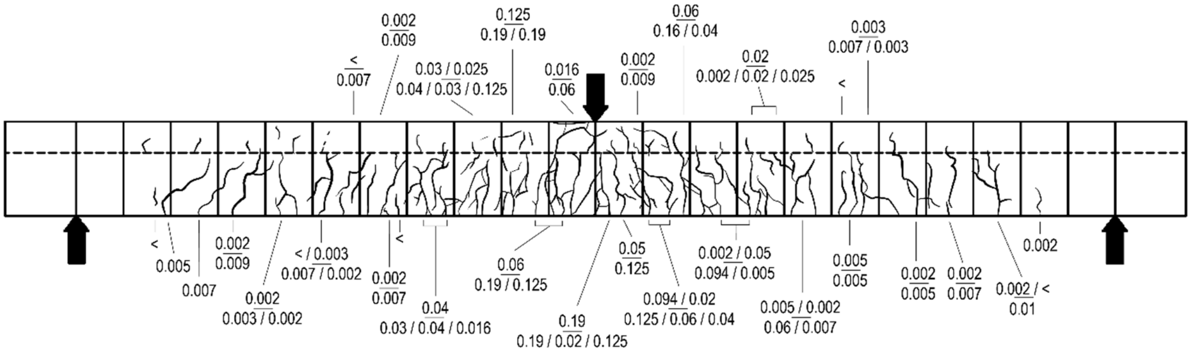

(j) $7\Delta_y$

Figure B.1.3: 1GBH60 crack patterns

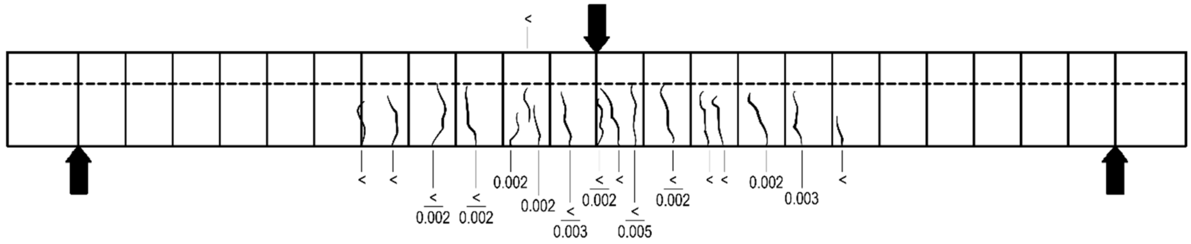

(a) $0.25P_y$

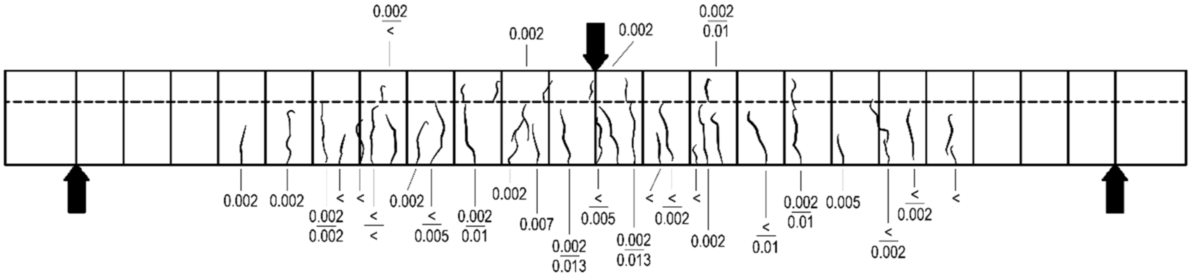

(b) $0.50P_y$

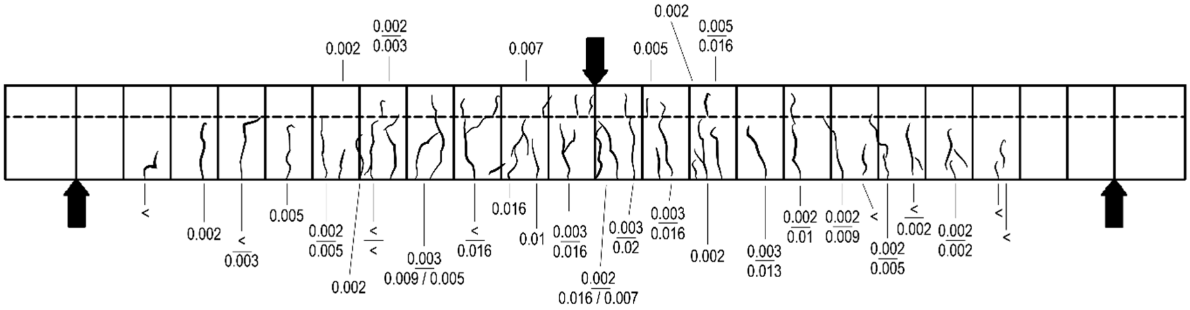

(c) $0.75P_y$

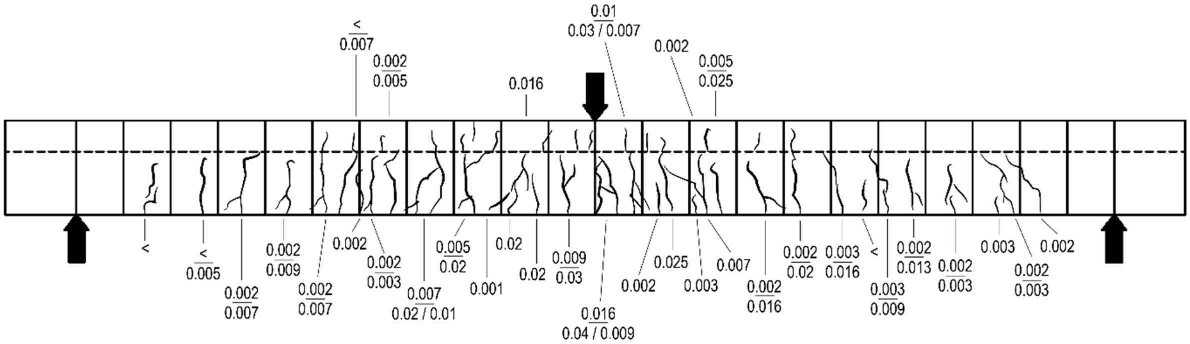

(d) Δ_y, P_y

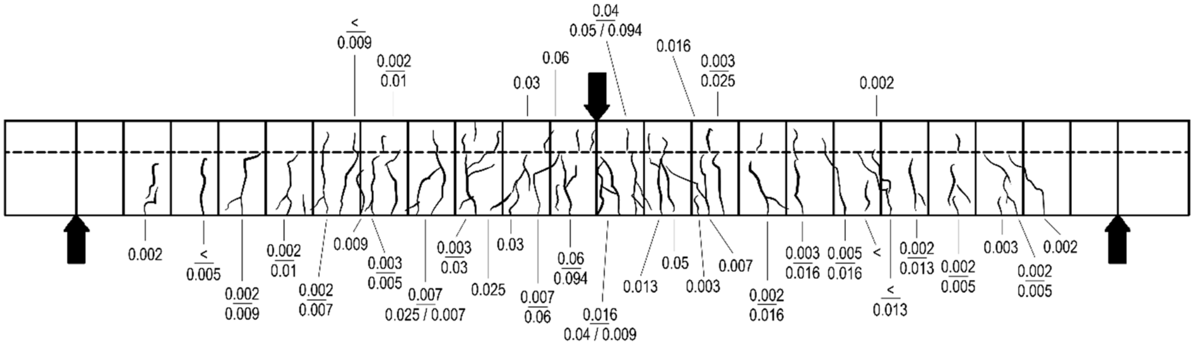

(e) $2\Delta_y$

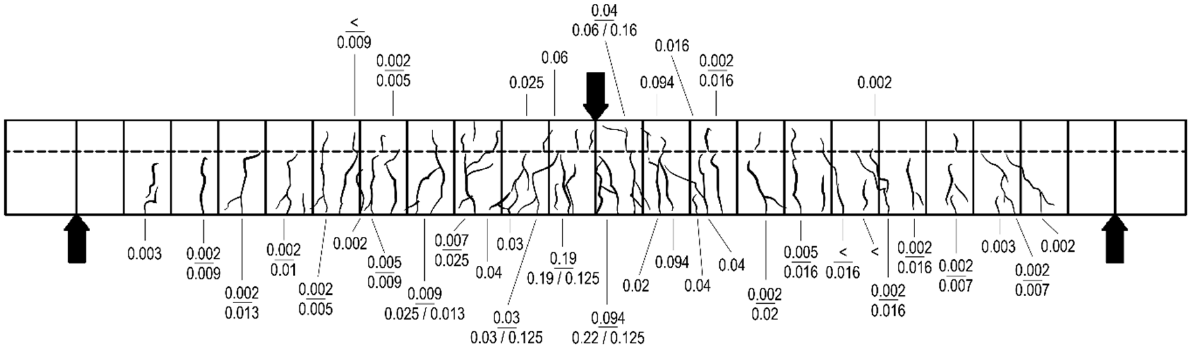

(f) $3\Delta_y$

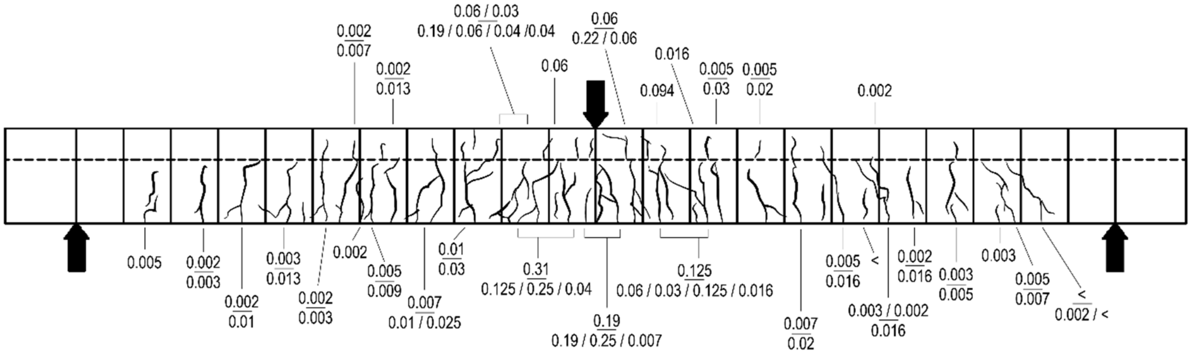

(g) $4\Delta_y$

Figure B.1.4: 1GBL100 crack patterns

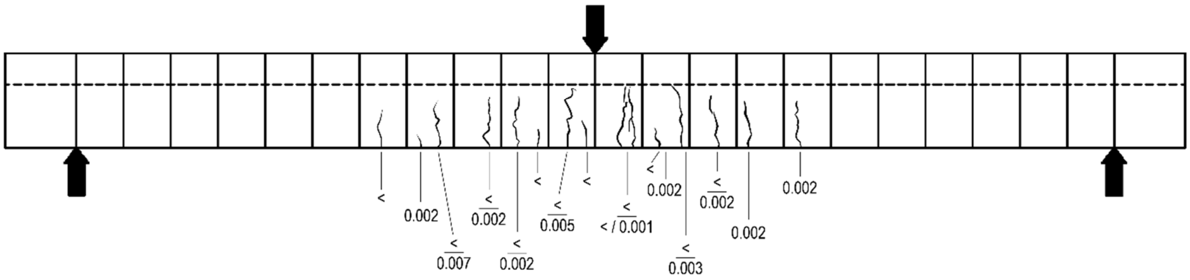

(a) $0.25P_y$

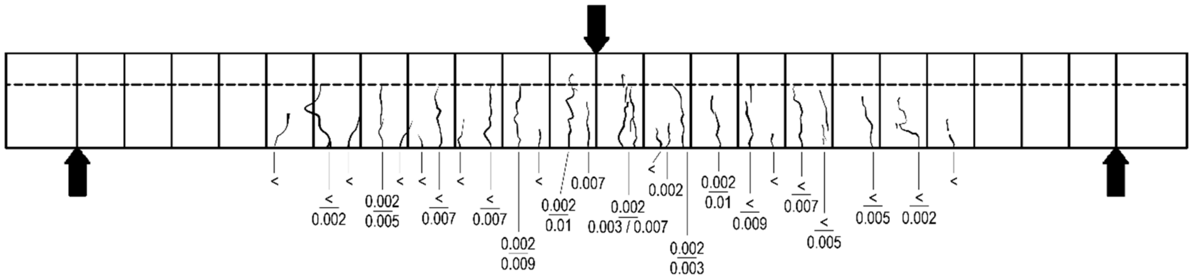

(b) $0.50P_y$

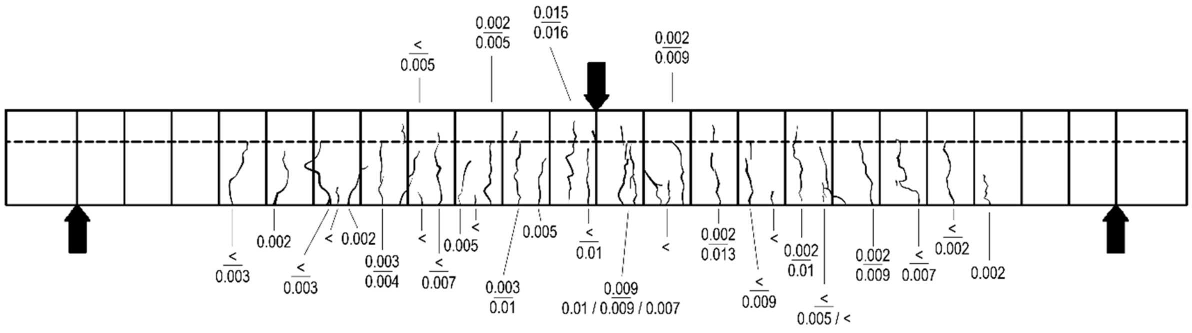

(c) $0.75P_y$

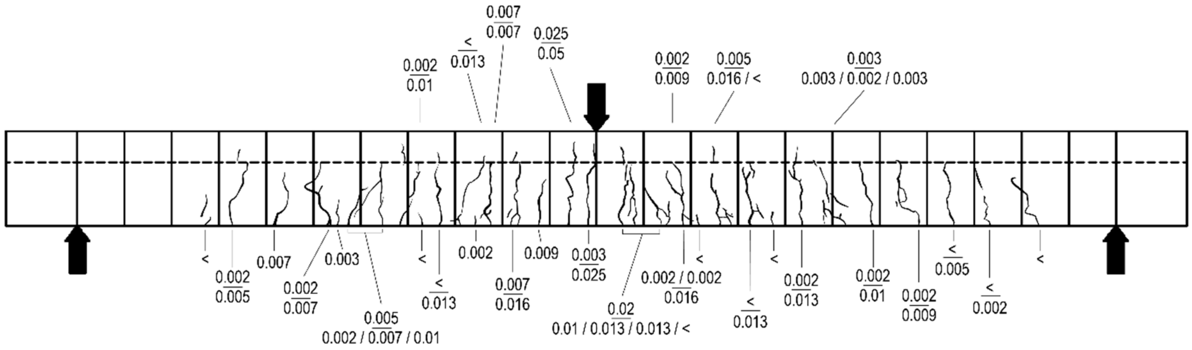

(d) Δ_y, P_y

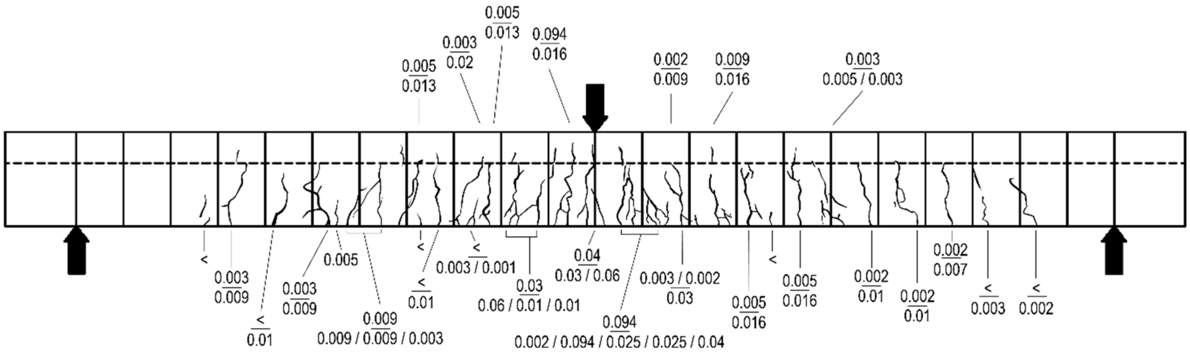

(e) $2\Delta_y$

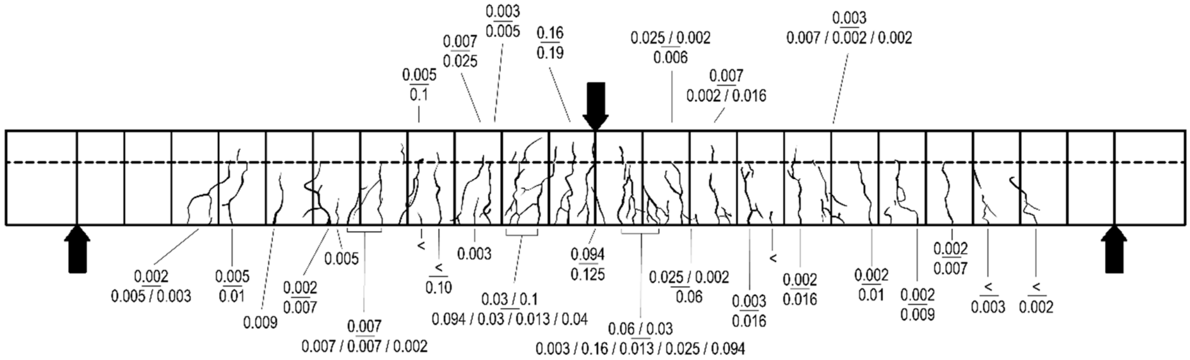

(f) $3\Delta_y$

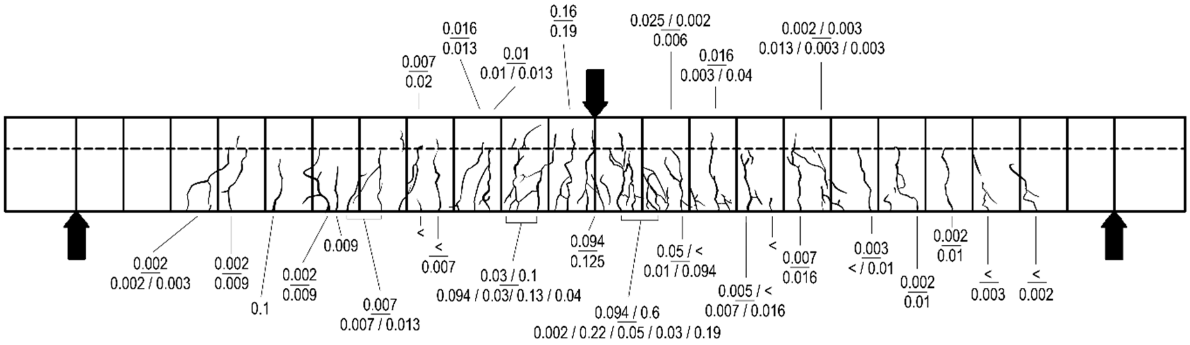

(g) $4\Delta_y$

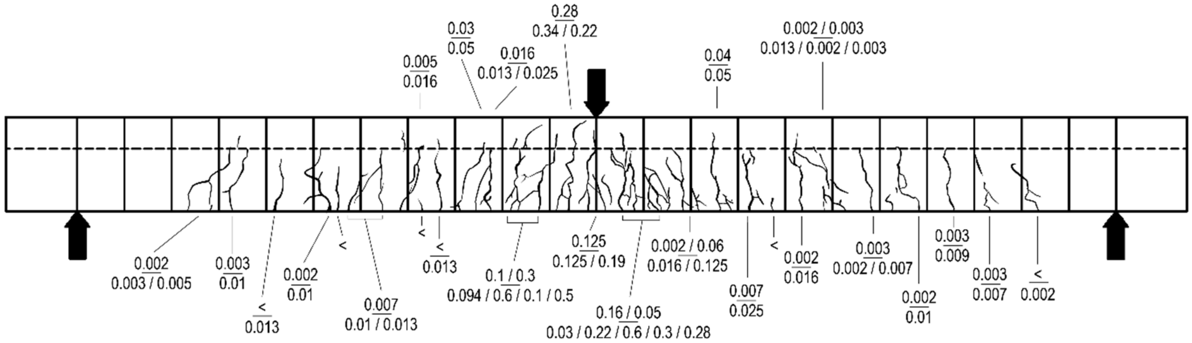

(h) $5\Delta_y$

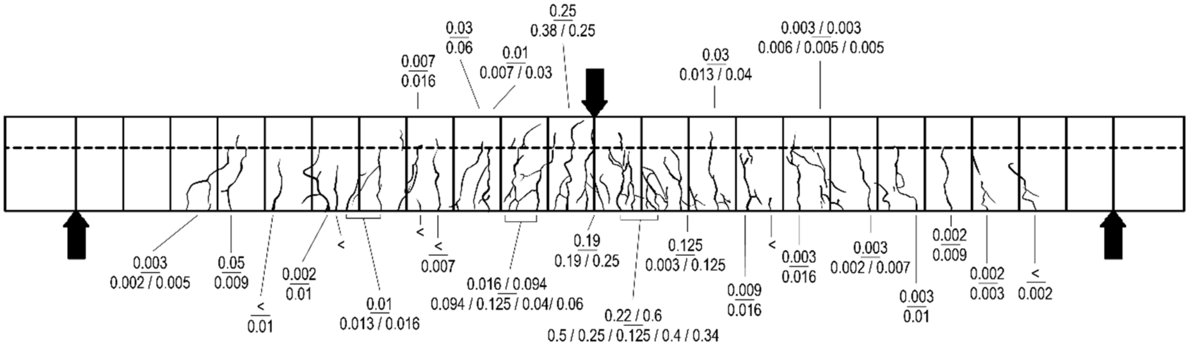

(i) $6\Delta_y$

Figure B.1.5: 1GBH100 crack patterns

B.1.3. Beam Photos

Photographs of beam faces at all load stops are shown below. The figure sub-caption indicates the midspan applied load and/or midspan measured deflection.

(a) $0.25P_y$

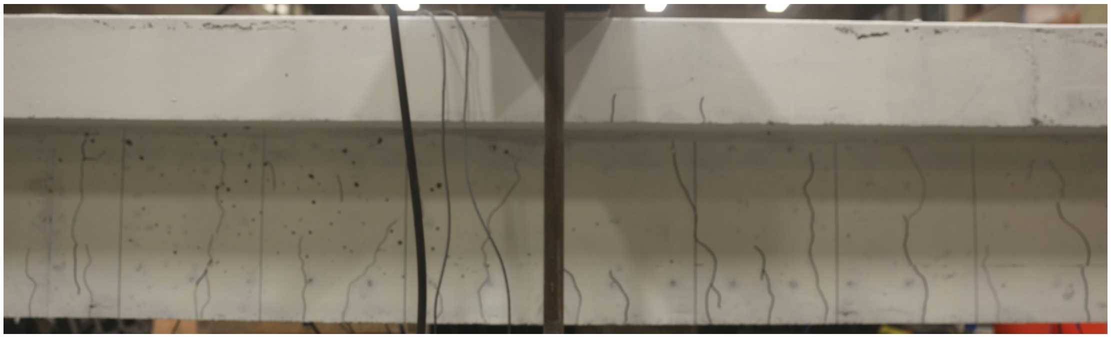

(b) $0.50P_y$

(c) $0.75P_y$

(d) Δ_y, P_y

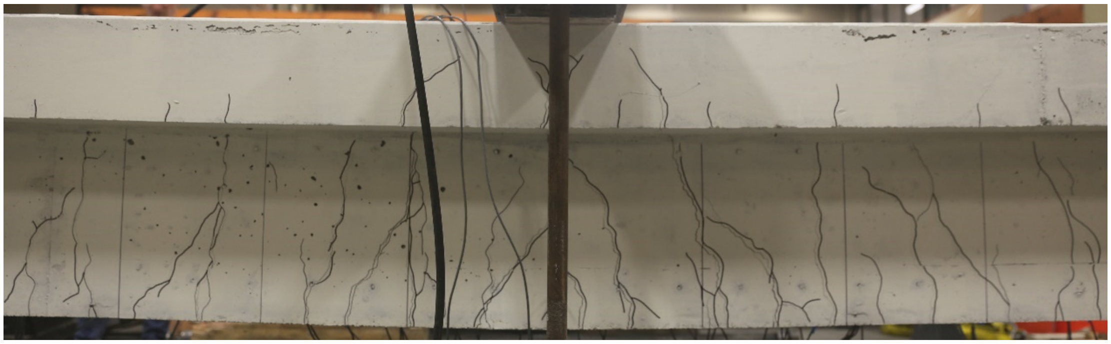

(e) $2\Delta_y$

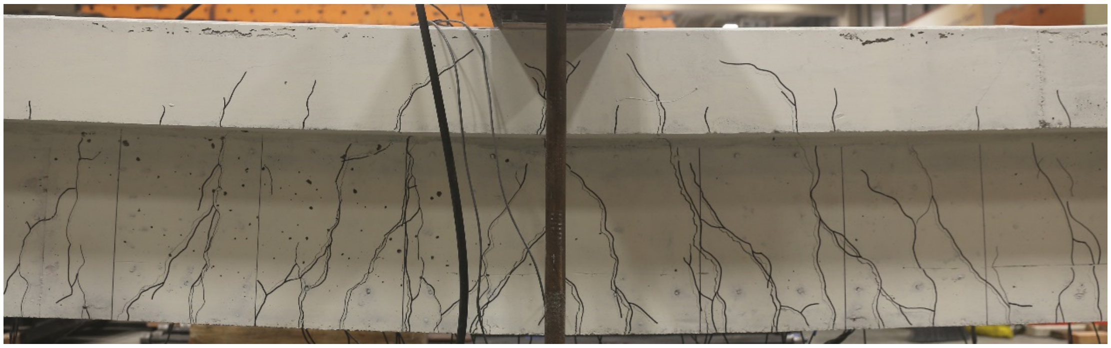

(f) $3\Delta_y$

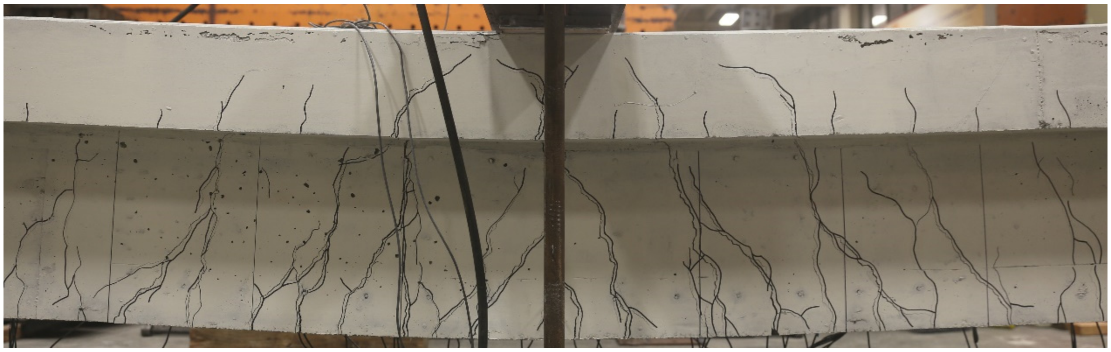

(g) $4\Delta_y$

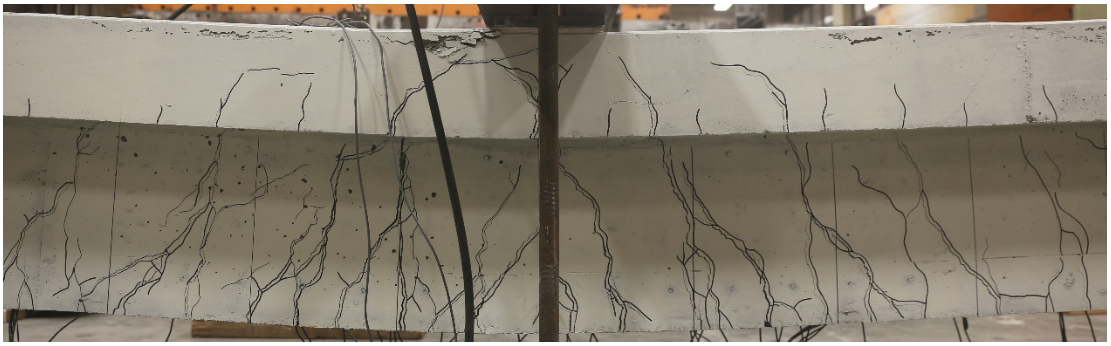

(h) $5\Delta_y$

(i) $6\Delta_y$

(j) $7\Delta_y$

Figure B.1.6: 1GBH60 photos

(a) $0.25P_y$

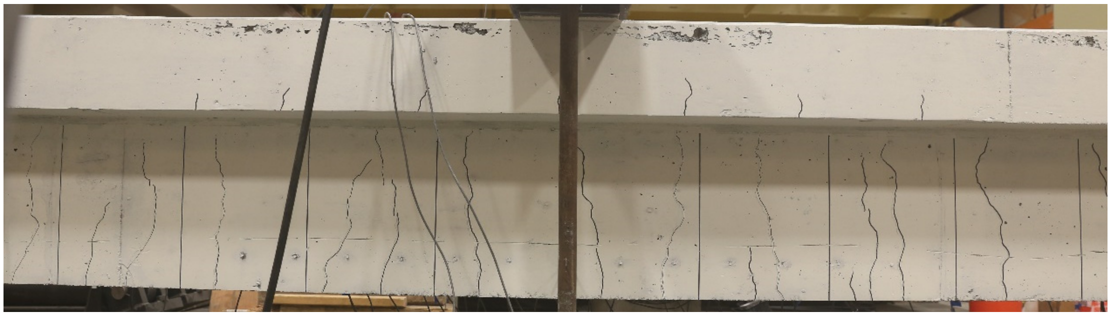

(b) $0.50P_y$

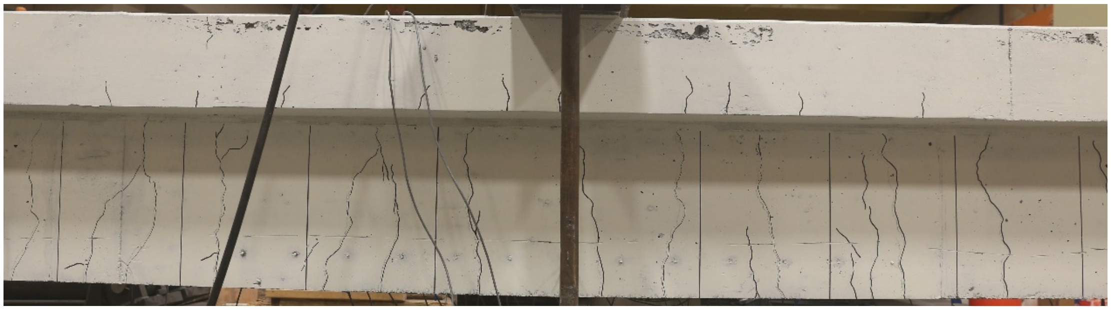

(c) $0.75P_y$

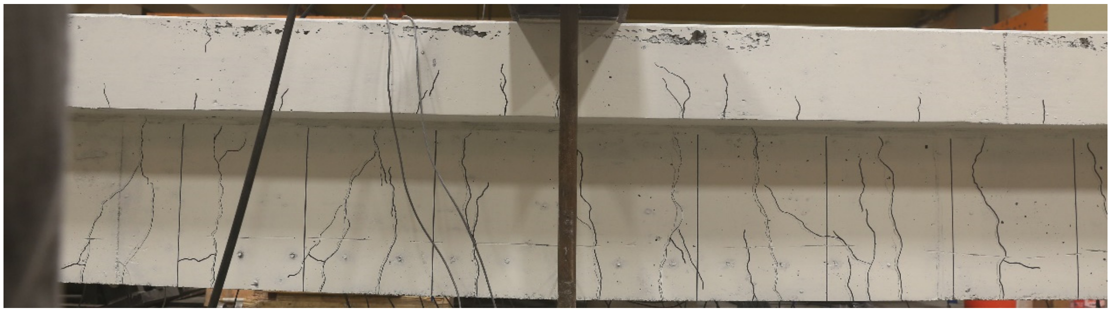

(d) Δ_y, P_y

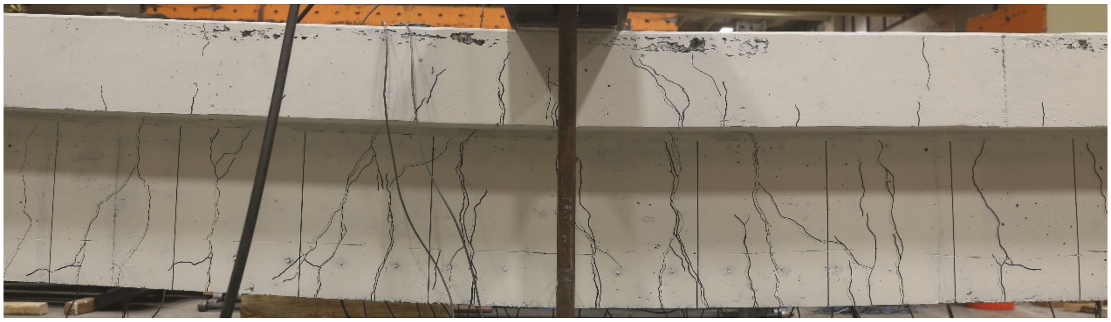

(e) $2\Delta_y$

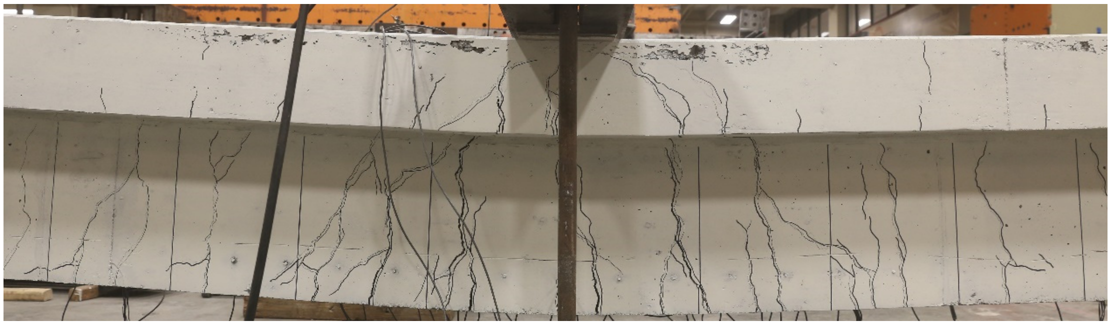

(f) $3\Delta_y$

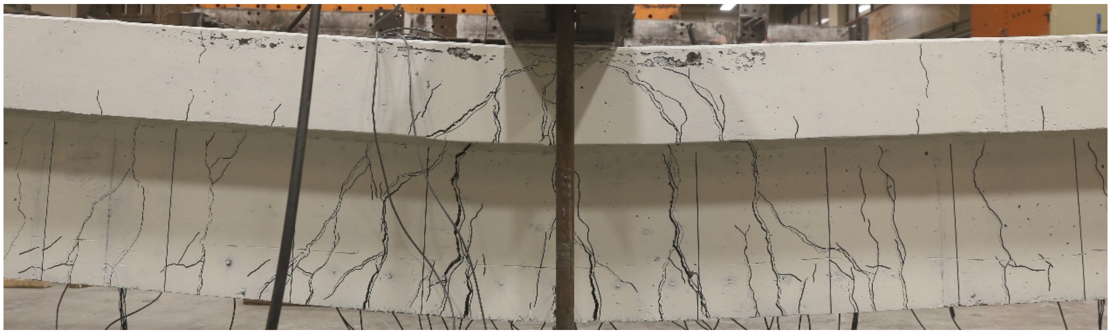

(g) $4\Delta_y$

(h) Failure

Figure B.1.7: 1GBL100 photos

(a) $0.25P_y$

(b) $0.50P_y$

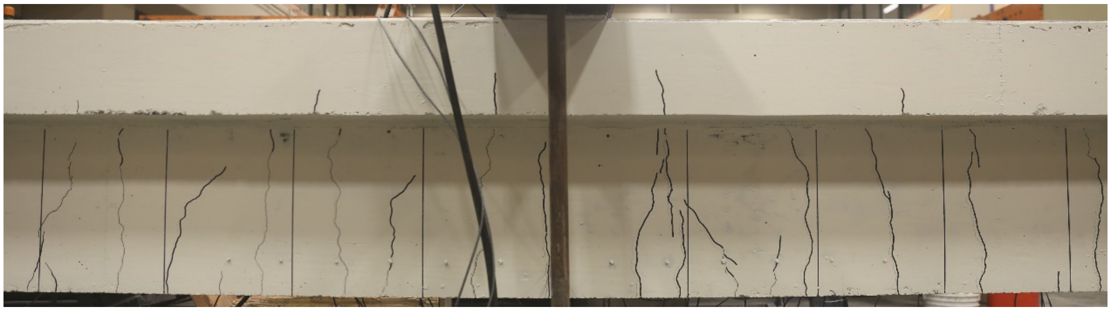

(c) $0.75P_y$

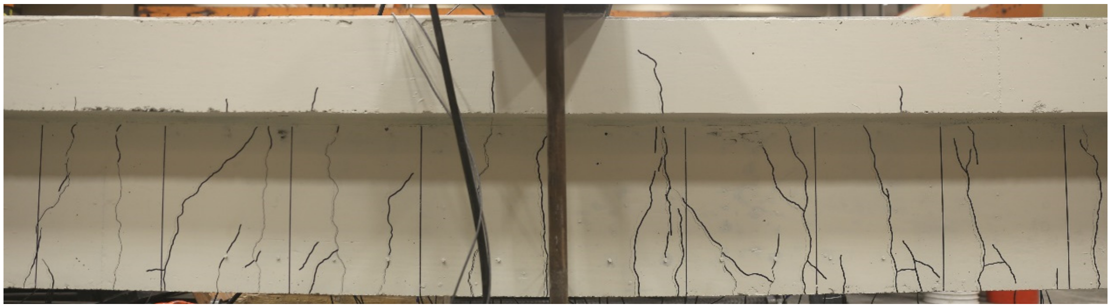

(d) Δ_y, P_y

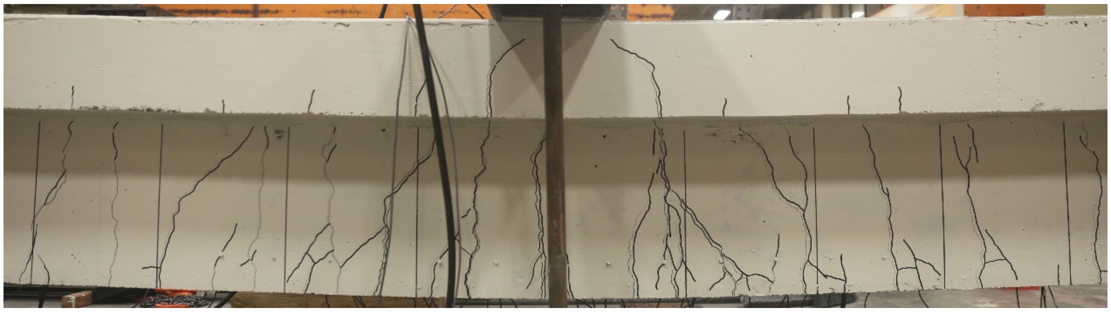

(e) $2\Delta_y$

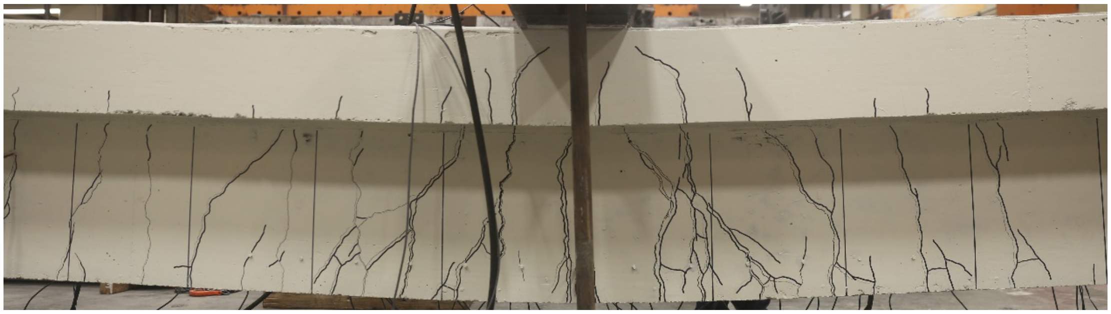

(f) $3\Delta_y$

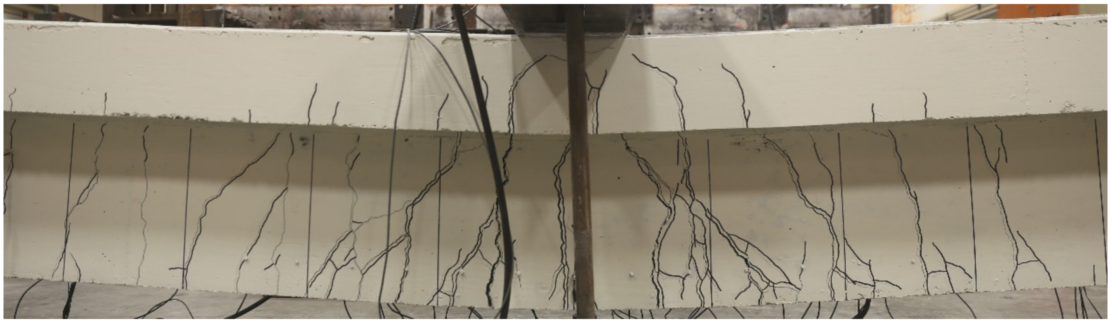

(g) $4\Delta_y$

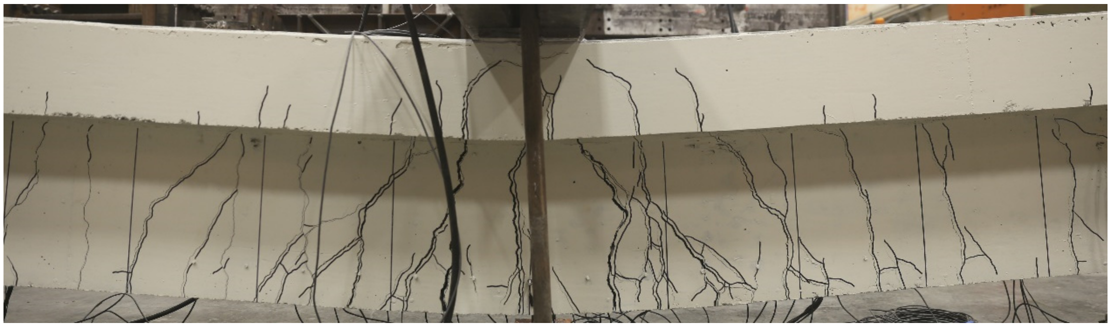

(h) $5\Delta_y$

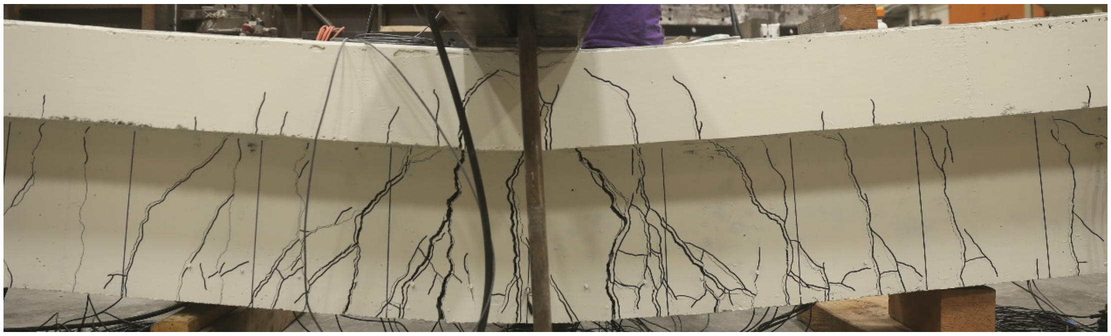

(i) $6\Delta_y$

Figure B.1.8: 1GBH100 photos

B.2. Series 2

B.2.1. Load-Deflection

Figure B.2.1 presents the measured relations between concentrated load applied at midspan and measured vertical displacement at midspan.

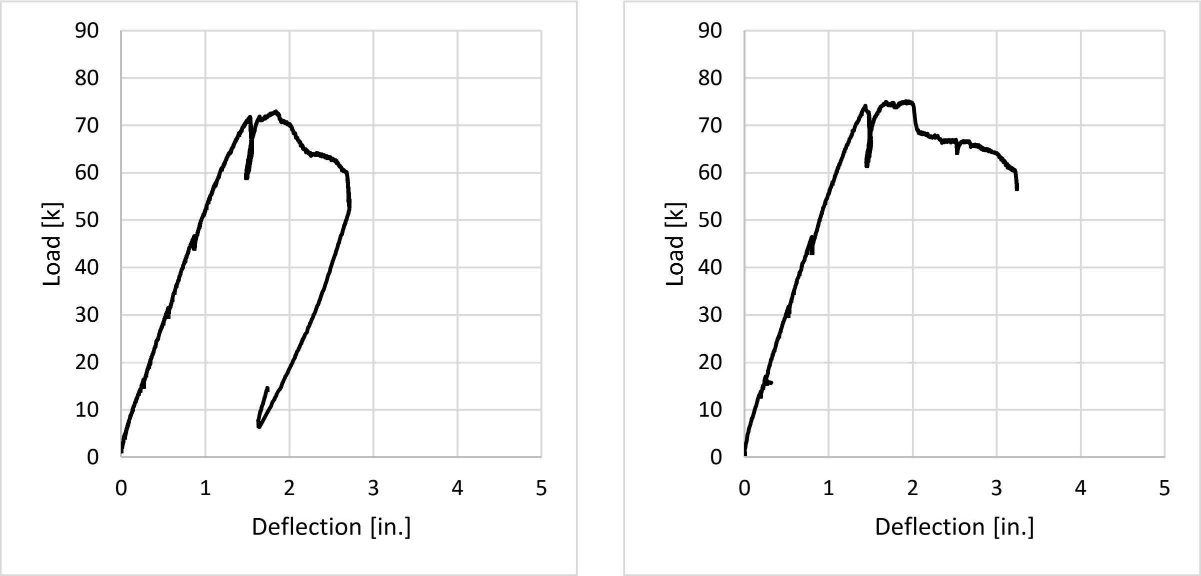

(a) 2GBL60 (b) 2GBH60

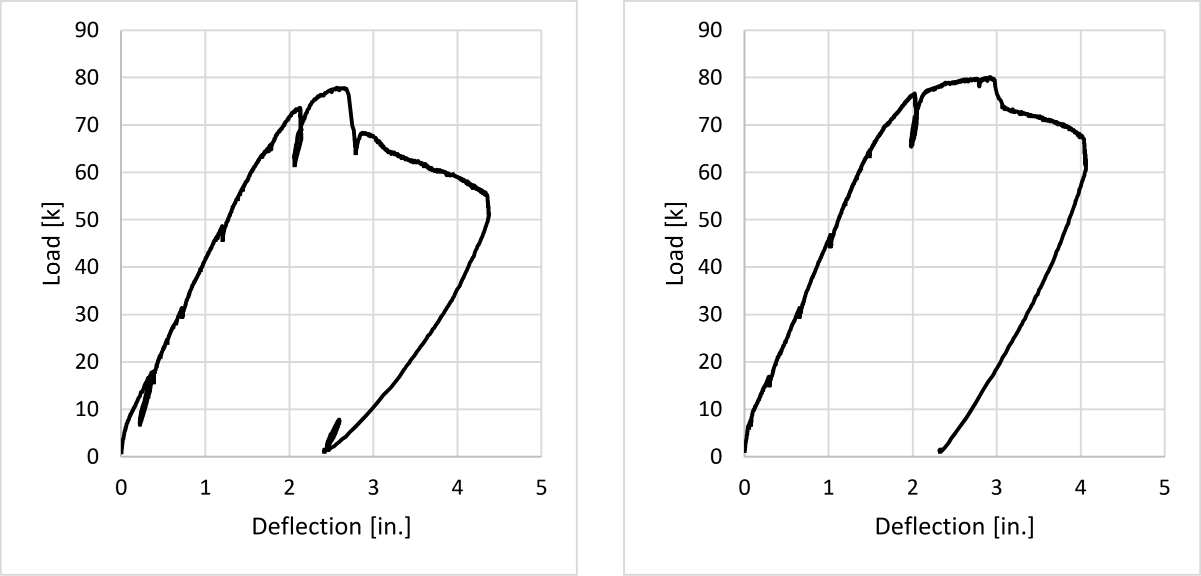

(c) 2GBL100 (d) 2GBH100

Figure B.2.1: Series 2 load-deflection relations

B.2.2. Crack Patterns

Crack patterns were recorded at various points during each test. The drawings below show the recorded crack patterns. The figure sub-caption indicates the midspan applied load and/or midspan measured deflection. Reported top values are crack widths at the mid-height of the beam. Bottom values are crack widths at the beam bottom. If only one value is shown, it is the width at the bottom. The “<” symbol denotes a crack that was visible, but less than 0.002-in. wide (the smallest width that could be measured). All measurements are reported in inches.

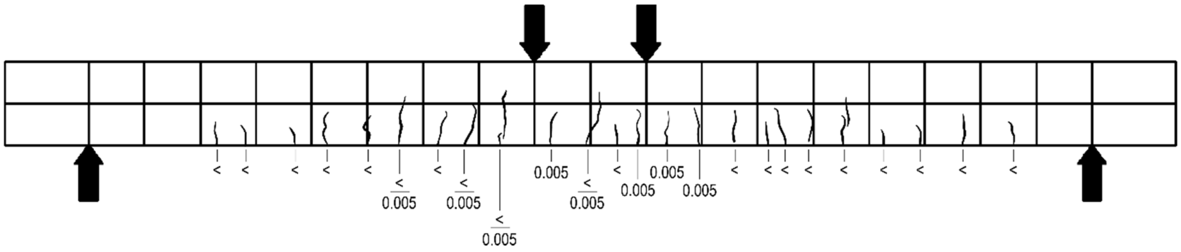

(a) $0.25P_y$

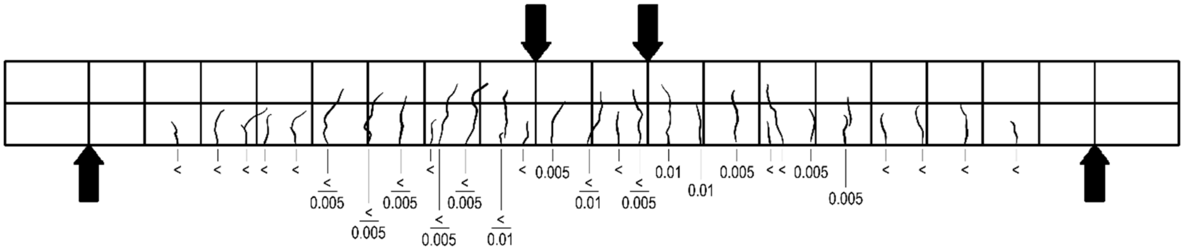

(b) $0.50P_y$

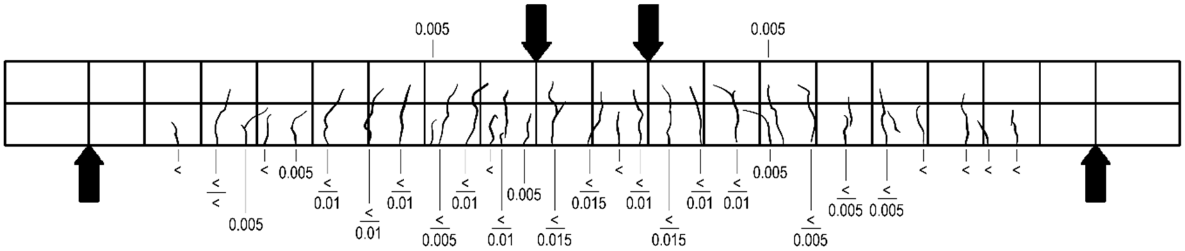

(c) $0.75P_y$

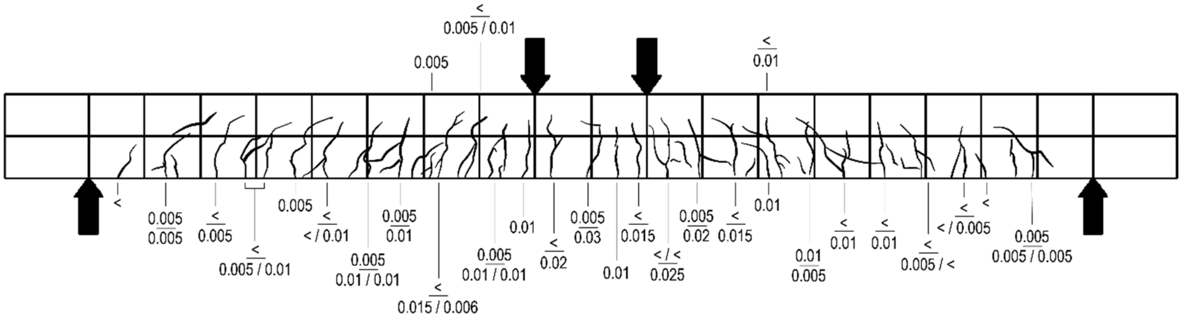

(d) Δ_y, P_y

Figure B.2.2: 2GBL60 crack patterns

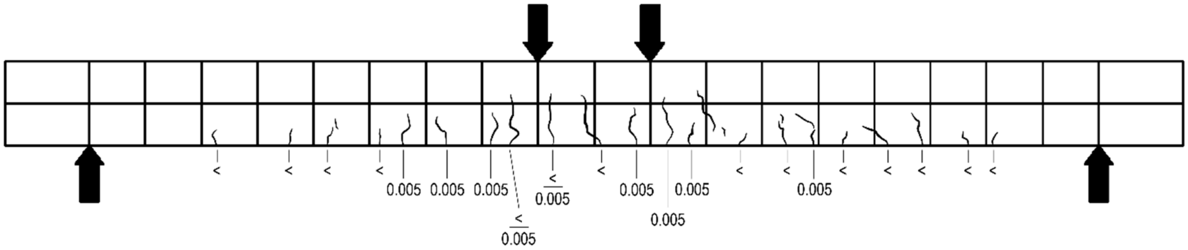

(a) $0.25P_y$

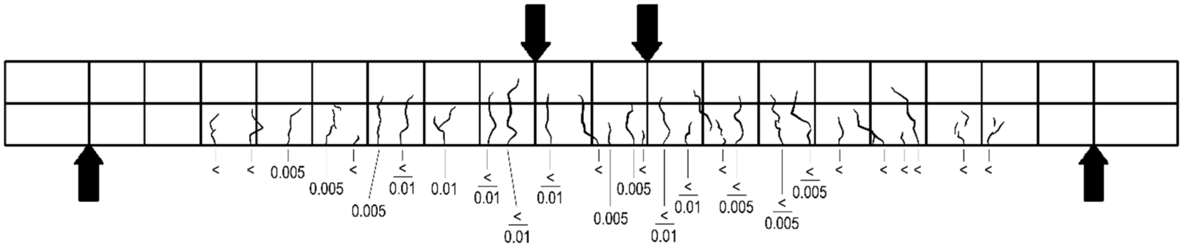

(b) $0.50P_y$

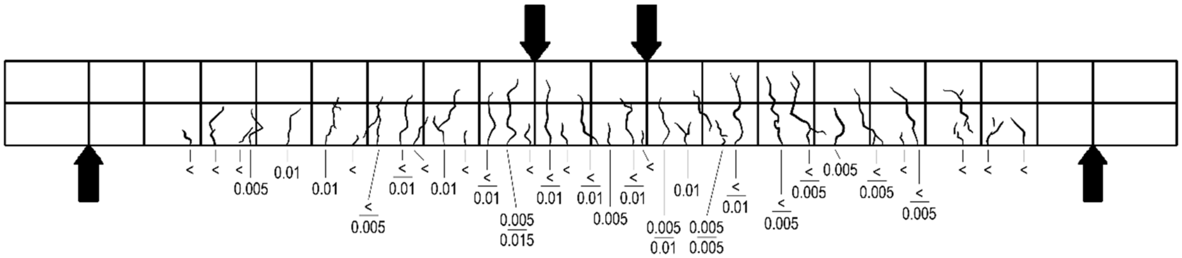

(c) $0.75P_y$

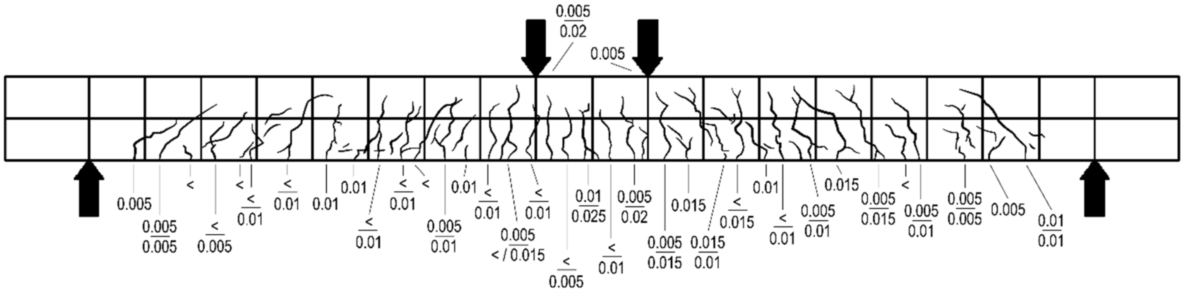

(d) Δ_y, P_y

Figure B.2.3: 2GBH60 crack patterns

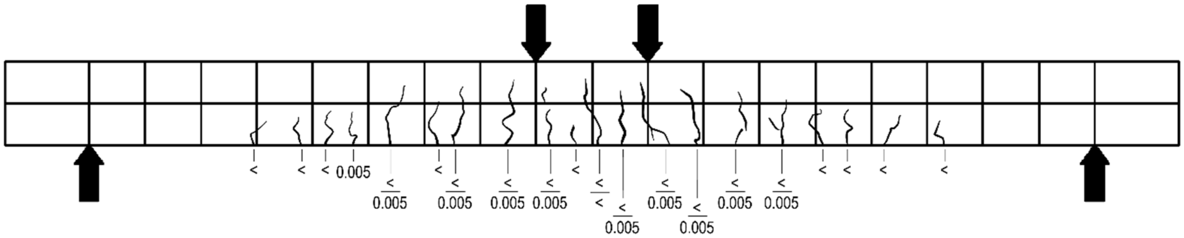

(a) $0.25P_y$

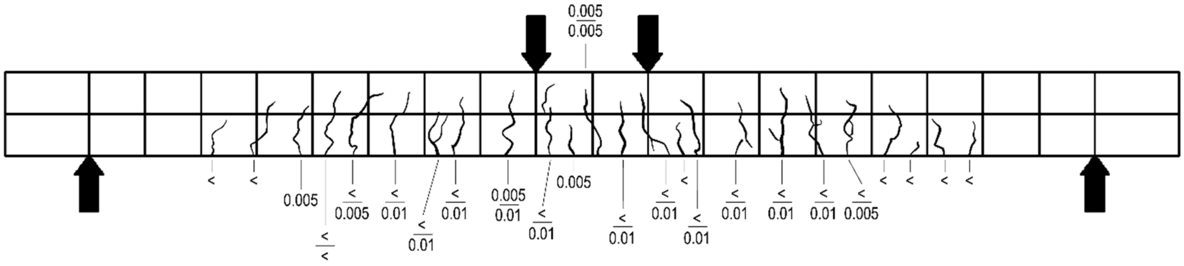

(b) $0.50P_y$

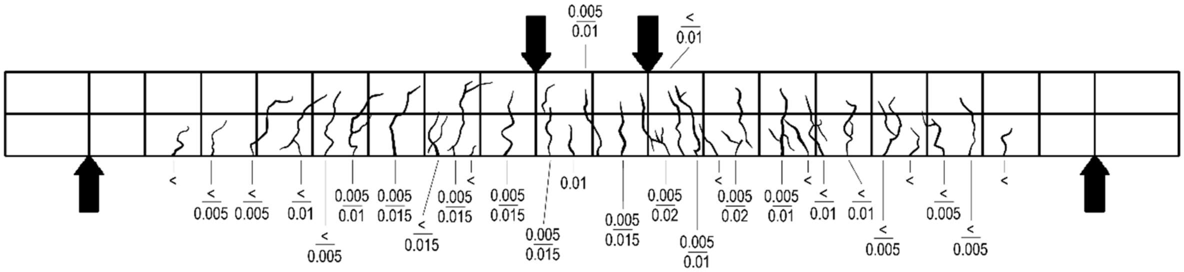

(c) $0.75P_y$

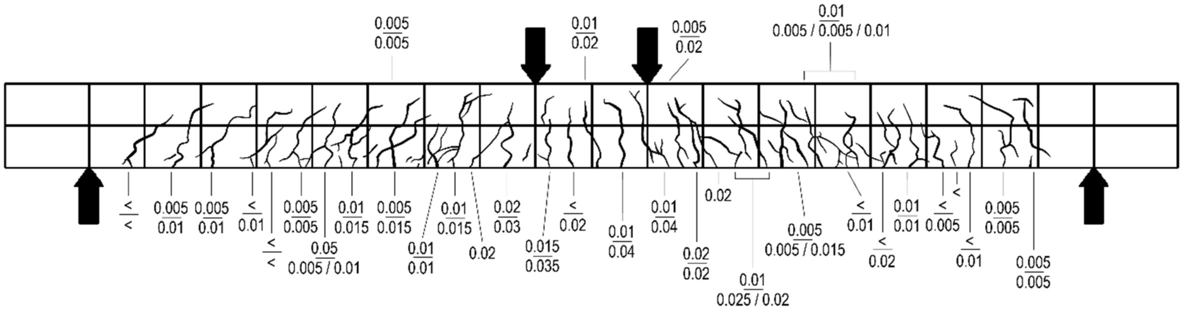

(d) Δ_y, P_y

Figure B.2.4: 2GBL100 crack patterns

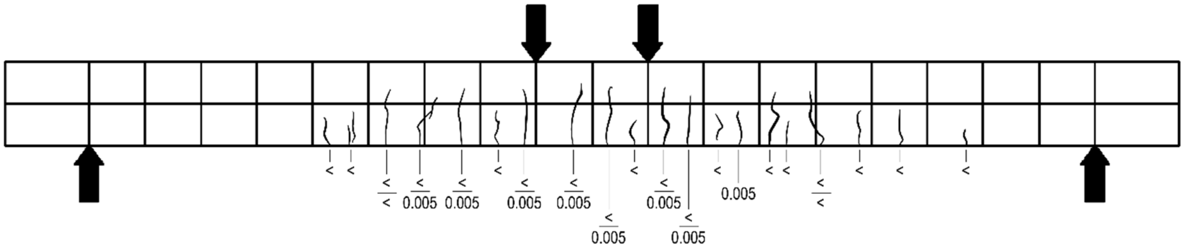

(a) $0.25P_y$

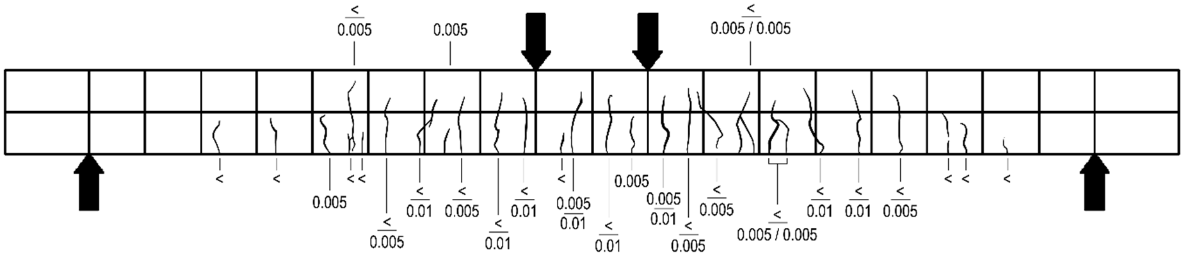

(b) $0.50P_y$

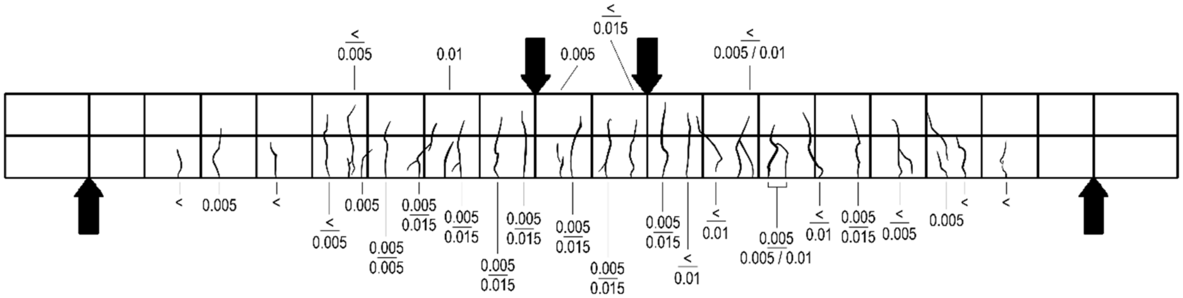

(c) $0.75P_y$

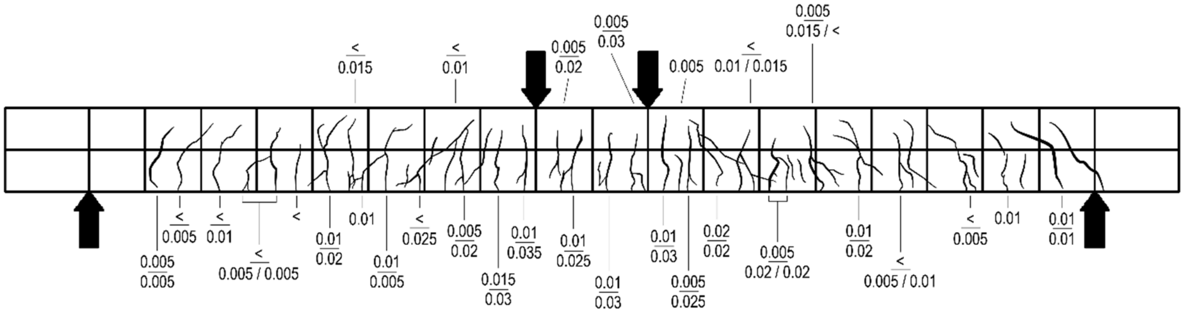

(d) Δ_y, P_y

Figure B.2.5: 2GBH100 crack patterns

B.2.3. Beam Photos

Photographs of beam faces at all load stops are shown below. The figure sub-caption indicates the midspan applied load and/or midspan measured deflection.

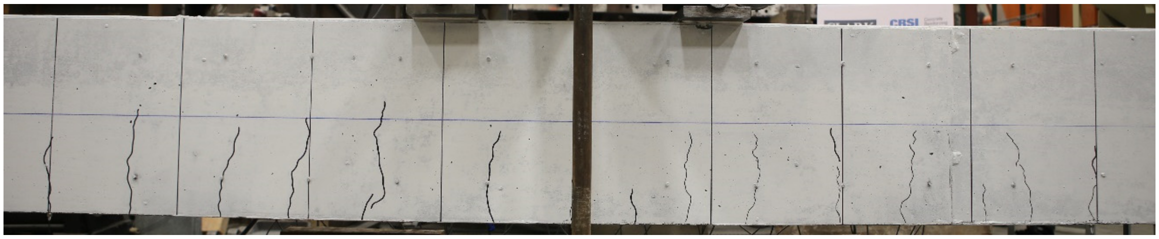

(a) $0.25P_y$

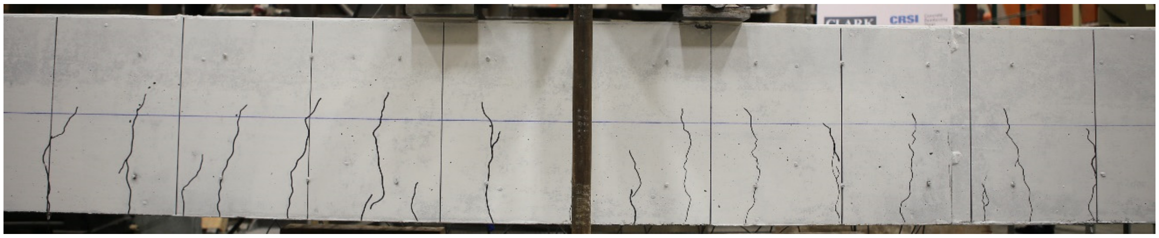

(b) $0.50P_y$

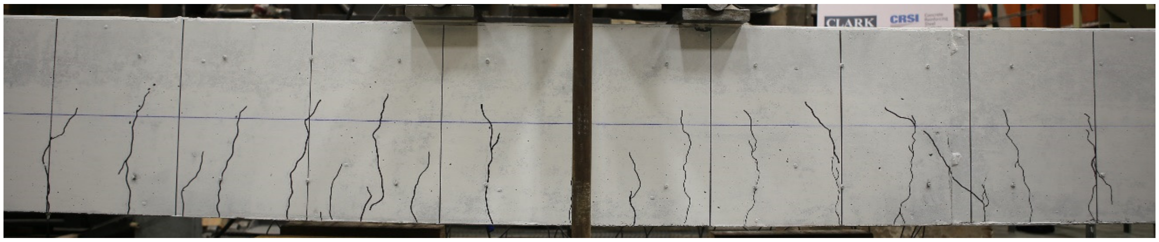

(c) $0.75P_y$

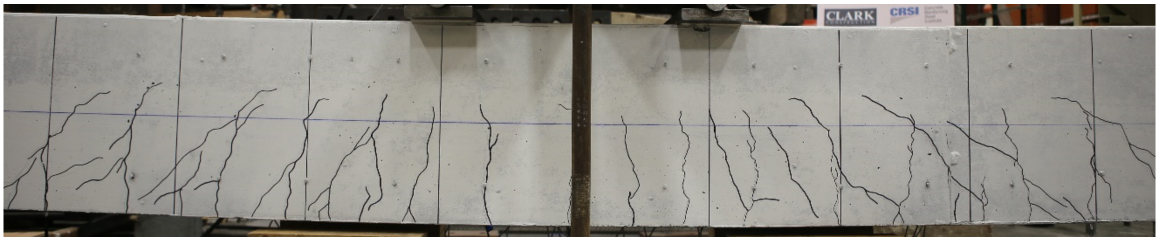

(d) Δ_y, P_y

Figure B.2.6: 2GBL60 photos

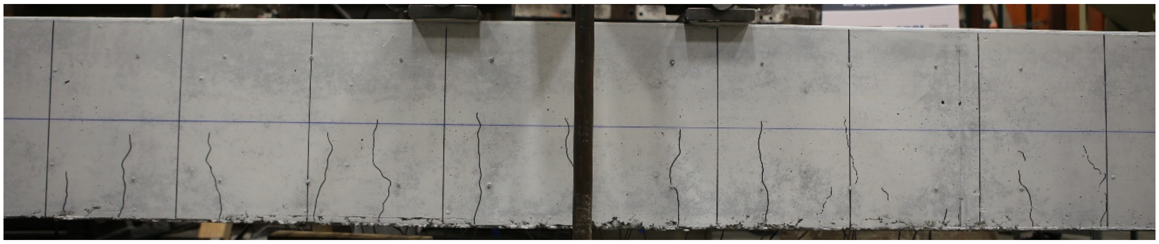

(a) $0.25P_y$

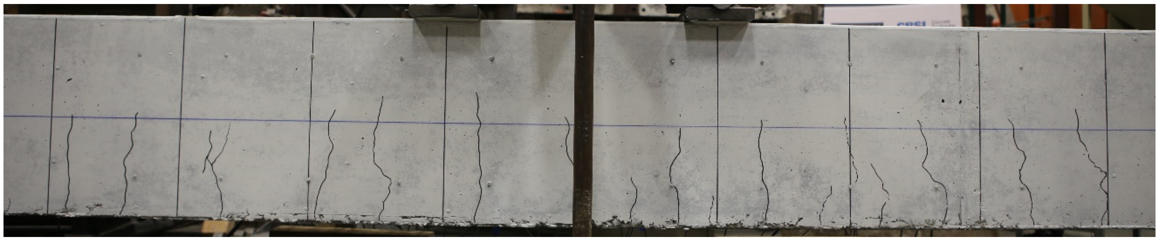

(b) $0.50P_y$

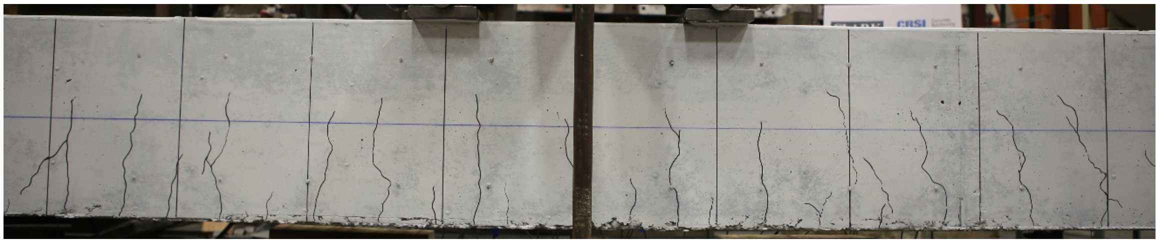

(c) $0.75P_y$

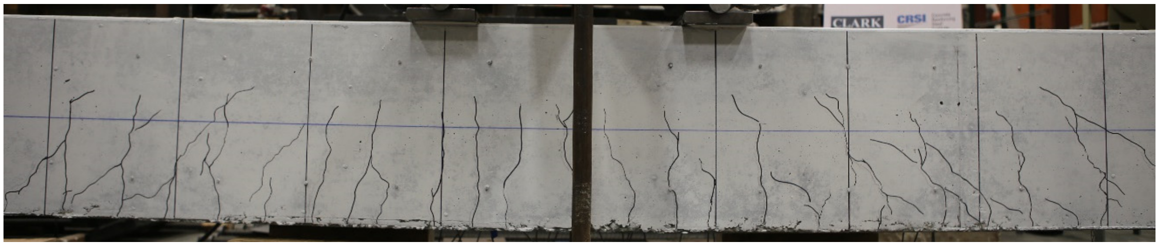

(d) Δ_y, P_y

Figure B.2.7: 2GBH60 photos

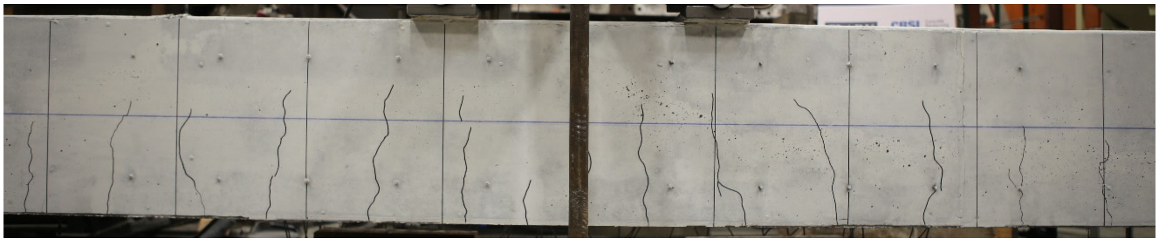

(a) $0.25P_y$

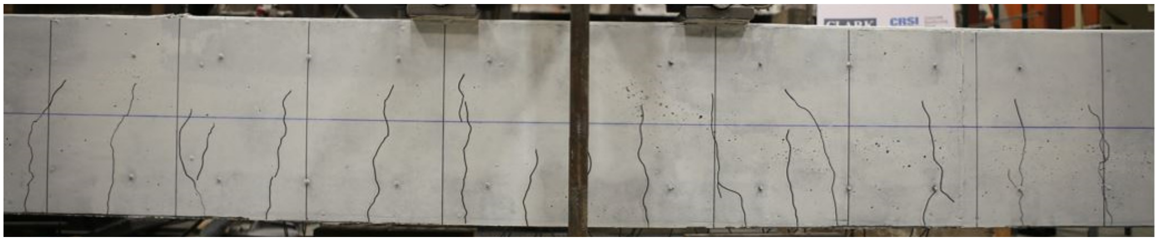

(b) $0.50P_y$

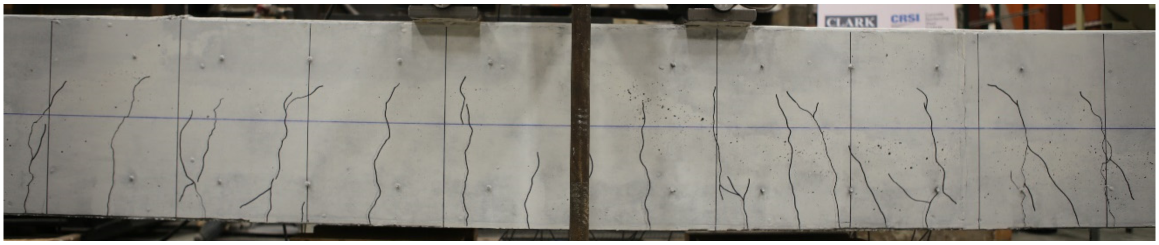

(c) $0.75P_y$

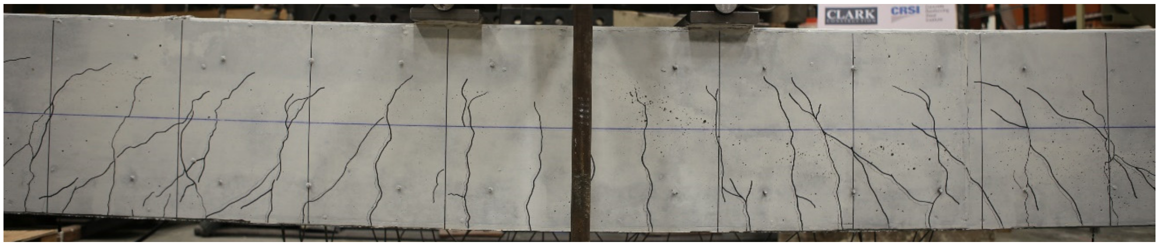

(d) Δ_y, P_y

Figure B.2.8: 2GBL100 photos

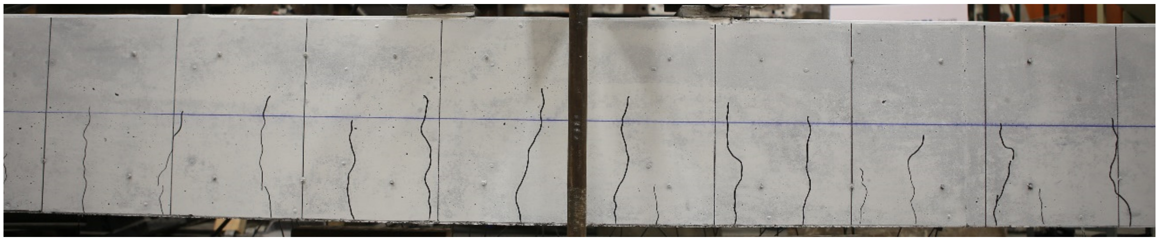

(a) $0.25P_y$

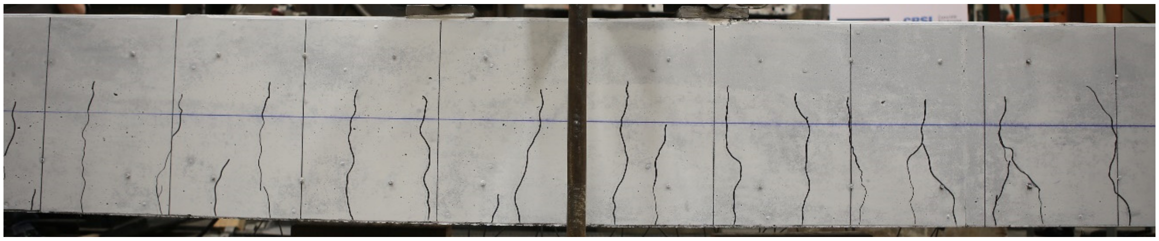

(b) $0.50P_y$

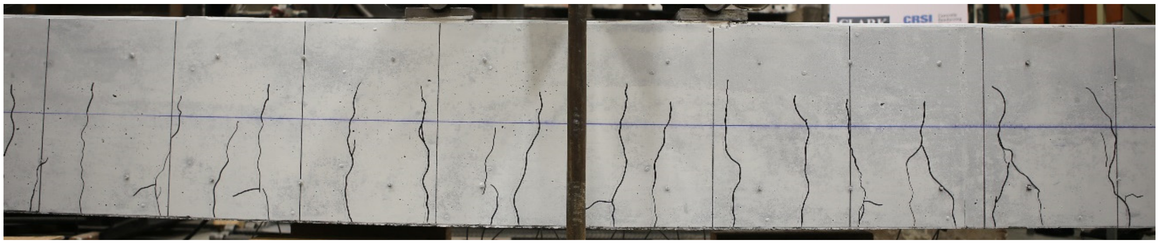

(c) $0.75P_y$

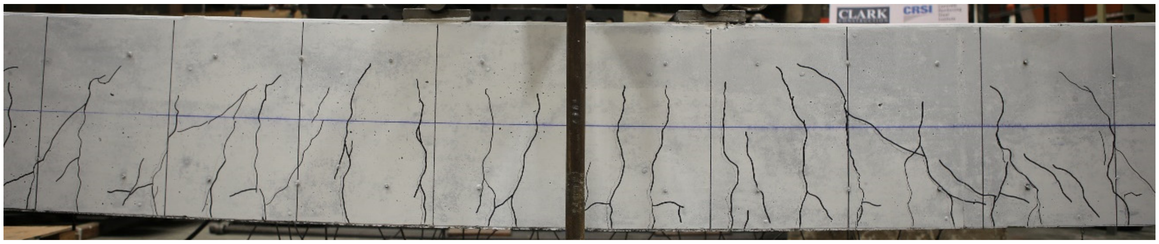

(d) Δ_y, P_y

Figure B.2.9: 2GBH100 photos

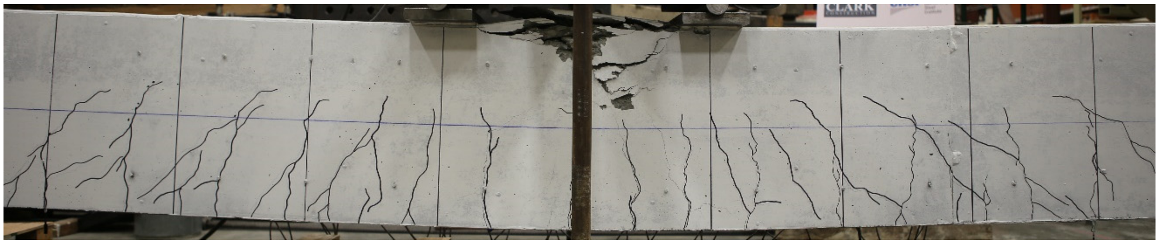

(a) 2GBL60

(b) 2GBH60

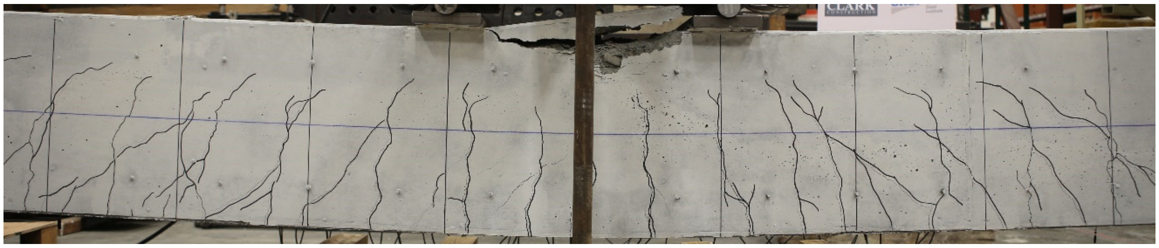

(c) 2GBL100

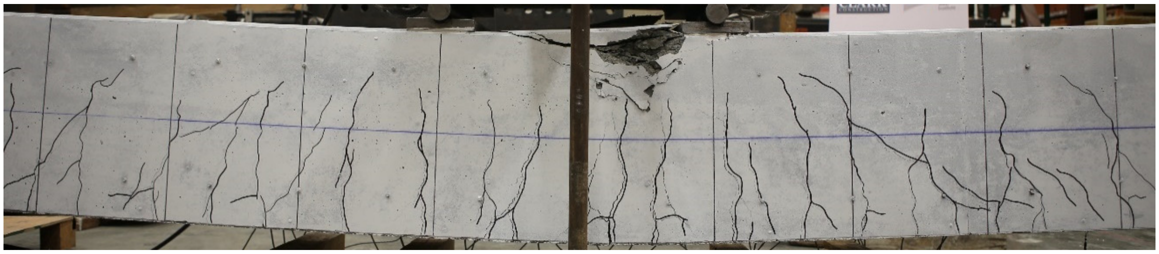

(d) 2GBH100

Figure B.2.10: Beam photos at failure

Appendix C

C.1. Numerical Modeling

Finite-element models were built in GiD (2019) and analyzed using ATENA (2019). GiD allows construction of models using a graphical user interface but does not analysis itself. Therefore, only information related to ATENA will be discussed in the following sections.

C.1.1. Background

All documentation, including a much more exhaustive description of the methods used in ATENA can be found in the program theory (ATENA, 2018). However, a basic description will be provided here.

All derivations and solution procedures in ATENA are based on the deformational form of the finite-element method and make use of the updated Lagrangian formulation, where the model configuration is updated after each step and incremented from there. Strain smoothing is employed to translate between the continuous displacement field and discontinuous stress and strain field for materials. This smoothing is conducted using the techniques described by Červenka et al. (1993). All end restraints as well as master-slave conditions were boundary conditions of Dirchilet types. Material matrices are derived using the nonlinear elastic approach, as described by Chen (1994). Additional details related to this process can be found in Zienkiewicz and Taylor (1989).

The ascending portion of the concrete stress-strain relationship used the relationship provided in CEB-FIP Model Code 90. After peak stress, concrete followed the constitutive model proposed by van Mier (1986) where the end point of the softening curve is defined by means of a plastic displacement which is then related to the limit compressive strain. This formulation is intended to reduce dependency on element mesh size. The suggested default value of 0.2 in. was not used. Instead, it was assumed that the concrete crushed completely at a strain of 0.005 over a length of 6 in. (consistent with observations in Series 2), which provided a slightly higher value of 0.3 in. To avoid dependence on mesh size, this displacement was modified to reflect a 6 in. crushing length by adjusting the crushing displacement by the number of elements that would fit in the 6-in. failure length. This way, the integral sum of displacements over adjacent elements would produce the observed failure mechanism. The results of Series 2 finite-element analyses, where limiting behavior was dictated by concrete in compression, indicate this modified technique effectively eliminated mesh dependence. Except where specified otherwise, concrete strength and modulus of elasticity were from the material-testing results given in Appendix A.3.1. Biaxial stress failure criterion according Kupfer et al. (1969) was employed to define the limiting behavior of concrete in three dimensions. After cracking, concrete compressive strength in the direction parallel to cracks was based on the relationship proposed by Kollegger and Melhorn (1988). Concrete behavior in shear uses the relationship established by Vecchio and Collins (1986). In tension, before cracking, concrete is assumed to behave linearly. After cracking in tension, behavior of concrete follows the exponential crack opening law defined by Hordijk (1991). Defaults in the program are those recommended by the source. Orientation of cracks was defined by the fixed crack model described by Červenka (1985) and Darwin (1974). Tension stiffening, which sets a lower bound for the tensile strength after cracking, was used to help with numerical stability in the model. The residual tensile strength was set to 0.25% of the strength in concrete in tension. Doing this resulted in models running to larger displacements with no discernable effect on global response. Ultimately, all of these material models were combined into a fracture-plastic model unique to ATENA. The full formulation of this model is provided in the program theory (ATENA, 2018)

Reinforcement behavior was modeled as multilinear with seven segments. Seven was the maximum number permitted by the software and did not include the portion of the relationship from zero load until yield. The first linear portion of the relationship incremented the steel stress-strain to the end of the yield plateau, adding 0.5 ksi along the yield plateau for numerical stability. The remaining strain capacity between the strain at the onset of strain hardening and the uniform elongation strain was divided into equal increments and matched to results of the material tests described in Appendix A.3.2. It was assumed the reinforcement behavior in compression and tension were equal. A smeared approach is used to model distributed reinforcement, which results in perfect bond between concrete and reinforcement.

For each nonlinear step, ATENA conducted Newton-Raphson iterations using PARDISO, a direct sparse solver from the Math Kernel Library provided by Intel with Intel Composer XE 2011. A new tangent-stiffness matrix was assembled for each iteration using the line-search method. More information related to the solver can be found at https://

pardiso-project.org/. For all models, the direct method with LU decomposition was employed. The displacement error, residual error, and absolute residual error were limited to 0.01. The energy error was limited to 0.0001. All error limits were the default values provided in ATENA. The maximum number of iterations was limited to 60. Reaching this number without keeping one of those errors less than their limiting value resulted in termination of the model run.

Where not specified, program defaults were used. Defaults can be found in the ATENA documentation (ATENA, 2018), the paper that provides the constitutive model for a given behavior, or FEB-CIP Model Code 90.

C.1.2. Series 1

All elements and their layout for an example model are depicted in Figure C.1.1. The bottom left longitudinal reinforcement has been divided in to 10-in. segments for monitoring, as described in Section 3.5.2. All longitudinal reinforcement ran from face-to-face of the model. Transverse reinforcement running laterally near the top of the beam was offset from the U-shaped stirrups by 3/8 in. to avoid creating a closed loop, replicating the conditions of the specimen as constructed. Dimensions and reinforcement locations were based on the as-built dimensions provided in Appendix A.1.2.1.

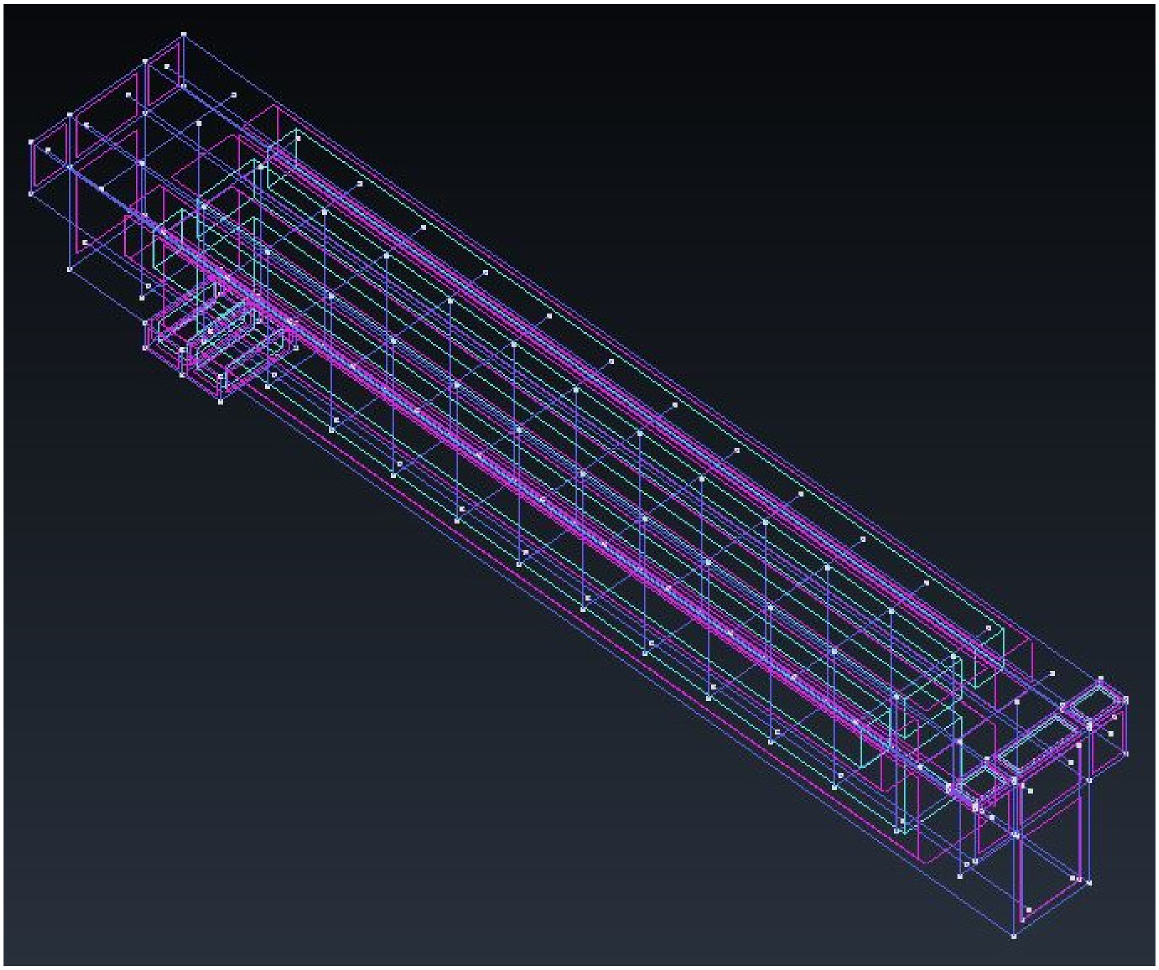

Figure C.1.1: Series 1 finite-element model layout (1GBH60)

Figure C.1.2 provides a sample mesh for a beam in Series 1. For the example given, the approximate mesh size is 3-in. square. The support plate is to the left of the image, the load plate is to the right, and the rightmost surface represents the centerline of the beam. The stirrup at the beam center can be seen on the face of the beam. Though not apparent in the image provided, reinforcement was meshed to have the same dimensions as the elements it ran through.

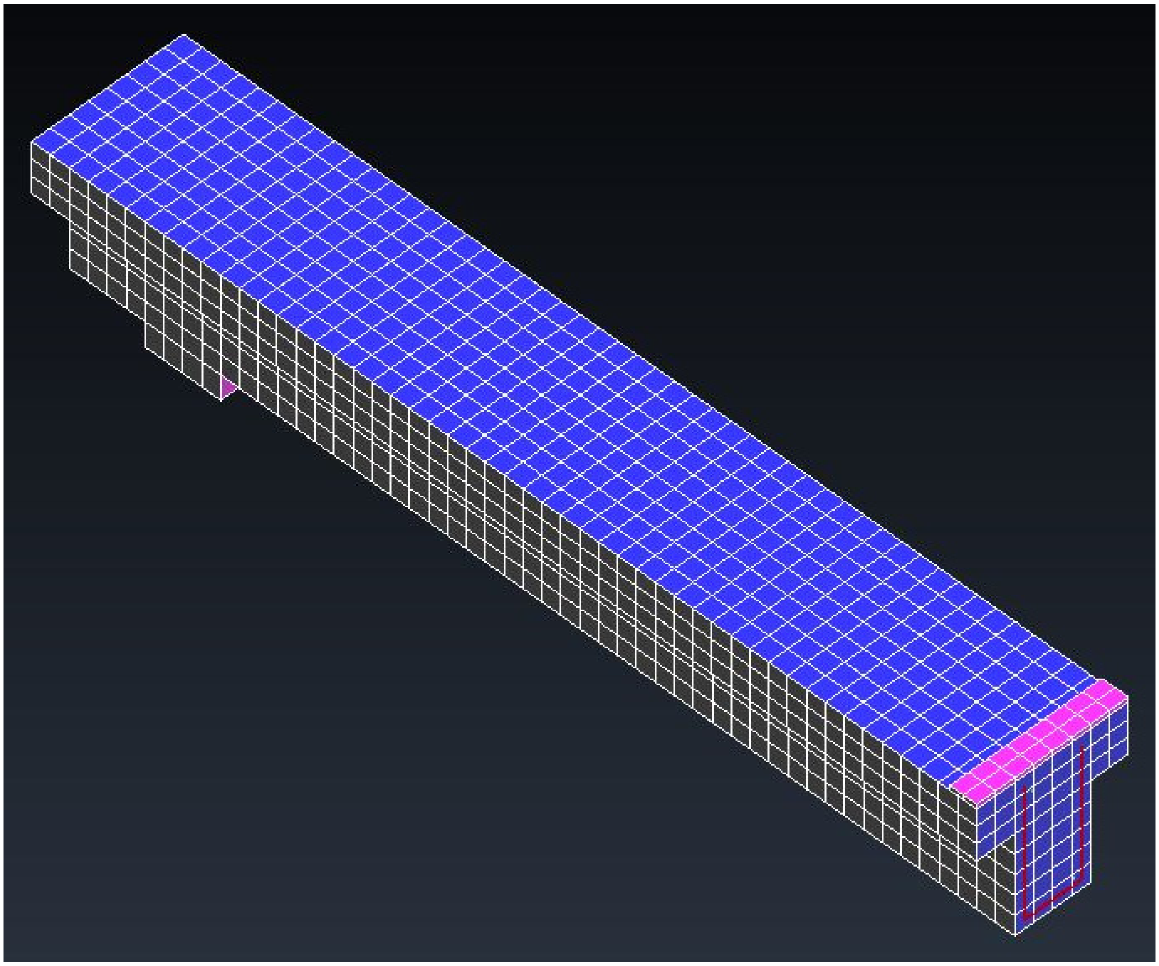

Figure C.1.2: Series 1 finite-element model mesh (1GBH60)

Boundary conditions for a representative model in Series 1 are shown in Figure C.1.3. In the physical test, the beam center displaced vertically while supports were allowed to move, so the beam could elongate without restraint. To enforce the conditions of the test, the bottom line of the support block was prevented from displacing laterally, and all surfaces and reinforcement end nodes at the beam centerline were constrained longitudinally. Additionally, the top edge of the load plates was constrained against vertical and lateral movement, while the bottom edge had only lateral movement arrested, so the beam could elongate over its height. To account for the effect of the load frame on the load plate, the top surface of the load plates was also constrained against vertical movement. Doing this prevented flexure in the load plate. These conditions forced symmetry about the beam centerline and with them in place, a displacement increment of 1/160 in. upward was imposed at the line in the center of beam support. As such, the incremental analysis of the model was displacement controlled.

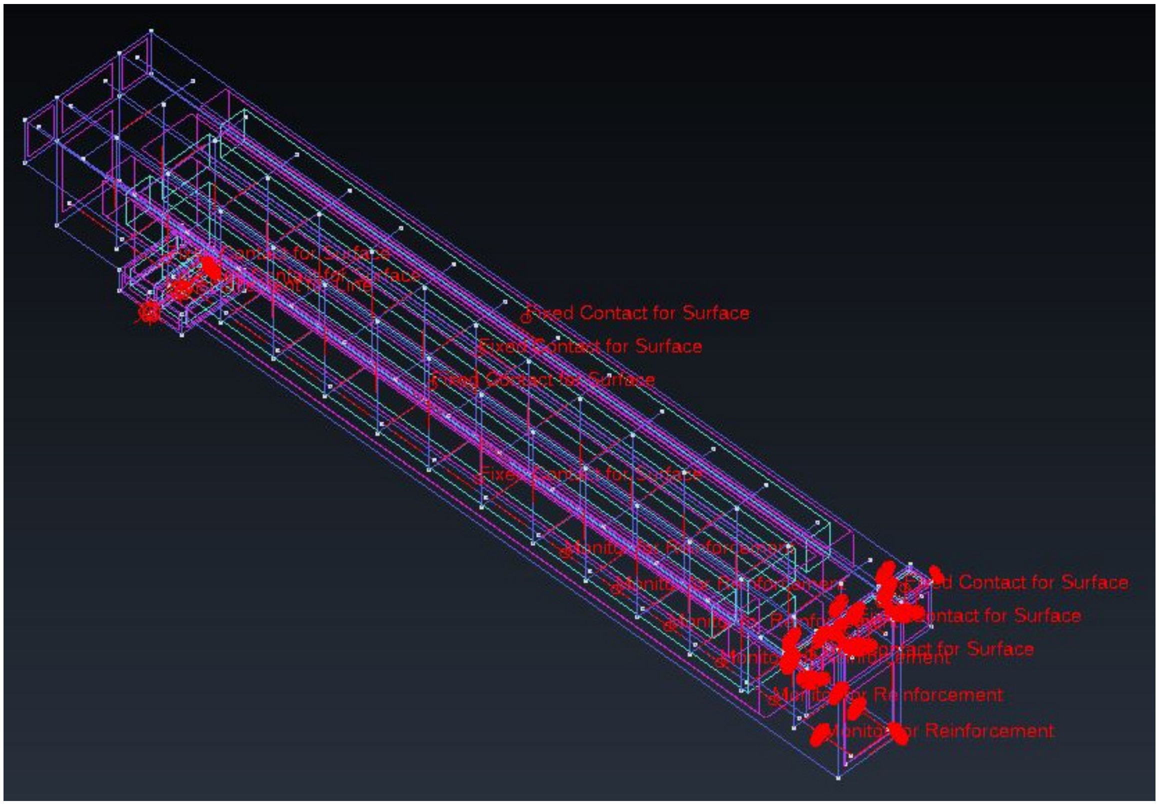

Figure C.1.3: Series 1 finite-element model boundary conditions (1GBH60)

Figure C.1.4, which is intended to serve a qualitative check on model behavior, gives a representative crack pattern and displaced shape for the example beam while being run in ATENA. The displaced shape of the beam looks as anticipated. Curvature is higher at the beam center (the point of maximum moment) and decreases closer to the support. At the beam center, where flexural forces are largest compared to shear stresses, cracks tend to be larger and are primarily vertical. Cracks appear slightly less wide at the level of the tensile longitudinal reinforcement. Consistent with expectations from moment-curvature analyses, vertical cracks extend into the flange, where the neutral axis is expected to lie. Some horizontal cracks are present at the beam's top in this same location due to the axial compressive forces causing transverse tension cracking. Moving away from the beam center, cracks to not extend as high from the bottom surface of the beam, and they become more inclined.

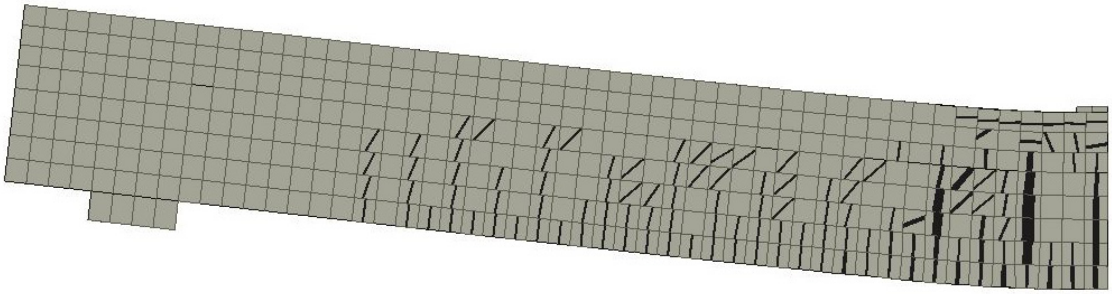

Figure C.1.4: Series 1 finite-element model during run (1GBH60)

C.1.3. Series 2

Figure C.1.5 displays an example of the finite-element model layout showing all elements present in a model as well as their location. Longitudinal reinforcement was modeled as running from centerline to end surface. Dimensions and reinforcement locations were based on the as-built dimensions provided in Appendix A.1.2.2.

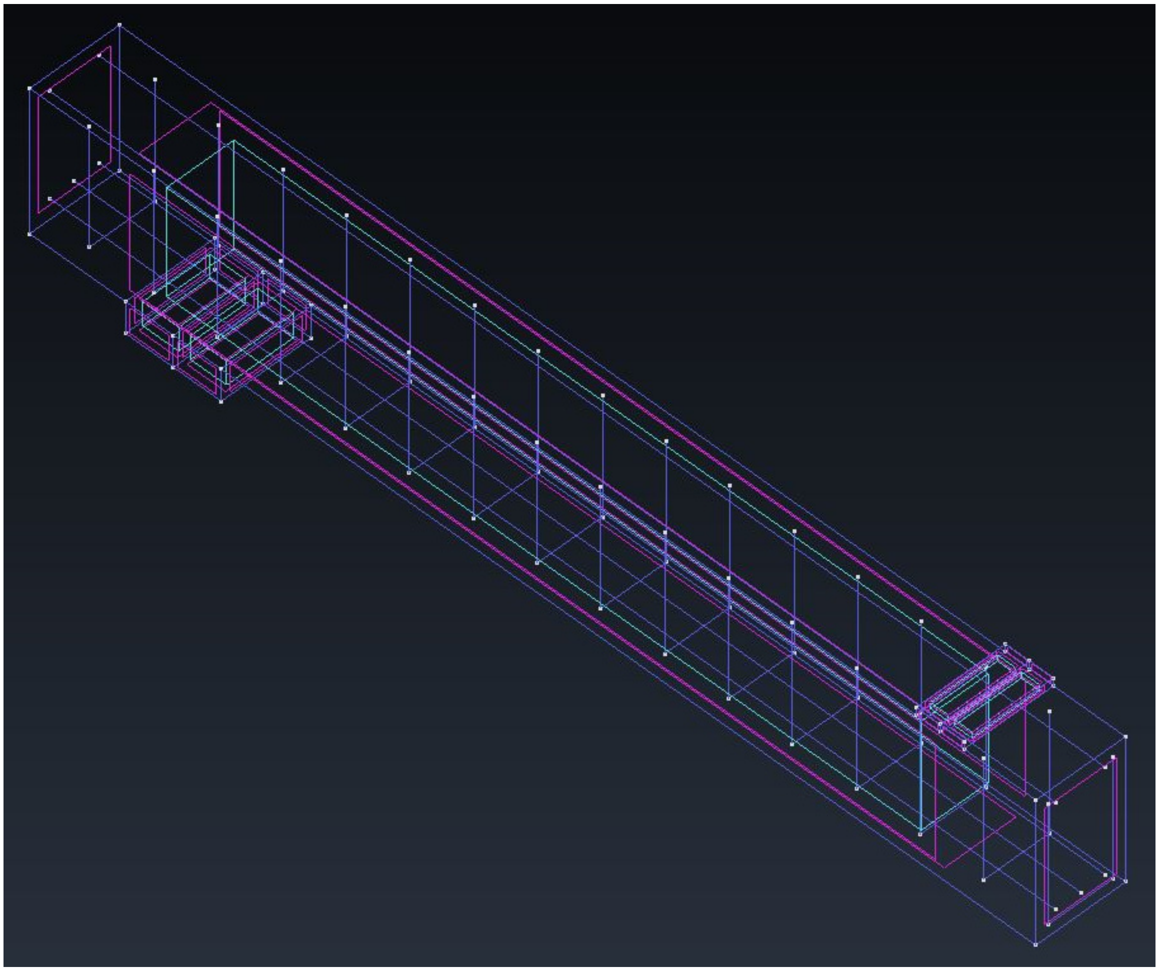

Figure C.1.5: Series 2 finite-element model layout (2GH60)

A representative model with its mesh displayed is shown in Figure C.1.6 for an approximate mesh size of 2 in. The beam surface to the right, where a stirrup can be seen, defines the centerline of the beam. The load plate is the plate closest to the centerline and the support plate is on the underside of the beam at its left end. Reinforcement was meshed to have the same length per segment as the elements it ran through.

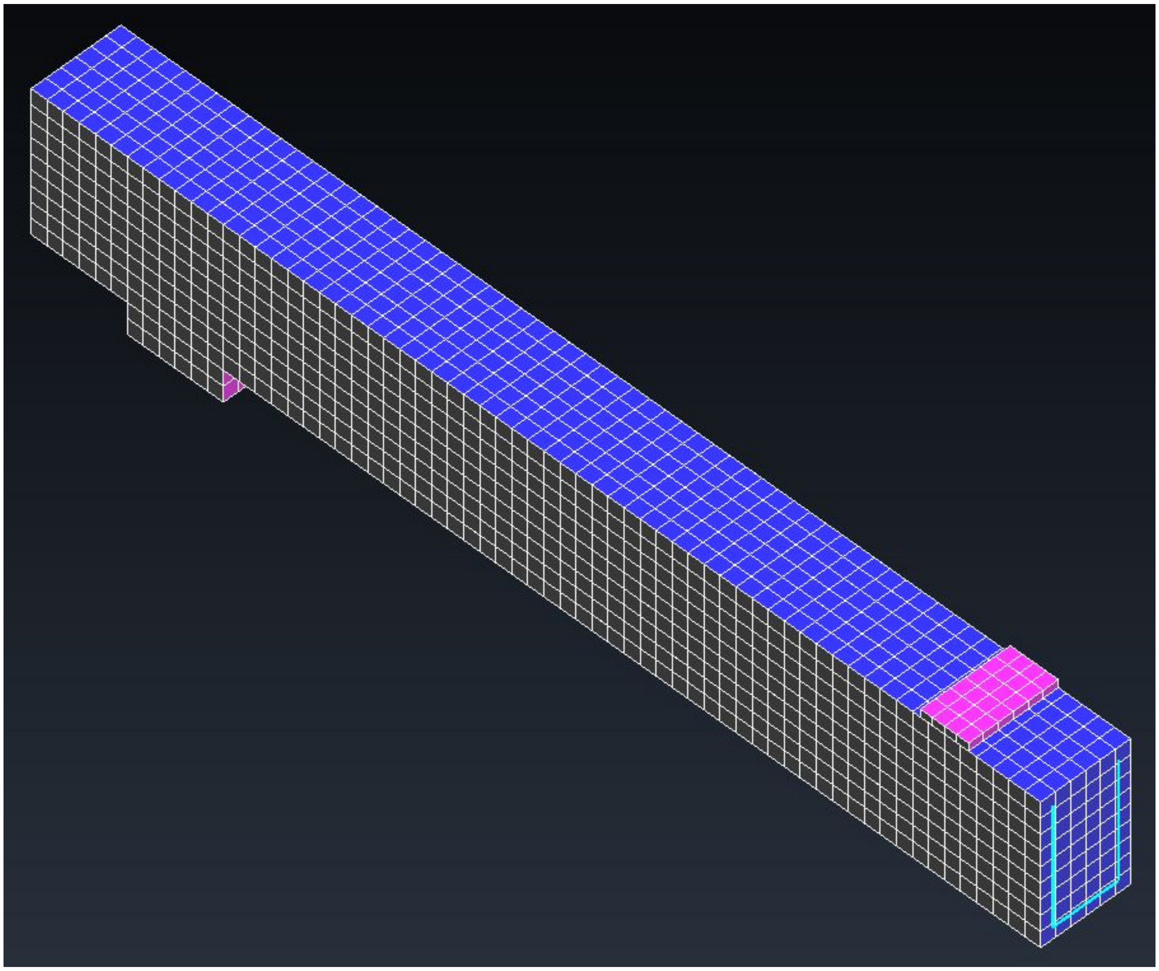

Figure C.1.6: Series 2 finite-element model mesh (2GBH60)

Figure C.1.7 shows the boundary conditions for a representative model in Series 2. Load locations were displaced while beam supports were held in place vertically but allowed to slide, so elongation would not be restrained during the physical test. To enforce these conditions in the model, lateral and vertical movement of the bottom line of the support block was arrested, while longitudinal movement of all reinforcement end nodes and surfaces at the beam centerline was restrained. The bottom edge of the centerline surface was fixed laterally to prevent out-of-plane movement. With these conditions in place, a displacement increment of 1/185 in. downward was imposed along the line at the center of the load plate, where a roller met the load plate in the physical test. These conditions forced symmetry about the beam centerline and the incremental analysis of the model was displacement controlled.

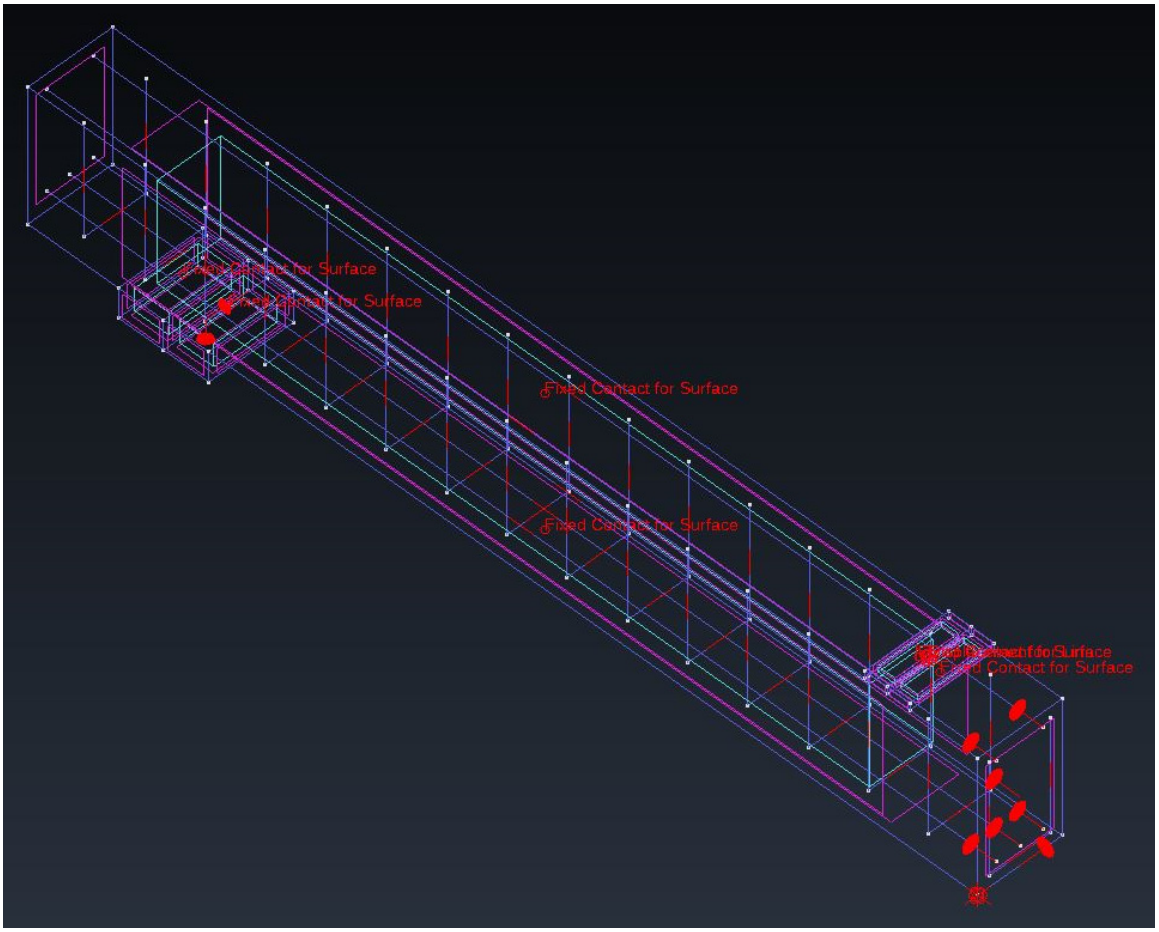

Figure C.1.7: Series 2 finite-element model boundary conditions (2GBH60)

Figure C.1.8, provides a representative example of the displaced shape and cracking behavior of a model for a point during its run in ATENA. Curvature seems higher at the beam center and large, flexural cracks are present in the constant-moment region of the model. These are accompanied by large horizontal cracks extending relatively deep into the cross section of the beam that result from tensile forces generated by the high compressive stresses in the concrete perpendicular to the cracking. Moving towards the support, cracks extend less high and are more inclined compared to cracks in the constant-moment region, consistent with the what is expected both in terms of displaced shape and cracking. Some cracks are smaller at the level of the tensile longitudinal reinforcement.

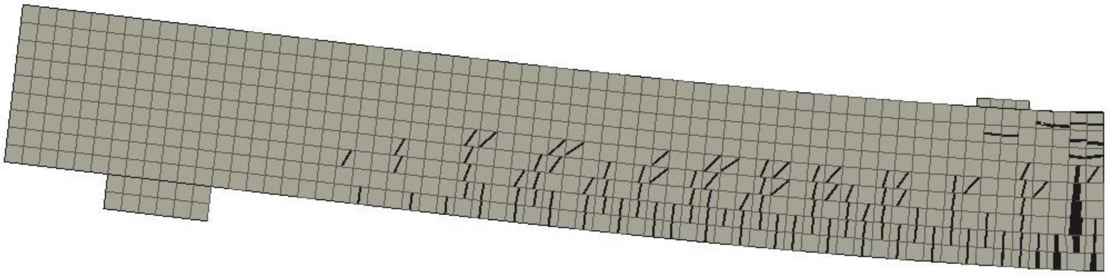

Figure C.1.8: Series 2 finite-element model during run (2GBH60)

C.1.4. Parametric Studies

A representative layout of elements for a finite-element model used in this study is displayed in Figure C.1.9. End blocks were used to constrain movement and enforce boundary conditions, as explained later in this section. Nodes defining the ends of the longitudinal reinforcement were placed on the surfaces representing the beam centerline and fixed end. Dimensions and reinforcement locations are provided in Section 6.3.

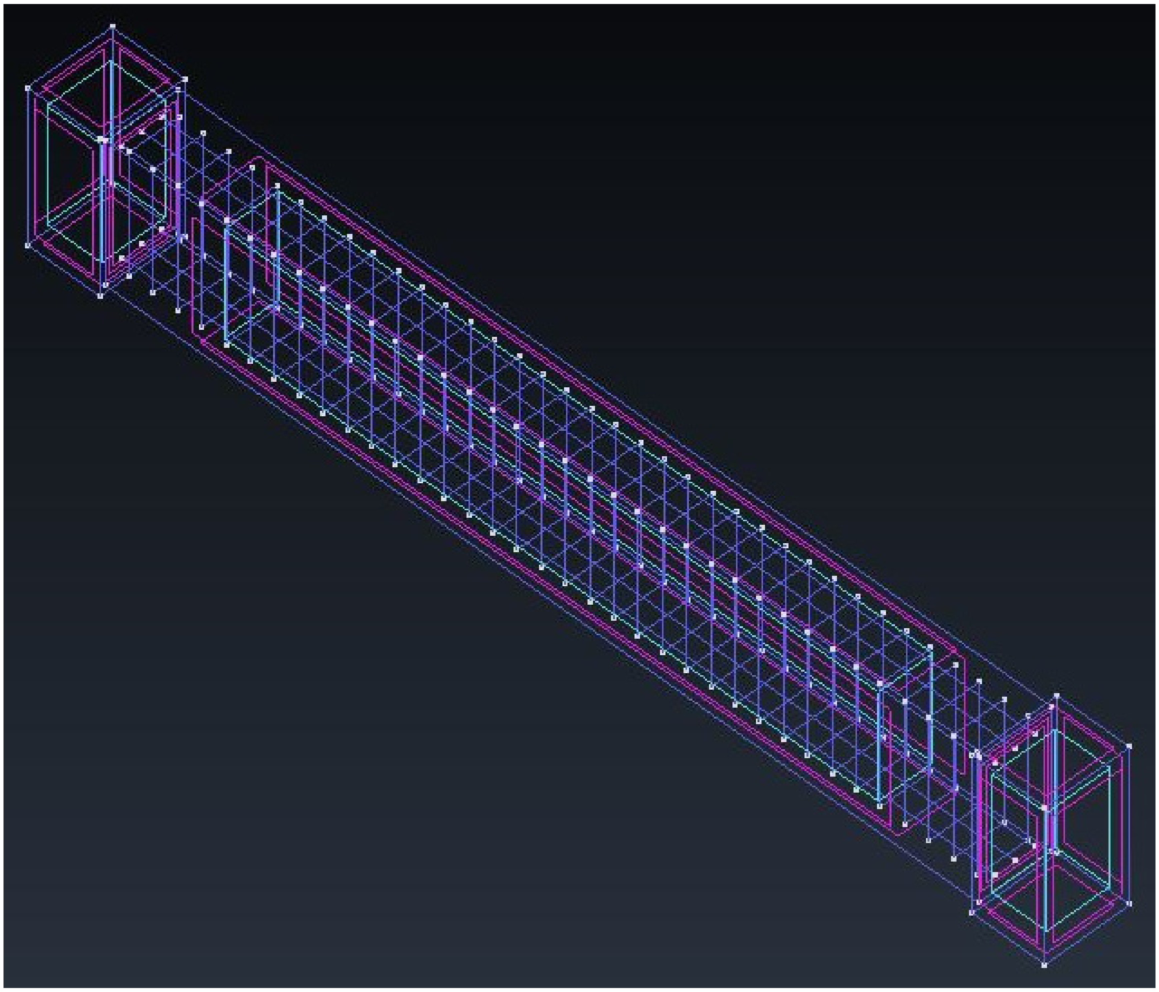

Figure C.1.9: Parametric study finite-element model layout (24FB60)

An example of a meshed member is depicted in Figure C.1.10. Here, the mesh size is exactly 2-in. square. The end representing the fixed support is to the left of the figure and the centerline is to the right. Reinforcement was meshed to give it the same length as elements it passed through (2 in. in this case).

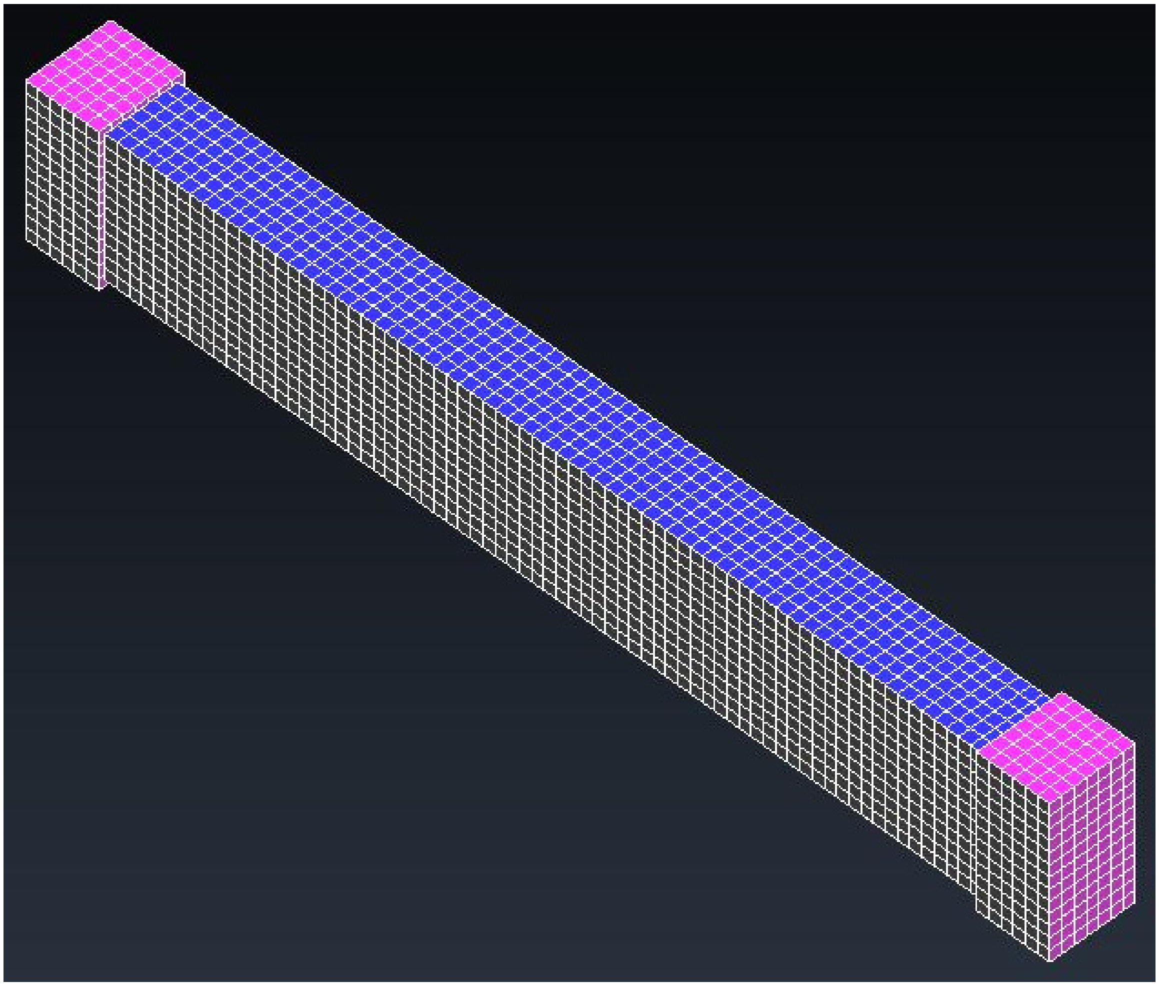

Figure C.1.10: Parametric study finite-element model mesh (24FB60)

Figure C.1.11 shows the boundary conditions for a representative model analyzed to investigate moment redistribution. End blocks were used to permit elongation of the beam while not allowing rotation of the surface at either end. This was accomplished by slaving infinitely rigid end blocks to either end of the half beam being analyzed, constraining the lateral and vertical displacement of the top and bottom surfaces of the left-end block, and fixing the end surface of the right end block against longitudinal and out-of-plane movement. After imposing these conditions on the model, a load increment of 0.1 lb/ft^2 downward was imposed. Thus, the incremental analysis of the model was displacement controlled. This may have caused issues with convergence at higher levels of load and displacement and is the reason for truncating the model output provided and discussed in Section 6.3.

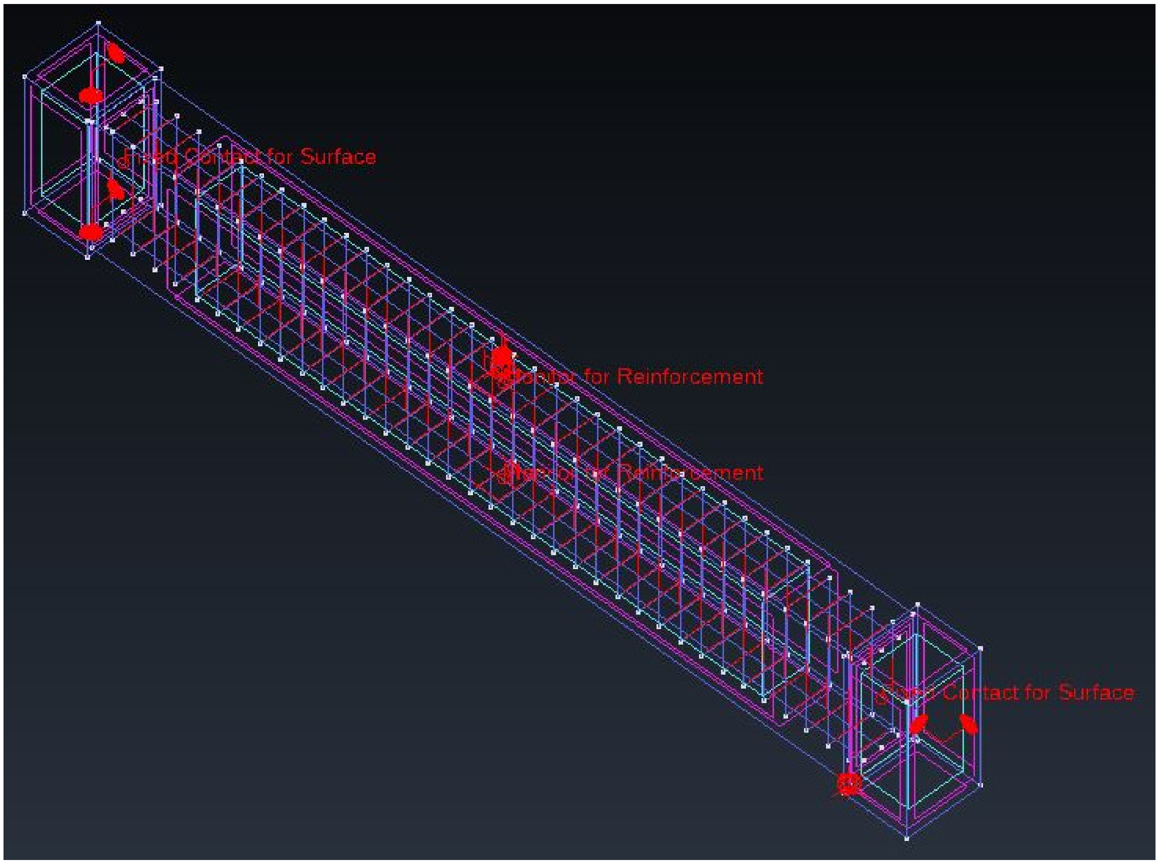

Figure C.1.11: Parametric study finite-element model boundary conditions (24FB60)

A representative displaced shape and cracking pattern for a beam during analysis in ATENA is given by Figure C.1.12. This figure is intended to give qualitative insight into the performance of the model. The fixed-end support is to the left and the centerline is to the right. The support, where yielding was expected first, shows larger and denser flexural cracking than the centerline. In addition, the cracks extend deeper into the section at the support, where a plastic hinge would be expected to form. Inclined cracks are present in locations of largest shear and absent in locations near zero shear, consistent with expectations. No cracking is present in the location where curvature reverses direction. The reverse-curvature displaced shape is also consistent with theoretical performance under the given loading.

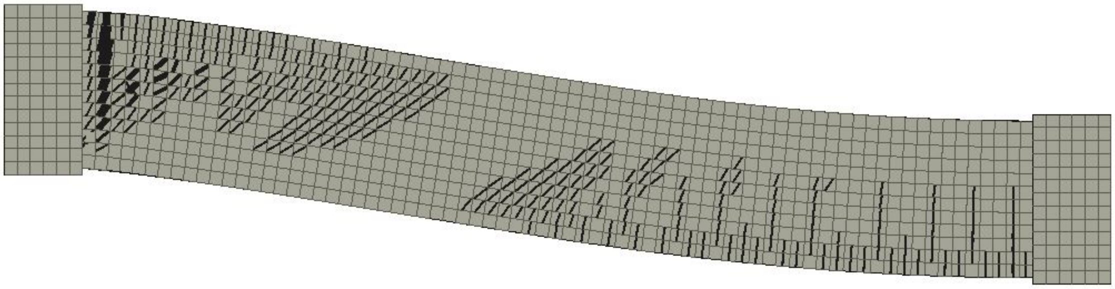

Figure C.1.12: Parametric study finite-element model during run (24FB60)